



Shear banding and the solid/liquid transition in yield stress fluids

Peder Moller

► To cite this version:

Peder Moller. Shear banding and the solid/liquid transition in yield stress fluids. Data Analysis, Statistics and Probability [physics.data-an]. Université Pierre et Marie Curie - Paris VI, 2008. English.
NNT: . tel-00327143

HAL Id: tel-00327143

<https://theses.hal.science/tel-00327143>

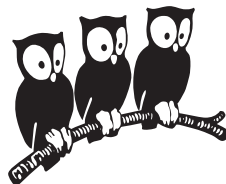
Submitted on 7 Oct 2008

HAL is a multi-disciplinary open access archive for the deposit and dissemination of scientific research documents, whether they are published or not. The documents may come from teaching and research institutions in France or abroad, or from public or private research centers.

L'archive ouverte pluridisciplinaire **HAL**, est destinée au dépôt et à la diffusion de documents scientifiques de niveau recherche, publiés ou non, émanant des établissements d'enseignement et de recherche français ou étrangers, des laboratoires publics ou privés.

Département de Physique
de l'École Normale Supérieure

LABORATOIRE DE PHYSIQUE STATISTIQUE



THÈSE DE DOCTORAT
DE L'UNIVERSITÉ PARIS 6 – PIERRE ET MARIE CURIE
Spécialité: Physique des Liquides

présentée par
Peder MØLLER

pour obtenir le grade de
DOCTEUR DE L'UNIVERSITÉ PARIS 6

Sujet de la thèse:

**Bandes de cisaillement et la transition
solide/liquide dans les fluides à seuil**

(Shear banding and the solid/liquid
transition in yield stress fluids)

Prévue en 6 octobre 2008 devant le jury composé de :

J.-L. BARRAT	Rapporteur
M. VAN HECKE	Rapporteur
M.A.J. MICHELS	Examinateur
P. COUSSOT	Examinateur
E. CLEMENT	Président du jury
D. BONN	Directeur de thèse

Acknowledgements

After three years of scientific training and discoveries, my thesis with all its ups and downs has come to an end. Numerous people have helped me achieve this goal and make the downs fewer, the ups more plentiful, and the general process more enjoyable. I owe them my gratitude.

First I would like to thank my supervisor Daniel Bonn for welcoming me into his team, and for letting me benefit from his scientific creativity, enthusiasm, and physical intuition. I have learned a lot from him! Numerous experimental techniques and procedures, but most notably how to leap haphazardly into a complex scientific problem with daring confidence rather than being paralyzed by the challenges.

Secondly I want to thank Sébastien Moulinet for many helpful discussions, showing me experimental techniques, and for running the practical side of the lab in S11 after Daniel moved to Amsterdam. Also the other permanent members of the team; Jacques Meunier, and Anne-Marie Cazabat are thanked for useful discussions.

In addition I wish to thank all the other people that have been part of the Soft Matter Physics, Instabilities, and Phase Transitions group during my stay here. I have had interesting discussions with all of them, and have learned a lot. Notably I need to thank Nicolas Huang who introduced me to the rheometers and practical rheometrical techniques. In addition I'm especially grateful to Mehdi Habibi, Dirk Aarts, Abdoulaye Fall, Didi Derks, Christophe Chevallier, and Ulysse Delarbre, for countless useful and interesting discussions, exchange of experimental skills, and small experimental collaborations that I have enjoyed greatly.

In addition to the scientific acknowledgements I want to thank all those people from the group (and other groups) that I have come to count among my friends for exactly that.

I have also had collaborations and discussions with people from different institutions. I owe thanks to Thijs Michels from Eindhoven University of Technology for providing a model for the viscosity of colloidal aggregates, and for discussions about the modeling of carbopol-like materials. I am also grateful to Stéphane Rodts from the University of Eastern Paris for configuring the MRI setup for measurements on the colloid-salt water mixture. And I want to thank Jan Mewis from Katholieke Universiteit Leuven for collaboration on the thixotropy of yield stress fluids.

In addition to the people mentioned above, I have had numerous interesting and encouraging discussions with several people at various conferences, and even if I can't mention all of them here I have enjoyed those discussions as well.

I also would like to thank the scientists who have agreed to be members of the jury of my defense for taking their time to examine my work and to contribute with their comments and critique at the defense. I thank the rapporteurs Martin van Hecke and Jean-Louis Barrat, the examinateurs M.A.J. Michels and Philippe Coussot, and the president of the jury Eric Clement.

I am grateful to the EU Framework Programme 6 Marie Curie Research Training Networks scheme (under grant MRTN-CT-2004005728 (PATTERNS)), who have provided the funding for my thesis. I also owe thanks to the institutions that have made my stay here practically possible: Laboratoire de Physique Statistique and its directors during my stay here; Jacques Meunier and Eric Perez, and to Département de Physique de l'Ecole Normale Supérieure and its director Jean-Michel Raimond. And also the Centre National de Recherche Scientifique and Université Paris VI. I also owe thanks to certain people in the LPS for help with technical or administrative tasks. Notably the secretaries Nora, Annie, and Marie, and José and Olivier in the workshop.

Least but certainly not last I'm eternally grateful to a number of people who have not been directly involved in the scientific work during my thesis. Some of these people have helped me a lot along the way, and some of them have been outright essential for me even beginning my thesis, and also for *much* more important things. First and foremost I need to thank my wonderful and loving family for so many and essential things that I cannot even begin to mention them here. And secondly, I am lucky to have a truly fantastic girlfriend together with whom I came to Paris. Her wonderful company here have turned miserable times into agreeable ones, and agreeable times into happy ones. Finally I want to thank Sid Nagel and Lene Oddershede for being great inspirations as scientists as well as persons.

Contents

Acknowledgements	iii
I Introduction to Rheology	1
1 Rheology: The study of non-Newtonian fluids	3
1.1 Introduction	3
1.2 The response of simple materials to an external stress	4
1.3 The flow properties of simple yield stress fluids	4
1.3.1 Flow curves and phenomenological models for simple yield stress fluids	6
1.4 The flow properties of thixotropic yield stress fluids	9
1.4.1 The problems with <i>the</i> yield stress	10
1.4.2 Viscosity bifurcation and avalanche behavior	11
1.4.3 Aging and rejuvenation: A toy-model of a thixotropic fluid	13
1.5 Micro- and mesoscopic models for complex fluids	16
1.5.1 Molecular dynamics simulations	16
1.5.2 reptation, an example of polymer scaling concepts	16
1.5.3 The SGR model, an example of a mesoscopic model	17
1.6 Granular materials as a complex fluid	18
1.7 This thesis	19
2 Measurement techniques	21
2.1 Introduction	21
2.2 Active rheological techniques	22
2.2.1 The rheometer	22
2.2.2 The Couette, double-gap, and vane-cup geometries	23
2.2.3 Shear banding of simple yield stress fluids	24
2.2.4 The cone-plate geometry	26
2.3 Active rheological tests	26
2.3.1 Shear stress/rate sweep tests	27
2.3.2 Shear strain/stress-relaxation tests	27
2.3.3 Oscillatory sweep tests	27

2.4	Passive measurement techniques	28
2.4.1	Brownian motion	29
2.4.2	Microrheology	29
2.4.3	Dynamic Light Scattering and Diffusing Wave Spectroscopy	30
2.5	Magnetic Resonance Imaging (MRI) velocimetry	31
II	Simple yield stress fluids	35
3	The yielding behavior of simple yield stress fluids	37
3.1	Introduction	37
3.2	Materials and Methods	39
3.3	Experimental results	39
3.4	A simple physical model for carbopol	43
3.5	Simulation results and comparison to experiments	46
3.6	Discussion of the model and results	48
3.7	General discussion	50
3.8	Conclusion	52
III	Thixotropic yield stress fluids	55
4	What makes a fluid thixotropic	57
4.1	Introduction	57
4.2	Colloidal interactions: van der Waals forces and Debye lengths	58
4.3	Ludox spheres and salt water	59
5	The negative slope of the flow curve	63
5.1	Introduction	63
5.2	Behavior of the λ -model away from the steady state	64
5.2.1	The evolution of the λ -model under an imposed stress	64
5.2.2	The yield stress measurement problems explained by the λ -model .	66
5.2.3	How to experimentally demonstrate the negative slope of the steady state flow curve	68
5.3	Experimental results	69
5.4	Conclusion	71
6	Shear banding in thixotropic yield stress fluids	73
6.1	Introduction	73
6.2	Some previous shear banding experiments	74
6.3	Shear banding in the λ model	74
6.3.1	Shear banding in heterogeneous stress fields	75
6.3.2	Shear banding in homogeneous stress fields	75
6.3.3	The <i>lever rule</i>	76

6.4	MRI velocimetry experiments	77
6.4.1	Experimental procedure	77
6.4.2	MRI velocimetry results	78
6.4.3	Experimental demonstration of the lever rule	79
6.5	Comparing the MRI and rheometrical measurements	80
6.5.1	A negative slope in the steady state flow curve can result in a stress plateau under imposed shear rate	81
6.6	Measuring the local state of the material	83
6.6.1	DWS measurements inside and outside the flowing band	84
6.7	A serious limitation of the lever rule	86
6.8	Practical handling of thixotropic yield stress fluids	88
6.9	Conclusion	89
7	A physical model for the rheology of colloids in salt water	91
IV	Moist granular materials	95
8	The elastic modulus of moist granular matter	97
8.1	Introduction	97
8.2	Materials and methods	98
8.3	Experimental results	100
8.4	Predicting the elastic shear modulus of moist granular materials	100
8.5	Discussion	103
8.6	Conclusion	106
9	General conclusion	107
A	Numerical code for simulating carbopol	111
B	Publications	113
C	Bibliography	141

Part I

Introduction to Rheology

Chapter 1

Rheology: The study of non-Newtonian fluids

Contents

1.1	Introduction	3
1.2	The response of simple materials to an external stress	4
1.3	The flow properties of simple yield stress fluids	4
1.3.1	Flow curves and phenomenological models for simple yield stress fluids	6
1.4	The flow properties of thixotropic yield stress fluids	9
1.4.1	The problems with <i>the</i> yield stress	10
1.4.2	Viscosity bifurcation and avalanche behavior	11
1.4.3	Aging and rejuvenation: A toy-model of a thixotropic fluid	13
1.5	Micro- and mesoscopic models for complex fluids	16
1.5.1	Molecular dynamics simulations	16
1.5.2	Reptation, an example of polymer scaling concepts	16
1.5.3	The SGR model, an example of a mesoscopic model	17
1.6	Granular materials as a complex fluid	18
1.7	This thesis	19

1.1 Introduction

In freshman classical mechanics a physics or engineering student will normally encounter two types of materials (apart from ideal particles and gases): Elastic solids, and Newtonian fluids. An elastic solid is a material that when subject to a force undergoes a total deformation that is proportional to the size of the force. At sufficiently low levels of deformation (and sufficiently short measurement times) *all* solids are elastic solids and

some materials (notably rubber) are elastic for large deformations and long times. A Newtonian fluid is a material where the *rate* of deformation is proportional to the forcing involved. Many of the materials that are ubiquitous in our everyday life are neither elastic solids nor Newtonian fluid however. This is especially true for many foodstuffs like mayonnaise, whipped cream, gels, whipped egg whites, custards etc., which will flow readily like a fluid when stirred with a spoon or savored in the mouth, but will nevertheless keep their shape like a solid if left under only the force of gravity. Rheology is the study of the wealth of such very different materials whose mechanic properties cannot be reduced to either an elastic constant or a viscosity. The behavior of these substances varies greatly, spanning from shear-thinning fluids where the viscosity decreases with the rate of deformation [1–11] over shear-thickening fluids where the viscosity increases abruptly and strongly at high shear rates [1, 2, 6, 7, 12–18], to shake-gels where a fluid is reversibly turned into a solid state when shaken and return to a liquid under rest [19, 20], and strongly thixotropic fluids that do exactly the opposite [21–32]. In this chapter I will present an fundamental introduction to the rheological materials and concepts that are relevant for understanding the subsequent chapters.

1.2 The response of simple materials to an external stress

Consider the response of an infinite plate of an elastic solid of height, h , subject to a **shear stress** (the tangential force, F , per unit area, A) of $\sigma \equiv F/A$ in opposite directions on the two opposing faces as in Fig. 1.1. The external force will deform the material - moving the upper plate some distance d with respect to the lower one - until it is balanced by the elastic response of the material. It is easily seen that if all other parameters are fixed d will be proportional to h , so in order to get a parameter independent of the height of the block the **shear strain** of the material is defined as $\gamma \equiv d/h$. For an elastic solid the shear strain is proportional to the shear stress - it follows **Hooke's law**:

$$\sigma = G' \gamma \quad (1.1)$$

where the constant of proportionality, G' , is the **shear elastic modulus**. If the infinite plate was not an elastic solid but a Newtonian fluid no final shear strain exists. The material will keep deforming and it will do so at a constant rate - the **shear rate** - defined as $\dot{\gamma} \equiv d\gamma/dt$. For a **Newtonian fluid** the shear rate is proportional to the shear stress, and the constant of proportionality is called the **viscosity**:

$$\sigma = \dot{\gamma}\eta \quad (1.2)$$

1.3 The flow properties of simple yield stress fluids

Many of the materials we encounter on a daily basis are neither elastic solids nor Newtonian fluids, and attempts to describe these materials as either fluid or solid fail; try for

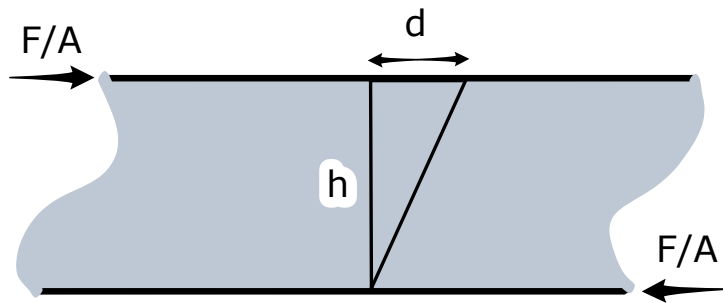


Figure 1.1: The finite response of an elastic solid confined between two infinite plates to a tangential force per unit area of $F/A \equiv \sigma$ applied to the two plates in opposite directions. The material is strained by $\gamma = \sigma/G'$, causing the upper plate to move a distance $d = h\gamma$.

instance to determine which material has the higher “viscosity” whipped cream or thick syrup: When moving a spoon through the materials we clearly conclude that syrup is the more viscous fluid, but if we leave the fluids at rest the syrup will readily flatten and become horizontal under the force of gravity while whipped cream will keep its shape and we are forced to conclude that whipped cream is more viscous than syrup (Fig. 1.2). The problem is that while the syrup is a Newtonian fluid, whipped cream is not, and its flow properties cannot simply be reduced to a viscosity.



Figure 1.2: Comparing the flow properties of whipped cream and thick pancake syrup: While few people would hesitate to say that the syrup has the higher viscosity when stirring the two materials with a spoon, the situation is reversed when observing the flattening of two piles of the material. So which fluid *does* have the higher viscosity? The “answer” is that the question is ill posed; the flow properties of whipped cream cannot be reduced to a viscosity.

1.3.1 Flow curves and phenomenological models for simple yield stress fluids

To quantify the steady state flow properties of non-Newtonian fluids, since the viscosity is not defined, one typically measures the **flow curve** which is a plot of the shear stress *vs.* the shear rate such as in Figs. 1.3A and 1.3B. There it can be seen that while syrup is Newtonian, whipped cream is not at all: It hardly flows if the imposed stress is below about 33 Pa , but it flows at very high shear rates at stresses above this value. A material with this property is called a **yield stress fluid** and the stress value that marks this abrupt transition is called the **yield stress**. Yield stress fluids come in two distinct flavors: thixotropic and non-thixotropic (or simple) yield stress fluids. A **simple yield stress fluid** is one for which the shear stress (and hence the viscosity) depends only on the shear rate, while for thixotropic fluids the viscosity depends also on the shear *history* of the sample. While thixotropic materials are treated in section 1.4, the present section deals with simple yield stress fluids.

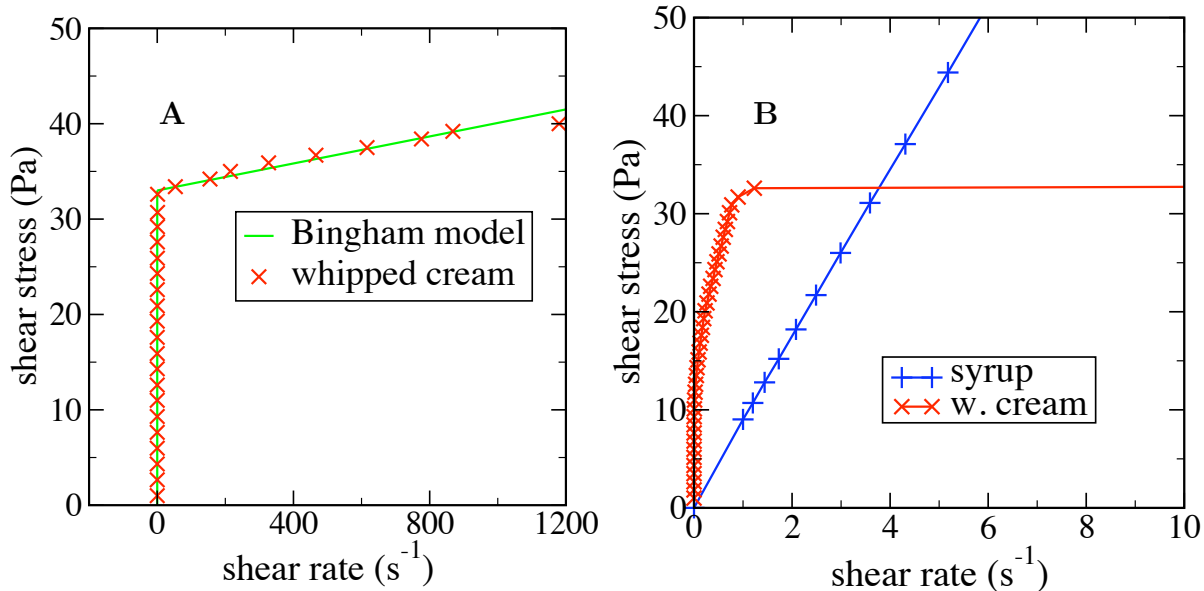


Figure 1.3: **A:** The Bingham model gives an excellent fit to the flow curve of whipped cream in this figure and the yield stress is seen to be about 33 Pa . **B:** The flow curves of syrup and whipped cream at low shear rates. Data points are connected by lines. It is seen that for stresses above about 33 Pa whipped cream flows more easily while the opposite is true below 33 Pa . In this close up on the flow curve of whipped cream at low shear rates it is also seen that the Bingham model no longer provides an equally good fit to the data.

The most basic model for catching simple yield stress fluid behavior is the

Bingham model [33]:

$$\sigma < \sigma_y \Rightarrow \dot{\gamma} = 0 \quad (1.3)$$

$$\sigma > \sigma_y \Rightarrow \sigma - \sigma_y = A\dot{\gamma} \quad (1.4)$$

where σ_y the yield stress and A a model parameter designating the slope of the flow curve in the fluid region. The Bingham model is seen to result in an **effective viscosity** which is asymptotically A at high stresses and diverges continuously as the stress drops towards the yield stress: $\eta_{eff} = \sigma/\dot{\gamma} = A + \sigma_y/\dot{\gamma}$. In Fig. 1.3A the flow curve of whipped cream is shown and it can be seen that the Bingham model gives an excellent fit to the flow curve with a yield stress of about 33 Pa. In Fig. 1.3B the flow curves of whipped cream and syrup are shown together and it can be seen that the answer to the question of which "fluid" has the higher viscosity depends on the relevant shear rates/stresses; for shear rates (stresses) above 4 s⁻¹ (33 Pa), syrup is clearly the more viscous material, but for shear rates (stresses) below that value, whipped cream is by far the more "viscous" material. It is also evident that while the Bingham model gives an excellent fit to the flow curve of whipped cream when the shear rate resolution is above unity it fails once the resolution is improved, and from Fig. 1.3B one would conclude that the yield stress is about 10 Pa rather than 33 Pa. This is something *very* often encountered when working with complex fluids: Before a question about the flow properties of a complex material can be satisfactorily answered one needs to know what the relevant range and resolution of shear rates/stresses is.

Not all yield stress materials are well described to the desired resolution and over the desired range of shear rates by the Bingham model, and a large number of similar models exist (see [34, 35] and references therein). Probably the model used most often to fit the flow curve of yield stress fluids is the **Herschel-Bulkley model** [36] which is a modified Bingham model where the shear stress does not depend linearly on the shear rate, but on the shear rate to some power, B :

$$\sigma < \sigma_y \Rightarrow \dot{\gamma} = 0 \quad (1.5)$$

$$\sigma > \sigma_y \Rightarrow \sigma - \sigma_y = A\dot{\gamma}^B \quad (1.6)$$

Flow curves with different exponents of B can be seen in Fig. 1.4. Using the Herschel-Bulkley model in place of the Bingham model can to some degree solve the problems defining the proper yield stress for simple yield stress fluids (as that for the whipped cream in Fig. 1.3B) since an exponent $B < 1$ gives a more smooth transition between the flowing and solid state which is seen to be required for whipped cream. On the other hand, the yield stress becomes more diffuse since the optimal value of the yield stress will depend greatly on the exponent, B , and the resulting yield stress can sometimes be greatly different from the effective yield stress. In Fig. 1.4 the Herschel-Bulkley model provides a very good fit the the flow curve of an aqueous carbopol sample which is *the* material most often used by scientists as a 'model' simple yield stress fluid (see [37] for a review on carbopol and [38] for a special issue of Journal of Non-Newtonian Fluid Mechanics dedicated to simulations of simple yield stress fluids that are almost exclusively compared

to measurements on carbopol). A detailed study of the compositional and flow properties of carbopol is presented in chapter 3.

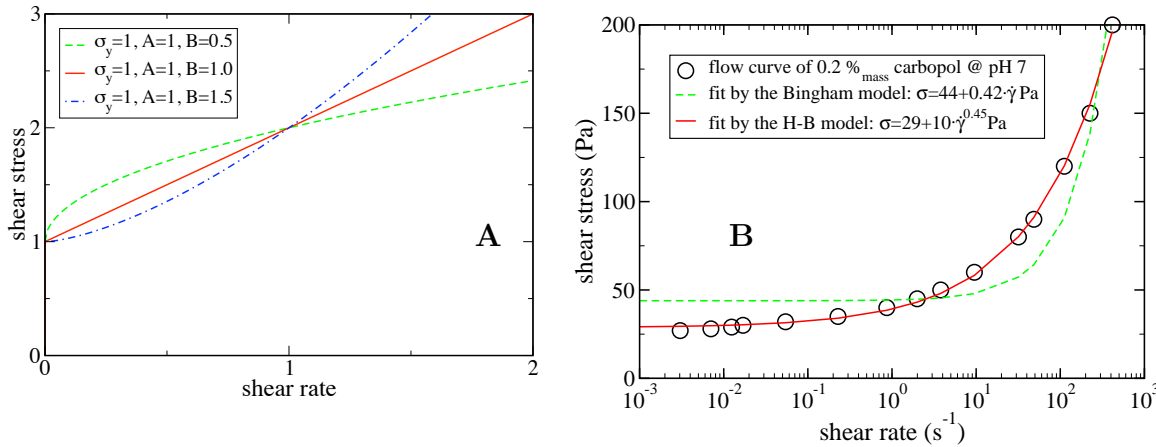


Figure 1.4: **A:** Flow curves from the Herschel-Bulkley model (equations 1.5 and 1.6) with different values of the power law exponent B . When $B = 1$ the Herschel-Bulkley model reduces to the Bingham model. **B:** While the Bingham model (equations 1.3 and 1.4) gives a moderate fit to the flow curve of 0.2 % carbopol in water at $pH = 7$, the Herschel-Bulkley model gives an impressive fit over a *very* large range of shear rates (NB: Log scale).

Probably the most spectacular feature of yield stress fluids is observed also at the breakfast table: While stirring a teaspoon in a teacup readily sets the whole fluid in motion, stirring a teaspoon in the sugar bowl has not at all the same effect; only material relatively close to the spoon is sheared while the remainder of the material stays motionless. This phenomenon where one part of the material is being sheared at a high rate while the material behaves like a solid elsewhere is called **shear banding** and can be observed for all yield stress fluids - simple and thixotropic. While shear banding in thixotropic yield stress fluids is a slightly complicated affair to which I shall return in chapter 6, shear banding in simple yield stress fluids is not all that complicated and, as I will show in chapter 2, it can be understood fully as a consequence of having a yield stress fluid in a heterogeneous stress field.

Shear banding occurs in numerous industrial applications where yield stress fluids are handled, like mold filling and materials transport and processing. In such situations shear banding is mostly not desired since it can result in partially filled molds, spoilable materials left in transportation tubes, only partial mixing of materials, etc. In order to prevent such problems, engineers wish simulate the behavior of a material in a processing/transport system in order to design it for optimal performance. Such simulations are done almost exclusively on simple yield stress fluid models since the phenomenological understanding of simple yield stress fluids such as carbopol is very good indeed: Experimental measurements of the materials properties are easily performed. These quantitative

data are readily fit by the Herschel-Bulkley or similar models. Feeding these fitting parameters and a flow geometry into a computer, the resulting flows can be simulated to an impressive precision that predict full scale, three dimensional flows very well (see for instance the special issue of Journal of Non-Newtonian Fluid Mechanics dedicated to this type of simulations, [38]). Using such simulations engineers can design their mold filling equipment, transportation systems, oil drilling facilities, mixing systems etc. to perform optimally. If the handled materials *are* indeed simple yield stress fluids like carbopol, that is. One of the difficulties in the field is that many yield stress materials such as oil drilling muds, crude oils, clayey soils etc. are not, because they are thixotropic.

1.4 The flow properties of thixotropic yield stress fluids

Actually, the simple yield stress behavior of carbopol is the exception rather than the rule. By far the majority of yield stress materials are *not* 'simple yield stress fluids' and they do *not* behave like carbopol. They are **thixotropic** materials, which means that they have a viscosity that depends not only on the instantaneous shear rate (as is the case for simple yield stress fluids) but also on the shear *history* of the sample [21, 23, 31, 34, 35]: at high shear rates the viscosity is decreasing in time while it is restored with time at low shear rates. This shear history dependent viscosity is due to the *microstructure* of the fluid being built up at rest, and broken down under shear. For natural and synthetic clays (which constitute a large group of thixotropic yield stress fluids), this microstructure is composed of the clay platelets sticking together and forming a 'house of cards' structure that resist flow. Since the microstructure is automatically built up at low and zero shear rates, and broken down at high shear rates, thixotropy is a completely reversible phenomenon. Since for yield stress fluids, it is the microstructure of the material that is resisting flow and giving rise to the yield stress, it is perhaps not surprising that the phenomena of thixotropy and yield stress are intimately linked, and only very rarely do the one show up without the other (indeed, I know of no other example for this than carbopol). Whether a material is thixotropic or not is measured by increasing the shear stress/rate and then decreasing it while continuously measuring the resulting shear rate/stress. If the viscosity is a function of the shear rate only, the two curves should coincide. If the viscosity depends also on the shear history of the sample, they should not - the increasing part of the curve should show a larger viscosity than the decreasing part. An example of thixotropic behavior is shown in Fig. 1.5. The material in that figure is 10 % bentonite clay suspended in water, and it is clearly *very* thixotropic - the viscosity at a shear stress of 15 Pa varies five orders of magnitude! As is described in the following sections, while the phenomenological understanding of carbopol-like materials is very impressive, the same cannot be said for thixotropic materials: It is far from trivial to perform reproducible measurements on such materials. The obtained data are rarely described well by Herschel-Bulkley or similar models. Agreement between large scale flows and simulations based on rheological measurements is generally very poor. And finally, even qualitatively the simple yield stress picture that works so well for simple yield stress fluids often fails dramatically

for thixotropic materials.

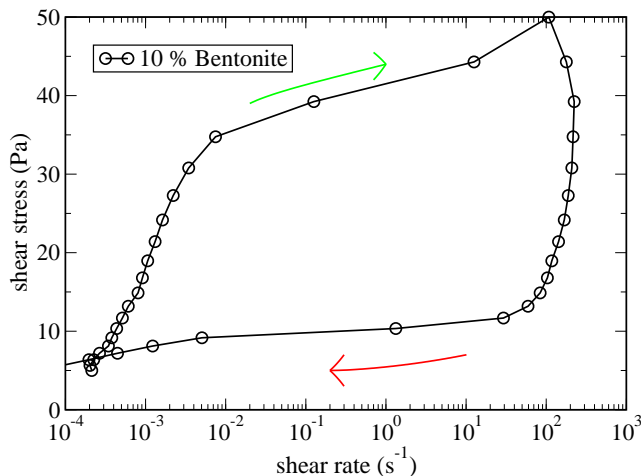


Figure 1.5: Thixotropy of a 10 %_{mass} bentonite solution under an increasing and then decreasing stress ramp. Since the data from the increasing and decreasing ramps do not coincide the sample is thixotropic, and the larger the area between the two curves the more thixotropic the sample is. Indeed, at a stress of 15 Pa the difference in shear rates between the increasing and decreasing ramps is five orders of magnitude! The bentonite and water is mixed at a shear rate of 20 s^{-1} for 4 hours, and then left to rest for 20 minutes. Then the imposed stress is increased logarithmically from 5 Pa to 50 Pa in 20 steps and then decreased in the same way. Each stress is imposed for 15 seconds, and the data points are averages over the last 5 seconds.

1.4.1 The problems with *the yield stress*

Maybe the most ubiquitous problem encountered by scientists and engineers dealing with everyday materials such as food products, powders, cosmetics, crude oils, concrete etc. is that the yield stress of a given material has turned out to be very difficult to determine [28, 31, 39]. In the concrete industry the yield stress is very important since it determines whether air bubbles will rise to the surface or remain trapped in the wet cement and weaken the resulting hardened material. Consequently a large number of tests have been developed to determine the yield stress of cement and similar materials [40–43]. However, the different tests often give very different results and even in controlled rheology experiments the same problem is well documented: Depending on the measurement geometry and the detailed experimental protocol, very different values of the yield stress can be found [23, 39, 44–46]. Indeed it has been demonstrated that a variation of the yield stress of *more than one order of magnitude* can be obtained depending on the way it is measured [44]. The huge variation in the value for the yield stress obtained cannot be

attributed to different resolution powers of different measurement techniques, but hinges on more fundamental problems with the applicability of the picture of simple yield stress fluids to many real-world yield stress fluids. This is of course well known to rheologists, but since no reasonable and easy way of introducing a variable yield stress is generally accepted, researchers and engineers often choose to work with the yield stress nonetheless and treat it as if it is a material constant which is just tricky to determine, or as Nguyen and Boger put it [46]: “Despite the controversial concept of the yield stress as a true material property ..., there is generally acceptance of its practical usefulness in engineering design and operation of processes where handling and transport of industrial suspensions are involved.” One method that has been used for such applications is to work with two yield stresses - one static and one dynamic - or even a whole range of yield stresses (Mujumdar et al. [28] and references therein). The static yield stress is the stress above which the material turns from a solid state to a liquid one, while the dynamic yield stress is the stress where the material turns from a liquid state to a solid one. For example in Fig. 1.5, one would take the static yield stress to be about 35 Pa , and the dynamic yield stress to be about 10 Pa .

These difficulties have resulted in lengthy discussions of whether the concept of the yield stress is useful for thixotropic fluids and how it should be defined and subsequently determined experimentally if the model is to be as close to reality as possible. In Fig. 1.6A schematic time evolutions of the shear stress resulting from different constant shear rates being imposed on a typical yield stress fluid are shown [45]. As can be seen in that figure, the stress at the end of the linear elastic region, the maximum stress, and the stress at the plateau beyond the peak have all been suggested as possible definitions of the yield stress. This figure is idealized however, and determining the yield stress from actual data is even more difficult as can be seen from Fig. 1.6B. Perhaps even worse, almost unrelated to the exact definition and method used, yield stresses obtained from experiments generally are not adequate for determining the conditions under which a yield stress fluid will flow and how exactly it will flow, since generally the yield stress measured in one situation is different from the yield stress measured in a different situation [23, 29, 39, 45–48]. The problem is, that in spite of the fact that it is the microstructure that gives rise to both the yield stress and thixotropy, the two phenomena are never considered together. For instance, Barnes wrote two different reviews on the yield stress [39] and thixotropy [23], each without considering the other.

1.4.2 Viscosity bifurcation and avalanche behavior

A very striking demonstration of how the simple yield stress fluid picture often fails predicting even qualitatively the flow of actual yield stress fluids is the ‘avalanche behavior’ which has recently been observed for thixotropic yield stress fluids [47]. One of the most simple tests to determine the yield stress of a given fluid is the so-called inclined plane test [50, 51]. A large amount of the material is deposited on a plane which is subsequently slowly tilted to some angle, α , when the fluid starts flowing. According to the Herschel-Bulkley and Bingham models, the material will start flowing when an angle is reached

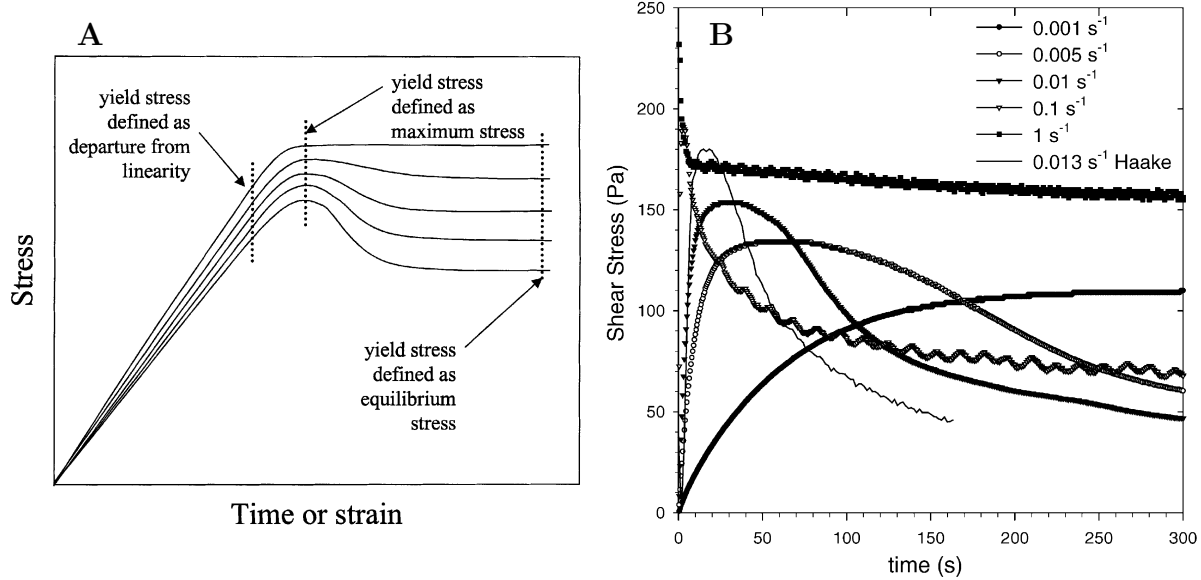


Figure 1.6: **A:** Schematic time evolution of the stress for imposed shear rate experiments at different imposed rates, and different attempts at defining a yield stress [45]. **B:** Time evolution of the stress from actual experiments - on a lamellar gel-structured cream - at different imposed shear rates and different instruments [49]. Choosing a value for the yield stress is far from obvious.

for which the tangential gravitational force per unit area at the bottom of the pile is larger than the yield stress; $\rho gh \sin(\alpha) > \sigma_y$, with ρ the density of the material, g the gravitational acceleration and h the height of the deposited material. In reality however, inclined plane tests on a clay suspension reveal that for a given pile height there is a critical slope above which the sample starts flowing, and once it does, the thixotropy leads to a decrease in viscosity which accelerates the flow since fixing the slope corresponds to fixing the stress [47]. This in turn leads to an even more pronounced viscosity decrease and so on; an avalanche results, transporting the fluid over large distances, where a simple yield stress fluid model predicts that the fluid moves only infinitesimally when the critical angle is slightly exceeded, since the pile needs only flatten a bit for the tangential gravitational stress at the bottom of the pile to drop below the yield stress. That indeed a constant, imposed stress can result in a strongly decreasing viscosity (and correspondingly dramatically increasing shear rates) can be seen in Fig. 1.7 where the viscosity of a 10 % bentonite suspension is seen to decrease more than four orders of magnitude during 500 seconds under an imposed stress of 60 Pa. In Fig. 1.8 photos and quantitative data from an inclined plane experiment on a bentonite suspension are shown [47]. It is clearly seen that once the fluid gets going, it accelerates and flows to cover large distances rather than only spreading slightly as predicted by simple yield stress models. In the same figure the Herschel-Bulkley model is seen to provide a very poor fit to the data - it is clearly an inadequate description of the material. It is interesting to compare the results of the inclined plane tests with experiments showing avalanches in granular materials

- a situation for which there is a general agreement that avalanches exist. The exact same experiment had in fact been done earlier for a heap of dry sand, with results that are strikingly similar to those observed for the bentonite - notably identical horse-shoe shaped piles are seen to be left behind the avalanche in both experiments - see Fig. 1.9A.

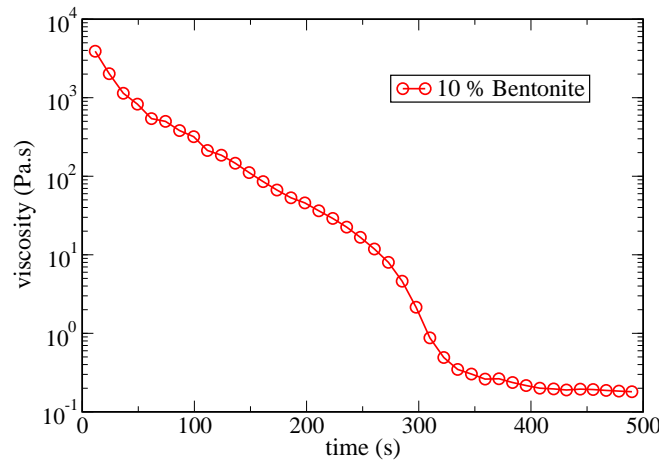


Figure 1.7: Thixotropy of a 10 %_{mass} bentonite solution under a constant shear stress. The measurement is performed on the same sample as in Fig. 1.5 which has been allowed to age overnight. The viscosity is seen to decrease more than four orders of magnitude within 500 seconds. Since the shear stress is constant, this leads to a 10,000 fold increase in the shear rate within 500 seconds - avalanche behavior!

In the more quantitative experiment accompanying the inclined plane test [29], a sample of 4.5% bentonite solution, which is a thixotropic fluid as can be seen in Fig. 1.5, was brought to the same initial state by a controlled history of shear and rest. Starting from this identical initial condition, different levels of shear stress were imposed on the samples and the viscosity was measured as a function of time. The result is shown in Fig. 1.9B and deserves some discussion. For stresses smaller than a critical stress, σ_c , the resulting shear rate is so low that build up of structure wins over the destruction of it, and the viscosity of the sample increases in time until the flow is halted altogether. On the other hand, for a stress only slightly above σ_c , destruction of the microstructure wins, and the viscosity decreases with time towards a low steady state value $\eta_0 \approx 0.1$ Pa.s. The important point here is that the transition between these two states is discontinuous as a function of the stress. This phenomenon is now called **viscosity bifurcation**.

1.4.3 Aging and rejuvenation: A toy-model of a thixotropic fluid

Since the increase of viscosity with time is also seen in glasses where it is called **aging**, the same term is used to describe the same phenomenon in yield stress fluids, while the oppo-

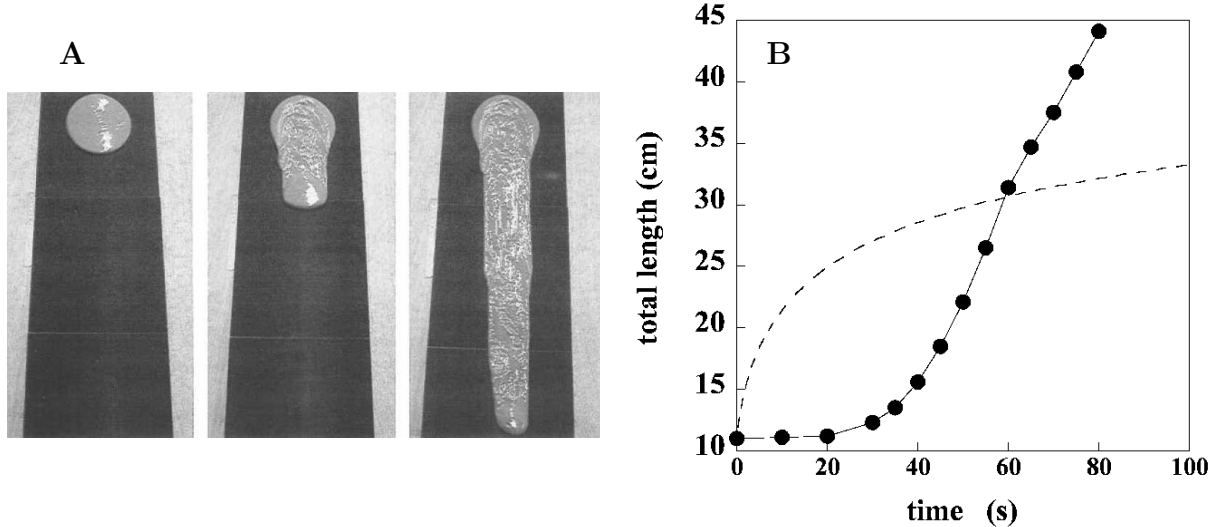


Figure 1.8: **A:** Avalanche-like flow of a clay suspension over an inclined plane covered with sandpaper. The experiment was performed *just* above the critical angle below which the fluid behaves like a solid [47]. While any simple yield stress fluid model would predict only infinitesimal spreading of the pile when the yield stress is slightly exceeded, in reality an avalanche results. **B:** Distance covered by the fluid front in an inclined plane experiment [47]. The Herschel-Bulkley model is seen to provide a very poor fit (dashed line) to the experimental points that evolve in the “opposite” manner.

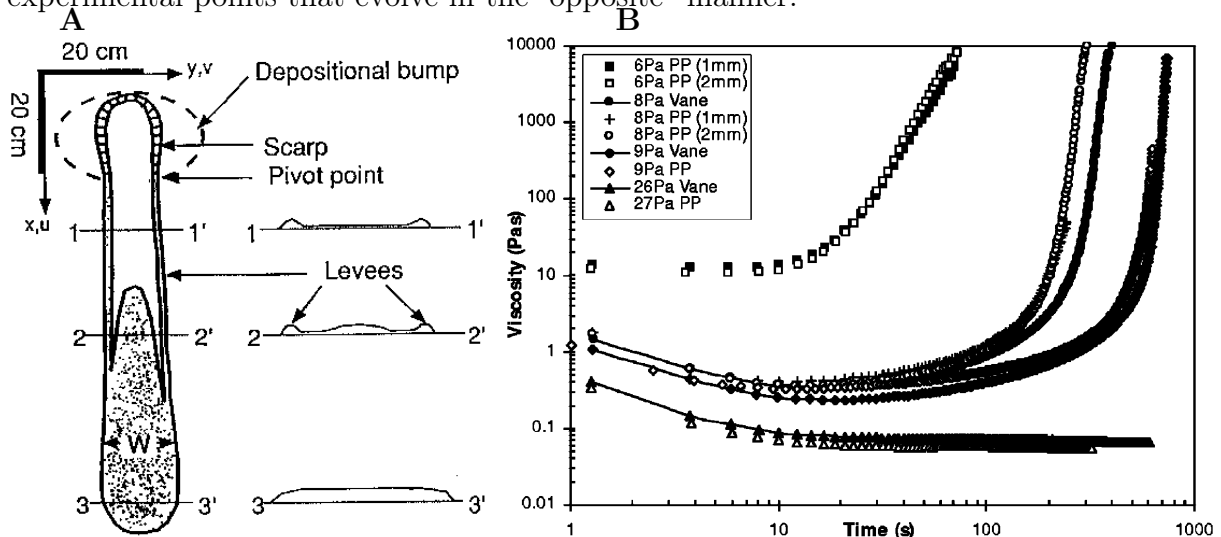


Figure 1.9: **A:** The inclined plane experiment with a heap of dry sand. The similarity of the resulting avalanche deposit with that of the clay avalanche is striking, especially the very characteristic ‘horseshoe’ form at the top of the plane [52]. **B:** The time evolution of the viscosity of identical initial states with different applied stresses. A bifurcation in the steady state viscosity is seen to occur at a critical stress, σ_c , between 9 and 26 Pa.s [29].

site phenomenon - that of the viscosity decreasing under high shear rates - is called **shear rejuvenation**. Thixotropy is the phenomena of reversible aging and shear rejuvenation. It is generally perceived that what causes thixotropic behavior is the individual particles in the material assembling into a flow-resisting microstructure when the fluid is at rest, and that the microstructure is torn apart to give a lower viscosity under shear [31]. A simple toy-model based on this feature of a thixotropic fluid is used by the authors of [29, 47] in order to qualitatively understand their avalanche and viscosity bifurcation data. The basic assumptions of the model are:

1. There exists a structural parameter, λ , that describes the local degree of interconnection of the microstructure.
2. The viscosity increases with increasing λ .
3. For an aging system at low or zero shear rate λ increases, while the flow at sufficiently high shear rates breaks down the structure and λ decreases to a low steady state value.

These assumptions are quantified into a toy-model for the evolution of the microstructure and the viscosity as [29]:

$$\frac{d\lambda}{dt} = \frac{1}{\tau} - \alpha\lambda\dot{\gamma} \quad \text{and} \quad \eta = \eta_0 \cdot (1 + \beta\lambda^n) \quad (1.7)$$

where τ is the characteristic aging time for build up of the microstructure, α determines the rate with which the microstructure is being broken down under shear, η_0 is the limiting viscosity at high shear rates, and β and n are parameters designating how strongly the microstructure influences the viscosity. Since the symbol λ is used to designate the structural parameter of the material, this model is called the **λ -model** [29, 31, 47]. In steady state, $d\lambda/dt = 0$ and the resulting steady state flow curve is easily found:

$$\frac{d\lambda}{dt} = 0 \Rightarrow \lambda_{ss} = \frac{1}{\alpha\tau\dot{\gamma}} \Rightarrow \quad (1.8)$$

$$\sigma_{ss}(\dot{\gamma}) = \dot{\gamma}\eta(\lambda_{ss}) = \dot{\gamma}\eta_0 + \frac{\eta_0\beta}{(\alpha\tau)^n\dot{\gamma}^{n-1}} \quad (1.9)$$

From the equation for steady state flow curve it is easily seen that when $n > 1$ the shear stress diverges both at zero and infinite shear rates so there exists a finite shear rate at which the shear stress has a minimum. Once the stress is dropped below this minimum the steady state shear rate drops abruptly from the value corresponding to the minimum in the flow curve to zero, so the steady state viscosity jumps discontinuously from some low value to infinity - a viscosity bifurcation. This is in contrast to a simple yield stress fluid where the viscosity diverges continuously when the stress is lowered towards the yield stress (a behavior that is also seen in the λ -model when $0 < n \leq 1$). So while the Herschel-Bulkley model and other simple yield stress models fail to describe qualitatively avalanche behavior and viscosity bifurcation, the λ -model can at least qualitatively capture the right

behavior when $n > 1$. In chapters 5 and 6 I examine what further qualitative predictions can be obtained from this toy model and how they can be successfully compared to experimental observations.

1.5 Micro- and mesoscopic models for complex fluids

Apart from numerous purely phenomenological descriptions of complex fluid rheology such as the Bingham model, the Herschel-Bulkley model, and (to some degree) the λ -model, there exists a very large number of models that take the micro- or mesoscopic physical properties of the material as a starting point for describing the fluid macroscopic properties. These range from doing molecular dynamics simulation on fluids composed of hard spheres (see for instance [53]), over the famous scaling theories for polymers in melts of solution [54] and mode-coupling theory for the glass transition [55, 56], to mesoscopic approaches such as the Soft Glassy Rheology (SGR) model for soft glassy materials [57, 58]. A few examples of such models that give macroscopic predictions based on a fundamental understanding of the microscopic (or mesoscopic) physics will be given below.

1.5.1 Molecular dynamics simulations

The advantage of molecular dynamics simulations is that only *very* few and reasonable “assumptions” have to be made about the molecular interactions. Typically the only assumptions are that the simulated particles interact only via the Lennard-Jones potential, and (in order to avoid crystallization) that the fluid is a binary mixture of particles of two slightly different sizes (e.g. [53]). Some of the disadvantages of such a fundamental approach with so few simplifications are that analytical results are hard to come by, and that a simulation of any large number of particles is so immense that the simulation span only very short physical times. Maybe the most impressive molecular dynamics simulation to be performed so far was the simulation of the complete satellite tobacco mosaic virus composed of 1 million atoms [59]. The physical time simulated was 50 ns, and the simulation would have taken a 2006 desktop computer 35 years to complete! In addition to these complications, if a molecular dynamics simulation has successfully reproduced experimental behavior one can say that the simple assumptions that go into the simulation is sufficient to give the observed behavior, but *how* the observed behavior results from the assumptions is often not clear.

1.5.2 Reptation, an example of polymer scaling concepts

Single chain polymeric fluids are the most studied of all complex fluids [35], and even though this thesis do not deal with such systems at least one example of models for polymeric fluids should be given if only for the elegance of the underlying concepts. The most famous of all the concepts for concentrated polymer solutions and melts is probably that of “reptation”, a name coined by de Gennes to describe the snake-like motion of one polymer chain in between all the other chains [60]. De Gennes argued that for low

shear rates the main relaxation mechanism is reptation, and that the individual chains perform a random walk to escape from the initial “tube” it was constrained into by neighboring chains. The diffusion coefficient is inversely proportional to the chain mass, M , and the square of the tube contour length is proportional to M^2 , so that the time required for complete renewal of the chain conformation, τ_r , is proportional to M^3 . Thus the limiting viscosity at low shear rates should scale as M^3 , which was in good agreement with experiments, where a scaling law of $\eta \sim M^{3.4 \pm 0.1}$ had been found [61]. The picture of reptating chains also allows one to define the dimensionless *Deborah number* for the system: $De = \tau\omega$. Generally, the Deborah number is the ratio of the internal relaxation time scale of the system, in this case $\tau_{r,i}$, to the time scale of experimental probing ω^{-1} . If the Deborah number is small, $\omega^{-1} \gg \tau_r$ and the elasticity of the polymer chains is not felt since they relax on the timescale of probing and only the viscosity is probed. If the Deborah number is very large on the other hand, $\omega^{-1} \gg \tau_r$ and the situation is completely reversed. More generally [35]:

$$G'(\omega) = \sum_i G_i \frac{\omega^2 \tau_i^2}{1 + \omega^2 \tau_i^2} \quad (1.10)$$

$$G''(\omega) = \sum_i G_i \frac{\omega \tau_i}{1 + \omega^2 \tau_i^2} \quad (1.11)$$

where the sum is over different relaxation modes with characteristic relaxation time τ_i .

1.5.3 The SGR model, an example of a mesoscopic model

Where microscopic models such as molecular dynamics simulations and polymer reptation models use the well understood smallest elements of the material as building blocks of the system, mesoscopic models such as the Soft Glassy Rheology model use an intermediate mesoscopic scale to predict macroscopic rheology. This mesoscopic scale is taken to be so large that for an element of this size a strain, γ , can be defined, but yet so small that the strain is approximately uniform [57, 58]. The elastically stored energy of each element is given by $E_{elastic} = 0.5k\gamma^2$, where k is the spring constant of an element. Each element is assumed to have a maximum yield energy (reaction barrier), E taken from some distribution, and the evolution of element strain and yield energy distribution is taken to be:

$$\frac{d}{dt} P(\gamma, E, t) = -\dot{\gamma} \frac{d}{d\gamma} P(\gamma, E, t) - \Gamma_0 e^{-(E-0.5k\gamma^2)/x} P(\gamma, E, t) + \Gamma(t) \rho(E) \delta(\gamma) \quad (1.12)$$

where $P(\gamma, E, t)$ is the distribution of elements with strain γ and reaction barrier E at time t , x the effective temperature an element experiences, $\Gamma_0 e^{-(E-0.5k\gamma^2)/x}$ the probability for overcoming the energy barrier per unit time, $\Gamma(t)$ the total number of elements relaxing per unit time, $\rho(E)$ the density of reaction barriers that relaxing elements relax to, and δ is the delta function. Thus the SGR model simply assumes that elements are strained with the macroscopic strain until the element relaxes to an unstrained state with some

new reaction barrier. After this the element is again strained with the macroscopic strain etc. Of special interest in the SGR model is the distribution of reaction barriers, $\rho(E)$, and the effective temperature, x . For an unstrained material at high effective temperatures, the equilibrium distribution of reaction barriers is given by the Boltzmann distribution $\rho(E)e^{E/x}$. If $\rho(E) \sim e^{-E}$, then the equilibrium is given by $e^{E(1/x-1)}$, which is clearly not normalizable for $x \leq 1$, so that $x = 1$ signifies a glass transition below which no steady state exists and where the material is aging. Such a behavior is especially interesting since many complex fluids show such non-equilibrium and aging behavior, and this is the reason why $\rho(E) \sim e^{-E}$ is chosen [57, 58].

An attractive feature of the SGR model is that many results can be obtained analytically, such as the elastic moduli as function of x :

$$G' = \omega^2 \quad \text{for } 3 < x, \quad \sim \omega^{x-1} \quad \text{for } 1 < x < 3, \quad (1.13)$$

$$G'' = \omega \quad \text{for } 2 < x, \quad \sim \omega^{x-1} \quad \text{for } 1 < x < 2. \quad (1.14)$$

Also the steady state of $P(\gamma, E, t)$ under an imposed shear rate can be found analytically as function of x , and from it the steady state flow curve as function of x . It was found that for $1 < x$ the material has no yield stress, but when x is lowered below the glass transition at $x = 1$ a yield stress develops linearly $\sigma_y \sim 1 - x$.

1.6 Granular materials as a complex fluid

Physicists have for quite some time been fascinated by the far from equilibrium properties of granular systems and the phenomena they give rise to. Tremendous activity within the field of granular research gives proof of this [62–64]. Furthermore, the properties of granular materials are of huge importance to engineers and it is estimated that about 10 % of all energy consumption on earth is spent on the handling of granular materials [65]. In spite of the huge interest of both scientists and engineers the properties of granular systems are still imperfectly understood [66].

Granular materials such as sand, grains, etc. have traditionally not been considered as fluids since they evidently have many properties that set them apart from Newtonian liquids; a sand pile on a horizontal surface does not flatten as would a fluid, and walking on the beach does not cause one to sink halfway into the sand until the buoyancy force of the sand (density about 2 g/cm^3) balances the gravitational pull in a human (density about 1 g/cm^3). Sand also has some properties that sets it apart from many traditional complex fluids; notably sand does not have any surface tension [67], and the forces inside the medium can be more strongly anisotropic than for most complex fluids - squeezing two horizontal plates with sand in between together will result in *huge* resisting forces, but if the plates are tilted 90 degrees the sand grains will readily “drip” out of the gap by the small force of gravity (at least if the sand is dry - wet sand will actually stay in place if the gap between the plates is not very large). In recent years however, there has been a growing consensus that granular materials can be considered as being complex *fluids*, and

considerable progress into the understanding of granular materials as a fluid in certain flow regimes has been made [67–74].

One of the most spectacular and fascinating properties of granular materials is how the addition of a small amount of fluid dramatically changes the macroscopic properties of the material. While any child in a sandbox can tell you that you need a bit of water to turn a boring pile of dry sand into a spectacular sandcastle [75–77], too much water will destabilize the material as observed in landslides [78]. Somewhere in between the extremes of a completely dry and a completely wet materials, an optimum for the composite material strength as function of volume fraction is found. But where this optimum is and why is presently not understood.

1.7 This thesis

In view of what precedes and after presenting some basic rheological measurement techniques (Chapter 2), I will aim in this thesis at answering the following questions:

- Why is carbopol a yield stress fluid, and how does the yield stress behavior come about? (Chapter 3)
- What actually happens below the yield stress? *Does* carbopol flow or not? (Chapter 3)
- Why is the yield stress of so many yield stress fluids so difficult to measure and use to predict flows? (Chapters 4 and 5)
- Can shear banding of yield stress fluids occur also in homogeneous stress fields? (Chapters 6 and 7)
- How much liquid should be added to a dry, granular material for the resulting mixture to be strongest, and why? And how does the strength of the mixture depend on the material composition apart from the liquid volume fraction? (Chapter 8)

Chapter 2

Measurement techniques

Contents

2.1	Introduction	21
2.2	Active rheological techniques	22
2.2.1	The rheometer	22
2.2.2	The Couette, double-gap, and vane-cup geometries	23
2.2.3	Shear banding of simple yield stress fluids	24
2.2.4	The cone-plate geometry	26
2.3	Active rheological tests	26
2.3.1	Shear stress/rate sweep tests	27
2.3.2	Shear strain/stress-relaxation tests	27
2.3.3	Oscillatory sweep tests	27
2.4	Passive measurement techniques	28
2.4.1	Brownian motion	29
2.4.2	Microrheology	29
2.4.3	Dynamic Light Scattering and Diffusing Wave Spectroscopy	30
2.5	Magnetic Resonance Imaging (MRI) velocimetry	31

2.1 Introduction

While the previous chapter dealt with the viscosity, elasticity, yield stress, and other flow properties of Newtonian and complex fluids, this chapter is an introduction to how these properties are determined experimentally. Measurements of the rheological properties of a material can be either active or passive. In active rheological measurements an external forcing is imposed on the material and its rheological properties are deduced from its response. In passive measurements the thermal agitation of the constituents

of the material plays the role of forcing, and the motion of particles in the material in response to the thermal agitation is used to determine the rheological properties of the sample. Just as is the case for most practical applications active rheology is normally performed on macroscopic samples and, as described in the previous chapter, complex fluids in macroscopic flow situations often do not flow homogeneously. For this reason it is often desirable to be able to determine the full flow field of a fluid in macroscopic flows. Methods that allow for such a mapping of the velocities inside a fluid are called velocimetry techniques. Since a basic understanding of these experimental methods and their applicability is needed to understand the work presented in this thesis, the basic principles and methods of these techniques will be presented in this chapter.

2.2 Active rheological techniques

In contrast with what is the case for passive rheological techniques, the forcing of a material is externally controlled in active rheological techniques. One of the main advantages with this is that it is possible to determine how the response of the material changes with the amplitude of the forcing rather than being stuck with the forces of thermal agitation. While passive rheological techniques can determine $G'(\omega)$ and $G''(\omega)$ (see section 2.4), such techniques cannot determine $\eta(\dot{\gamma})$ which is non-linear for non-Newtonian fluids. Another advantage of active techniques is that it is possible to control the shear history of the sample which is needed to get reproducible results with thixotropic fluids. It is possible to do passive measurements on samples with a controlled shear history by combining passive techniques with active control techniques, but it is still not possible to determine the response on the material to different forcing ranges. For materials that respond linearly to the forcing this is not a problem at all, but most complex fluids to *not* respond linearly to the forcing and for those materials active rheological techniques are needed to determine the full flow properties of the material.

2.2.1 The rheometer

By far the most widely used device for active rheological tests is the **rheometer**, which in principle is a device that functions in one of two ways; either it controls the torque along the axis of a rod that is free to rotate and measures the resulting angular motion, or it does precisely the opposite (i.e. controlling the angular motion and measuring the resulting torque) [34, 35]. Apart from controlling the shear history of a material, this allows for determining all of $\eta(\dot{\gamma})$, $G'(\omega)$, and $G''(\omega)$ as well as other properties of the material such as the degree of thixotropy, and the yield stress etc. On the rotating rod of a rheometer one can install different types of **measurement geometries** that convert the torque and angular motion into shear stress and strain (rate) evolution respectively. For this reason one normally says that the rheometer imposes the shear stress or the shear rate in place of the torque and angular motion respectively. To be able to impose the shear stress and measure the resulting shear rate or vice versa (which are actually quite

demanding tasks in themselves); since the material response is computed from comparing the torque on the rod and its angular motion it is necessary that the rod rotates in frictionless bearings in the rheometer. To allow for performing both controlled stress and controlled rate measurements, the rheometer must have a control loop that allows an inherent shear stress controlled rheometer to effectively control the shear rate. In addition to this, some geometries (notably the cone-plate which is presented below) demand that the rheometer can control very accurately the vertical displacement of the rotating rod. If the rheometer is to be able to measure the frequency and stress/strain dependency of the storage and loss moduli G' and G'' (see subsection 2.3.3) it must also be able to control the forcing accordingly. The viscosities of the fluids typically measured in a rheometer range from 10^{-3} Pa.s to 10^7 Pa.s, and the shear rates from 10^{-4} s $^{-1}$ to 10^4 s $^{-1}$, requiring an impressive dynamical shear stress range from 10^{-7} Pa to 10^{11} Pa! For these reasons, and because of the high accuracy required, rheometers are in practice often quite sophisticated and complicated machines. This can be appreciated in Fig. 2.1A where the rheometer used in this work - a Stresstech from Rheologica Instruments - has been partially opened to expose the mechanics inside.

2.2.2 The Couette, double-gap, and vane-cup geometries

Measurements of a materials' viscosity, elastic shear modulus and most other rheological quantities are normally done on a rheometer using an adapted measurement geometry. A measurement geometry is installed on the rheometer and converts the torque to a shear stress and the angular motion to a shear strain. For the experimental data presented in this work I have used three different types of measurement geometries: Couette geometries, vane-cup geometries, and cone-plate geometries. In a *Couette geometry*, which is also called a *Couette cell* or a *bob-cup geometry*, the material to be measured on is placed in the annulus between two concentric cylinder shells, where in our case the inner cylinder moves with respect to the outer one as illustrated in Fig. 2.1B [34, 35]. In steady state the shear stress in the material in our Couette geometry can be easily computed since the total torque on a co-axial annulus of material is zero since the annulus does not accelerate. Hence, the torque, $\tau = 2\pi Rh\sigma R$, must be independent of radius, R (h is the height of the geometry). Rearranging gives the shear stress as function of radius in a Couette cell:

$$\sigma = \frac{\tau}{2\pi h R^2} \quad (2.1)$$

Thus the stress is highest at the inner cylinder and decreases with radius as R^{-2} . The average shear rate in the geometry is roughly given by the relative speed of the two cylinder shells divided by the gap between them:

$$\dot{\gamma} \approx \frac{\omega(R_i + R_o)/2}{R_o - R_i} \quad (2.2)$$

where ω is the angular velocity and R_i and R_o are the inner and outer radii respectively. Equation 2.2 is exact in the limit where $R_o/R_i \rightarrow 1$, which is the limit where the Couette

geometry becomes identical to the infinite, parallel plates shown in Fig. 1.1. For real systems however, $R_o/R_i > 1$ and equation 2.2 is approximate. Also, equation 2.1 shows that the shear stress is not the same everywhere in the fluid but varies with radius. Typically $R_o/R_i \approx 1.1$ which results in a stress variation of about 20 % inside the material.

The **double-gap** geometry is displayed in Fig. 2.1. It consists of a stationary inner and outer wall, and a rotating cylinder shell in between the two. The stress variation is $\sigma \sim R^{-2}$ like the Couette geometry. The double-gap geometry has the advantage that the surface in contact with the material is large, allowing for measuring low viscosities.

The **vane-cup** geometry is identical to the Couette geometry except that the inner cylinder is replaced by a vane of the same radius (Fig. 2.2A). A vane-cup geometry is used when one wants to insert a measurement geometry with minimal disturbance of the material (because of thixotropy) or in order to avoid **wall-slip**, where the geometry wall moves without dragging the material at the wall at the same speed - it slips. The material between the vanes moves as a solid block - effectively making the vane-cup geometry identical to the Couette geometry but without any wall slip on the inner cylinder. Putting sandpaper on the wall of the outer cylinder and replacing the inner cylinder by a vane (or putting sandpaper on it) effectively counters the problem of wall slip while retaining the properties of the Couette geometry [45].

2.2.3 Shear banding of simple yield stress fluids

As already mentioned, stirring a teaspoon in a cup of tea readily sets the whole fluid in motion. The shear rate is slightly higher near the spoon than further away, but everything is sheared and at roughly the same shear rate. Stirring a teaspoon in the sugar bowl has not at all the same effect; only material relatively close to the spoon is sheared while the remainder of the material stays motionless. This phenomenon of concentration of shear in a highly sheared zone while the material behaves like a solid elsewhere is called *shear banding* and is observed for all yield stress fluids - simple and thixotropic [31, 79–89]. While shear banding in thixotropic yield stress fluids is a slightly complicated affair to which I shall return in chapter 6, shear banding in simple yield stress fluids is not all that complicated: Replacing the tea spoon and cup with a Couette geometry, we know that the shear stress decreases as R^{-2} . For a Newtonian fluid the decrease in the shear rate is proportional to the decrease in the shear stress and not very dramatic, but this is not the case for a simple yield stress fluid for which there exists a critical radius, R_c , beyond which the stress is lower than the yield stress, σ_y , and the material does not flow at all:

$$R_c = \frac{\tau^{1/2}}{(2\pi h \sigma_y)^{1/2}} \quad (2.3)$$

In a Couette geometry, shear banding therefore happens when the yield stress is below the stress on the inner wall and above the stress on the outer wall. Since the stress variation in a Couette geometry is typically about 20 % one might expect shear banding to happen rarely, but in fact it is very often observed in Couette geometries and other flow situations.

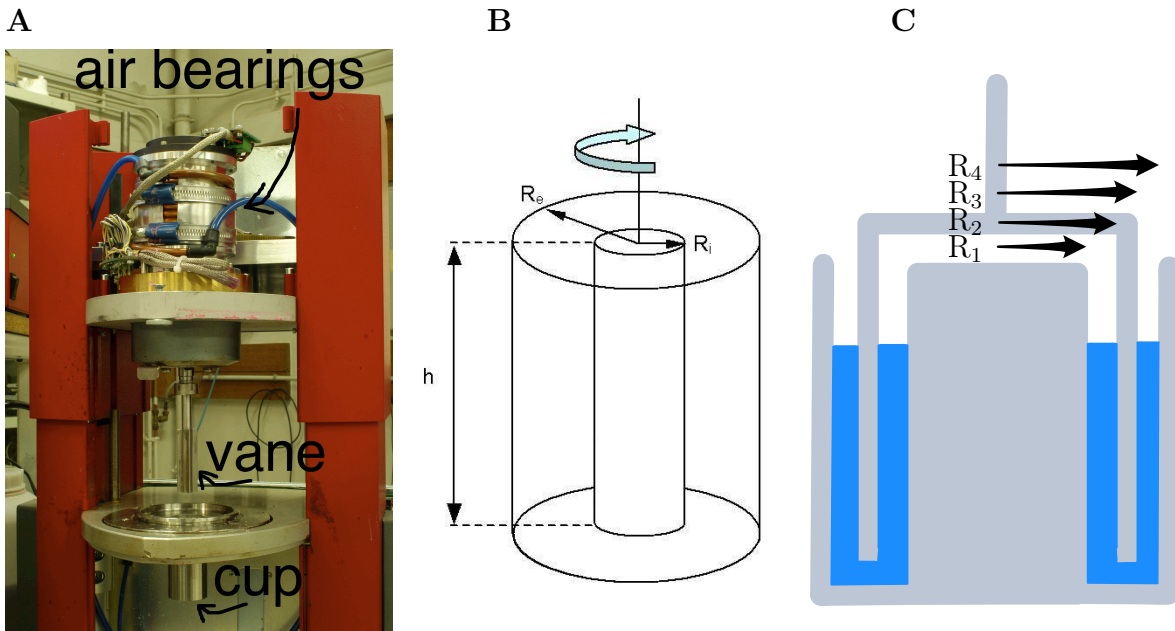


Figure 2.1: **A:**The Stresstech rheometer by Rheologica. The whole upper section can be translated horizontally to make the vane descend into the cup (other geometries can be inserted as well). Some shielding of the upper part of the rheometer has been removed to expose the sophisticated mechanics that control the torque on the vane, measure its angular motion, and make sure there is no friction inside the rheometer. **B:** The Couette geometry. The material is confined in the annulus between the interior and exterior cylinder shells of radii R_i and R_e respectively. **C:** The double-gap geometry. The innermost and outermost walls are stationary and the wall in the middle of that gap is rotating.

The reason is that even if the range of shear stresses where shear banding occurs is narrow, the shear rate range is not. Taking the whipped cream in Fig. 1.3A in a Couette cell with a 20 % stress variation as an example, it can be seen that if the stress on the outer wall is 33 Pa so that the material there *just* flows, the shear stress on the inner wall is about 40 Pa and the material flows with a shear rate of about $1,200 \text{ s}^{-1}$ there, giving an average shear rate of about $1,000 \text{ s}^{-1}$. This means that the material will shear band if a shear rate below $1,000 \text{ s}^{-1}$ (which is a very high value for typical measurements) is imposed on the sample. Since it is often not the shear stress that is imposed but rather the shear rate, the flow speed, or the pressure gradient (and since often the stress variation is much bigger than 20 %), shear banding occurs in many industrial applications where yield stress fluids are handled, like mold filling, materials transport and processing, etc. In such situations shear banding is most of the time not desired since it can result in partially filled molds, spoitable materials left in transportation tubes and partial mixing of materials, etc. In order to prevent such problems, engineers wish to simulate the behavior of a material in a processing/transport system in order to design it for optimal performance.

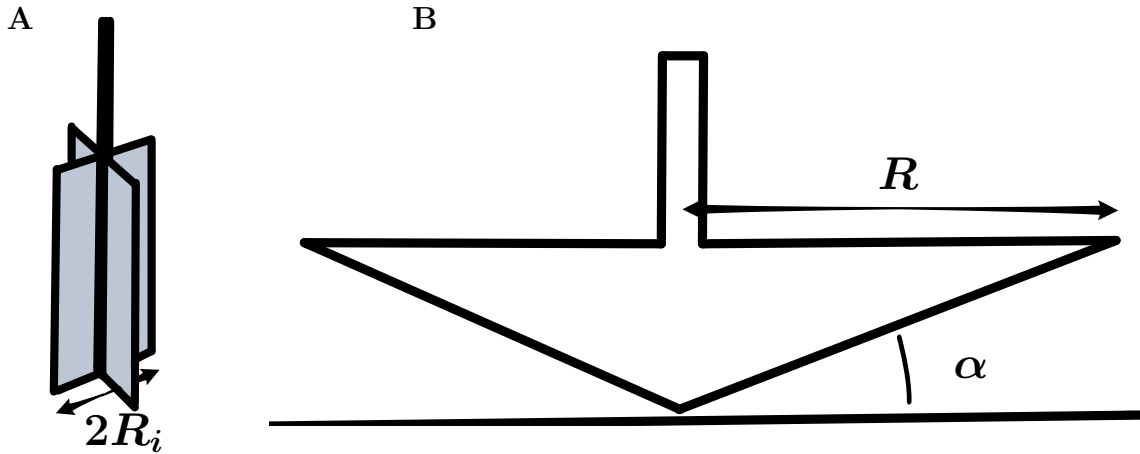


Figure 2.2: **A:** The inner cylinder in a Couette geometry can be replaced by a vane to make a vane-cup geometry. The vane typically has four to six blades of the same radius, R_i , and the same height as the cylinder it replaces. **B:** In a cone-plate geometry the material is confined in the gap between a plate and a cone with a radius R and an angle α to the plate.

2.2.4 The cone-plate geometry

A geometry which has a more well defined shear rate than the Couette geometry and an essentially homogeneous shear stress field is the cone-plate geometry illustrated in Fig. 2.2B. The shear rate of a concentric annulus of material confined between the cone and the plate is given by the relative speed of the top and bottom of the shell divided by its height:

$$\dot{\gamma} = \frac{v}{h} = \frac{\omega R}{\sin(\alpha_c)R} = \frac{\omega}{\sin(\alpha_c)} \quad (2.4)$$

where α_c is the angle between the cone and the plate. Expressing the requirement that in steady state the torque must be constant everywhere in the material in spherical coordinates, an equation for the shear stress inside the material is easily obtained [34, 35]:

$$\sigma = \frac{3\tau}{2\pi R_c^3 \cos^2(\alpha)} \quad (2.5)$$

Typically the angle in a cone-plate is 4° or less which gives a stress variation below 0.5 % which is *much* lower than the typical variation in a Couette geometry and effective negligible.

2.3 Active rheological tests

For a Newtonian fluid or an elastic solid it does not matter much which kind of test one chooses to measure its properties - one will always be able to determine the viscosity/elastic modulus of the material. Not surprisingly the situation is more complicated

for complex fluids and for this reason a wealth of different ways of probing non-Newtonian fluids exists. The most important of these are presented below.

2.3.1 Shear stress/rate sweep tests

While one might be content by imposing a single shear stress on a material if it is Newtonian (or if it is thixotropic and one want to study the viscosity evolution in time) it is often most interesting to probe the material over a range of different shear stresses. A measurement where different stresses are subsequently imposed on the sample for some time and the resulting shear rate measured is called a **shear stress sweep**. It is particularly useful for finding the yield stress and/or the flow curve of a material. **Shear rate sweeps** work in exactly the same way except that the shear rate rather than the shear stress is imposed.

2.3.2 Shear strain/stress-relaxation tests

In a **shear strain-relaxation** test a shear strain (typically a few to several percent) is imposed on the material at time $t = 0$, and the stress evolution is followed in time. For a typical complex fluid the stress initially jumps abruptly according to $\sigma = \gamma G'$ and then slowly decreases as the material relaxes viscously. The rate with which the material relaxes and the final stress level it relaxes to say something about the yielding behavior of the material. In **shear stress-relaxation** tests a shear stress (typically just around the yield stress) is imposed on the material *between* times t_1 and t_2 , and the strain evolution is recorded both during and after the stress. The rate with which the material deforms ($\dot{\gamma} > 0$ during the stress and $\dot{\gamma} < 0$ after the stress), and the intermediary and final strain levels give information about the yielding properties of the sample. Examples of strain-relaxation tests can be seen in Fig.3.12.

2.3.3 Oscillatory sweep tests

The data obtained from shear strain/stress relaxation tests are not easily quantified into more general material parameters. Oscillatory sweep tests are a more easily quantifiable way of testing the yielding behavior of a material. Here a sinusoidal forcing is imposed on the sample and the response recorded. For an elastic solid the response is in phase with the *forcing*: $\sigma(t) = G'\gamma(t) = \gamma_0 G' \sin(\omega t)$, where ω is the forcing frequency and γ_0 the amplitude the the strain. For a Newtonian fluid the response is in phase with the forcing *rate*: $\sigma(t) = \eta\dot{\gamma}(t) = \eta\omega\gamma_0 \cos(\omega t)$. For a complex fluid the response is generally a mixture of a component in phase with the forcing and a component in phase with the forcing rate, and the response is written [34, 35]:

$$\sigma(t) = \gamma_0[G' \sin(\omega t) + G'' \cos(\omega t)] \quad (2.6)$$

where G'' is the **loss modulus**. In addition to being called the elastic shear modulus, G' is also called the **storage modulus**. Generally the behavior is non-linear, and the

values of the storage and loss moduli vary with the amplitude of the shear stress (or conversely, the strain amplitude) being imposed and/or the forcing frequency, ω . For this reason one often measures the storage and loss moduli in a range of shear stress amplitudes (**oscillatory stress sweep**), a range of shear strain amplitudes (**oscillatory strain sweep**), or frequencies (**oscillatory frequency sweep**). An example of a material which has storage and loss moduli that vary with the forcing is a simple yield stress fluid; at stresses below the yield stress the response is mainly elastic, while the response is mostly viscous at stresses significantly above the yield stress. Such measurements can be seen in Fig. 2.3. An example of materials that have frequency-dependent moduli is a polymer melt, where the long polymers are entangled, but reorganize themselves due to thermal fluctuations with some characteristic time, τ [35]. If probed with a frequency much higher than $1/\tau$ the response of such a material is elastic since the polymers have no time to reorganize but simply stretch elastically. If a frequency much lower than $1/\tau$ is imposed on the other hand, the response is entirely viscous since the polymers reorganize before elastic energy is stored in them. Another example of frequency-dependence of G' and G'' is given in the section below.

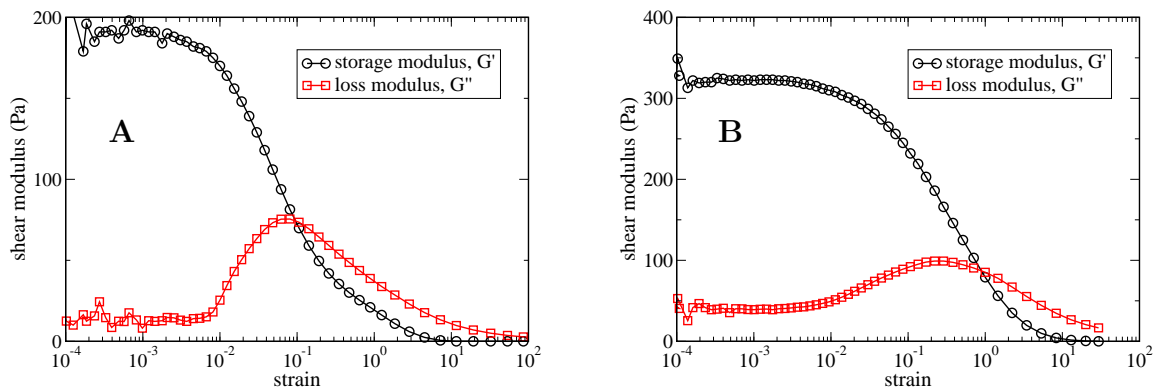


Figure 2.3: Oscillatory measurements of the storage modulus, G' , and the loss modulus, G'' , as function of strain at a measurement frequency of 1 Hz. **A:** 0.2 % carbopol, $G' \approx 190$ Pa, yield strain ≈ 10 %. **B:** Hair gel, $G' \approx 320$ Pa, yield strain ≈ 30 %. Notice the difference of scales of the y-axis.

2.4 Passive measurement techniques

Passive rheological measurement techniques either directly or indirectly measure the ease with which small particles move around in a material and deduces rheological properties from this motion: In **Microrheology** the thermal motion of introduced test particles (typically about a micron in size) is detected directly using a microscope and recorded for data treatment . In **Dynamic Light Scattering (DLS)** the motion of scattering centers

(from about ten nanometers to about a micron in size) is determined indirectly from the correlation of the interference of photons scattered elastically *once* from moving particles. **Diffusing Wave Spectroscopy (DWS)** is similar to DLS except that the interfering photons rather than being scattered only once, is being scattered multiple times and the light is effectively diffusing through the sample. Common for all of these techniques is that they rely on the theory about the Brownian motion of colloidal particles.

2.4.1 Brownian motion

One day in 1827 when the botanist Robert Brown was examining pollen grains under his microscope he noticed that, within the vacuoles of the pollen grains, tiny particles were executing a jittery motion. By successfully repeating the experiment with particles of dust, he was able to rule out that the motion was caused by life processes in the pollen. Something else was somehow causing small particles to move around in an apparently random fashion. Although others described the mathematics of what we now know as **Brownian motion** before him, it is Albert Einstein who is credited with discovering and describing that the motion of the small particles is caused by solvent molecules that continuously hit the particles, transferring momentum to them and changing their direction of motion. The random impacts of solvent molecules cause a particle to move around, and while the average position of such a particle does not move in time, its mean square displacement along some axis, $\langle(x - x_0)^2\rangle$, generally does. If the particle is suspended in a Newtonian fluid [90]:

$$\langle(x - x_0)^2\rangle = 2Dt \quad (2.7)$$

where D is the diffusion constant of the particle. For spherical particles in a Newtonian fluid the diffusion constant is given in terms of the solvent viscosity, η , the particle radius, a , and the thermal energy, $k_B T$ [90]:

$$D = \frac{k_B T}{6\pi\eta a} \quad (2.8)$$

Thus one can determine the viscosity of a Newtonian fluid by observing the mean square displacement of a small spherical particle in the fluid if the radius of the sphere and the temperature is known.

2.4.2 Microrheology

While the mean squared displacement of a small bead in a Newtonian fluid will keep increasing linearly in time, this is not true for a small bead in an elastic medium where the bead is trapped in a harmonic potential. On average each degree of freedom has an energy of $k_B T/2$ so the spring constant of the trap, k , can be determined by:

$$\frac{1}{2}k\langle(x - x_0)^2\rangle = \frac{1}{2}k_B T \quad (2.9)$$

When dealing with complex fluids that are neither purely fluid nor purely elastic, the behavior of the bead is of course more complicated. For a simple example of this, consider for instance a small bead chained to the substrate by a long polymer, and surrounded by a Newtonian fluid: At short times the bead does not move significantly with respect to the polymer chain length, so the chain is not felt by the bead and the motion is governed by only the fluid response. At long times on the contrary, the bead remains trapped by the polymer chain and the movement is elastic. At intermediate times it is a combination of the two. Another example is a bead trapped in the “cages” in a gel: At short times the bead does not feel the cage and the motion is Brownian. At intermediate times the bead is trapped by the cage it is in and the motion is sub-diffusive. At very long times the bead can escape the cages and effectively “diffuses” from cage to cage, but with a different diffusion constant than for the diffusion within the cage. Measuring the mean square displacement of a particle as function of waiting time, $\tau = t_2 - t_1$, it is possible to determine $G'(\omega)$ and $G''(\omega)$ over quite large frequency ranges [91].

2.4.3 Dynamic Light Scattering and Diffusing Wave Spectroscopy

When a laser beam is sent through a scattering sample, the scattered light interferes to form a so-called speckle pattern where the light intensity varies spatially because the electric fields being added together sometimes are in phase and sometimes out of phase, resulting in constructive and destructive interference respectively. If the individual scatterers move around, the pattern will change in time because of the phases of the scattered light changes. When a particle moves a distance of one wavelength, λ/n (where λ is the light wavelength in vacuum and n the fluid index of refraction), the phase of the emitted light changes 2π . Thus, when a particle moves a distance which significantly changes the phase of the electric field it emits, say $\lambda/2\pi n$, the intensity in a point of the speckle pattern changes significantly. By equation 2.7, the time it takes a spherical scattering center in a Newtonian fluid to move this distance is:

$$\tau = \frac{\lambda^2}{8\pi^2 n^2 D} \quad (2.10)$$

Generally, the normalized autocorrelation function of a varying signal intensity, $I(t)$, is defined as [92]:

$$g(t) \equiv \frac{\langle I(t)I(0) \rangle}{\langle I^2 \rangle} = 1 + \frac{\langle \delta I(t)\delta I(0) \rangle}{\langle I^2 \rangle} \quad (2.11)$$

where $\delta I(t) \equiv I(t) - \langle I \rangle$. It turns out that the autocorrelation function depends a bit on which angle from the propagation of the laser beam, θ the intensity is measured. In total, the autocorrelation function from singly scattered light from small particles in a Newtonian fluid is given by [92]:

$$g(t) - 1 = \frac{\langle \delta I(t)\delta I(0) \rangle}{\langle I^2 \rangle} = \exp(-4 \sin^2(\theta/2) \frac{t}{\tau}) = \exp(-\frac{2t}{\tau}) \quad (2.12)$$

where the last equality is true for a scattering angle of $\theta = \pi/2$.

Because of the requirement that the detected light has been scattered only once, DLS can be used only on almost transparent samples (if a sample is completely transparent scattering centers can be added). On optically white samples one has to use Diffusing Wave Spectroscopy. DWS is similar to DLS except that it is used in the limit where the detected light has been scattered not one, but multiple times [93].

2.5 Magnetic Resonance Imaging (MRI) velocimetry

In optically transparent samples it is possible to look into the fluid and directly observe the motion of visible elements there. On large samples this can be done by adding scattering particles to the fluid, choosing an observation plane by illumination with a two-dimensional laser sheet and observing the motion of the illuminated particles. By changing the observation plane the flow profile in the whole sample can be measured [94–97]. On microscopic samples the same can be done using a confocal microscope where the imaging plane is the focal plane of the microscope and the particles are seen by fluorescence [98–104]. On microscopic samples this can also be done using laser-interferometric techniques in optical tweezers [105–108]. But if the sample is not optically transparent, other methods must be used. One of these is ultrasound velocimetry where doppler shifting of the scattered sound from moving, scattering particles are used to detect flow speed, and the delay of the scattered signal is used to determine the location in the fluid [109–113]. For this technique to be applied the sample must be acoustically transparent. The method used for velocity profiling in this thesis is MRI velocimetry where the response of the sample to spatially and temporally changing magnetic fields are recorded and manipulated to yield the material speed as function of space [114–122]. Although a complete description of this technique is far too long to be given here, the basic principles behind it will be given below.

Even if the interaction between the spin of an atomic nucleus, its magnetic moments, and their interaction with magnetic fields is quantum mechanical, the principles of MRI can be understood classically. A nucleus has an angular momentum, \mathbf{L} , which through the gyromagnetic ratio, γ , results in the nucleus having a magnetic moment, $\mathbf{M} = \gamma\mathbf{L}$. In a magnetic field, \mathbf{B}_0 , there is a torque, $\boldsymbol{\tau} = \mathbf{M} \times \mathbf{B}_0$, acting on the angular momentum and hence on the magnetic moment:

$$\frac{d\mathbf{M}}{dt} = \gamma \frac{d\mathbf{L}}{dt} = \gamma \boldsymbol{\tau} = \gamma \mathbf{M} \times \mathbf{B}_0 \quad (2.13)$$

If the magnetic field is constant in time and directed along $\hat{\mathbf{z}}$ the solution to equation 2.13 is a precession of the angular momentum around the direction of the magnetic field with a precession frequency $\omega_0 = \gamma \| \mathbf{B}_0 \|$ called the Larmor frequency:

$$M_z(t) = M_z(0), \text{ and } M_{\perp\hat{\mathbf{z}}}(t) = M_{\perp\hat{\mathbf{z}}}(0) \exp(-i\omega_0 t) \quad (2.14)$$

This oscillation of the perpendicular magnetic field can be picked up by a radio-antenna, and it is such oscillations of the magnetic moments of hydrogen nuclei that compose

the signal, $S(t)$, which is recorded in MRI experiments. However, the nuclei are not completely isolated and the interactions with the surroundings cause it to lower its energy in the magnetic field and align its magnetic moment along \hat{z} with some relaxation time, T_2 .

$$S(t) = M_{\perp\hat{z}}(t) = M_{\perp\hat{z}}(0) \exp(-i\omega_0 t - \frac{t}{T_2}) \quad (2.15)$$

Hence, the measured signal relaxes exponentially. But a brief magnetic perturbation orthogonal to \mathbf{B}_0 and oscillating at the Larmor frequency, $\omega_0 = \gamma \parallel \mathbf{B}_0 \parallel$, can switch the nuclear spins from being parallel to being perpendicular to the magnetic field (and hence measurable) again [114, 123]. If the stationary magnetic field is not homogeneous but has a spatial gradient, say $\mathbf{B}(\mathbf{r}) = \mathbf{B}_0 + \mathbf{B}_1 \cdot \mathbf{r}$, the resonance frequency will also vary spatially, $\omega(\mathbf{r})$. Thus, brief switch-pulses with different frequencies, corresponding to the Larmor frequency in different positions in the fluid, makes it possible to switch only the magnetic moments in one spatial region, and consequently only the signal from that spatial region is measured.

An MRI velocimetry measurement consists of several measurement sequences: First a spatial region of the material is selected by a switch-pulse, and then some time varying magnetic field gradient, $\mathbf{G}(t)$, is added to perturb the evolution of the switched moments. The resulting signal is given by [114]:

$$S(t) = M_{\perp\hat{z}}(0) \exp\left(-i\omega_0 t - i\gamma \int_0^t \mathbf{G}(t') \cdot \mathbf{r}(t') dt' - \frac{t}{T_2}\right) \quad (2.16)$$

Apart from $M_{\perp\hat{z}}(0)$ and T_2 that depends on the density of hydrogen nuclei and the local physical chemistry, the signal also contains the integral over $\mathbf{G}(\mathbf{r}, t') \cdot \mathbf{r}(t')$ which holds information about the motion of the fluid element as can be seen by a Taylor expansion:

$$\int_0^t \mathbf{G}(\mathbf{r}, t') \cdot \mathbf{r}(t') dt' = \mathbf{r}(t=0) \cdot \int_0^t \mathbf{G}(t') dt' + \frac{d\mathbf{r}}{dt}(t=0) \cdot \int_0^t t \mathbf{G}(t') dt' \quad (2.17)$$

$$+ \frac{d^2\mathbf{r}}{dt^2} \cdot \int_0^t t^2 \mathbf{G}(t') dt' + \dots \quad (2.18)$$

Since different fluid elements will interact with experience different magnetic fields, their emitted signals will differ. By first selecting different spatial regions by varying the frequency of the initial switch pulse, then cleverly choosing several different shapes of $\mathbf{G}(t')$ and combining the resulting signals, the MRI scientist can extract the position, velocity, and acceleration of the fluid elements contributing to the total signal, and thus obtain the full flow field inside a fluid. Since recording the full flow field to a high accuracy requires many measurements with different frequencies and $\mathbf{G}(t')$, such measurements can be a lengthy process. Even getting just a 1D map of the flow field in a rotationally and translationally invariant geometry (such as a Couette geometry) can take several hours if the “MRI contrast” of the material is very low. This can happen for instance if the density of hydrogen nuclei is very low or if the nuclei rapidly relaxes along the magnetic

field - i.e. if T_2 is very low. For this reason it is strongly desirable to use a fluid with a high MRI contrast. Especially if trying to accurately determine the 2D flow fields inside a small volume of fluid such as in a small-angle cone plate.

Part II

Simple yield stress fluids

Chapter 3

The yielding behavior of simple yield stress fluids

Contents

3.1	Introduction	37
3.2	Materials and Methods	39
3.3	Experimental results	39
3.4	A simple physical model for carbopol	43
3.5	Simulation results and comparison to experiments	46
3.6	Discussion of the model and results	48
3.7	General discussion	50
3.8	Conclusion	52

3.1 Introduction

As described in chapter 1 the yield stress picture and the models associated with it, such as the Bingham or the Herschel-Bulkley models, can successfully describe the flow behavior of the non-thixotropic yield stress fluids - carbopol being the pertinent example - over large ranges of shear rates. The fact that the same fluid seems of low viscosity when stirring it and at the same time seems to be very viscous when observing that a small pile of material does not flatten under the force of gravity is well explained, as well as the phenomenon of shear banding in inhomogeneous stress fields. However, for a number of years there has been a controversy about whether or not the yield stress marks a transition between a solid and a liquid state, or a transition between two liquid states with very different viscosities. Numerous papers have been published that apparently demonstrate that these materials flow as very viscous Newtonian liquids at low stresses [34, 35, 39, 124–127], as well as many replotted data sets shown in [39]. Another issue with the yield stress models is that they are all phenomenological. Different models are found to describe different

materials to different degrees of success, but it is rarely understood *why* a given material behaves like a yield stress fluid. The questions of to what degree yield stress materials flow or do not flow below the yield stress, and how the yield stress fluid behavior can emerge from microscopically reasonable assumptions are treated in this chapter.

Possibly the earliest work that seriously question the solidity of yield stress fluids below the yield stress is a 1985 paper by Barnes and Walters [124], where they show data on carbopol samples apparently demonstrating the existence of a finite viscosity plateau at very low shear stresses - rather than an infinite viscosity below the yield stress. In 1999 Barnes published another paper on the subject, titled "The yield stress - a review or ' $\pi\alpha\nu\tau\alpha\rho\epsilon\iota$ ' - everything flows?", where he presents numerous viscosity *vs.* shear stress curves with viscosity plateaus at low stresses [39]. One of these curves is shown in fig. 3.1 where the viscosity plateau appears very convincing. Following the initial publication

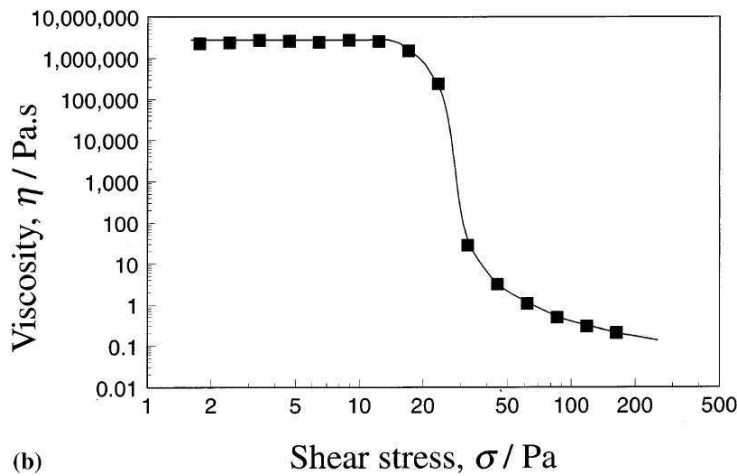


Figure 3.1: A viscosity *vs.* shear stress curve from [39] of an aqueous Carbopol sample (0.2 %_{mass} at $pH = 7$) apparently demonstrating the existence of a nice viscosity plateau below a critical stress. This figure is representative of the figures often used to argue that fluids normally considered to be yield stress fluids are in fact not solid below the yield stress - but flow with a very high viscosity.

by Barnes a number of papers appeared, discussing the definition of yield stress fluids, whether such things existed or not, and how to demonstrate either way, e.g. [39, 128–132]. The outcome of this debate has been that the rheology community presently holds two coexisting and conflicting views: (1) the yield stress marks a transition between a liquid state and a solid state, and (2) the yield stress marks a transition between two fluid states that are not fundamentally different - but with very different viscosities.

In this chapter I reproduce the experiments used to demonstrate Newtonian limits at low stresses and I also find the apparent viscosity plateaus at low stresses. But I also show that such curves can be very misleading and that extreme caution must be taken before concluding that a true viscosity plateau exists. Taking such caution I examine some typical yield stress fluids and show that the apparent viscosity plateau can be an artifact

arising from falsely concluding that a steady state has been reached. For measurement times as long as 10,000 seconds I find that viscosities for stresses below the yield stress increase with time and show no signs of nearing a steady value. This extrapolates to a steady state material that is solid, and does not flow below the yield stress.

3.2 Materials and Methods

For the experimental examination of the nature of the yield stress transition for simple yield stress fluids two materials were used; 0.2 %_{mass} aqueous carbopol sample (neutralized to a *pH* of 8 by NaOH) and a commercial hair gel containing carbopol and stabilizing agents (Gatsby Water Gloss/Wet Look Soft). Carbopol is being used on a huge industrial scale as a thickening/yield stress agent for cosmetics, pharmaceuticals, soaps etc. But because it is simple and safe to prepare and use, and since it is fit extremely well by the Herschel-Bulkley model, carbopol is also a favorite 'model' non-thixotropic yield stress fluid for researchers [37, 39, 124, 133–135]. Carbopol powder consists of small particles of cross-linked polyacrylic acid resins, that under neutral *pH* swell so enormously in water that concentrations of carbopol even below 0.1 %_{mass} is sufficient for the particles to jam together to form a yield stress fluid [37]. The carbopol sample used for the experiments presented here was prepared by mixing 0.2 % by mass of "CARBOPOL ULTREZ U10" from "Laboratoire DISTRI B3" and ultra-pure water thoroughly for at least an hour which forms an opaque, viscous fluid with no yield stress. The *pH* is then adjusted to about 8 by adding sodium hydroxide (NaOH). After the addition of NaOH the yield stress of the resulting material makes mixing with magnetic stirrers impossible and the material must be thoroughly mixed by other means to assure homogeneity - here simply by violently shaking a partially filled bottle of the material. After pH calibration and thorough mixing the fluid was left for at least a day before any measurements were done. The commercial hair gel was also mixed prior to use to assure homogeneity. The rheological properties of the materials were examined using a vane-cup geometry (four blades of 52 mm height and 4.5 mm width attached to a rod of 4 mm radius inserted in a cup with sandpaper covered inner wall with a diameter of 26.5 mm) in the controlled stress rheometer, Stresstech, from Rheologica Instruments. All measurements for each material presented here were made on the very same sample. Two different samples from the same batch gave identical results to within the error of the filling height of the cup. Near the end of a series of measurements, initial measurement points were reproduced to make sure that evaporation or material degradation had not changed the properties of the material. In order to get reproducible results it was found necessary to let the material relax at zero stress for about half an hour after loading and between measurements.

3.3 Experimental results

The measurements shown in Fig. 3.1 are so-called creep tests; measurements where the shear stress is imposed and the resulting shear rate is recorded. In order to test these

findings I performed similar measurements on the 0.2 % carbopol sample (same concentration as in Fig. 3.1) and on the hair gel sample. The resulting viscosity curves are shown in Fig. 3.2 and Fig. 3.3 respectively, showing the apparent viscosity as a function of the imposed stress. Measurements are shown where the viscosity is determined at several different times after each stress has begun being imposed. The results demonstrate that for both samples low-stress viscosity plateaus are found, and a “yield stress” can be reasonably determined. However, while all measurements collapse at stresses higher than the yield stress, below the yield stress the apparent viscosity values depend on the delay time between beginning the stress, and measuring the viscosity: the insets in Fig. 3.2 and Fig. 3.3 show that the viscosity value of the low-stress viscosity plateau increases with the delay time as $\eta \sim t^{0.6}$ and $\eta \sim t^{1.0}$ respectively. It is clear that each of the several curves in Fig. 3.2 and in Fig. 3.3 when seen individually greatly resembles the curves of Barnes and others, and that such curves can be misleading since one assumes that the data represent measurements in steady state while in fact the flows may well be changing with time as is the case here.

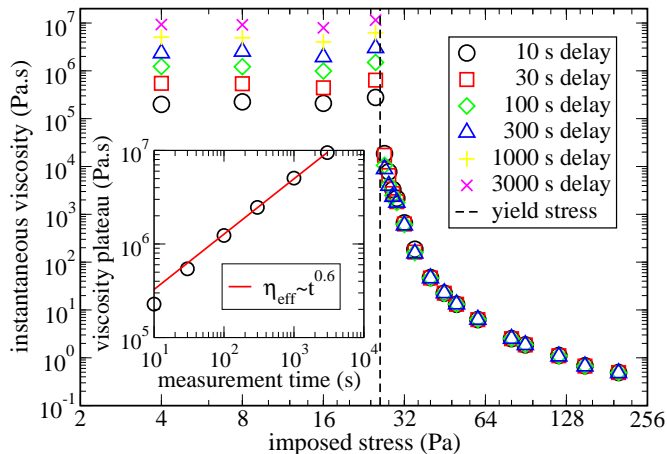


Figure 3.2: A reproduction of the measurements on Carbopol from Fig. 3.1. Each of the curves here show the same qualitative behavior as the curve in fig. 3.1 but the curves presented here are all for the same material - only with the viscosity recorded at different delay times after the stress had begun. The inset shows how the viscosity plateau increases with time as roughly $\eta \sim t^{0.6}$. Note that this cannot be an evaporation or aging effect since all measurements were done on the same sample after it had been allowed to relax after the previous experiment.

In Fig. 3.4 the strain and shear rate evolution for the carbopol sample is shown for a stress of 25 Pa which is the highest stress still on the viscosity plateau of Fig. 3.2. The inset show the shear rate which seems to be noisy at times lower than about three seconds but this noise is actually inertio-elastic vibrations as can be seen in the main figure. The

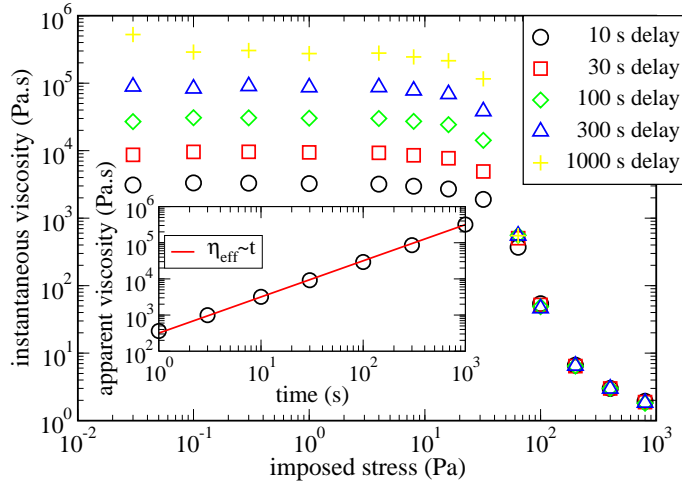


Figure 3.3: Similar measurements as in Fig. 3.2 but on a commercial hair gel (Gatsby Water Gloss/Wetlook Soft) show the same behavior except that here $\eta \sim t^{1.0}$.

figure emphasizes the findings in Figs. 3.2 (and 3.3): it is seen that the shear rate is steadily decreasing and shows no signs of reaching a steady value even 10,000 seconds after the measurement has begun which is of course why the value of η at the viscosity plateau keeps on increasing with time. The noise level in Fig. 3.4 is very low, so the behavior in Fig. 3.2 and Fig. 3.3 cannot be caused by artifacts. Since evidently no steady state shear is observed one should *not*, contrarily to what is suggested by Barnes, take the instantaneous shear rate at any arbitrary point in time to be proof of a high-viscosity Newtonian limit at low stresses for these materials.

In Fig. 3.5 it can clearly be seen that the apparent viscosity increases in time for stresses at 25 Pa and below while it rapidly reaches a proper, steady state viscosity for stresses at 27 Pa and above.

The behavior of carbopol below the yield stress at a first glance resembles the behavior of aging, glassy systems. However, carbopol is normally considered to be a model *non-thixotropic* (i.e. non-aging) system and apart from material degradation for very high shear rates over extreme measurement times carbopol is indeed non-thixotropic as seen in Fig. 3.6. Also, this strange “aging” only seems to happen when the sample is under load - and not at rest where it seems to be “rejuvenating” - which is the exact opposite of soft glassy materials that show shear rejuvenation and aging at rest [57, 58, 136–145]. Something else must cause this apparent aging.

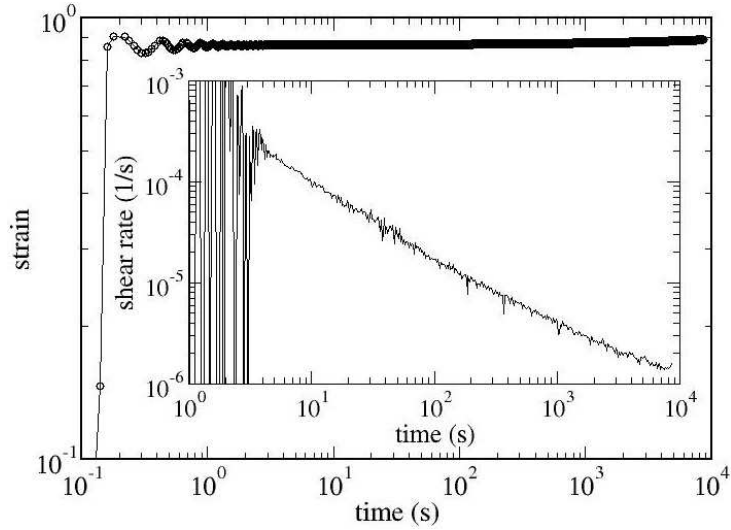


Figure 3.4: The deformation and shear rate (inset) of the carbopol sample as function of time for a stress of 25 Pa (the last point in the viscosity plateau in Fig. 3.2). The initial 'noise' in the shear rate is caused by inertio-elastic effects as can be seen in the main figure. The shear rate is steadily decreasing even 10,000 seconds after the stress has been imposed.

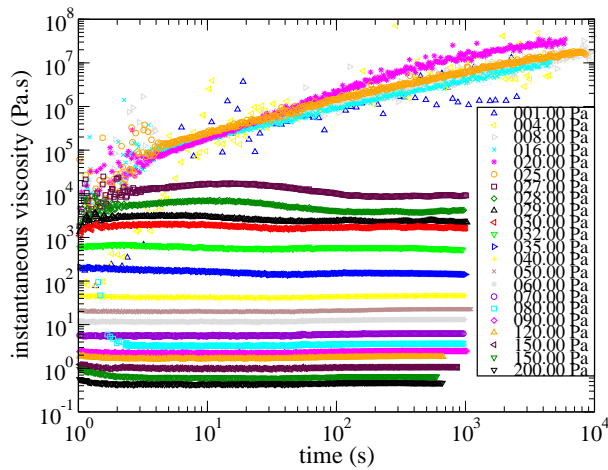


Figure 3.5: The instantaneous viscosity as function of time for different imposed stresses for 0.2 % carbopol at $pH = 7$. While the viscosity for the stresses at and above 27 Pa is seen to be constant in time, at 25 Pa and below the viscosity continuously increases. The viscosity increase shows no signs of leveling off, but if in spite of this one expects that the viscosity levels off at some high value, it is clear that experiments *much* longer than 10,000 seconds are needed to see this.

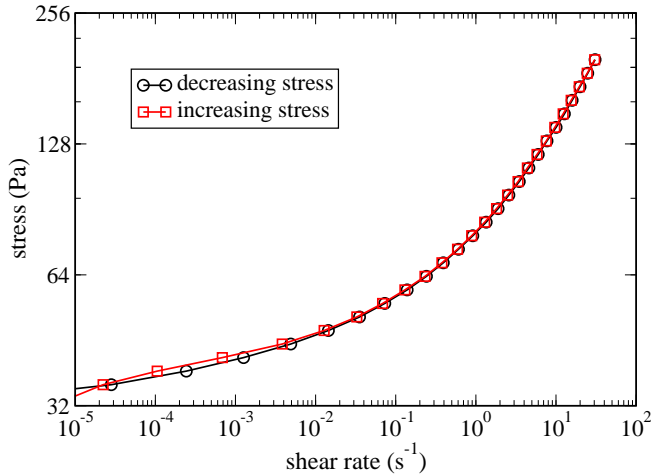


Figure 3.6: The behavior of the hair gel under increasing and decreasing shear stresses clearly shows that this material is indeed *non-thixotropic*. To comparison, bentonite was seen to be extremely thixotropic in Fig. 1.5.

3.4 A simple physical model for carbopol

To try to get some insight into the flow properties of carbopol and carbopol-like fluids I made a simple physical model for a system of soft, jammed particles to compare simulations of this model with the experimental flow behavior of carbopol and hair gel. The model is as follows:

1. The fluid consists of small carbopol particles of size l and the particles have an elastic shear modulus, G' .
2. These particles are jammed together and each particle is subject to some local strain γ , caused by the particle being jammed together with the surrounding particles.
3. In the initial state the distribution of the internal strains is assumed to be a normal distribution with width w .
4. When a macroscopic stress, σ_m , is imposed on the material it starts deforming as $\frac{d\gamma}{dt} = \frac{\sigma_m - G' \langle \gamma \rangle}{\eta}$, where η is the limiting viscosity of the fluid at high shear rates and $\langle \cdot \rangle$ denotes ensemble average.
5. Each time step dt there is a chance of $P_r = dt \cdot A \cdot \exp(-\frac{E-W}{kT})$ that a particle relaxes its strain to the initial distribution, where A is the reaction rate, E is the reaction barrier, and $W = 0.5 \cdot G' \cdot l^3 \cdot \gamma^2 = 0.5 \cdot l^3 \cdot \sigma^2 / G'$ is the work stored as elastic energy in the deformation of the particle.

The individual assumptions of the model are justified as follows: 1+2: As previously mentioned carbopol consists of acrylic acid resins that are cross linked to form very small "sponges" of roughly the same size. These sponges swell enormously in water at neutral pH values and jam together to form a yield stress fluid at mass fractions even below 0.1 % [37]. This along with the fact that a yield stress fluid can sustain local stresses (as long as they are below the yield stress) justifies 1+2. 3: In view of point 5 the normal distribution is an obvious candidate for a distribution of internal strains. I checked that the width of the distribution did not affect the steady state viscosity significantly and expect that this is neither the case for the precise choice of reasonable distributions. 4: This is just the classical Kelvin-Voigt model (spring and dash-pod in parallel). 5: This is simply classical reaction chemistry/statistical physics.

Although the spirit of the proposed model shows some similarities with the rather famous Soft Glassy Rheology (SGR) model by Sollich et al. [57,58] (see section 1.5.3) there are notable differences. Like the SGR model, the model proposed here simulates numerous small particles that become strained during macroscopic deformation, and the larger the deformation of a particle, the larger is its chance of relaxing to a less strained state. And in both the models, the rate of relaxation is proportional to $\exp(-(E-W)/x)$, with E the energy barrier, w stored elastic energy, and x the (effective) noise. The major difference between the two models is that while the SGR model assumes a delta distribution of initial and relaxational strains, and a wide distribution of energy barriers E , I assume a finite distribution of initial and relaxational strains, but that all energy barriers have the same value, E . One of the main consequences of the model differences is that the SGR model gives yield stress materials only when the noise level is so low that the system is out of equilibrium and aging - i.e. a thixotropic material. This makes the SGR model a bad choice for fluids such as carbopol that are demonstrably *non-thixotropic*. Contrarily, the model presented here is inherently non-thixotropic and at the same time has a yield stress at all noise levels (although the abruptness of the yielding transition depends on the value of x).

One of the big virtues of the presented model is that it is possible to measure or compute most of the relevant parameters. Since the particles are soft and jammed closely together G' of the individual particles can reasonably be assumed to be that of the material which can easily be measured in a rheometer. Measurements of G' and G'' as function of strain at a frequency of 1 Hz is shown in Fig. 3.7 and gives values of G' of about 190 Pa and 300 Pa for the carbopol sample and hair gel respectively. Knowing the concentration of particles, C , the average size of a particle can readily be computed as $l^3 = C^{-1}$ since the particles are soft and expanded until they jam together. The molecular weight of carbopol (depending on the degree of cross linking) is typically between 400,000 and 4,000,000 Dalton [146], which gives concentrations of $3 \cdot 10^{17-18} \text{ molecules/L}$ for the 0.2 % carbopol sample and something probably a bit higher for the hair gel (since it has a higher G' and yield stress). If one assumes $V_{\text{tot}} = V_{\text{molecule}} \cdot \text{molecules} = l^3 \cdot \text{molecules}$ one gets $l = (10^{-3} m^3 / (\text{molecules/L}))^{1/3} = 70 - 150 \text{ nm}$. The value of kT is of course well known and the viscosity, η , is the "limiting viscosity" at very high stresses which is readily measured in a rheometer, giving about 0.4 Pa.s and 2 Pa.s for carbopol and hair

gel respectively (Figs. 3.2 and 3.3). This means that only A , E , and w are not known a priori. However, from the measurements of G' and G'' (Fig. 3.7) one can measure the strain at which the material starts to flow ($\gamma_y \approx 10\%$ for carbopol and $\gamma_y \approx 30\%$ hair gel) and estimate that $E \approx 0.5 \cdot G' \cdot C^{-1} \cdot \gamma_y^2$ so that the material relaxes in unit time when strained γ_y , which gives $E \approx 10^{-18} J$ for carbopol and something somewhat bigger for hair gel (the latter cannot be accurately estimated since the concentration is unknown). Also from the yield strain an upper bound can be put on w , demanding that in the unstrained material only very few particles are strained beyond γ_y - giving a w of about 0.05 for carbopol and 0.15 for hair gel. I further checked that the steady state flow curve did only depend very weakly on w . This leaves A as the only truly free parameter since one can only get a very rough idea of what it should be by comparing to other reaction rates. Furthermore, many of the parameters merge such that the governing equation for the rate of relaxation has only two parameters:

$$R = P_r/dt = A \cdot \exp\left(-\frac{E - \sigma^2/2G'C}{kT}\right) \quad (3.1)$$

$$\equiv \alpha \cdot \exp(\sigma^2/\beta) \quad (3.2)$$

with $\alpha = A \cdot \exp(-E/kT)$ and $\beta = 2G'CkT$. Thus the model has at the very most two parameters, where the one (α) is largely unknown and the other (β) can be estimated relatively accurately for the carbopol sample, giving $\beta = 0.47-4.7$, and something somewhat higher for the hair gel. The fact that the model can be reduced to containing only one free parameter and one that is strongly bounded makes it easy to compare simulations to experiments.

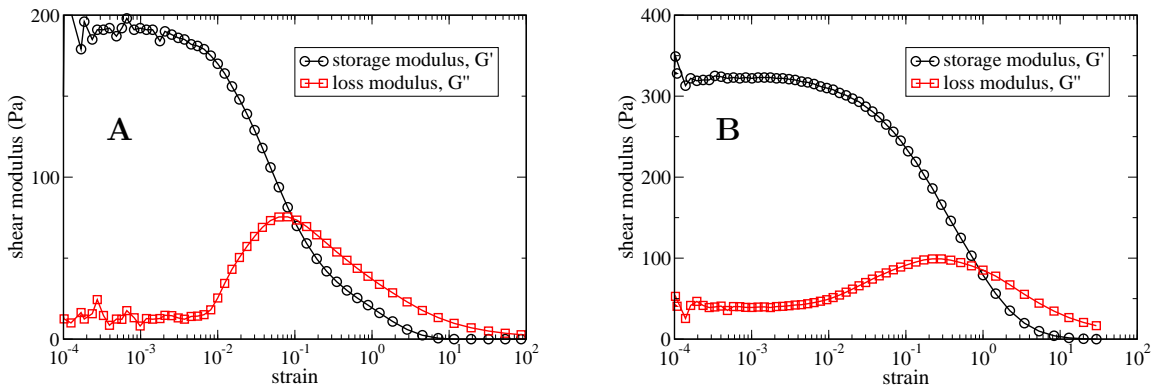


Figure 3.7: Oscillatory measurements of the storage modulus, G' , and the loss modulus, G'' , as function of strain at a measurement frequency of 1 Hz. **A:** 0.2 % carbopol, $G' \approx 190$ Pa, yield strain $\approx 10\%$. **B:** Hair gel, $G' \approx 320$ Pa, yield strain $\approx 30\%$. Notice the difference of scales of the y-axis.

3.5 Simulation results and comparison to experiments

In order to compare the model with the experiments I simulated the startup of flow after a stress had been imposed for several parameter values. The resulting steady state viscosity and stress were then compared to the experimental viscosity *vs.* stress curves for carbopol and hair gel. For each material the results for the parameter pairs that gave the best “fit” are shown along with the experimental data in Figs. 3.8 and 3.9. In both figures the agreement between experiments and simulations is quite good, and the value of the parameter β that gives the optimal fit is very reasonable: $\beta = 1.55$ for carbopol where a value between 0.47 and 4.7 was expected, while $\beta = 6$ for the hair gel where it was expected to be somewhat bigger than for carbopol.

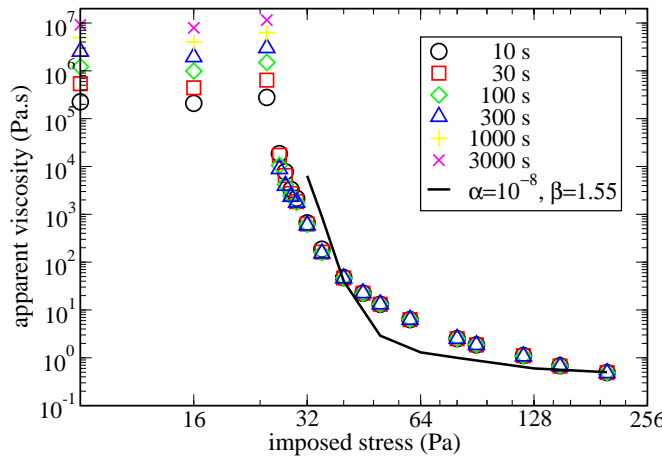


Figure 3.8: Comparison of the simulation results with experiments on the carbopol sample. The parameter value of $\beta = 1.55$ is in the middle of the range of initially estimated values for carbopol: $\beta = 0.47\text{--}4.7$. It can be seen that the increase in viscosity when the stress is reduced is more abrupt in the simulation than in the experiments as is the case in Fig. 3.9.

Below the yield stress, the viscosity in the experiments is seen to steadily increase with time as a power law - independently of the imposed stress: $\eta \sim t^{0.6}$ for carbopol (Fig. 3.2) and $\eta \sim t^{1.0}$ for hair gel (Fig. 3.3). In Fig. 3.10 this is seen to also be the case for the simulation where stresses of 15 Pa and 25 Pa imposed on “carbopol” result in identical viscosities that increase as $\eta \sim t^{0.8}$.

Considering the simplicity of the model and the few adjustable parameters it contains the quantitative agreement between experiments and simulations is quite impressive. Unfortunately simulations with the parameters that give the optimal ‘fit’ to the experimental data in Figs. 3.8 and 3.9 is very time consuming compared to other parameters that show the same qualitative behavior, since the number of steps required to reach a steady state

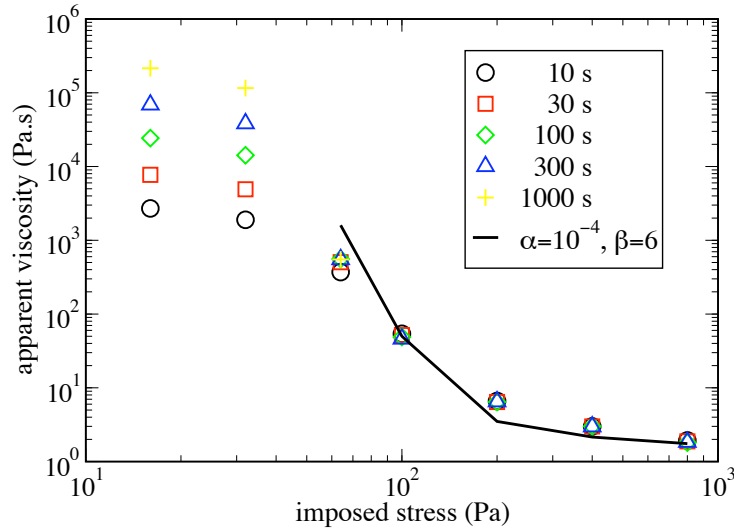


Figure 3.9: Comparison of the simulation results with experiments on the hair gel sample. The parameter value of $\beta = 6$ is close to the initial estimated range of β for carbopol ($\beta = 0.47\text{--}4.7$) but bigger than the best fit for the carbopol data ($\beta = 1.55$) which is consistent with the concentration of carbopol in the hair gel sample being bigger than the 0.2 % in the carbopol sample. As in Fig 3.8 the increase in viscosity when the stress is reduced is more abrupt in the simulation than in the experiments.

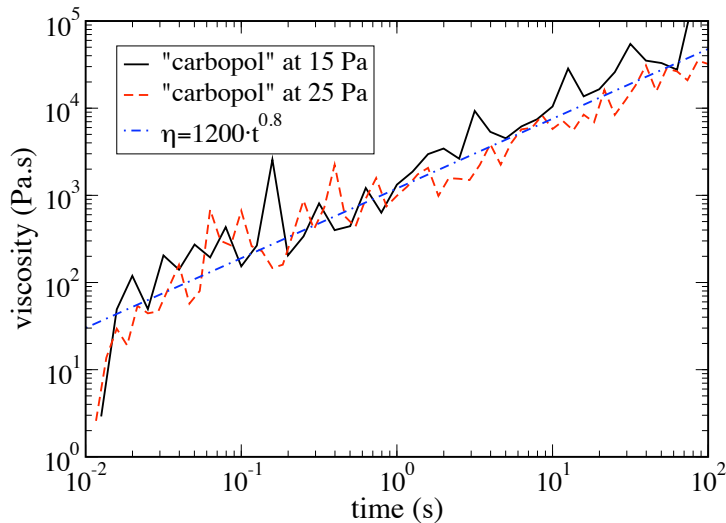


Figure 3.10: Time-evolution of the viscosity for stresses lower than the yield stress. For the parameter values that fit the carbopol data, stresses of 15 Pa and 25 Pa are below the yield stress and result in the curves shown. The resulting viscosity is independent of the imposed stress (viscosity plateau) and increase with time as $\eta \sim t^{0.8}$.

varies enormously. Since the qualitative behavior of the model is the same for most parameter choices I also did some simulations with parameter values chosen for computational

speed in order to compare the qualitative behavior of the model with experiments. In Fig. 3.5 the viscosity of carbopol is seen to evolve differently on either side of the yield stress: above the yield stress, lower stresses result in higher, time-independent viscosities, but below the yield stress all stresses result in identical viscosities that increase in time. This behavior is qualitatively reproduced in simulations as seen in Fig. 3.11. Also the strain response to a stress imposed between t_1 and t_2 is reproduced qualitatively as seen in Figs. 3.12A and 3.12B.

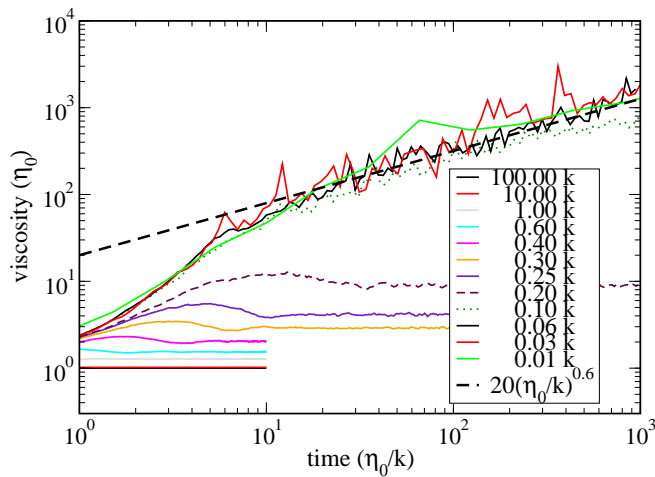


Figure 3.11: The evolution of viscosity with time is qualitatively similar to the experimental evolution of carbopol in Fig. 3.5. The simulation data are given in units of the limiting viscosity, η , the spring constant of an element, k , and a time unit, η/k . It is interesting to note that the small viscosity “overshoot” just before the steady state is seen both in simulations and experiments.

3.6 Discussion of the model and results

The simulation of the model reproduces both quantitative and qualitative behavior of the real systems quite nicely. However, the model has a slightly more abrupt change in the viscosity around the yield stress than do the real fluids (Figs. 3.8 and 3.9). There are at least two simplifications present in the model that would have this effect and which should be addressed in future work: I assume that all particles are trapped with the same energy barrier, and I assume that the strain resulting from relaxation of a particle is distributed equally over all particles. Since carbopol is believed to consist of soft particles packed randomly and jammed together, they will most certainly not all have the same energy barrier for stress-releasing rearrangements. Some will be strongly opposed by their neighbors while others can move much more freely in the direction of strain. Rather than

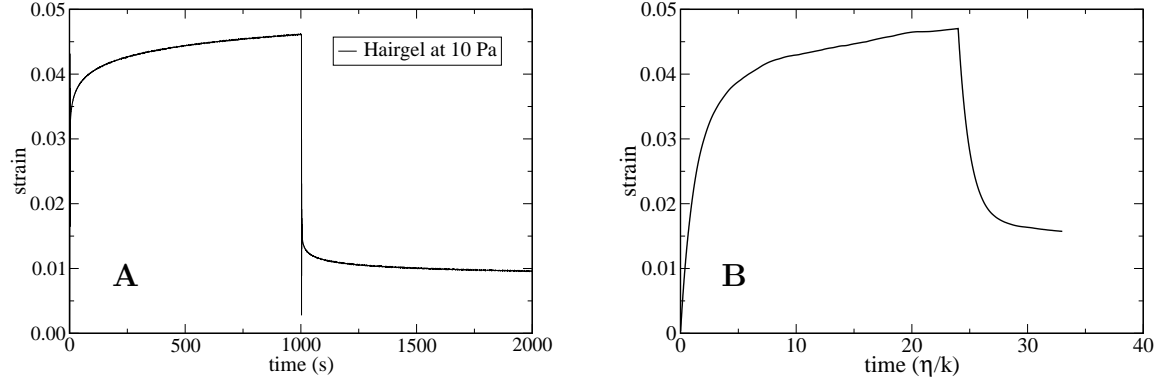


Figure 3.12: **A:** Experimental strain *vs.* time curve of hair gel with a stress of 10 Pa being imposed between time = 0 s and time=1000 s. **B:** Simulation of a stress of about one third of the yield stress being imposed between time = 0 and time = 24 shows great qualitative resemblance with the experimental curve.

being a delta peak, the values of the energy barriers should be some distribution with a finite width. This would make the viscosity change happen over a larger range of stresses of course, since some elements begin relaxing at low stresses and other elements only at high stresses, and thus smooth out the viscosity transition to some degree that depends on the width of the distribution of energy barriers. The assumption that relaxation of one particle results in an identical strain-increase for all particles is also not an accurate description of a three-dimensional structure of jammed particles. In such a system the relaxation of one particle results in a higher stress on the surrounding particles, but less so for particles further away. This means that the distribution of stresses experienced by the particles is broader in reality than in the model which again will smooth out the viscosity transition to an extent depending on the broadening of the stress distribution resulting from the local interaction in the three-dimensional structure. A final improvement that might be made on the model is changing the initial and/or the relaxational distribution of internal strains which are probably not normal distributions with identical widths. Certainly the tails that in principle expands to infinite strains are not physical. However, this is not a real problem in practice since the percentage of particles initially in (or relaxing to) “forbidden” strains will be very small and such particles will relax immediately. Besides, the stress and strain impact of a particle with twice the “allowed” strain will be minor and since its relaxation rate is *much* higher than a particle with half the strain the effect will be felt only for one time step, dt . But the strain distributions can probably be improved in other aspects than just the tails. While changing distributions of the energy barrier, initial strain, and relaxation strain is easy to implement, making the relaxation of a particle affect mainly its neighbors in a reasonable way is not. As importantly, any of these changes will necessarily introduce more parameters and unless the exact changes and values of the parameters can be justified physically it simply provides more free ‘fitting’

parameters', which may well provide a less clear picture than a simpler model with fewer parameters. For this reason I started out trying to find a physical 'minimal model' which (at least qualitatively) showed all the features of the real systems with as few parameters as possible. The first (and most simple) model I could imagine did this (and even allowed for quantitative comparisons), so I decided to compare its behavior to experiments before introducing more parameters.

3.7 General discussion

Since the model reproduces many features of the real systems one might hope that the mechanisms that make the model behave in this way are the same as for the physical materials and that understanding what gives rise to the model behavior also sheds light on the behavior of real yield stress fluids. Since the viscosity is inversely proportional to the rate of relaxation, the abrupt change in viscosity at the yield stress is easily understood from equation 3.2 where the relaxation rate of a particle is given by a very small pre-factor times the exponential of the stress on the particle squared. This powerful dependence on the stress means that in a small range of stresses around the yield stress the viscosity changes from a very high value given by one over the pre-factor to a very low value given by the limiting viscosity at high stresses. This also explains why carbopol-like materials are yield stress fluids and why there is a stress plateau at small shear rates. Here it should also be noted that the limiting rate of relaxation at low stresses is independent of stress, so that in fact this model *does* predict a viscosity plateau at low stresses such as numerous authors claim to have found. This is not a surprise however, since the only alternative to a Newtonian limit at low stresses is an aging system and carbopol and other simple yield stress fluids are demonstrably non-aging. Theoretically, even crystals have a Newtonian limit at low stresses but this does not mean that this limit can be accessed experimentally in rheological tests. But technically this does mean that 'the yield stress' is not the stress below which the material does not flow at all (since any material always will flow if only *very* slowly) but rather the stress around which the steady state viscosity changes tremendously - between a low value and one so high it cannot be measured in reasonable time scales. But how can a non-aging system show a viscosity that increases with time as is the case for the carbopol sample and hair gel as well as in model simulation below the yield stress? In the model this can be understood as an effect of the finite width of the distribution of internal strains: When a stress is imposed on the sample all particles are strained an equal amount in addition to their initial internal strain, and the particles in the 'high-strain tail' will relax faster than the average particle. When these high-strain particles relax to the initial distribution with an average strain of 0 all other particles are strained a bit further, but since few particles relax and the extra strain is distributed over many particles the effect of this early relaxation on the distribution is to replace particles that relax easily with particles that hardly relaxes at all (since a particle relaxes to the initial distribution where the strain is well below the yield strain) and then strain all particles a tiny bit more. But since the relaxation rate is highly nonlinear in the

strain, redistributing the strain of a few highly strained particles over many moderately strained particles results in an overall reduced probability for relaxation and hence a higher viscosity. This results in a viscosity that increases in time. For a given stress the distribution which gives the highest viscosity is a delta peak where all particles are strained identically. Once the high-strain tail of the initial distribution has relaxed the resulting distribution is as close as it will get to such a delta peak, since in the steady state there will be more particles at lower strain, and the viscosity has a local maximum in time. Such a small ‘hump’ in the viscosity just at the start of the steady state can be seen in both the experimental and simulation data (Figs. 3.5 and 3.11), and this effect may also play a role in the famous “stress overshoot”, where the stress as function of strain in constant shear rate experiments shows a maximum at the transition between the initial elastic regime and the final viscous regime. Figures 3.13A and 3.13B show how the internal strain distribution affects the viscosity at different times in the flow evolution: during startup, at the viscosity maximum, and in the steady state. While it can be understood why the viscosity will be increasing with time during startup flows, it is not immediately clear why this increase with time is a power law in both the experiments and the simulations and future work will have to address this.

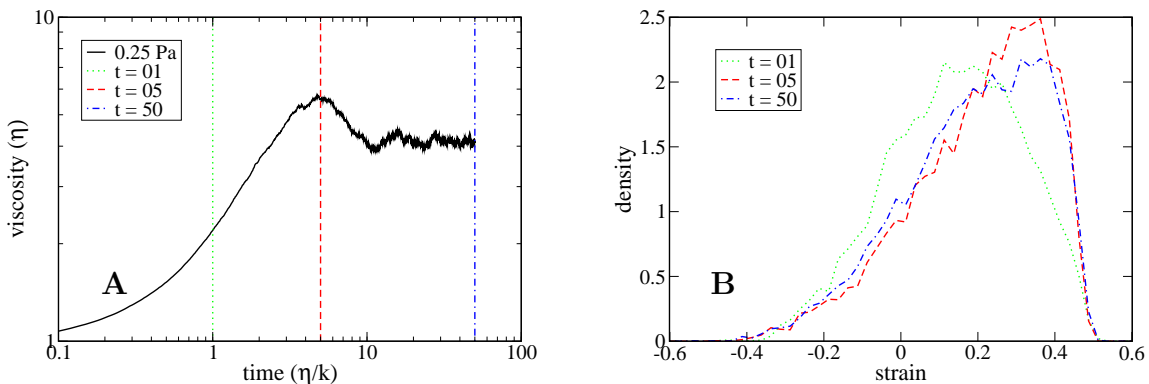


Figure 3.13: **A:** A close-up of the 0.25 Pa curve in Fig. 3.11. **B:** Internal strain distributions for the simulation in Fig. 3.13 during startup ($t = 1$), viscosity maximum ($t = 5$), and steady state ($t = 50$).

All these phenomena are reproduced by the model and all phenomena can be qualitatively understood through the model (except why the viscosity increase with time is exactly a power law). The idea that the time-dependent viscosity is caused by the internal strain distribution not yet having reached a steady state also allows for an estimate of how long one could expect to wait before a steady state is reached in experiments assuming that the distribution has reached a steady state when the material has undergone a deformation of $\gamma \approx 1$. From Figs. 3.2 and 3.3 I get that below the yield stress the viscosity is given by $\eta \approx 5 \cdot 10^4 \cdot (t/s)^{0.6}$ Pa.s and $\eta \approx 3 \cdot 10^2 \cdot (t/s)$ Pa.s for the carbopol sample and hair gel respectively. For stresses just below the respective yield stresses (25 and 32

Pa) this gives shear rates of $\dot{\gamma} \approx 5 \cdot 10^{-4} \cdot (t/s)^{-0.6} s^{-1}$ and $\dot{\gamma} \approx 0.1 \cdot (t/s)^{-1} s^{-1}$ and strains of $\gamma \approx 10^{-3} \cdot (t/s)^{0.4}$ and $\gamma \approx 0.1 \cdot \ln(t/s)$ and equilibration times ($\gamma(t_{eq}) \approx 1$) of $t_{eq} \approx 10^7 s$ and $t_{eq} \approx 10^4 s$ for the carbopol sample and hair gel respectively. One can then get an estimate for the viscosity by assuming $\eta_{\text{steady state}} \approx \eta(t_{eq})$ which gives $\eta_{\text{steady state}} \approx 10^9 Pa.s$ and $\eta_{\text{steady state}} \approx 3 \cdot 10^6 Pa.s$. This estimate can be compared to the low-stress limiting viscosity predicted by the model fitting parameter α , which can be obtained as follows: When the stress is so low that $\exp(\sigma^2/\beta) \approx 1$ the relaxation rate no longer depends on the stress, but the global strain increase when an element relaxes does; $\Delta\gamma = \sigma/N/G'$, where N is the total number of elements. The number of elements relaxing per second is $N\alpha$ so that the shear rate is simply given by $\dot{\gamma} = \frac{d\gamma}{dt} = \sigma\alpha/G'$ and the viscosity by $\eta = \sigma/\dot{\gamma} = G'/\alpha$, which gives values of $10^{10} Pa.s$ for the carbopol sample and $3 \cdot 10^6 Pa.s$ for hair gel. Considering the approximative nature of these estimations the agreement between the low-stress limit viscosities obtained from extrapolating the experimental data and from the values obtained from fitting the model to the steady viscosity *vs.* stress curves above the yield stress is very impressive.

The measurements presented in section 3.3 very clearly demonstrate that if one aims at obtaining viscosity *vs.* stress curves for even non-thixotropic yield stress fluids one must very carefully verify that a steady state has been reached before registering a point on this curve. The apparent viscosity plateau at low stresses, that have appeared in numerous papers and sparked lots of discussions, at a first glance seems to demonstrate that a steady and Newtonian regime has been reached. But the measurements in section 3.3 show that this is not necessarily the case at all: Surprisingly, the instantaneous viscosity increases in time in exactly the same way for all the stresses I tested below the yield stress - a range of stresses of three orders of magnitude! For both the samples a sharp transitionary stress is seen above which the fluids quickly reaches a steady state and below which the viscosity increases with time independently of the stress. This transition stress can reasonably be called *the* yield stress. Below the yield stress the viscosity increase with time follows a power law for both fluids: 0.6 for the 2 % carbopol sample and 1.0 for the hair gel.

3.8 Conclusion

In conclusion I have shown in this chapter that the many viscosity *vs.* stress curves showing Newtonian limits at low stresses should not be trusted if data proving that the points represent a steady state are not provided. This is because, below the yield stress, the viscosity is independent of stress but increases in time after the stress has been imposed, so that recording the viscosity after say 100 seconds will give one viscosity plateau while data at 1,000 seconds will give another. So the instantaneous viscosity measured does not represent a steady state and should not be reported as *the* viscosity for the material at a given stress. I also presented a simple physical model that both qualitatively and quantitatively agrees extremely well with the experimental data. Through the model it is possible to understand what physically gives rise to the known characteristics of non-thixotropic yield stress fluids: A dramatic viscosity change over a very small range of stresses and the

stress plateau at low shear rates; why the viscosity at low stresses increases with time; why the viscosity at intermediate stresses (and possibly also low stresses at very long measurement times?) experiences a small hump just before the steady state is reached. This hump should exist also in imposed shear rate experiments and may explain the well known “stress overshoot” for yield stress fluids seen in such tests. Future work based on the findings in this chapter would focus on adjusting the model to become more realistic without introducing many more free parameters and do simulations in order to compare the improved model to experiments. This should also be done quantitatively for transitory flows and not just steady state flows. Apart from simulations on the model there is also an analytical challenge aiming at understanding among other things why the viscosity evolves as a power law in time after a stress below the yield stress has been imposed.

The remaining challenges for understanding non-thixotropic yield stress fluids are mainly of a fundamental modeling and/or theoretical nature and not of a phenomenological one, and apart from the slight problem with time-evolution below the yield stress such systems are well understood experimentally. By this I mean that it is clear how to get reproducible measurements and how measurements in the rheometer can be used to predict flows in very complicated geometries by numerically simulating the behavior of a fluid with the measured flow properties under such circumstances. As I mentioned in chapter 1 this is not at all the case for the flow properties of *thixotropic* yield stress fluids which is the topic of the following chapter.

Part III

Thixotropic yield stress fluids

Chapter 4

What makes a fluid thixotropic

Contents

4.1	Introduction	57
4.2	Colloidal interactions: van der Waals forces and Debye lengths	58
4.3	Ludox spheres and salt water	59

4.1 Introduction

As described in section 1.4, the viscosity of thixotropic fluids depends not only on the shear rate, but also on the shear rate history; at high shear rates the steady state viscosity of a thixotropic fluid is relatively low, but as soon as the shear is stopped (or significantly decreased) the viscosity starts increasing in time. If the flow is subsequently started again the viscosity start decreasing towards the steady state value. One archetypical example of a material that behaves in this way is a natural clay, bentonite, which has been used in numerous experiments including the inclined plane/avalanche experiments [23, 29, 47, 147, 148]. That bentonite is thixotropic can be seen in Fig.1.5 where the viscosity at 15 Pa changes five orders of magnitude depending on whether the stress is imposed as part of an increasing or decreasing ramp. But what actually *causes* this shear-history dependent viscosity? The λ -model speculates that it is “the microstructure” that resists flow (and hence results in a high viscosity) and is broken down with shear and rebuilt at rest. Since the aim of the λ -model is to give a general conceptual frame for understanding thixotropy in materials as different as clays, colloidal glasses, polymer gels, and granular materials [29, 31, 47], the authors do not go into a detailed discussion of what “the microstructure” actually *is*. In this chapter I will explain; exactly what causes thixotropy in our system of a colloidal suspension of sticky spheres (and in similar systems), how to make such a thixotropic fluid, how to do so reproducibly, and how to tune its thixotropic properties. Being able to make highly thixotropic fluids with tunable properties will make measurements on thixotropic properties easier since shear thinning

effects from hydrodynamic interactions and other “noises” will be weaker compared to the thixotropy.

In a Newtonian fluid the interaction forces between the individual molecules are so weak that the attractive interactions between them are readily broken up by the thermal noise of the system, which also allows the molecules to reorganize. For a thixotropic material with a yield stress this is not the case. In order for the material to resist low stresses, the binding energies between components (or the energies required to reorganize them) in yield stress fluid must be so big that the thermal noise does not break them apart. At the same time the binding energies must be sufficiently low that the material will be fluidized at stresses above the yield stress (unlike solids that fracture [16, 149]). And finally, there must be some reaction barrier towards formation of new bonds that is just so high that the material regains its flow resistance after shear secession at some detectable rate (and not instantaneously, or the material wouldn’t be thixotropic). As I will show below, the interactions between charged colloids in suspension meet all these criteria, and is a perfect candidate for making a highly thixotropic fluid on which to do experiments.

4.2 Colloidal interactions: van der Waals forces and Debye lengths

Solids are generally bound together with (a mixture of) one of the three strong chemical bonds; metallic, covalent, or ionic. There are no such permanent bonds in fluids, but yet the individual molecules stay together rather than evaporating to gain entropy. The forces that bind them together are not static, but caused by temporary dipole-dipole interactions. Even if two molecules have no net charge, they can attract or repel. Polar molecules have a charge distribution which is asymmetric - such that the molecules have a positively charged region and a negatively charged region - but not (necessarily) a net charge. Hence the molecules will have dipole moments and depending on their relative orientation, two polar molecules can either attract or repel. As the bonds between the molecules are so weak that they are constantly broken up by the thermal noise, the molecules are constantly changing their relative position, but since they tend to minimize their interaction energy the molecules will spend most time in the attractive configuration and there will be an overall attractive force between them. If only one molecule is polar there is also an interaction force since the polar molecule polarizes the non-polar molecule to create a force that is mostly attractive as above. Finally, even two intrinsically non-polar molecules attract since they induces oscillating polarizations in each other that are overall attractive. These forces, that are known as **van der Waals forces**, of course also exist between larger structures composed of molecules such as **colloids** (aggregate particles so small that they are mostly unaffected by gravity - typically about a micron in size or smaller). The total attractive van der Waals potential for two colloids of radius

a , Hamaker constant A_H , and separation, D is given by ([35] chapter 7):

$$U_{VDW} = -\frac{A_H}{12} \left(\frac{4}{4D/a + (D/a)^2} + \left[\frac{2}{2 + D/a} \right]^2 + 2 \ln \left[1 - \left(\frac{2}{2 + D/a} \right)^2 \right] \right) \quad (4.1)$$

The potential has been plotted in Fig. 4.1A where it can be seen to always be attractive and diverging at short separations, but rather short ranged. This means that the attractive forces between colloids are felt only when they are very close together. Even so, colloids in suspension would quickly aggregate into large structures if the van der Waals forces were the only forces present. For this reason colloids in suspension are always stabilized by some interaction that prevents them from coming too close. One way of doing this is by having a surface charge on the colloids that then repel each other electrostatically. The repulsion is not as powerful as the pure Coulomb force would be however: ions in the solvent will be repelled by the colloids if they have the same charge, and attracted if they have the opposite charge. This means that charged colloids will be surrounded by higher concentrations of oppositely charged ions and lower concentrations of same-charge ions, which effectively “screens” the charges of the colloids, making them repel less than they would in the absence of ions. For not too high charges the effective repulsion between two charged colloids is given by ([35] chapter 2):

$$U_e = \frac{4\pi\epsilon\epsilon_0 a(D/a + 1)\psi^2}{D/a + 2} \ln \left[1 + \frac{1}{D/a + 1} \exp(-\kappa a D/a) \right] \quad (4.2)$$

where ϵ_0 is the permittivity of space, ϵ is the dielectric constant of the medium, ψ is the electrostatic potential at the surface of the colloids, and κ^{-1} is the **Debye length** which signifies the length over which the electric fields from the colloids is screened out by the free ions. The Debye length is given by:

$$\kappa^{-1} = \left(\frac{\epsilon\epsilon_0 kT}{\sum_i C_i q_i^2} \right)^{1/2} \quad (4.3)$$

where C_i is the bulk concentration of the ionic species i and q_i is its charge. The electrostatic potential between two colloids as function of separation in solvents with different ionic concentrations, and hence different Debye lengths is shown in Fig. 4.1B. There it can be seen that the potential changes from a constant value to zero at a separation of about κ^{-1} , so that charged colloids will generally stay roughly κ^{-1} apart.

4.3 Ludox spheres and salt water

Two things are obvious from looking at the attractive and repulsive potentials in Fig. 4.1: The total potential is attractive at sufficiently short distances, and depending on the Debye length there can be a larger or smaller energy barrier to overcome before two colloids can feel the attractive force and stick. These two facts hints that it should be possible to make a highly thixotropic yield stress fluid with tunable properties from colloids and salt water:

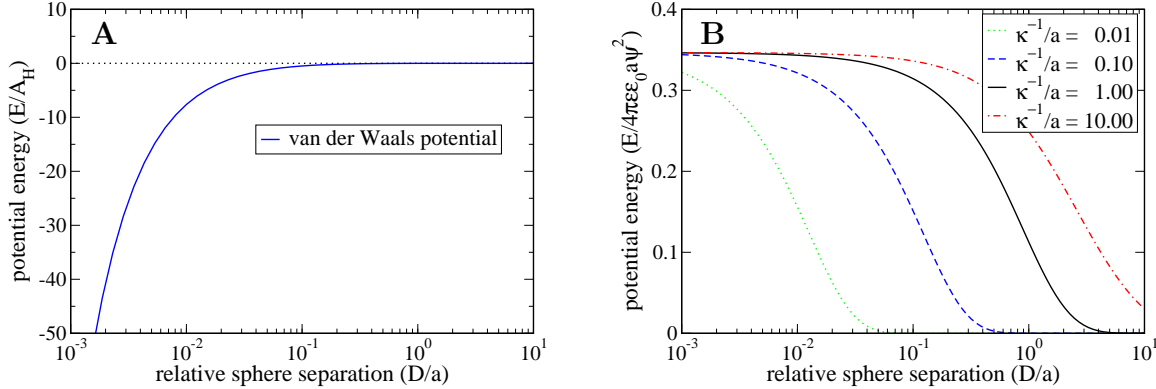


Figure 4.1: The interaction potentials between two charged colloids in a solvent containing ions as function of separation. **A:** The attractive van der Waals forces diverge when the beads get very close, but fall off quickly with separation. **B:** The repulsive force between two colloids of identical electrostatic potential in a solvent with different ion concentrations. The potential has decayed significantly when $D = \kappa^{-1}$.

When the colloids get sufficiently close they are strongly attracted and will stick. Since the binding energy is many times kT the colloids will not be teared apart by thermal noise, so a system spanning aggregate of colloids will not yield unless an external stress sufficiently big to destroy the structure - i.e. the material has a yield stress (which can be adjusted by changing the colloid concentration). The rate with which the colloids overcome the energy barrier and stick together depends on the energy barrier which can be controlled by changing the ionic concentration - i.e. the “aging time” of the fluid can in principle be controlled. To try to make highly thixotropic yield stress fluids with different aging times, yield stresses etc. I mixed different concentrations of sodium chloride (NaCl) and Ludox spheres in water and measured their thixotropic properties. **Ludox spheres** are silica-oxide (SiO_2) particles of about 10 nm in radius that are commercially available from Sigma-Aldrich*. Several flavors of Ludox spheres with varying surface chemistry are available. I made attempts with Ludox CL-X and TM-40, of which I had most success with TM-40. The Hamaker constant for SiO_2 in water with itself is $1.69 \cdot 10^{-20}\text{ J}$ ([150] chapter 6). The permittivity of space is $8.854 \cdot 10^{-12}\text{ C}^2/\text{Nm}^2$, and the dielectric constant of water at 20°C is 80 ([35] chapter 2). In order to be able to compute the total interaction potential between Ludox spheres in water for different salt (NaCl, ultra pure, from Sigma) concentrations it is also necessary to know the surface potential of the spheres which is unfortunately not provided by the producer. However, a value of about -70 mV is a reasonable guess ([35] chapter 2). The total interaction between two Ludox spheres in water with two different salt concentrations that correspond to the stock concentration and the concentration I finally used for the experiments is shown in Fig. 4.2. There it can

*I determined the colloid size by Dynamic Light Scattering (DLS) measurements.

be seen that in the stock solution the energy barrier is about $33 kT$, which means that the colloids are *very* stable since an energy fluctuation of $33 kT$ is *extremely* rare. But when the concentration of salts is increased to $1.1 M$ the energy barrier shrinks to $5 kT$, which means that the reaction will happen at a modest rate.

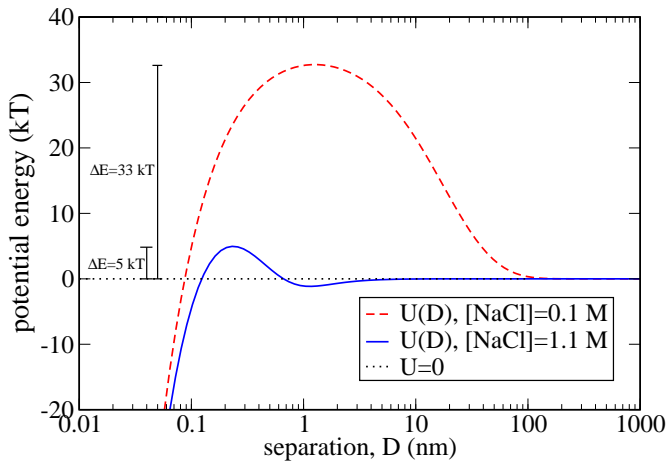


Figure 4.2: The full interaction potential of two Ludox spheres at different ionic strengths as function of separation, D . In the stock solution at low ionic strengths the energy barrier that must be overcome for two particles to feel the attractive van der Waals forces is on the order of $33 kT$ so agglomeration does not happen. When the concentration NaCl is increased to $1.1 M$ the energy barrier is lowered to $5 kT$, so agglomeration will happen, but at a modest rate. The Ludox spheres have a 10 nm radius, and a Hamaker constant of $1.69 \cdot 10^{-20} \text{ J}$. The surface potential of the spheres in not known exactly, but the -70 mV chosen here is reasonable compared to similar systems.

Mixing colloids, salt and water in different ratios, completely different materials were obtained; from fluids that never became viscous to fluids that solidified even before the constituent materials had been completely mixed, and fractured rather than fluidizing when sheared. The material used for the experiments presented in chapters 5 and 6 is prepared by mixing a stock suspension of TM-40 Ludox spheres with a 0.1 mass fraction salt water (NaCl) solution in the mass ratio 6:13. This gives a colloid volume fraction of 0.07 and a 1.1 molar NaCl concentration.

Getting reproducible results with the hard physical gels formed from flocculated colloids is notoriously difficult, since the resulting gel depends very sensitively on the exact preparation of the gel and on the shear history of the sample [126, 151, 152]. For this reason a detailed preparation protocol was established and followed each time, which gave a reproducible gel: A total volume of 200 mL of the two fluids are mixed together in a 0.5 liter bottle with a 6.7 cm diameter, given on hard shake to homogenize the material, and then immediately placed in a horizontal tube of a 7.0 cm diameter which turns at

13.5 rpm for one minute after which the bottle is taken out and left to age for at least 12 hours. Immediately after mixing the two liquids together the fluid rapidly changes from transparent and slightly yellowish to completely opaque and white, which signifies that large aggregates are being formed. The resulting material is almost perfectly suited for the experiments I wanted to conduct:

- It can be reproducibly prepared and give reproducible results.
- It is *very* thixotropic - having an effective change in the viscosity of more than a factor of 10^8 at a stress change of 1 % at the yield stress[†].
- At an imposed shear rate the fluid reaches a steady state within a few minutes, which means that shearing the fluid for just a few minutes erases the shear history of it prior to that shear, which is very important for practical experiments.
- The material reaches a steady state within a few minutes, and then does not change for several hours of shear.
- The fluid gives reproducible results over periods of more than a week.
- It turns out that the MRI signal from this material is very strong, and so in addition it is very well adapted for MRI velocimetry experiments.

Having thus introduced a way of making strongly thixotropic fluids with tunable yield stress and aging timescale by mixing different concentrations of salt and colloids stabilized by a surface charge in water, and having achieved a highly thixotropic fluid with aging times of an experimentally practical scale, I set about measuring its detailed rheological properties using classical rheometrical techniques and local MRI velocimetry measurements. The results of these measurements are presented in chapters 5 and 6 respectively.

[†]This will be discussed in the following chapter, see Fig. 5.3

Chapter 5

The negative slope of the flow curve

Contents

5.1	Introduction	63
5.2	Behavior of the λ-model away from the steady state	64
5.2.1	The evolution of the λ -model under an imposed stress	64
5.2.2	The yield stress measurement problems explained by the λ -model	66
5.2.3	How to experimentally demonstrate the negative slope of the steady state flow curve	68
5.3	Experimental results	69
5.4	Conclusion	71

5.1 Introduction

While the phenomenological understanding of carbopol-like materials is very impressive, this cannot be said for thixotropic materials: It is far from trivial to perform reproducible measurements on such materials [23, 31, 39, 44, 46], and even when this has been done it is not possible to present the information contained in the measurements in a form one can successfully feed into a flow model and predict flows [29, 47]. As described in section 1.4 even qualitatively the yield stress picture that works so well for simple yield stress fluids often fails dramatically for thixotropic materials.

The property of the λ -model that allowed Coussot and co-workers to explain the viscosity bifurcation experiments on thixotropic yield stress fluids is a steady state flow curve which has a negative slope at low shear rates. A material having this property - which implies that in steady state the shear stress *decreases* when the shear rate *increases* from zero - is not very intuitive, and many scientists resist the idea. Indeed it has been “proven” that such a slope cannot exist [153]. A statement that has been revisited and reversed by the same author almost 40 years later [88].

For surfactant systems where the surfactants self-assemble into larger structures that affect macroscopic properties - so called micelles - it is generally accepted that the steady state flow curve has a negative slope between $\dot{\gamma}_1$ and $\dot{\gamma}_2$ [80, 82, 84, 85, 154, 155], and the negative slope in this region has also been demonstrated experimentally [156]. For some reason there has been a much greater resistance to this thought when it comes to yield stress fluids, and the existence of a negative slope of the steady state flow curve has yet to be demonstrated experimentally for such systems.

The aim of this chapter is to demonstrate experimentally that the steady state flow curve for yield stress *can* in fact have a negative slope. The consequences of such a flow curve will be examined analytically in order to establish an experimental procedure for testing for it. This analytical examination also explains why it can be difficult making reproducible measurements and predicting flows for thixotropic yield stress fluids. In addition, it also becomes clear that the intuitive conclusion that a lower stress should not result in a higher shear rate is in fact not all wrong. Finally it is demonstrated experimentally that the Ludox-salt water mixture presented in the previous chapter indeed *does* have a steady state flow curve with a negative slope at low shear rates.

5.2 Behavior of the λ -model away from the steady state

Since the λ -model is the simplest possible model that captures qualitatively the aging and shear rejuvenation properties of thixotropic fluids, the λ -model is used as a starting point for understanding thixotropic yield stress fluids. In order to get a more complete understanding of the λ -model than that which is provided by the steady state flow curve, I will examine how the model behaves also away from the steady state. It turns out that doing so allows for understanding; avalanche behavior, problems with reproducibly measuring the yield stress [31, 47], and - last but not least - how to directly measure whether or not a given material has a negative slope of the steady state flow curve. Even though the λ -model is the starting point of the discussion, both the discussion itself and the conclusions are qualitatively valid for any thixotropic fluid with a negative slope of the steady state flow curve at low shear rates.

5.2.1 The evolution of the λ -model under an imposed stress

The λ -model consists of two equations; one for the viscosity as function of the structural parameter, and one for how the parameter evolves in time as function of the shear rate [29, 47]:

$$\eta = \eta_0 \cdot (1 + \beta\lambda^n) \quad \text{and} \quad \frac{d\lambda}{dt} = \frac{1}{\tau} - \alpha\lambda\dot{\gamma} \quad (5.1)$$

where β , n , η_0 , τ , and α are model parameters. Fixing the time scale and the stress scale by demanding $\tau = \eta_0 = 1$, and for simplicity setting the two dimensionless parameters,

$\alpha = \beta = 1$, the equations reduce to:

$$\eta = 1 + \lambda^n \quad \text{and} \quad \frac{d\lambda}{dt} = 1 - \lambda \dot{\gamma} \quad (5.2)$$

which gives an equation for the steady state flow curve:

$$\frac{d\lambda}{dt} = 0 \Rightarrow \lambda_{ss} = 1/\dot{\gamma} \Rightarrow \eta_{ss} = 1 + \dot{\gamma}^{-n} \Rightarrow \quad (5.3)$$

$$\sigma_{ss} = \dot{\gamma} + \dot{\gamma}^{1-n} \quad (5.4)$$

If $n > 1$ the steady state flow curve then has a minimum at $\dot{\gamma}_c \neq 0$:

$$\frac{d\sigma_{ss}}{d\dot{\gamma}} = 0 \Rightarrow 0 = 1 + (1-n)\dot{\gamma}_c^{-n} \Rightarrow \quad (5.5)$$

$$\dot{\gamma}_c = (n-1)^n \quad (5.6)$$

This can be seen in Fig. 5.1 where the steady state flow curve for $n = 2$ is illustrated and the slope is negative below $\dot{\gamma}_c = 1$.

Even if the steady state flow curve is of major importance, the fluid is of course not always in steady state and points off the steady state flow curve can be visited. In the λ -model there is a one-to-one correspondence between the viscosity of the fluid and the structural parameter λ . Since all values of lambda are allowed in principle, all non-dimensionalized viscosities between 1 and ∞ are possible which means that all $(\dot{\gamma}, \sigma)$ points in Fig. 5.1 with a viscosity (slope) above 1 can be visited if only temporarily. Such a point of corresponding instantaneous shear rate and shear stress values is called a **flow point**. Assuming that the imposed shear stress is constant in time, a flow point on the steady state flow curve is stationary in time while a flow point off the steady state curve can move only on a horizontal line as time goes on.

Let some initial flow point be given by $(\dot{\gamma}_i, \sigma)$. There then exists one critical stress, $\sigma_c(\dot{\gamma}_i)$, such that $(\dot{\gamma}_i, \sigma_c(\dot{\gamma}_i))$ lies on the steady state flow curve and $\frac{d\lambda_{ss}}{dt} = 1 - \lambda_{ss}\dot{\gamma}_i = 0$. If the flow point lies above the steady state flow curve, then $\sigma > \sigma_c(\dot{\gamma}_i)$ which means that the initial viscosity is higher than the steady state viscosity for $\dot{\gamma}_i$, and hence that $\lambda > \lambda_{ss}$. This implies that $\frac{d\lambda}{dt} = 1 - \lambda \dot{\gamma}_i < 1 - \lambda_{ss}\dot{\gamma}_i = 0$ so that λ and hence the viscosity is decreasing in time. Since σ is fixed, the decreasing viscosity leads to an increasing shear rate and the flow points moves to the right in the flow diagram. Conversely, a flow point that starts out below the steady state flow curve moves to the left. *Thus, above the steady state flow curve the viscosity decreases in time and flow points move to the right on a horizontal line, and below the steady state flow curve the viscosity increases in time and flow points move to the left.* This is seen to lead to a steady state flow curve which is stable at shear rates above $\dot{\gamma}_c$, but linearly unstable below it, as illustrated in Fig. 5.1 where small arrows indicate the evolution of flow points under different imposed shear stresses and initial shear rates. The fact that the steady state flow curve is linearly unstable below $\dot{\gamma}_c$ demonstrates that the intuitive resistance towards the negatively sloped flow curve is not all wrong, since practically the situation where the shear rate increases when the

shear stress decreases will never be encountered. It also explains why flow curves with negative slopes have not already been demonstrated for many thixotropic materials - it simply does not show up in steady state measurements. So to prove experimentally that a material has a steady state flow curve with a negative slope, some protocol that does not rely on steady state measurements is needed. In the following section I will show how the reproducibility problems of yield stress measurements can be understood from the λ -model. And how this understanding can be used to construct a measurement method for experimentally demonstrating the negative slope of the steady state flow curve.

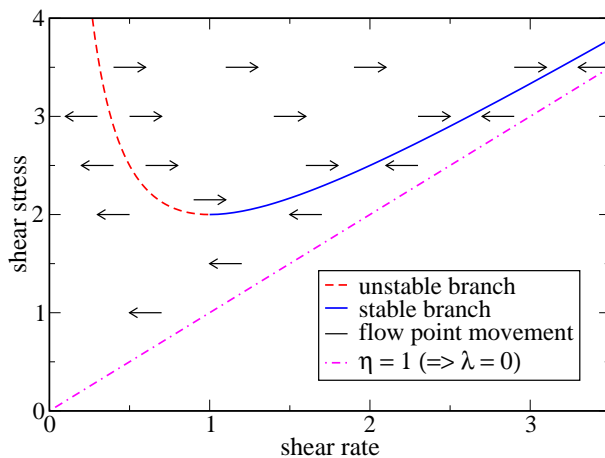


Figure 5.1: The flow diagram of equation 5.2 with $n = 2$. As shown in section 5.2.1, while the flow points move to the right above the steady state flow curve (the viscosity is decreasing in time), they move to the left below it (the viscosity is increasing in time). This means that the part of the steady state flow curve that has a positive slope is stable and the part with a negative slope is linearly unstable. If $\lambda = 0$, then $\eta = 1$ which is a lower limit for the viscosity, so it is not possible for a flow point to enter the region below the $\eta = 1$ line in the diagram.

5.2.2 The yield stress measurement problems explained by the λ -model

As already mentioned, reproducibly measuring the yield stress of typical yield stress fluid is often very difficult, and the measured yield stress can vary more than one order in magnitude depending on the measurement protocol. These problems can be understood through the λ -model. Let the initial structural parameter of a material be λ_i . This defines an initial viscosity, η_i , which in turn defines a straight line in the flow diagram of corresponding values of initial shear rates and shear stresses which intersects the steady state flow curve at some stress, σ_c , as shown in Fig. 5.2A and 5.2B. If the intersection is

in the region where the steady state flow curve has a positive slope (Fig. 5.2A), σ_c is of no crucial importance. Imposed stresses above σ_c will result in slightly higher shear rates, and stresses below σ_c will result in slightly lower shear rates, but only if the imposed stress drops below the stress corresponding to the minimum of the flow curve, σ_{\min} , will the flows eventually stop. So σ_{\min} is the yield stress in this sense - independently of λ_i , η_i , and σ_c .

If the intersection between the steady state flow curve and the straight line defined by the initial viscosity is in the region with a negative slope however, things are quite different (Fig. 5.2B). In this case σ_c is a yield stress since an imposed stress above this value results in a high steady state shear rate (corresponding to the intersection between σ and the stable branch of the steady state flow curve), while an imposed stress below this value results in arrested flows. But σ_c is not the yield stress in the sense of simple yield stress fluids since the material *can* flow in a steady state at shear stresses as low as σ_{\min} . Also, if in a second measurement on the same material λ_i is no longer the same as before, then the apparent yield stress, σ_c , will no longer be the same. If the material to be measured on is simply spooned out from a jar, casually loaded into the measurement geometry and the measurement then begun, it is not hard to imagine that λ_i (and hence σ_c) will vary significantly from measurement to measurement because of the different shear histories of the samples measured. Hence, yield stress measurements will not be reproducible! The λ -model can also explain qualitatively why people have chosen to work with more than one yield stress - for instance one dynamic and one static: The relevant yield stress when the material is already flowing in some steady state (the dynamic yield stress) is σ_{\min} , but if the material has been motionless for long enough that η_i intersects the unstable branch then the relevant yield stress (the static yield stress) is σ_c .

If the λ -model correctly describes why it is hard to get reproducibly measurements it might be possible to use this understanding to devise measurement protocols that allow for reproducibility. According to it, reproducible measurements of the yield stress will generally be achieved if and only if λ_i is identical for all samples. This is not generally the case though, since one often prepares a large batch of material in order to avoid concentration differences between samples, and since different measurements will be preformed on increasingly older samples from the same batch. Fortunately, according to the results from the λ -model - and demonstrated experimentally by Coussot, Bonn and coworkers [29,47] - it is not necessary that two samples have exactly the same shear history to have identical λ_i . This can be achieved if the two samples have been brought to the same steady state ($\lambda_{ss}(\dot{\gamma})$) and then have identical shear histories after they leave the steady state. An effective way of achieving this in the lab is to “pre-shear” the sample at some fixed high shear rate (above $\dot{\gamma}_c$) for sufficiently long time that a steady state has been reached and then leaving the fluid at rest for some fixed time before a measurement is begun. This method has been used by many rheologists and engineers for several years even if it has mainly been based on experience rather than an understanding of why it works [128, 130, 131]. In section 5.3 I demonstrate how the method gives reproducible measurements even on a *very* thixotropic fluid.

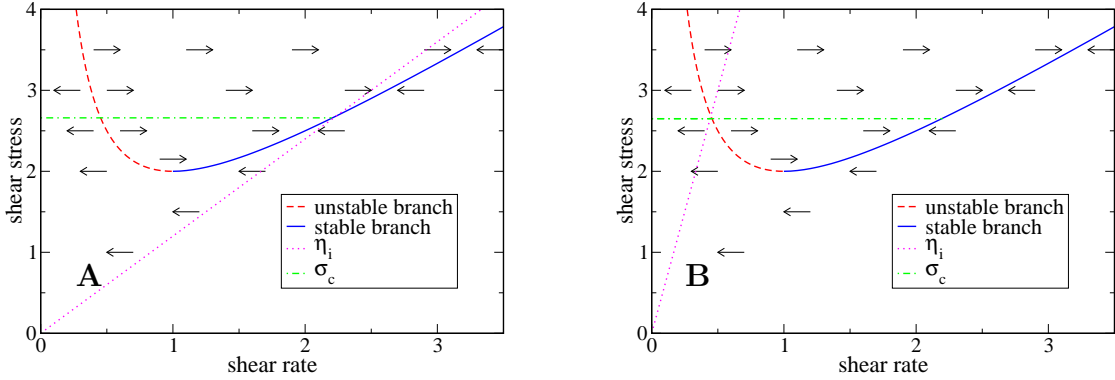


Figure 5.2: The initial value of the structural parameter, λ_i , defines an initial viscosity, η_i , whose intersection with the steady state flow curve defines a critical stress, σ_c , below which the flows slow down and above which they speed up. **A:** If the intersection is with the stable branch, the steady state shear rate is hardly different on either side of the critical stress. **B:** If the intersection is with the unstable branch however, the steady state shear rate jump from 0 to the shear rate corresponding to the intersection between σ_c and the *stable* branch of the steady state flow curve. This explains the spectacular avalanche behavior observed by Coussot and coworkers [47].

5.2.3 How to experimentally demonstrate the negative slope of the steady state flow curve

Apart from explaining the yield stress measurement difficulties and giving a protocol for making reproducible measurements, section 5.2.2 also makes it possible to device a measurement protocol that allows one to demonstrate experimentally whether or not a material has a steady state flow curve with a negative slope. According to Fig. 5.2 it is possible to detect whether the instantaneous flow-point of a given material is above or below the steady state flow curve simply by looking at the evolution of the shear rate: If the shear rate is increasing in time the flow-point is above, and if the shear rate is decreasing the flow-point is below. Thus, one knows that the steady state flow curve must be below any flow-point that speeds up and above any flow point that slows down. In principle then, it should be possible to find the steady state flow curve by simply probing random initial states with random initial shear stresses and observing the motion of the flow-points. Exactly such a procedure is used in the next section to experimentally demonstrate for the first time a negative slope in the steady state flow curve of a yield stress fluid.

5.3 Experimental results

The first experimental series was performed on the Ludox-salt water mixture described in chapter 4 in a double-gap geometry of a 57 mm height and radii of 18.25, 19.75, 20.75, and 22.25 mm (see Fig. 2.1 about double-gap geometries). Since I had verified that the material did not rapidly degenerate under even extensive shear, I used the exact same sample for all the measurements. The procedure was simple: On some random initial state I imposed some shear stress and observed the evolution of the shear rate for some time. I then stopped the flow for some variable amount of time to get a new “initial” state to which I imposed some shear stress and observed the shear rate etc. etc. For each measurement I plotted the initial and final flow-point in red if the shear rate decreased and blue if the shear rate increased. The resulting data are shown in Fig. 5.3, which greatly resemble Fig. 5.1, and clearly demonstrate that the steady state flow curve of the Ludox-salt water mixture has a negative slope for shear rates below about 100 s^{-1} . From Fig. 5.3 it can also be seen for one fixed stress the resulting shear rate can vary by more than eight orders of magnitude. It can also be seen that stresses as low as 3 Pa can result in a sheared material, and that stresses as high as 35 Pa can result in arrested states - i.e. a variation of “the yield stress” of more than one order of magnitude.

The second experimental series was performed on an identical Ludox-salt water mixture, but using a 4° cone-plate geometry since the stress variation in this geometry is less than a factor of 0.005, which is desirable because a strong stress dependence of the rheological properties of the fluid can lead to artifacts if the stress is heterogeneous (see section 2.2.3). The radius of the geometry is 2 cm. Using the qualitative understanding from Fig. 5.2 I made an attempt at measuring the full steady state flow curve both above and below the critical shear rate in a more controlled way. Since the steady state flow curve is stable above $\dot{\gamma}_c$, to get the stable branch I first pre-sheared the fluid at a high shear stress resulting in high shear rates to ensure complete fluidization of the sample. I then progressively lowered the stress, waited for a steady state to be reached, and recorded the imposed shear stress and the steady state shear rate as a point of the steady state flow curve. I did this until the imposed stress was lowered to a value where the steady state shear rate dropped abruptly to zero - indicating that the stress had been decreased below σ_{\min} . To pin the unstable branch of the steady state flow curve I several times prepared the fluid in some *reproducible* initial state* by pre shearing it until a steady state had been reached and then letting it rest for a certain amount of time. To several such identical initial states I imposed different shear stresses and recorded the initial shear rates and whether they increased or decreased. I could then pin the steady state flow curve to be between the initial flow-point for the highest stress that resulted in no flow and the lowest stress that resulted in high shear rates. The steady state flow curve is thus confined between the two points: $(\dot{\gamma}_{\text{initial}}(\sigma_{\text{slow down}}), \sigma_{\text{slow down}})$ and $(\dot{\gamma}_{\text{initial}}(\sigma_{\text{speed up}}), \sigma_{\text{speed up}})$. Doing this for several different rest-times (0, 10, 500, and 3,000 seconds) I was able to pin the steady state flow curve between such points over a considerable range of shear stresses. The combined result of these two different measurement methods for the stable and un-

*in contrast to the first series where the initial state was not controlled

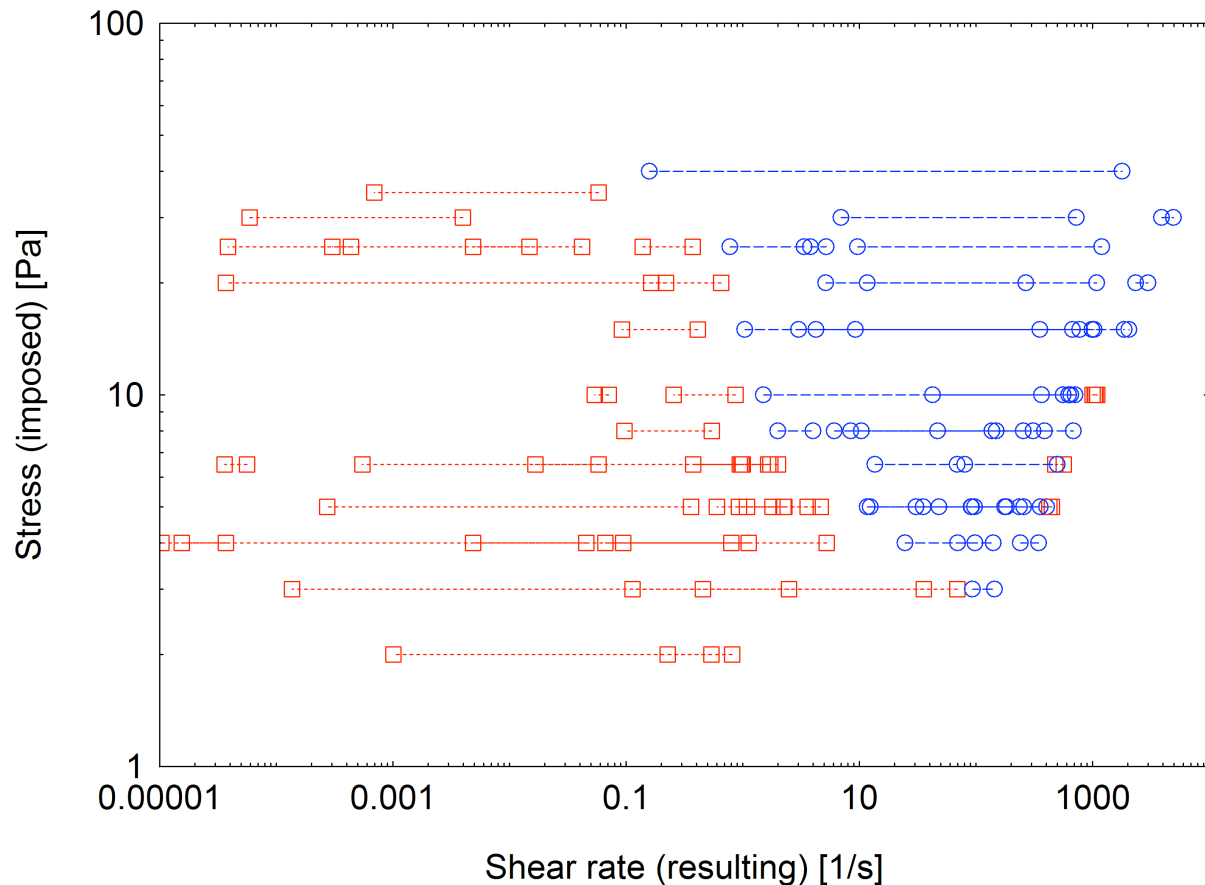


Figure 5.3: The material was brought to different random initial states by waiting some random time after the shear from the prior imposed stress had stopped. Then some new shear stress was imposed for some time. The initial and final shear rates resulting from imposing a given stress to some initial condition are connected by a line. Flows that slow down in time are marked by red squares and red lines, while flows that speed up are marked by blue circles and blue lines.

stable branch respectively is shown in Fig. 5.4. From this figure it is evident that the steady state flow curve of the material has a negative slope below a critical shear rate of about $\dot{\gamma}_c = 60 \pm 3 \text{ s}^{-1}$.

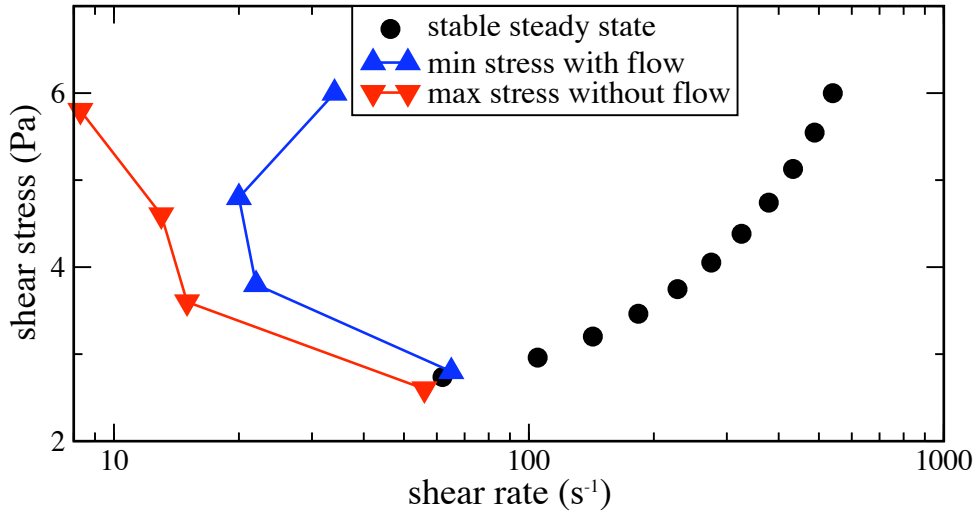


Figure 5.4: The full steady state flow curve can be found using two different types of measurements. The stable branch is simply found from imposing the shear stress and observing the steady state shear rate, while the unstable branch can be pinned from the left and right by (for each of several material ages) finding initial flow-points that respectively slow down and speed up under imposed shear stress. From the lower right corner the aging times after pre-shear at 150 s^{-1} is: 0, 10, 500, and 3000 seconds. The material is seen to have a critical shear rate of about $\dot{\gamma}_c = 60 \pm 3 \text{ s}^{-1}$.

5.4 Conclusion

In this chapter I have examined more closely the qualitative implications of the λ -model by Coussot, Bonn et al. that I presented in section 1.4. I have shown that in addition to viscosity bifurcation, both avalanche behavior, irreproducibility of yield stress measurements, and several flow behaviors that conflict with the picture of simple yield stress fluids can be qualitatively understood through the λ -model. Finally I have presented experiments that for the first time show (and very clearly so) the existence of the region of the steady state flow curve with a negative slope in thixotropic yield stress fluids. The existence of this negative slope is the central feature of the λ -model and is at the origin of all the interesting behavior that the model can give, but has never previously been demonstrated.

Chapter 6

Shear banding in thixotropic yield stress fluids

Contents

6.1	Introduction	73
6.2	Some previous shear banding experiments	74
6.3	Shear banding in the λ model	74
6.3.1	Shear banding in heterogeneous stress fields	75
6.3.2	Shear banding in homogeneous stress fields	75
6.3.3	The <i>lever rule</i>	76
6.4	MRI velocimetry experiments	77
6.4.1	Experimental procedure	77
6.4.2	MRI velocimetry results	78
6.4.3	Experimental demonstration of the lever rule	79
6.5	Comparing the MRI and rheometrical measurements	80
6.5.1	A negative slope in the steady state flow curve can result in a stress plateau under imposed shear rate	81
6.6	Measuring the local state of the material	83
6.6.1	DWS measurements inside and outside the flowing band	84
6.7	A serious limitation of the lever rule	86
6.8	Practical handling of thixotropic yield stress fluids	88
6.9	Conclusion	89

6.1 Introduction

When mixing dough for bread or a cake, or when dipping the knife in the mustard or mayonnaise before spreading it onto the sandwich bread, shear banding is observed; only

the fluid close to the moving tool in a Couette cell is sheared while the material further away is motionless. As was explained in chapters 2 and 3 such shear banding is well understood as a result of a simple yield stress fluid subject to a heterogeneous shear stress field; closer to the moving tool the stress is higher than further away, which results in a higher shear rate near the tool than near the walls. If the fluid is Newtonian, the shear rate variation is proportional to the stress variation, but if the material has a yield stress the shear rate will change dramatically within a small range of stress values around the yield stress. Since such a modest stress variation can occur in a very narrow spatial range, the change in local shear rate can be very dramatic. *A priori* one might think that a similar picture holds for thixotropic yield stress fluids - i.e. shear banding is the result of a critical stress and happens only in heterogeneous stress fields. As I will show in this chapter however, this conclusion is only partially correct: While shear banding may happen as a result of heterogeneous stress fields just as in simple yield stress fluids, it can also occur in completely homogeneous stress fields !

6.2 Some previous shear banding experiments

Numerous shear banding experiments, simulations and analytical work have been performed on several systems, including wormlike micelles [79, 84, 85, 154, 157], foams [117, 158, 159], pastes [160] emulsions [148] and, thixotropic yield stress fluids and glass-like systems [53, 141, 148]. By far the majority of experimental shear banding experiments are done in inhomogeneous stress fields - typically in a Couette geometry - which makes it difficult to say whether the shear banding is a result of a stress heterogeneity or a result of a flow instability intrinsic to the material. However, some experiments have been performed in cone-plate geometries with essentially homogeneous stress where shear banding was also observed [148]. In that experiment however (and contrarily to many experiments on micellar systems), that material did not shear band according to the 'lever rule', which makes for a particularly simple interpretation of why the material shear bands (see section 6.3.3).

6.3 Shear banding in the λ model

I will again use the λ model to qualitatively discuss the behavior of thixotropic yield stress fluids, but the discussion is equally valid for more general thixotropic yield stress fluids, where for instance the shear stress is a non-separable function of the structural parameter and the shear rate: $\sigma = \sigma(\lambda, \dot{\gamma}) \neq \dot{\gamma}\eta(\lambda)$. The only requirement for the validity of the results is that the steady state flow curve has a minimum at some non-zero critical shear rate, $\dot{\gamma} \neq 0$.

6.3.1 Shear banding in heterogeneous stress fields

The shear banding of thixotropic yield stress fluids under an imposed, heterogeneous shear stress field can be easily understood as a result of several simultaneous viscosity bifurcation experiments. As shown in the previous chapter, depending on the initial state of the fluid there exists some initial “yield stress” below which the material will eventually come to a halt and above which the fluid will flow at some high shear rate. The stress variation within the geometry simply corresponds to probing the material simultaneously with a continuous range of shear stresses - some of which will lead to flow and some of which will not. The instantaneous “yield stress” then plays exactly the same role as the proper yield stress of a simple yield stress fluid for the purpose of predicting shear banding in a heterogenous stress field.

The reasoning above is only correct under one crucial assumption though; namely that the stress on a fluid element does not change in time (i.e. $\frac{d\sigma}{dt} = 0$). Even if there is no explicit time-dependence of the stress field (i.e. $\frac{\partial\sigma}{\partial t} = 0$), the assumption will not hold if a fluid element moves between regions with different stresses (i.e. if $(\mathbf{u} \cdot \nabla)\boldsymbol{\sigma} \neq 0$). The assumption will be valid in rheological measurement geometries such Couette, cone-plate, plate-plate, etc. etc., but may not be valid for typical industrial processing or transportation applications where the shear stress will typically depend on the location along the pathline of a fluid element (i.e. the path a fluid element follows in time). If this is the case, it will be necessary to keep track of the evolution of λ for each fluid element and use $\eta(\lambda)$ and the stress to get the shear rate which then again affects λ . This process is of course very complicated and requires a very good characterization of the material. But in industrial applications it will actually often not be the shear stress that is imposed, but rather the shear rate. As I show below, imposing the shear rate on a flow curve with a minimum is fundamentally different from imposing the shear stress, and doing so can give some surprising results.

6.3.2 Shear banding in homogeneous stress fields

If a spatially homogeneous stress field is imposed on a thixotropic material the flow situation is very simple; either the initially imposed shear stress is above an initial “yield stress” and everything flows, or the imposed stress is below the yield stress and nothing flows. This almost trivial case is in stark contrast to what happens if, in a situation with a homogeneous stress field, it is not the shear stress but the shear rate that is imposed.

For a strictly monotonous steady state flow curve there is no difference between imposing the shear rate or the shear stress since there is a one-to-one correspondence between the shear stress and the shear rate. For a non-monotonous flow curve such as one with a minimum there is no such bijection between the imposed shear stress and the imposed shear rate since one shear stress can in practice result in two stable steady state shear rates; the intersection between the stress and the stable branch, and the point $(0, \sigma)$ (which implies $\lambda = \infty$). As shown in chapter 5, the viscosity bifurcation is caused by flow points being attracted to one or the other stable steady states - depending on the

initial stress and shear rate. For an imposed shear rate, there exists precisely one stress corresponding to a steady state for that shear rate (the stress corresponding to the intersection of the imposed shear rate with the steady state flow curve). For this reason one might expect that it should be possible to measure the unstable branch of the steady state flow curve simply by imposing different shear rates below $\dot{\gamma}_c$ and measuring the resulting shear stress, since the flow point “has nowhere to go” because it has to stay on the vertical line of the imposed shear rate. Even if such a reasoning has been proposed (see [88]) it is incorrect, as can be easily demonstrated: assume that a fluid with a critical shear rate, $\dot{\gamma}_c$, is confined between two infinite plates separated by a height, h , and moving tangentially with a relative velocity, U , resulting in a globally imposed shear rate of $\dot{\gamma}_{\text{global}} = U/h$. Assume also that the initial flow profile in the gap is linear; $u(y) = \dot{\gamma}_{\text{global}}y$, and that at time $t = 0$ there is a infinitesimal sinusoidal perturbation of the flow field of some wavelength consistent with the boundary conditions:

$$u(y, t) = \dot{\gamma}_{\text{global}}y + \delta u(t) = \dot{\gamma}_{\text{global}}y + u_1(t) \sin\left(\frac{y}{h}n\pi\right), \quad n \in \mathbb{N} \quad (6.1)$$

The stability of the linear profile will then be determined by whether the perturbation increases or decreases in time. This in turn is determined by Newtons second law:

$$\frac{d\delta u}{dt} = \frac{du}{dt} = \frac{F}{M} = \lim_{\Delta y \rightarrow 0} \frac{A[\sigma(y + \Delta y) - \sigma(y)]}{A\rho\Delta y} = \frac{1}{\rho} \frac{d\sigma}{dy} = \frac{1}{\rho} \frac{d\sigma}{d\dot{\gamma}_l} \frac{d\dot{\gamma}_l}{dy} = \frac{1}{\rho} \frac{d\sigma}{d\dot{\gamma}_l} \frac{d^2 u}{dy^2} \quad (6.2)$$

where F is the force of a fluid element, M its mass, Δy its height, A its surface area, ρ the density of the fluid, and $\dot{\gamma}_l$ is the local shear rate as function of y . Plugging in the form of the perturbation from equation 6.1 this gives:

$$\frac{d\delta u}{dt} = -\frac{d\sigma}{d\dot{\gamma}_l} \frac{n^2\pi^2}{\rho h^2} u_1 \sin\left(\frac{y}{h}n\pi\right) = -\frac{d\sigma}{d\dot{\gamma}_l} \frac{n^2\pi^2}{\rho h^2} \delta u \quad (6.3)$$

Hence the perturbation will grow in time exactly when $\frac{d\sigma}{d\dot{\gamma}_l}$ is negative - i.e. when $\dot{\gamma}_l$ is below $\dot{\gamma}_c$. Since in a homogeneously sheared material $\dot{\gamma}_l = \dot{\gamma}_{\text{global}}$, this means that a homogeneous shear profile will be linearly unstable when the globally imposed shear rate shear rate, $\dot{\gamma}_{\text{global}}$, is below $\dot{\gamma}_c$.

6.3.3 The lever rule

So if the linear flow profile is linearly unstable for imposed shear rates below $\dot{\gamma}_c$, which will be the stable one? The common experimental observation that in a dynamic system where energy is dissipated, the stable steady state will be the one where the rate of dissipation of energy is at a minimum within the constraints of the system, has previously been used to predict viscous flows [161]. In the case of a fluid in a homogeneous stress field with an imposed shear rate, the rate of energy dissipation per unit area is: $\dot{E}_{\text{dissipated}} = \sigma U = \sigma H \dot{\gamma}_{\text{global}}$, where U is the velocity of the moving surface and H is the separation between the two surfaces. Since H and $\dot{\gamma}_{\text{global}}$ are constant in an imposed shear rate experiment, the energy dissipated is minimized when σ is. This means that the steady state flow of

a flow curve with a minimum will occur at the lowest stress that is consistent with the boundary conditions: Above $\dot{\gamma}_c$ this lowest stress is simply the intersection of the imposed shear rate and the steady state flow curve, but below the critical shear rate the lowest stress is that corresponding to the minimum of the flow curve, σ_{\min} . At this stress there are precisely two steady shear rates the material can be in - either flowing at $\dot{\gamma}_c$, or solid; $\dot{\gamma} = 0$. The flow that results in the lowest rate of energy dissipated is then one where a part of the material is sheared at $\dot{\gamma}_c$ (say, the part between $h = 0$ and $h = h_{\text{sheared}}$) and the other part is solid. Any local shear rate above $\dot{\gamma}_c$ demands stresses higher than σ_{\min} , and any local shear rate below $\dot{\gamma}_c$ are linearly unstable as shown above (except for $\dot{\gamma} = 0$). The global, average shear rate is then given by:

$$\dot{\gamma}_{\text{global}} = \frac{v}{H} = \frac{h_{\text{sheared}}\dot{\gamma}_c + (H - h_{\text{sheared}}) \cdot 0}{H} = \frac{h_{\text{sheared}}}{H}\dot{\gamma}_c \equiv \alpha\dot{\gamma}_c \quad (6.4)$$

The fact that the fraction of the material which is sheared, α , grows linearly from zero to one as the global shear rate grows from zero to $\dot{\gamma}_c$ is known as the **lever rule** [29,31,47,148]. For wormlike micellar systems (see [162,163] for a review and also [164–166]) which have steady state flow curves with a flat stress plateau connecting two newtonian regimes with different viscosities, a similar lever rule has been demonstrated experimentally and understood theoretically [79,80,84–86,154,155,157,167–172]: $\dot{\gamma}_{\text{global}} = \dot{\gamma}_{\text{high}}\alpha + \dot{\gamma}_{\text{low}}(1-\alpha)$, but for yield stress fluids where the stress diverges at both low and high shear rates shear banding is much less well understood (see for instance the reviews *Perspectives on shear banding in complex fluids* [79] and *Complex dynamics of shear banded flows* [80], where many pages are spent on shear banding in wormlike micelles and lamellar surfactant solutions, but where shear banding in attractive colloidal gels is not treated at all) and the lever rule has hitherto only been suggested theoretically. While it has been shown experimentally that for thixotropic yield stress fluids the width of a sheared band increases with the imposed rate, the relation between the two was not linear, nor was the shear rate in the shear band independent of the imposed shear rate [148].

6.4 MRI velocimetry experiments

In order to try to verify experimentally the lever rule for a thixotropic yield stress fluid, MRI velocimetry measurements under different imposed shear rates were performed on the salt water-colloid material presented in chapter 4.

6.4.1 Experimental procedure

In order to have a very homogeneous stress field, a 4° cone-plate geometry with a 6 cm radius was used for most of these measurements. A 4° cone-plate gives a shear stress variation of less than 0.5 %. Some measurements were done using a 8° cone-plate with a stress variation four times as large. These measurements give similar results, indicating that the phenomenon is not caused by the stress variation, but is intrinsic to the material.

For each measurement, a fresh sample of the Ludox spheres/salt water system was loaded into the geometry and then subjected to a shear rate of 150 s^{-1} (which is well above the critical shear rate as seen in Fig. 5.4) for 5 min to get a reproducible initial state. Then a given shear rate was imposed. For 5 minutes the fluid was allowed to reach a steady state, and then the flow profile was measured for 5 minutes. Since for technical reasons the shear rate in the 4° cone-plate geometry can only be changed reliably between 15 and 150 s^{-1} the critical shear rate of the fluid has to lie in a narrow band for measurements in the shear banding regime to be successfully performed. In order to produce a steady state the critical shear rate must be so low that at 150 s^{-1} everything is fluidized, but it must also be so high that at 15 s^{-1} only a small fraction is sheared. Effectively it is required that $50\text{ s}^{-1} < \dot{\gamma}_c < 100\text{ s}^{-1}$. This was known already when the thixotropic properties of the fluid was adjusted as explained in chapter 4. Consequently, the colloid and salt concentrations were varied until a material with a critical shear rate in the requested range was achieved.

6.4.2 MRI velocimetry results

In Fig. 6.1 MRI “pictures” of the material velocities can be seen for both a homogeneous (Fig. 6.1A) and a shear banded (Fig. 6.1B) flow situation. Connected regions of black and white have about the same velocity. The experimental procedure presented in the section above was followed for several imposed shear rates, and the resulting flow profiles for several different globally imposed shear rates can be seen in Figs. 6.2A and 6.2B which show respectively the angular speed and the relative speed of a fluid element as function of the angle from the bottom plate. Using this rescaling, measurement points from different radii and heights from the bottom plate collapse onto a master curve. Evidently, quite distinct shear banding occurs even in a homogeneous stress field. Apart from the measurements in the 4° cone-plate geometry, experiments were also performed using an 8° cone-plate geometry, which has a shear stress variation 4 times as high. The obtained results were completely similar to those from the 4° geometry which indicate that the shear banding is not induced by the stress variation. Another important observation is that the transition between the sheared and the solid region is very abrupt and that the shear rate in the sheared region is constant in space which is incompatible with the behavior of a simple Herschel-Bulkley fluid in an inhomogeneous stress field.

In Fig. 6.2A it can be seen that the local shear rate in the sheared region (the slope of the curve) is constant for globally imposed shear rates below 60 s^{-1} , while the width of the sheared band increases with shear rate. Above 60 s^{-1} all the material is sheared and the “local” shear rate increases with the globally imposed one. In Fig. 6.2B it can be seen that the width of the sheared band increases about linearly from zero to one as the globally imposed shear rate increases from 0 to 60 s^{-1} .

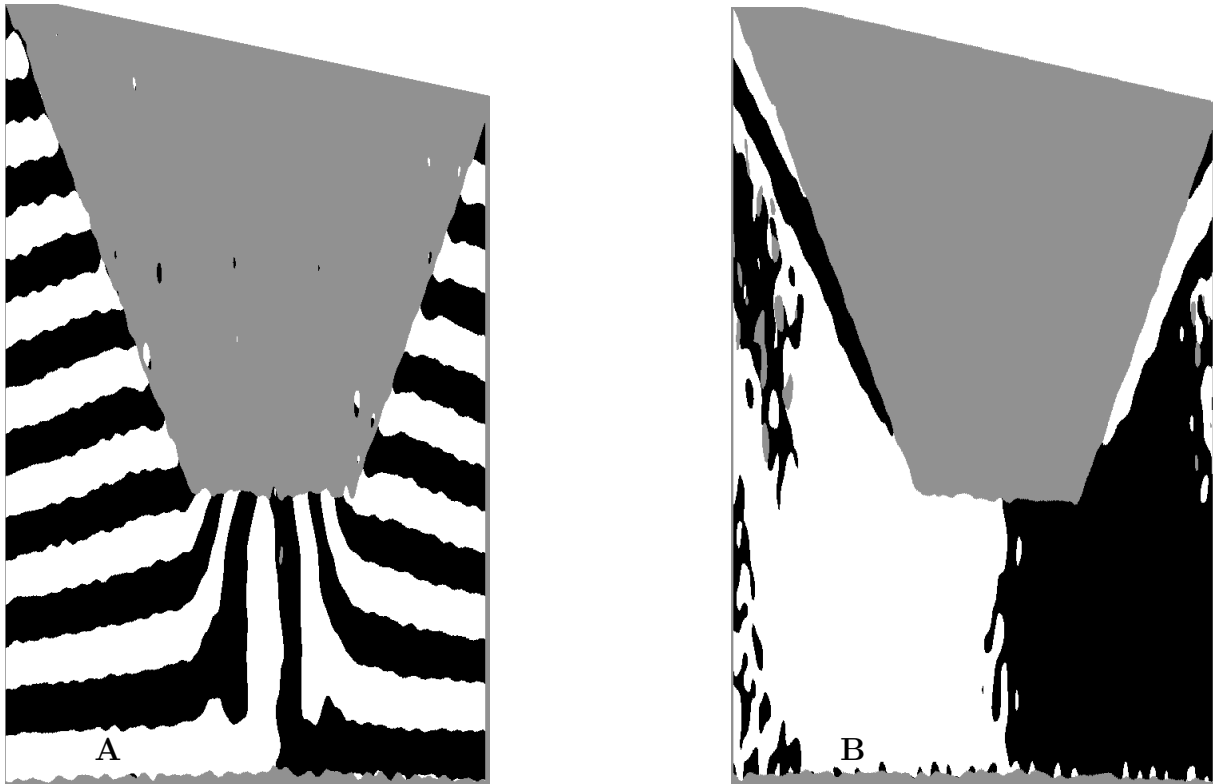


Figure 6.1: MRI ‘pictures’ of the velocities in the cone-plate geometry at different imposed shear rates. Connected regions of black and white marks regions of the with similar velocities (grey marks the surrounding geometry). Note that the r direction is strongly compressed compared to the z direction - the angle of the cone is 4° . The radius of the geometry is 6 cm and the height at the edge is 0.4 cm . The pictures are asymmetrical because of the software making the picture - not because of the data sets themselves (this has not been corrected since the pictures are normally intended for the scientist to get a quick qualitative feel for how the experiments are going). **A:** A situation where the imposed shear rate (60 s^{-1}) is just above the critical shear rate. Here it is seen that the velocity increases linearly with both r and z throughout the material - everything is sheared homogeneously. Interestingly the material ‘completes the cone’ and creates a solid tip of fluid that rotates with the cone as a solid body (seen as vertical stripes). This tip is about a millimeter in height. **B:** A situation where the imposed shear rate (15 s^{-1}) is below the critical shear rate. In spite of some noise it is seen that most of the fluid is solid while only a thin layer near the cone is being sheared.

6.4.3 Experimental demonstration of the lever rule

From the lever rule there are two different ways of finding the critical shear rate: The local shear rate in the partially sheared region during shear banding is equal to $\dot{\gamma}_c$. And $\dot{\gamma}_c$ is also the shear rate at which the fraction of the material which is sheared extrapolates to one. This is illustrated in Fig. 6.3A where the local shear rates and sheared fractions from

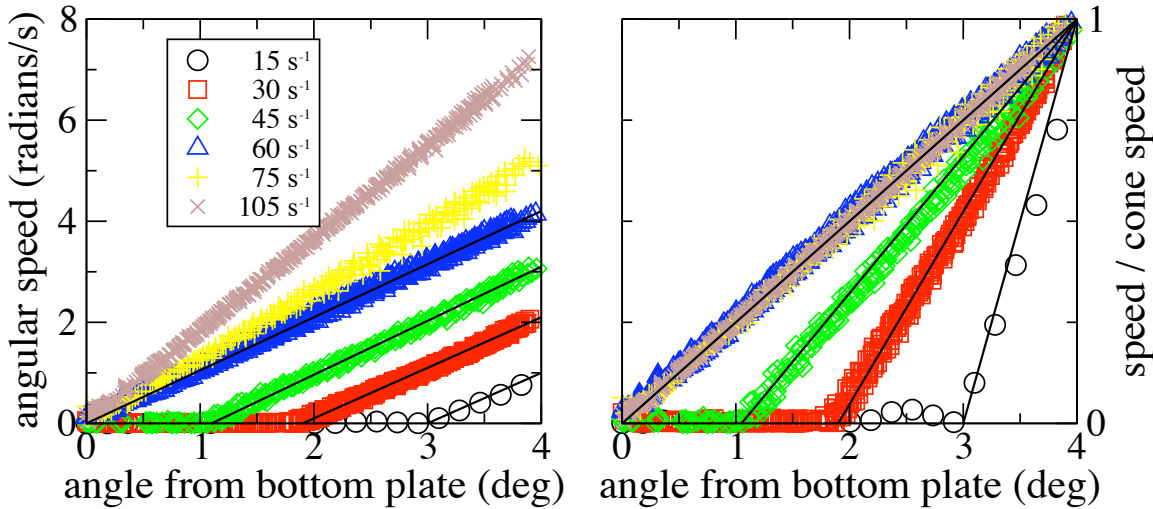


Figure 6.2: Velocity profiles in a 4 degree cone-plate geometry for different globally imposed shear rates. **a:** Fluid velocity in radians/s. **b:** Fluid velocity normalized by the cone velocity. Full lines are straight line fits to the flow profile in the sheared region. The data are plotted as radians/s and speed/cone speed *vs.* angle from the bottom plate in order to remove the radius and height dependence of the data and make the data at all radii and heights collapse.

the measurements in Fig. 6.2 are shown as functions of global shear rate. It can be clearly seen that the fraction of the material which is sheared increases linearly with the global shear rate until everything is sheared which happens at a shear rate of about 60 s^{-1} . It is also clear that at shear rates below about 60 s^{-1} , the shear rate in the sheared region is about 60 s^{-1} .

The fits to the data points in Fig. 6.3 gives a numerical value for the critical shear rate: $\dot{\gamma}_c = 60 \pm 1\text{ s}^{-1}$. The lever rule has thus been clearly shown to hold for yield stress fluids with a minimum in the flow curve.

6.5 Comparing the MRI and rheometrical measurements

In chapter 5 the steady state flow curve for the salt water-colloids mixture was shown to have a local minimum at a critical shear rate of about $\dot{\gamma}_c = 60 \pm 3\text{ s}^{-1}$. In this chapter I have shown that MRI velocimetry measurements on the same fluid shows that the material shear bands according to the lever rule when the imposed shear rate is below a critical shear rate of about $\dot{\gamma}_c = 60 \pm 1\text{ s}^{-1}$. In other words, the critical shear rate obtained from the velocimetry and the rheometrical measurements match perfectly as can also be seen in Fig. 6.4.

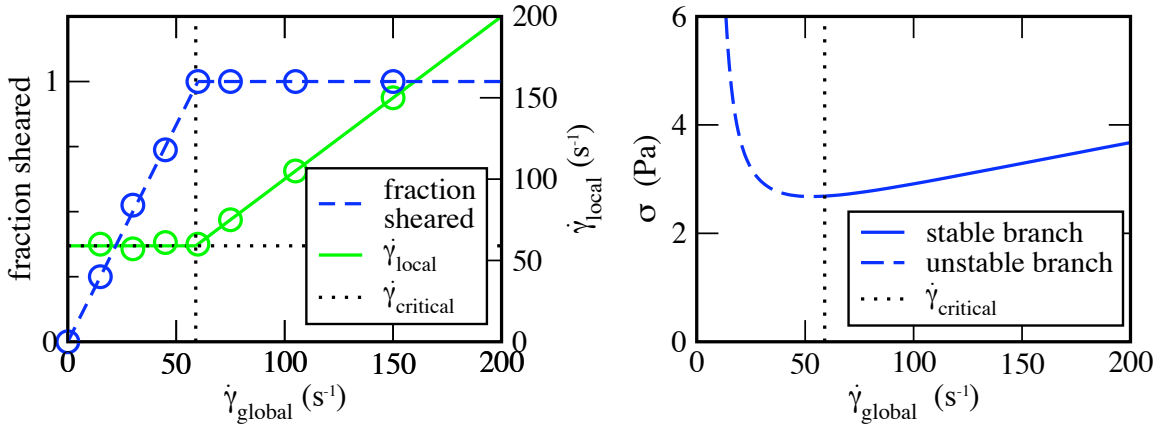


Figure 6.3: a) The 'lever rule' giving the fraction of the fluid which is sheared and the shear rate in that fraction depending on the critical shear rate. The data points are extracted from the fits in Fig. 6.2. b) Steady state flow curve as given by the model. The branch to the right of the critical shear rate is stable while the branch to the left is unstable.

6.5.1 A negative slope in the steady state flow curve can result in a stress plateau under imposed shear rate

According to the lever rule and the argument of minimization of the dissipation of energy that led to it, the shear stress in the MRI measurements should be equal to the stress at the minimum in the flow curve when the imposed shear rate is below the critical shear rate. Unfortunately there is no way of measuring the shear stress inside the MRI facility because of the limitation of which materials that can be present and functional inside the powerful magnetic fields there.* However, loading an identical sample into the 4° geometry in the rheometer and imposing an identical shear rate will result in the exact same shear stress as in the MRI measurements if the same procedure is followed. The result of such measurements are shown along with simple imposed stress measurements in Fig. 6.5. As expected, the measurements under imposed shear stress and imposed shear rate coincide above the critical shear rate and differ below it; the imposed shear rate measurements show a plateau at σ_{\min} , while the resulting shear stress measurements show a viscosity bifurcation at σ_{\min} , where the steady state viscosity jumps discontinuously from a low to an infinite value.

For imposed shear rates below 20 s^{-1} the recorded stress value is not stable but fluctuates, showing stick-slip behavior. This may be an indicator that the width of the sheared band becomes as small as the steady state cluster size. If the sheared band is only a few clusters wide it can easily block the shear. Since the intrinsically stress imposed rheometer controls the shear rate via a control loop, the rheometer increases the stress upon such blockage until the material starts flowing again, and then decreases the stress again. Since this control loop has some finite reaction time, such big variations in the

*The possibility of doing so is currently being installed, but the technical challenge is daunting.

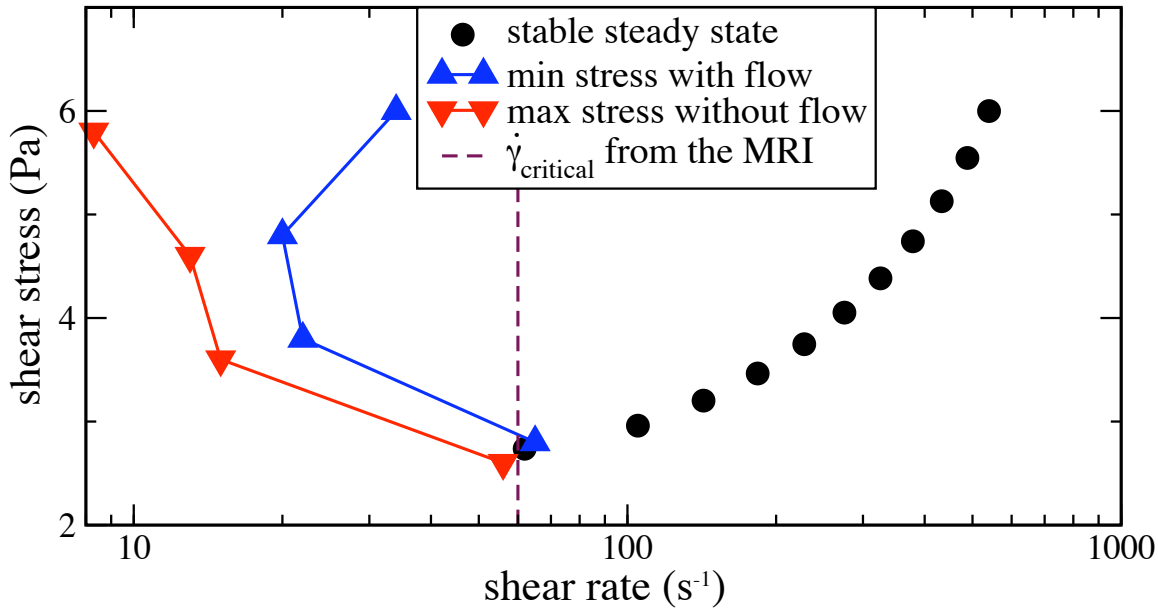


Figure 6.4: Combined figure with the rheometrical results from Fig.5.4, and the critical shear rate from the MRI measurements. The critical shear rate from the MRI measurements is seen to match perfectly the minimum of the flow curve from the rheometrical data.

resistance to flow may lead to stick slip behavior as observed here.

The interesting thing about Fig. 6.5 is that while the actual flow curve has a negative slope below the critical shear rate, the imposed stress measurements falsely “show” that the steady state flow curve has a plateau below $\dot{\gamma}_c$ because of the shear banding. This is particularly interesting since rheological measurements on yield stress fluids at low shear rates are often done using imposed shear rate measurements, and since such measurements *very* often show stress plateaus [29, 31, 39, 83, 124]. Such a behavior is exactly what one would expect for an ideal yield stress fluid where a small stress range just above the yield stress corresponds to a large range of shear rates, but it is also *exactly* the behavior one would expect for a fluid which actually has a minimum in the flow curve and is shear banding at low imposed shear rates as shown here. There should be a theoretical difference between the two; while the plateau for an ideal yield stress fluid should have a slight slope since the viscosity is diverging continuously, the plateau for a shear banding fluid should be *flat*. But since this difference may well be below the resolution of the rheometer, another way to distinguish between the two scenarios is needed. In principle the most easy way to know for sure is to do velocimetry to directly see if the material is shear banding, but in practice easiest way to know for sure whether a stress plateau is real or an artifact is to try to reproduce the plateau using imposed stress measurements after the “right” stress range has been found by an imposed rate experiment. If this can be done the fluid behaves like an ideal yield stress fluid. If not, it is a thixotropic yield stress fluid with a minimum at $\dot{\gamma}_c$ below which an artificial stress plateau appears because

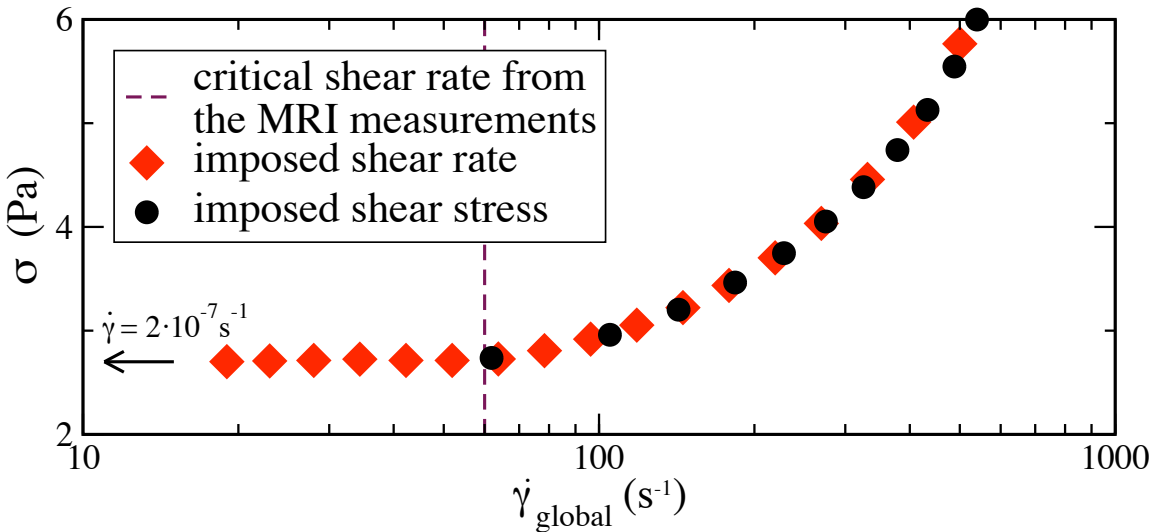


Figure 6.5: Steady-state flow curves at imposed shear rate and shear stress. As predicted by the model the experiments coincide above the critical shear rate while they differ below - showing a stress plateau and no flow respectively. For imposed shear rates below 20 s^{-1} the recorded stress value is not stable but fluctuates, showing stick-slip behavior. This may be an indicator that the width of the sheared band becomes as small as the steady state cluster size in the band leading to jamming. Note that here and elsewhere the microscopic model is applied only to the liquid phase, i.e. in steady state only above $\dot{\gamma}_c$ - also in the shear-banding regime. The arrow to the left indicates that for a stress 1% lower than the critical stress the resulting shear rate is $2 \cdot 10^{-7} \text{ s}^{-1}$ which is solid to the resolution of our rheometer.

of shear banding.

6.6 Measuring the local state of the material

So far, all the predictions about the behavior of the fluid have been successful. But in some sense they have all been indirect; the material has been assumed to be “older” in the solid state than in the flowing state, and the shear banding predicted from this assumption has been exact. To play the devils advocate however, one might argue that since the shear stress is never *perfectly* homogeneous even in a small angle cone-plate geometry, the shear banding might still be the result of inhomogeneous stresses on a fluid in a homogeneous stress rather than a fluid in two different states subject to the same stress. The way to counter such an argument is to measure directly the local state of the material inside and outside the flowing band non-intrusively. This must be done using a passive measurement technique such as DLS or DWS to avoid disturbing the local state. Since the material in question here is opaque however, only DWS can be used.

6.6.1 DWS measurements inside and outside the flowing band

As explained in section 2.4, in Diffusing Wave Spectroscopy, rheological properties of a material are determined by sending laser light into a strongly scattering medium and observing how fast the auto-correlation function of the scattered light intensity decays [93]. Individual scatterers in the material continuously receive small thermal kicks of a typical size of kT which cause them to move around. This in turn changes the interference of the scattered light at a detector, which causes the detected light intensity signal to fluctuate in time. Thus, the (Brownian) motion of the particles can be studied using light scattering.

I wanted a setup that made it possible to detect the local movement of scatterers in several locations inside and outside the sheared band, and at the same time detect by other means whether the measurement is done on material that is in the sheared band or not. This is most practically done in a Couette geometry since it is possible to mount a laser parallel to the rotation axis, send the laser light through the sample, and collect the light on the opposite side. The laser and detector can be moved to different radii and hence probe different locations of the fluid. The width of the shear band is also easily detected in a Couette setup by simply adding tracer beads on the surface and observing their motion. In order to get DWS measurements at several spatial locations with respect to the shear band (and for the tracking of the tracer beads to work), the gap in such a Couette cell must be relatively large. This in turn requires that the size of the whole cell is rather big if the stress variation inside the gap is not to become quite large. Since the outer radius of the normal Couette cells for our rheometer is only 13.5 mm, and since the laser and detector cannot be mounted on the rheometer, I decided to construct a completely new setup to perform the local DWS measurements. The setup is sketched in Fig. 6.6. The inner cylinder in the Couette cell has a radius of 75 mm and is turned at different controllable speeds by a stepper motor. The laser light is sent through a glass plate in the bottom of the cell and diffuses through the sample. A collimating optical fiber detects light emitted from a point at the surface of the material directly above the laser beam. The collected light is detected by a photomultiplier and sent to a correlation card that provides the autocorrelation function.

After a pre-shear were the whole of the material is sheared, a shear rate below the critical shear rate - such that the material shear bands - is imposed. The autocorrelation function is then measured at several positions in the gap by translating the laser and optical fiber to different radial positions. For the duration of each DWS measurement (one minute) the flow is stopped in order to detect only thermal diffusion of the scatterers and not the overall translation. As soon as the flow is stopped the material in the region that is fluidized under shear start aging and it will eventually become solid at rest. To prevent accumulated aging over the course of many measurements, the same sub-critical shear rate is imposed on the material between measurements to keep the material close to the steady state for all measurements. I verified that during a measurement time of one minute the material didn't age enough for the DWS measurement to change detectably. The resulting autocorrelation functions for several gap positions are shown in Fig. 6.7 from which a wealth of information can be read off directly [173]: Longer correlation

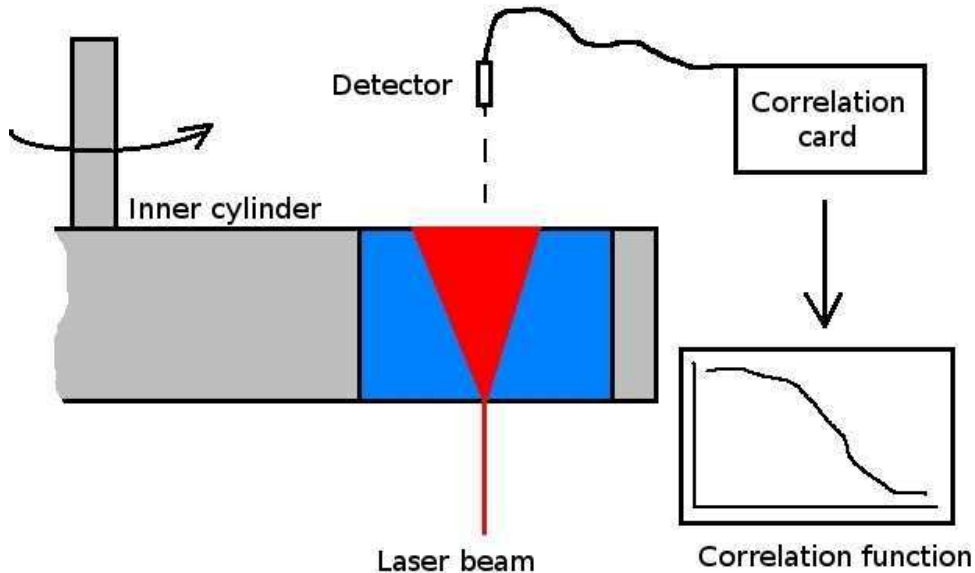


Figure 6.6: Illustration of the Couette cell with the DWS setup. The material in the annulus is sheared at a shear rate below the critical one so that shear banding occurs. The laser and detector are then placed above each other at some location in the gap, and the flow is briefly stopped while the autocorrelation is measured at this spatial location.

times corresponds to longer structural relaxation times of the fluid and hence higher viscosities. For a material in a liquid, ergodic state the correlation function decays rapidly and exponentially - as the measurements in the sheared band does. Correlation functions that decay slowly and partially, such as those in the non-sheared band, demonstrates that the material is in a non-ergodic out-of-equilibrium state that is aging - just like glasses [173]. Very interestingly almost identical findings were reported in a numerical study of the classic Lennard-Jones glass [53] (see Fig. 6.8). The qualitatively resemblance between this numerical investigation and the work I present here is even stronger than a comparison between Figs. 6.7 and 6.8 indicates. Just as I do, the authors of [53] find that the “static yield stress” (taken as the stress necessary to make an aged fluid flow at some finite, steady rate) is higher than the stress needed to keep a already fluidized sample flowing at shear rates approaching zero (Fig. 6.9A). And just as I do, the authors of [53] find that at very low imposed shear rates the resulting shear stress shows stick-slip behavior (Fig. 6.9B). In [53] this stick-slip behavior starts when the shear rate becomes so low that the sheared band is only a few particle diameters large, which is the interpretation I have for the stick-slip behavior I have a low shear rates (section 6.5.1). The fact that aging effects are demonstrated to be crucial for understanding shear banding in both a simple numerical and an actual experimental system hints that the concept of a steady state flow curve with a negative slope may be key to understanding shear banding in many if not all aging systems as suggested in [29, 47].

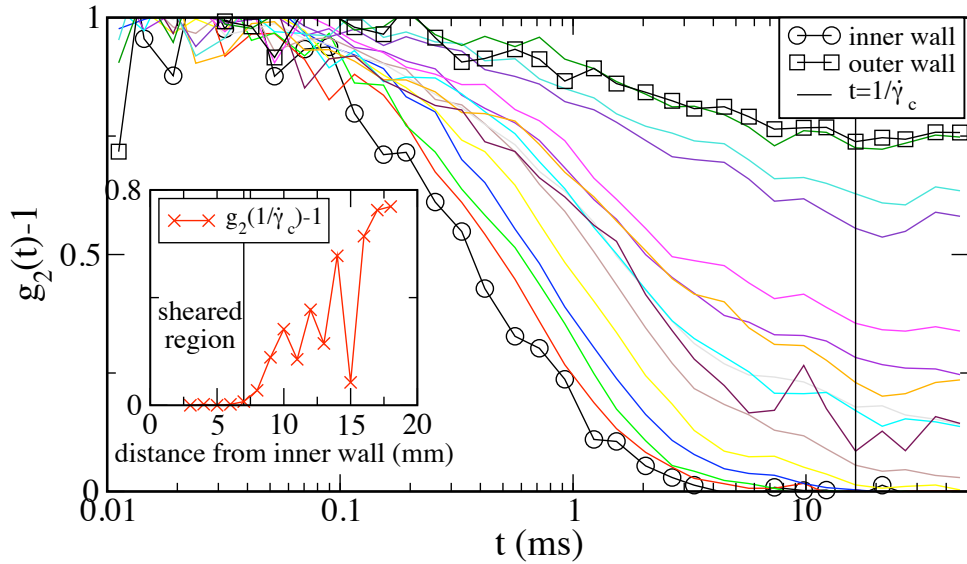


Figure 6.7: DWS autocorrelation functions measured at different positions in the Couette geometry in the setup sketched in Fig. 6.6. The inset shows the correlation function at $t = 1/\dot{\gamma}_c$ (which is a characteristic relaxation time of the material [53]) as function of the distance from the inner wall. Fast, exponential decay of the autocorrelation function - as happens in the sheared region - shows that the material has a short relaxation time (low viscosity) and is ergodic. Slow, and partial decay of the autocorrelation - as happens in the non-sheared region - demonstrates that the material has a long relaxation time and is non-ergodic [173]. The similarity of the figure to the results of a simulation on a model glass that exhibits shear banding is striking [53] (see Fig. 6.8).

6.7 A serious limitation of the lever rule

The deduction of the lever rule in section 6.3.3 utilizes the fact the the favored steady state of the system is the one with the lowest energy dissipation that is consistent with the boundary conditions, and the deduction assumes that the system will end up in this state. However, as is well known for fluids rapidly cooled below the glass temperature, a system can “fall out of equilibrium” and be prevented from reaching the stable steady state. This can happen also for an aging fluid in the λ -model. To illustrate how this can prevent the system from finding the least energy dissipating state, consider first a starting point where the material has been sheared at $\dot{\gamma}_{\text{global}} = \dot{\gamma}_c/2$ for a considerable amount of time. Then, the one half of the system will be in a low viscosity state and the other half will be in a *very* viscous state. If the imposed shear rate is increased, the width of the sheared band will increase only if the resulting stress in the fluid phase is big enough to fluidize the “solid” material - otherwise it will simply keep aging like a glass out of equilibrium and still only half of the material will be sheared. Another extreme initial condition that illustrates the problem is to consider a material that is generally very aged, but with a small variation in the local value of λ - like a solid with random weaknesses.

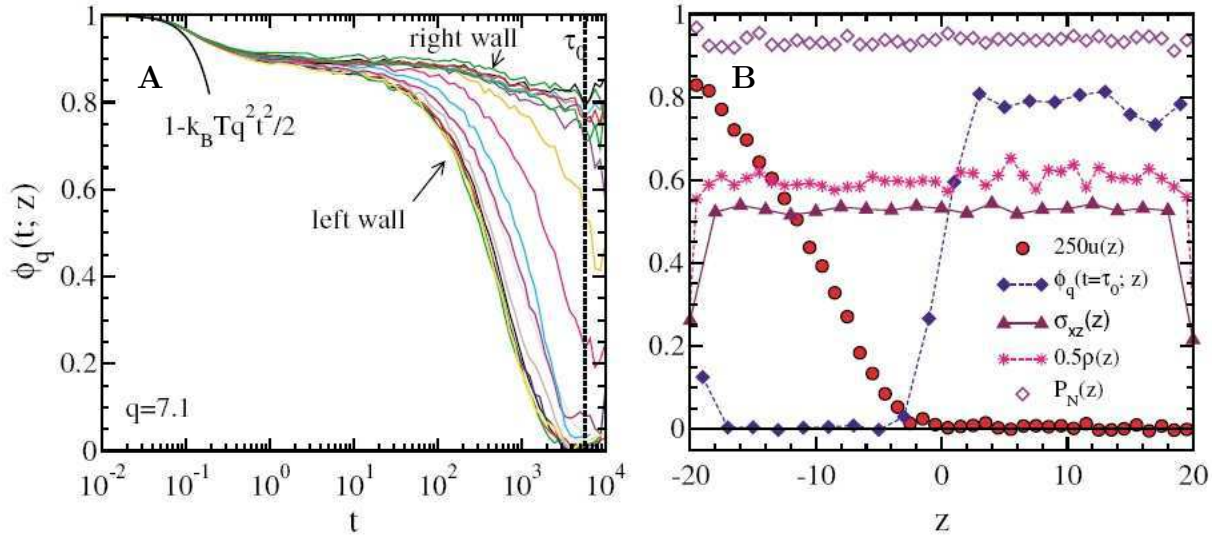


Figure 6.8: Results from a simulation on glass of particles with the archetypal Lennard-Jones potential from [53]. **A:** The “intermediate scattering function” (corresponding to the autocorrelation function in Fig. 6.7) for different distances from the shearing wall. The dashed vertical line at τ_0 corresponds to the vertical line at $t = 1/\dot{\gamma}_c$ in Fig. 6.7. **B:** Several functions plotted *vs.* the position in the gap. Of especial interest are the red circles that mark the local velocity (and through its derivative the local shear rate), and the filled, blue diamonds that mark the value of the intermediate scattering function at $t = \tau_0$. The behavior of this function inside and outside the sheared band is very similar to the corresponding function in the inset in Fig. 6.7.

Rather than being generally sheared when a deformation rate is imposed, such a material will “fracture” where the material was initially weakest, and the sheared band will grow only if the stress in the sheared band is sufficiently big to fluidize the material. Apart from depending on the imposed, global shear rate, the final width of the sheared band will depend also on the initial, overall age of the material. In short, the requirement for guaranteed applicability of the lever rule is that everywhere the initial state of the material is such that the initial, instantaneous flow curve intersects the steady state flow curve in the stable region as in Fig. 5.2B. Hence, pre-shear at a shear rate above $\dot{\gamma}_c$ just prior to the experiment is needed for the lever rule to give correct predictions.[†] This is very different from the case of a micellar fluid, where the lever rule always applies since the material is always in a stable steady state. If the initial state of the fluid does not meet the requirement given above, in order to correctly predict the effect of imposing a shear rate, *very* complete information about the material is required - not just $\dot{\gamma}_c$ or the steady state flow curve.

[†]This is why such an experimental procedure was followed for the MRI measurements.

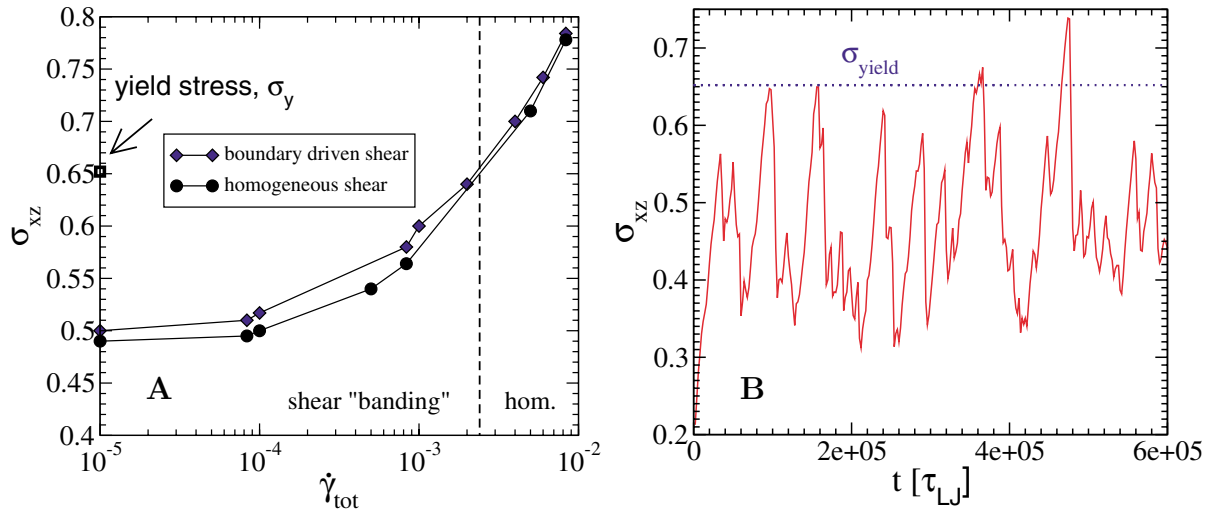


Figure 6.9: **A:** The flow curve resulting from a simulation on a Lennard-Jones glass. As in my experiments it is seen that the “static yield stress”, σ_y , (the one needed to get an aged sample flowing) is higher than $\sigma_{\text{shear banding}}(\dot{\gamma})$ for $\dot{\gamma} \rightarrow 0$ [53]. **B:** In the simulation on the Lennard-Jones glass the shear stress shows stick-slip behavior when the imposed shear rate becomes so low that the sheared band is only a few particles wide.

6.8 Practical handling of thixotropic yield stress fluids

Finally a short comment on how the work presented here could be of value to people involved in practical handling of yield stress fluids. As shown in this chapter and the previous one, predicting the flow of thixotropic yield stress fluids in all situations is extremely challenging: One needs to keep track of the local age of the material at all times to predict the flows, and then again feed the resulting flows back into the structural evolution of the fluid. While this is quite possible to do for some toy model like the λ -model, it gets more involved for models of a real fluid. Either one has to find a physical model of the material with (hopefully) relatively few fitting parameters, or one has to make a phenomenological model with a sufficient amount of parameters. Then the parameters have to be fit to measurements on the fluid. Since the steady state flow curve is probably not sufficient to determine all the parameters, also transient flows must be measured. When all parameters of the model have been determined, the “only” remaining task is to model the behavior of the fluid in the relevant flow situations. Keeping track of the interplay between the structure and the flow of the material is of course much more challenging than simply keeping track of the flow of a simple yield stress material such as the Bingham model or a Herschel-Bulkley model, which is already a difficult task.

Because of the challenges involved in predicting detailed flows of thixotropic yield stress fluids under all situations, one might decide to consider only some subset of all possible flows. Since I have shown that all the “interesting” behavior of thixotropic yield stress fluids is associated with the negative slope of the steady state flow curve, one might decide to look only at flows taking place around the stable branch. For instance, if one

wants to make sure that no material is left unyielded in a transport tube, this can be done simply by making sure that the fluid is pre-sheared so that the initial instantaneous flow curve intersects the stable branch of the steady state flow curve, and that the stress in the fluid is everywhere above the minimum of the flow curve, σ_{\min} . Computing everywhere the stress in the material is a comparatively simple task, if one makes the assumption that the material is well described simply by the stable branch of the steady state flow curve. This reduces the problem to one of the same type as the simulation of a Herschel-Bulkley type material which is well understood. This assumption that the fluid is always close to the steady state will be correct if the stress is always above σ_{\min} (and if the stress on a fluid element is not changing too rapidly for the material age to keep up). It is thus possible to test self-consistently whether material will end up being solid in the pipe, by assuming that the material is described by the stable branch of the steady state flow curve, and then seeing whether a given set of boundary conditions allow the stress to drop below the minimum in the flow curve. The only thing that needs to be measured for this procedure to work is the stable branch of the steady state flow curve which is readily measured simply by imposing different stress levels on a pre-sheared fluid.

6.9 Conclusion

In this and the preceding chapter I have examined how a thixotropic yield stress fluid behave in different flow situations with special focus on how its behavior differs from that of a simple yield stress fluid. I have made an analytical examination of the λ -model introduced by Coussot and coworkers [29, 47, 148], and the numerous qualitative predictions this work gave have all been verified experimentally:

- How to make reproducible measurements.
- During imposed shear stress measurements, one observed viscosity bifurcation at a critical stress that depends on the age of the material.
- During imposed shear rate measurements, if the imposed shear rate is lower than $\dot{\gamma}_c$, the material shear bands according to the lever rule.
- The material inside the sheared band is in a different state (has a different age) than the material in the quiescent region.
- And maybe most importantly, the region of the steady state flow curve with a negative slope, which is the central feature of the λ -model that leads to all the non-trivial behavior, has for the first time been demonstrated directly.

Chapter 7

A physical model for the rheology of colloids in salt water

As was clearly demonstrated experimentally in Fig. 5.4, the steady state flow curve of the Ludox-salt water mixture has a negative slope below shear rates of about 60 s^{-1} . In all the other rheological aspects of the material that was tested, the behavior was also qualitatively consistent with the λ -model. But since the colloidal interaction in salt water is quite well understood one might hope that it is possible to replace this toy-model by a real physical model that is based directly on the interaction between colloids and flow. For this purpose we collaborated with M.A.J. Michels from the Polymer Physics Group at Eindhoven University of Technology in the Netherlands, who was able to come up with such a model. The assumptions of the model are:

1. That in time the colloidal particles aggregate into fractal clusters that are non-draining and non-deformable [174]: $\phi = \phi(t)$ is then the 'hydrodynamic' volume fraction determined by the aggregate radius $R(t)$, rather than the much smaller actual volume fraction ϕ_0 of particles with radius R_0 (Fig. 7.1). The number of fractal aggregates decreases inversely proportional to the aggregate mass $M \sim R^{d_f}$ while their hydrodynamic volume scales as R^3 , where d_f is the fractal dimension of the aggregates. This means that the ratio between the effective hydrodynamic volume fraction of the clusters and the actual volume fraction of the individual colloids is given by: $\phi(t)/\phi_0 = (R(t)/R_0)^{3-d_f}$. Since $d_f < 3$ it is clear that continued aggregation will lead in time to a percolating gel.
2. That the effective viscosity η depends on the hydrodynamic volume fraction ϕ of the dispersed particles via a Krieger-Dougherty [175], mean-field [176,177] or more general scaling-type expression $\eta/\eta_0 = (1-\phi/\phi_p)^{-s}$, with η_0 the solvent viscosity and ϕ_p a gel-percolation point well below unity. The exponent s will be 2, $2.5\phi_p$ [175], 1 [176], or left as a fitting parameter, dependent on the chosen expression, but will anyway be of order unity.
3. That the flow breaks up the aggregates. Via different mechanistic assumptions of aggregation and break-up, different models can be constructed for the rate of change

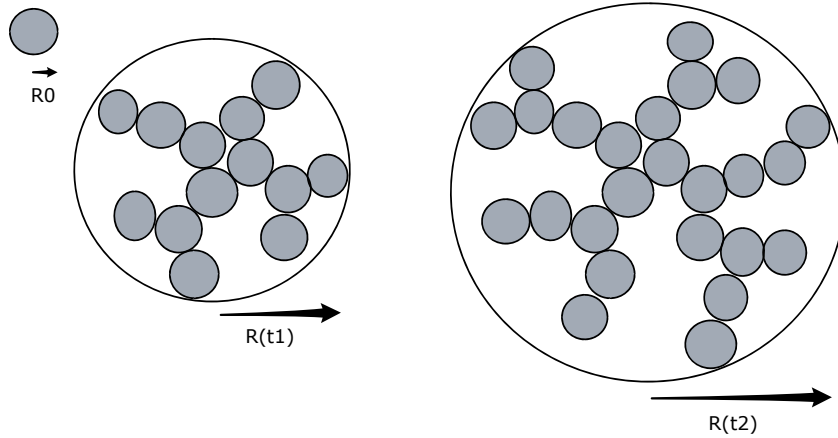


Figure 7.1: A sketch of the fractal clusters formed by the aggregation of individual colloids. While the effective hydrodynamic volume of a cluster is given by $\frac{4}{3}\pi R(t)^3$, the volume of constituent colloids is $\frac{4}{3}\pi R_0^3 \cdot (R(t)/R_0)^{d_f}$, where R_0 is the radius of a colloid, and d_f is the fractal dimension of the cluster. Hence the ratio of the effective volume fraction to the actual volume fraction is $\phi(t)/\phi_0 = (R(t)/R_0)^{3-d_f}$, so as $R(t)$ increases, so does $\phi(t)$.

dM/dt of the cluster mass. Depending on the stress or strain rate applied, a steady state $dM/dt = 0$ may or may not be reached between spontaneous aggregation and flow-induced break-up, which relates R to $\dot{\gamma}$. Fairly independently of the specific model, e.g. diffusion-limited cluster aggregation (DLCA, $d_f = 1.7 - 1.8$) [178] or shear-induced aggregation [179], size-scaling in fracture, etc., one arrives at a relation of the form $R/R_0 = (\dot{\gamma}/\dot{\gamma}_0)^{-n}$, with $\dot{\gamma}_0$ some typical high shear rate and n a model-dependent exponent smaller than unity; e.g. DLCA with break-up (mass loss per unit time) linearly proportional to the shear rate may be shown to give $n = 1/d_f = 0.55 - 0.60$, while for shear-induced aggregation a value $n = 1/3$ has been derived, in good agreement with some experimental data [179]. Rheometric studies with a similar modeling approach also show that shear may lead to more compact aggregates, with an increase in d_f towards 2.4-2.5 [180].

Combination of assumptions 1, 2 and 3 gives an effective steady state shear stress that depends on shear rate:

$$\sigma_{ss}(\dot{\gamma}) = \dot{\gamma}\eta_0(1 - (\frac{\dot{\gamma}_p}{\dot{\gamma}})^{(3-d_f)n})^{-s} \quad (7.1)$$

with $\dot{\gamma}_p$ corresponding to the percolation point ϕ_p also via assumptions 1-3:
 $\dot{\gamma}_p = \dot{\gamma}_0(\phi_0/\phi_p)^{1/(3-d_f)n}$.

Very interestingly the steady state stress is seen to diverge at both high and low shear rates just like the λ -model. And just like the λ -model, the steady state flow curve for colloids aggregating in salt water is predicted to have a minimum at some critical shear rate below which the slope in the steady state flow curve is negative:

$\dot{\gamma}_c = \dot{\gamma}_p [1 + sn(3 - d_f)]^{1/(3-d_f)n}$. If one is skeptical about whether real systems might behave like the λ -model (and hence about its pertinence), here is an example of a system that both experimentally and theoretically has been shown to display the same qualitative behavior.

In addition to demonstrating that a steady state flow curve with a negative slope can be predicted from physically reasonable assumptions, the model can also be favorably compared with the experimentally obtained steady state flow curve as shown in Fig. 7.2. From equation 7.1 it can be seen that the model contains a priory no less than four fitting parameters: η_0 , $\dot{\gamma}_p$, $(3 - d_f)n$, and s . However, the solvent viscosity is that of water at $20^\circ C$ which is of course well known; $\eta_0 = \eta_{\text{water}} = 1 \text{ mPa.s}$. Of the remaining three fitting parameters, $\dot{\gamma}_p$ is unknown while the other two can be limited to some reasonable range through the physics of the model: $(3 - d_f)n \approx 0.2 - 0.8$ and $s \approx 1 - 2.5$ as explained above. This leaves one completely free parameter and two that are strongly bounded. The optimal fit in Fig. 7.2 is achieved with fitting parameters that lie slightly outside the expected range; $(3 - d_f)n = 0.11$ and $s = 2.62$. It is the unstable part of the flow curve that is forcing these fitting parameters slightly out of the expected ranges - otherwise the model predicts a too abrupt increase in the stress as the shear rate is lowered. This means that the model does not give an entirely accurate description of the material when the effective volume fraction approaches the jamming point and the viscosity diverges. In this limit the clusters probably seize being non-draining and non-yielding as assumed by the model since the clusters are almost jammed completely together. If the clusters start deforming rather than being completely stiff, the increase of the shear stress at low shear rates will indeed be less abrupt than predicted by the model. With only one completely free, and two strongly bounded fitting parameters, the model must be said to give a surprisingly good fit to the experimental data over a large rage of shear rates and stresses in spite of this small discrepancy.

In conclusion, the rheology of mixtures of colloids and salty water are modeled directly from basic physical principles. The resulting steady state flow curve shows a negative slope at low shear rates just as the λ -model, lending theoretical support to the pertinence of this picture. In addition, the model provides an impressive fit to the experimental data on the steady state flow curve both above and below the minimum of the flow curve.

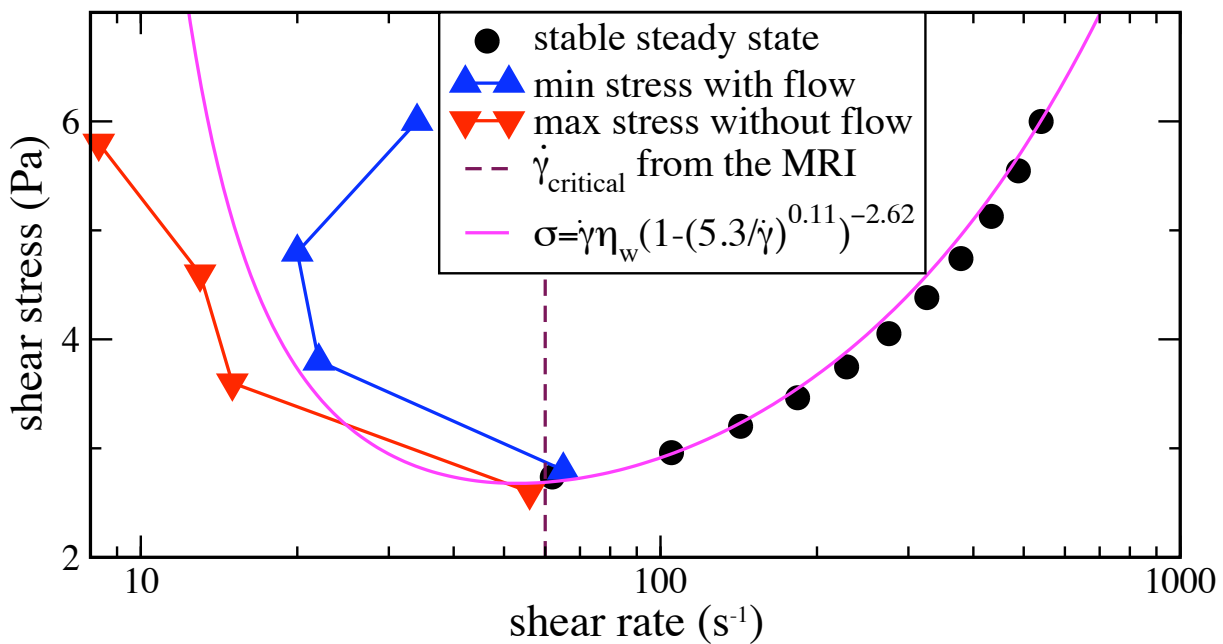


Figure 7.2: The model is seen to provide an excellent fit to the data from Fig. 5.4. The fitted parameters $n(3 - d_f) = 0.11$ and $s = 2.62$ are *just* outside the narrow expected ranges for them. This may be explained by the clusters starting to deform when the effective volume fraction diverges at low shear rates, rather than staying non-draining and non-deformable as assumed in the model.

Part IV

Moist granular materials

Chapter 8

The elastic modulus of moist granular matter

Contents

8.1	Introduction	97
8.2	Materials and methods	98
8.3	Experimental results	100
8.4	Predicting the elastic shear modulus of moist granular materials	100
8.5	Discussion	103
8.6	Conclusion	106

8.1 Introduction

A favorite tool for studying the strength of such moist granular systems has been the rotating drum experiment, where the material is put into a slowly rotating drum, and the angles of repose and avalanche are recorded as a measure of material strength [77]. This type of experiment by its nature limits one to examining relatively weak, non compacted materials, and does not allow for studying materials of a strength suitable for building sandcastles for instance. In a recent paper Fournier et al. imposed oscillatory shear deformation to wet granular materials in a pressure driven shear cell [181]. They recorded the hysteresis pressure as a measure of the material yield stress as function of liquid volume fraction. Because of considerable scatter the best one can say about the liquid volume fraction at which maximum strength occurs is that it is between 0.1 % and 5 % and the issue of what volume fraction of water gives the highest elastic strength of the granular assembly and why remains largely unresolved. Also the question of if and how the strength depends on other factors than the fluid content is unknown. These are the questions I will address in this chapter.

8.2 Materials and methods

While completely dry or wet sand has no cohesive strength and a block of the material cannot keep its shape, but “flows” into a pile, partially saturated sand is a material with macroscopic solid properties, and tall, slender columns can be built from such materials. In order to quantify the strength of moist granular matter I use a vane-cup geometry in a rheometer with roughened outer walls to measure the elastic shear moduli, G' and G'' , of different partially saturated granular materials as function of the liquid volume fraction. G' is related to the macroscopic Young’s modulus, E_{mac} , by $E_{mac} = 2(1+\nu)G' \approx 3G'$, where ν is Poisson’s ratio.* The grains used in the experiments are; sand (from Fontainebleau, sieved to have a radius between 90 and 110 μm), spherical glass beads of 25 and 100 μm radius, polystyrene beads of 100 μm radius (Dynoseeds, from Microbeads), and PMMA spheres of a 3 μm radius (Calibre, from Microbeads). All beads are thoroughly rinsed and dried before use. The fluids used are ultra pure water and silicone oil (Rhodorsil from CRC Industries France). The surface tensions of the fluids in presence of beads are determined using the Du Nuoy ring method. For water it is found to be 72 mN/m and 20 mN/m for silicone oil. After preparing a mixture of beads and fluid, a small quantity of this mixture is put in a vane-in-cup geometry in the rheometer. For the almost completely dry and almost completely wet mixtures the yield stress is quite low and the grains reach something resembling a close packing when just poured into the the rheometer geometry, but for the intermediate liquid volume fractions the yield stress is quite high and the material does not compact under its own weight, resulting in much lower grain packing fractions. In order to compare the elastic moduli at different liquid volume fractions and to get results not depending strongly on how the material is loaded into the cup, the material is after loading compacted by dropping a small thumper (12.5 mm in radius, 40 mm in height and with a 30 g mass) from a small height (about 10 mm) at least 100 times. I found that this ensures a reproducible compaction (a filling fraction of about 0.63 ± 0.01) for all liquid volume fractions and for each loading of the sample. This observation and the fact that the yield stresses of completely dry and wet materials were too low for their elastic moduli to be measured, demonstrates that the compaction of the materials does not squeeze the beads together in the cup. Since the capillary rise ($h = 2\gamma \cos \theta / \rho g r$ [182]) in the samples is at least 15 cm and thus much higher than the filling height, surface tension along with mechanical mixing prior to the experiment should prevent drainage and other inhomogeneities in the distribution of liquid among the grains.

The modulus G' is subsequently measured at a frequency of 1 Hz . I use 1 Hz since this allows for rapid measurements. I verified that G' does not depend on frequency for frequencies between 10^{-2} and 10 Hz , the frequencies readily accessible on the rheometer (see Fig. 8.1b). To ensure that the measurements probe the linear, elastic response, the

*In this chapter I assume that $\nu = 0.5$ which corresponds to that of an incompressible medium like rubber. If I choose $\nu = 0.3$ which corresponds to a medium as compressible as steel, the numerical values of the calculations change by only about 4 % so the conclusions are not very sensitive to the exact value of ν .

shear strain is continuously increased during the course of one experiment and the value of G' is averaged over the linear regime (see Fig. 8.1a). At least ten such measurements are performed for each material composition and for each volume fraction. The vane-cup geometry used for most of the experiments consists of four vanes of 10 mm in height and 5 mm in width attached to a rod 4 mm in radius, thus giving a total inner radius of 9 mm and a cup outer radius of 13 mm with a 10 mm strip of sandpaper glued on at the same height as the vanes. This gives a 4 mm gap corresponding to at least 20 bead diameters. To ensure that this gap size is sufficient to avoid confinement effects I checked that a vane-cup geometry with a much larger outer radius - 22.5 mm (corresponding to a gap of 13.5 mm) - gave results identical to the smaller one (Fig. 8.2)[†]. In all cases the distance from the bottom of the vane to the bottom of the cup (which was smooth to allow as much slip as possible) was 10 mm and the total filling height about 30 mm .

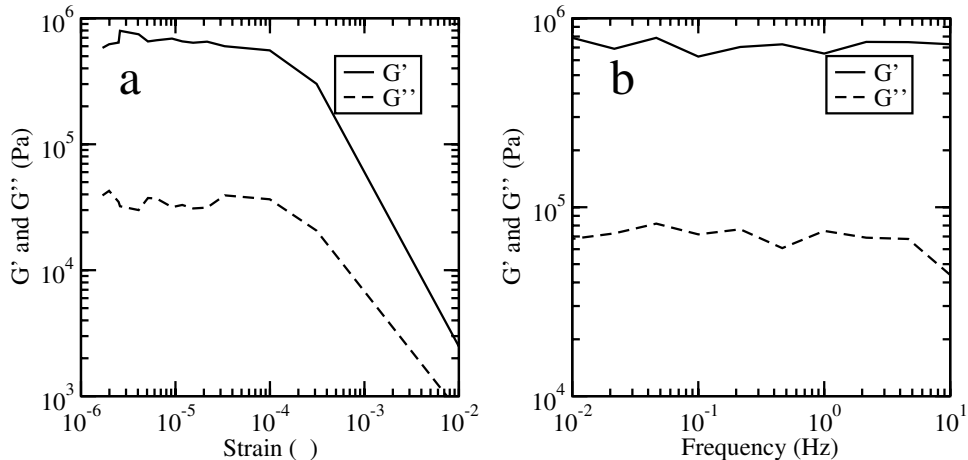


Figure 8.1: Typical measurements of the elastic storage and loss moduli G' and G'' as function of strain at a frequency of 1 Hz . **a:**, and as function of frequency at a fixed strain of $3 \cdot 10^{-6}$ **b:**. Since G' and G'' are seen to be independent of frequency between 0.01 and 10 Hz , all experiments presented below were done at 1 Hz . Since G' and G'' are seen to be roughly constant for strains between 10^{-6} and 10^{-4} , the average value of G' in this regime is taken for each experiment. The fact that G'' is more than an order of magnitude smaller than G' shows that this regime is one of elastic deformation and without viscous dissipation. Using a value of Poisson's ratio, G' can be converted into Young's modulus and the bulk modulus so that the exact material deformation to any type of load can be computed.

[†]In order to compare the G' measured in the two geometries, one needs a way for converting the torque, τ , and angular deformation, $\Delta\theta$, measured by the rheometer into a value for G' as function of the inner and outer radii, r_i and r_o : $\Delta\theta = \int_{r_i}^{r_o} \gamma/r \, dr = \int_{r_i}^{r_o} \sigma/rG' \, dr = \int_{r_i}^{r_o} \tau/2\pi hr^3G' \, dr \Rightarrow G' = (\tau/\Delta\theta) \cdot (r_i^{-2} - r_o^{-2})/4\pi h$.

8.3 Experimental results

Figure 8.2 depicts the elastic storage modulus for a variety of bead materials, fluids, and liquid volume fractions. The data show that at a given volume fraction, sand and water has a shear modulus similar to that of spherical glass beads and water, while that of spherical polystyrene beads and silicone oil is much smaller: the latter has a G' that is more than one order of magnitude lower. Apart from such differences in absolute strength the curves all show a similar dependence on the liquid volume fraction (Fig. 8.2A). In Figs. 8.2B, 8.2C, and 8.2D, it can be seen how the elastic modulus at a liquid volume fraction of 1 % change as properties of the mixture is changed; respectively the Young's modulus of the bead material, the surface tension of the fluid, and the bead size. The change of the elastic shear modulus as function of these mixture properties is consistent with a scaling law: $G' \sim E^{2/3} \gamma^{1/3} R^{-1/2}$.

8.4 Predicting the elastic shear modulus of moist granular materials

To understand how G' varies with the material of the beads, bead radius, surface tension, and volume fraction, one needs to look in detail at what happens when one adds a small volume of fluid to a stack of spherical grains. The surface tension of the fluid pulls it into small bridges connecting individual beads (Fig. 8.3). The attractive capillary force between two spheres is $F_{cap} = -\pi r_1^2 \Delta p + 2\pi r_1 \gamma = -\pi r_1^2 C \gamma + 2\pi r_1 \gamma$, where γ is the surface tension and C and r_1 are the curvature and the radius of the bridge respectively (Fig. 8.3(a)) [183, 184]. The curvature is a function of R , r_1 , and the separation between beads, d , but for $d = 0$ and $r_1 \ll R$, one can approximate $C \approx -1/r_2 \approx -2R/r_1^2$ so that the force is: $F_{cap} \approx 2\pi R \gamma$.

In practice it is well known that surface roughness and finite sphere separations mean that the actual force will not be independent of the bridge volume [185]. While the above formula is a very good approximation at intermediate volume fractions, it overestimates the strength at low ones where the fluid is trapped in the surface roughness and at high ones where single bridges merge into larger aggregates and loose strength. To allow for this dependence, I multiply the simplified bridge force equation with a factor between 0 and 1, depending on the liquid volume fraction: $F_{cap} = 2\pi R \gamma f(V_f)$. From AFM pictures of the bead surfaces (Fig. 8.3(b)) and fluorescence pictures of the liquid bridges (Fig. 8.6) this factor can be computed exactly as described in section 8.5, but for now I will treat $f(V_f)$ as some unknown dimensionless function bounded between 0 and 1.

The bridge force will suck the beads together and deform them elastically until balanced by the elastic response of the beads. The relation between force F , compression δ , of two identical spheres of radius R , and Young's modulus E is given by Hertzian response theory [186]: $F_H = -\frac{4\sqrt{2}}{9} R^{1/2} E \delta^{3/2}$. Linearizing the total force around the new equilibrium position where $F_{cap} + F_H = 0$, gives a spring constant against *further* displacement

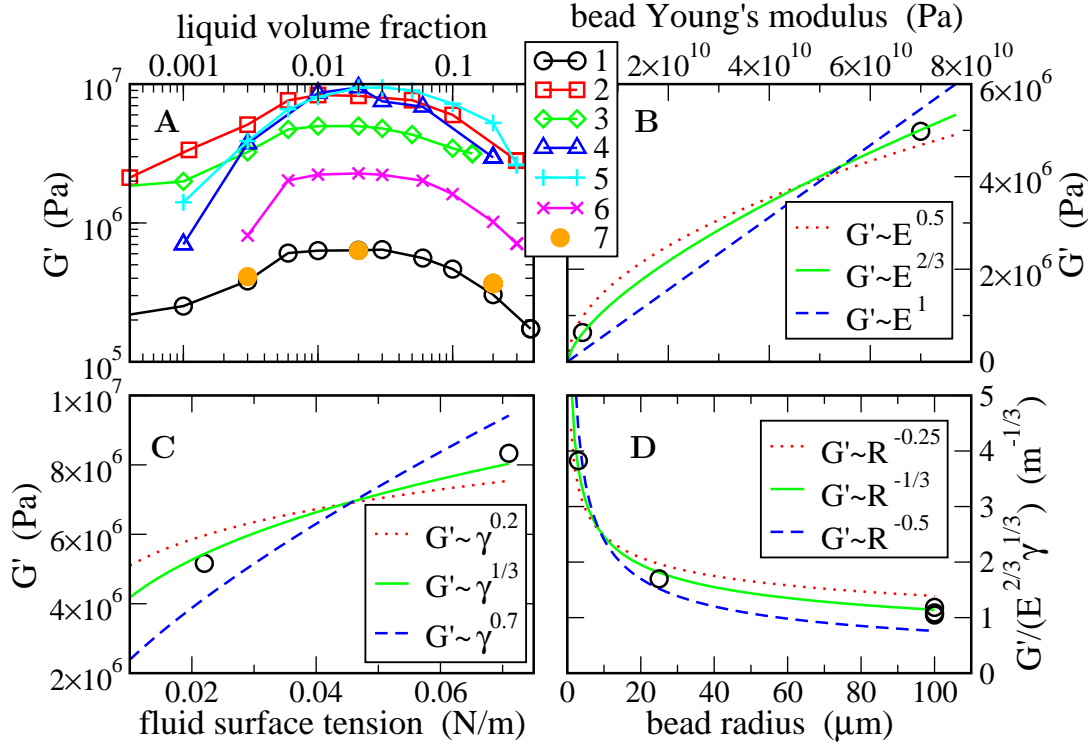


Figure 8.2: **A:** Measured elastic shear modulus G' as function of liquid volume fraction for different granular materials; 1: 100 μm polystyrene beads and silicone oil, 2: 100 μm glass beads and water 3: 100 μm glass beads and silicone oil, 4: 100 μm sand and water, 5: 25 μm glass beads and silicone oil, 6: 3 μm PMMA beads and silicone oil, 7: 100 μm polystyrene beads and silicone oil in a larger gap vane-in-cup geometry. Apart from the absolute value of G' , which differ more than an order of magnitude, the curves for different materials are seen to have similar shapes. Most measurements were performed in a geometry with a 4 mm gap, but measurements with a gap of 13.5 mm give identical results as seen in series 7. Note that none of the materials are completely wet or dry. Indeed, for completely wet materials and materials with too low a volume fraction, the elastic strength is too low to be measured by the rheometer. **B,C:** The dependence of G' at a 1% liquid volume fraction on the Young's modulus of the bead material and the surface tension of the liquid respectively. **D:** Rescaling G' by the relations found in sub-figures B and C, $G'/(E^{2/3}\gamma^{1/3})$ is plotted as function of the bead radius

of the beads:

$$F_{tot} = -\frac{4\sqrt{2}}{9}R^{1/2}E((\delta_{eq} + \Delta\delta)^{3/2} - \delta_{eq}) \quad (8.1)$$

$$\approx -\frac{2\sqrt{2}}{3}R^{1/2}E\delta_{eq}^{1/2}\Delta\delta \quad (8.2)$$

$$\approx -\left(\frac{\pi}{24}\right)^{1/3}R^{2/3}E^{2/3}\gamma^{1/3}f(V_f)^{1/3}\Delta\delta \equiv -k\Delta\delta \quad (8.3)$$

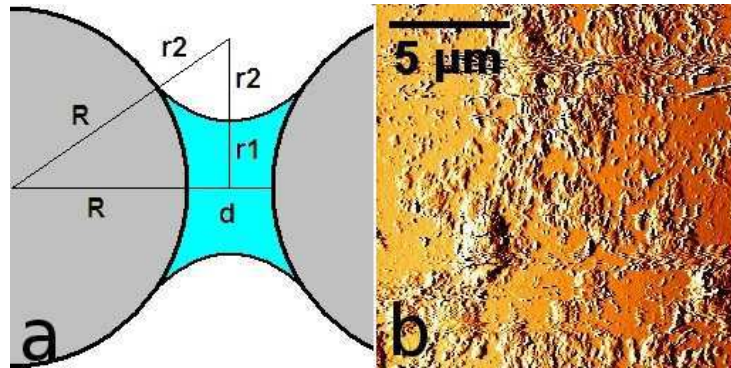


Figure 8.3: (a) Schematic of a liquid bridge. The distance between beads has been exaggerated for illustrative purposes. (b) An Atomic Force Microscopy (AFM) picture of the surface of a $100 \mu m$ glass bead. The height of the surface roughness is on the order of $1 \mu m$.

To compute how this spring constant results in G' one needs to average over all sphere-sphere bond orientations with respect to the shearing plane and to the shearing direction. To compute the macroscopic Young's modulus (E_{mac}) however, one needs only average over bond orientations with respect to the direction of the extensional force, which is much simpler. G' can subsequently be found from E_{mac} via $E_{mac} = 3G'$. Let Δl be the extension of the material along the direction of the pull on the material and F_e the extensional force. Then $E_{mac} \equiv \frac{F_e/A}{\Delta l/l}$, where A is the area where the force is applied and $\Delta l/l$ is the relative elongation of the material. Consider a sphere-sphere bond of length $2R$ oriented with polar angle θ to the direction of pull, and azimuthal angle ϕ . Then $\Delta\delta = \Delta l \cos \theta$, $l = 2R \cos \theta$ and $F_e = F \cos \theta$. If one now takes the area where the force is applied to be $(2R)^2$, one gets:

$$E_{mac} = \frac{F_e/A}{\Delta l/l} = \frac{F \cos^3 \theta}{2R \Delta \delta} = \frac{k}{2R} \cos^3 \theta \quad (8.4)$$

And averaging over all angles, θ and ϕ :

$$\langle E_{mac} \rangle = \frac{k}{\pi R} \int_0^{\pi/2} \cos^3 \theta \sin \theta \, d\theta = \frac{k}{4\pi R} \quad (8.5)$$

leading to

$$\langle G' \rangle = \frac{k}{12\pi R} \approx 0.054 R^{-1/3} E^{2/3} \gamma^{1/3} f(V_f)^{1/3} \quad (8.6)$$

This simple formula gives the scaling relation that was seen to be consistent with the measurements in Figs. 8.2B, 8.2C, and 8.2D, and directly explains why moist polystyrene beads have a much smaller G' than moist sand or glass beads. This is because the Young's modulus of sand is like that of glass, namely 68 GPa , while that of polystyrene and PMMA

is only 3 GPa [187]. Furthermore, the surface tension of water is 72 mN/m, while that of oil is 20 mN/m; the difference in the measured value of G' between sand and water one the one side and polystyrene beads and silicone oil on the other is indeed on the order of $(68/3)^{2/3}(72/20)^{1/3} \approx 12$. This therefore gives a quantitative explanation for the one order of magnitude difference between glass and polystyrene beads observed in Fig. 8.2A. Systematically and independently varying the grain size (a factor of 30), fluid surface tension (a factor of 4), and the Young's modulus of the grain material (a factor of 20), the measured elastic moduli over a wide range of material compositions are shown to collapse onto a single master curve when rescaled according to equation 8.6 as seen in Fig. 8.4.

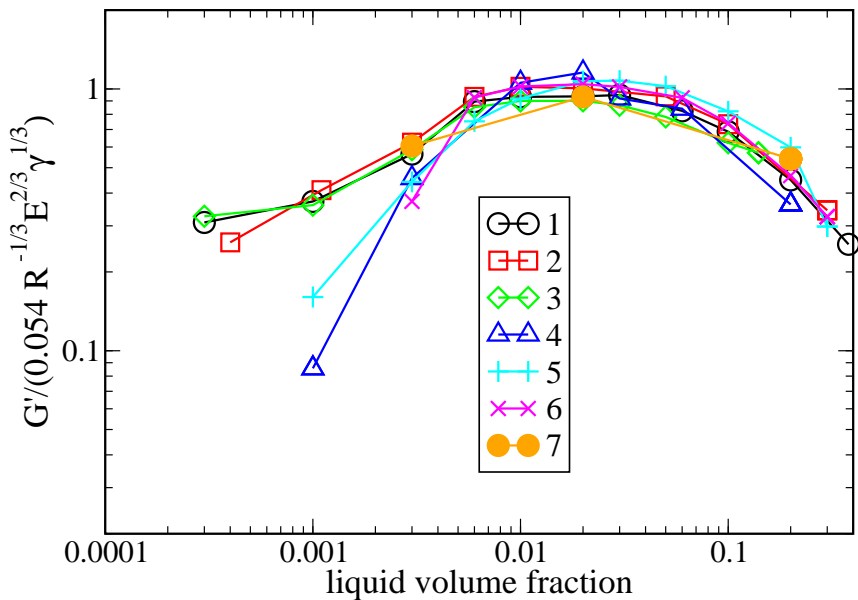


Figure 8.4: Master curve of G' for several materials (see the caption of Fig. 8.2 for the legends). The curves for the different materials have been rescaled using: $G' \rightarrow G'/(0.054 R^{-1/3} E^{2/3} \gamma^{1/3})$, where R is the bead radius, E the Young's modulus of the beads material and γ the surface tension of the fluid.

8.5 Discussion

The model that successfully allowed the measurements for several different material compositions to collapse onto a single master curve for the evolution of G' as function of the liquid volume fraction assumes that the bridge strength is given by $F_{cap} = 2\pi R\gamma f(V_f)$, but says nothing about $f(V_f)$ except that it varies between 0 and 1. What can be seen

from the master curve is that the strength of all the grain/liquid systems depends strongly on the liquid volume fraction, with a maximum strength at about 2 % of liquid, independently of the system details (Fig. 8.4). Because of the relatively low scatter in the data of this figure, the liquid volume fraction for maximum strength can be limited to the range of 1-3 % which is a significant improvement compared to the previous range of 0.1-5 % [181]. Furthermore it can be seen that the behavior of rough sand is like that of spherical glass beads which was hitherto an open question. It is perhaps surprising that my experiments and those of [181] give similar curves for strength as function of volume fraction since the measurement methods are quite different - linearly elastic measurements here, and oscillating deformations in [181]. Strength is maximized when the liquid bridge attraction peaks however, which should not depend much on the measurement method.

What happens when the bridge volumes grow is qualitatively well understood [185]: At very low volume fractions, most of the fluid is trapped in the surface roughness, and the bridge force is dominated not by the curvature of the sphere, but by the local roughness. At higher volume fractions, a significant fraction of the fluid is still caught in the surface roughness but the bridge force is dominated by the curvature of the spheres. At even higher volume fractions, the bridges start merging and loose strength. From Fig. 8.4 it is seen that some materials loose their strength faster as the volume fraction is decreased below about 1 %. This is very reasonable since the fraction of fluid caught in the surface roughness increase as the liquid volume fraction is lowered and exactly the materials that loose their strength faster (4: 100 μm sand and water, 5: 25 μm glass beads and silicone oil, and 6: 3 μm PMMA beads and silicone oil) have higher surface areas per unit volume of material, so that at low volume fractions a larger fraction of the fluid will be trapped at the surface for these materials than compared to the materials with smaller surface to volume ratios.

Since the elastic moduli of the materials in Fig. 8.4 are rescaled by $G'' \rightarrow G''/(0.054 R^{-1/3} E^{2/3} \gamma^{1/3})$, both the experimental data and the prediction are actually showing the shape of $f(V_f)^{1/3} = (F_{cap}/2\pi R \gamma)^{1/3}$. To predict not only how the modulus of a material depends on the bead material, the bead size, and the fluid surface tension, but also on the liquid volume fraction one needs to predict how $f(V_f)$ varies. To get an accurate value of the bridge force one needs to integrate the Laplace equation in cylindrical symmetry: $\Delta p = \gamma(1/r + 1/r')$, where r and r' are the principal radii of curvature [182]. As boundary conditions for this equation, one needs to know; the bridge radius, the sphere radius, and the sphere separation[‡]. The sphere radii are known from standard optical microscopy, the sphere separation is taken to be equal to the height of the surface roughness which was found with an AFM (Fig. 8.3), and the bridge radii as function of volume fraction was found with fluorescence microscopy (Fig. 8.6). Using these values as boundary conditions, I numerically integrated the Laplace equation to give a prediction of $G''/(0.054 R^{-1/3} E^{2/3} \gamma^{1/3})$ which is shown in Fig. 8.4 along with the experimental data. As this calculation assumes that bridges do not merge and needs the

[‡]In principle one also needs to know the contact angle, but since the contact angles in these mixtures are always very low and since the resulting force depends very weakly on the contact angles they are all assumed to be zero.

bridge radii as input values, predictions can only be made in the regime where bridge radii are optically measurable and bridges have not yet merged. Since single bridges can be observed only between volume fractions of 0.3 % and 3 % (Fig. 8.6), the theoretical prediction to this range. As seen in Fig. 8.5, the prediction is very good between volume fractions of 0.6 % and 3 %, while it is too big at 0.3 %.

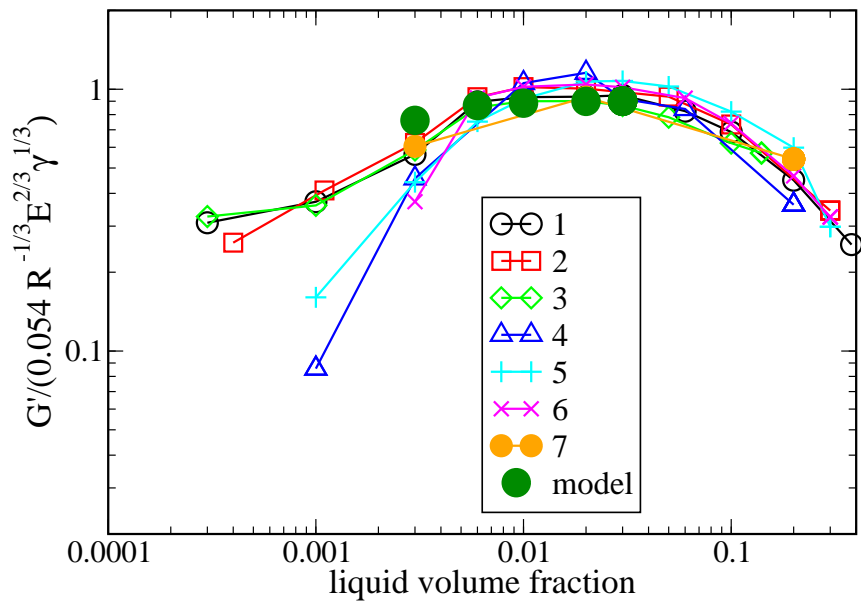


Figure 8.5: Master curve of G' for several materials (see the caption of Fig. 8.2 for the legends). The curves for the different materials have been rescaled using: $G' \rightarrow G'/(0.054 R^{-1/3} E^{2/3} \gamma^{1/3})$, where R is the bead radius, E the Young's modulus of the beads material and γ the surface tension of the fluid. The theoretical prediction has been computed directly from the known values of these parameters and from the measurements of the liquid bridge diameter for each volume fraction (see section 8.5). It contains no fitting parameters.

A second effect of the separation between beads is that bridges cannot exist below a critical volume. The number of bridges has been demonstrated to increase abruptly with volume fraction (from about one per sphere to about six) at a volume fraction of about 0.2 % [181]. This change in bridge number is not included in my model, and this may be the reason why for the lowest volume fraction the model slightly overestimates the modulus.

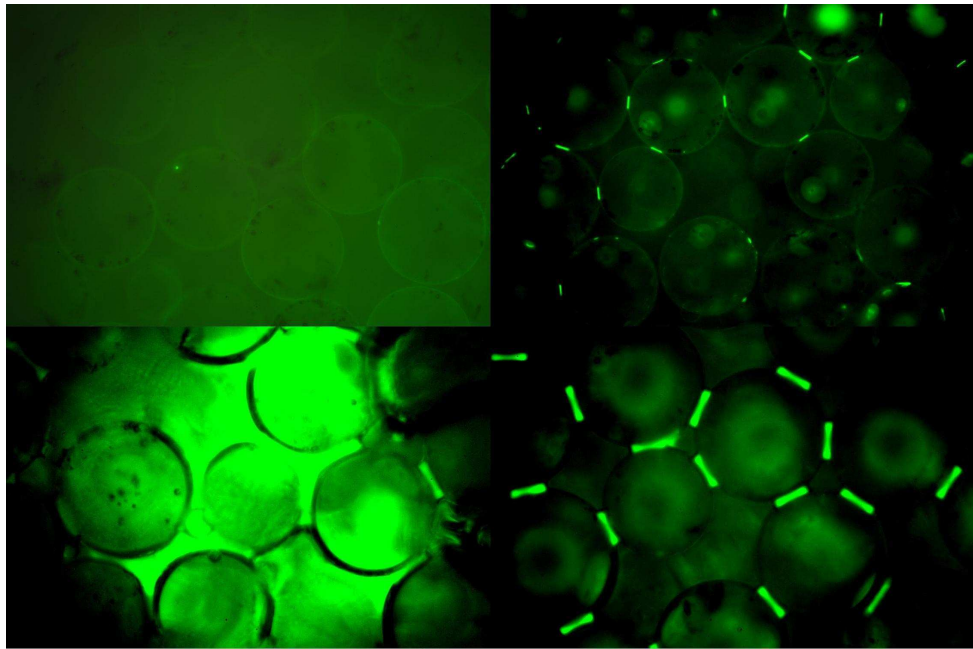


Figure 8.6: The liquid bridges between beads as seen in fluorescence microscopy. From upper left corner and clockwise, volume fractions of 0.1 %, 0.3 %, 3 % and 6 % respectively. At a volume fraction of 0.1 % the fluorescence of the fluid caught in the surface roughness is seen to dominate that of the fluid in the bridges. At a volume fraction of 6 % a significant number of the bridges are merged into large aggregates. The bridges consist of water with added fluorescein and the interstitial air has been replaced by an oil with an index of refraction matching that of the glass beads.

8.6 Conclusion

I have investigated the impact of the amount of fluid and composite material on the strength of a partially saturated granular material and found that the optimum is achieved at a liquid volume fraction as small as 1-3%. I also present a very simple model that successfully describes the elastic modulus of wet granular matter. This is of practical interest for civil engineering and soil mechanics, as well as of fundamental interest to come to a better understanding of partially saturated granular materials.

Chapter 9

General conclusion

I am now able to answer the questions I posed in the introduction of this thesis.

Why is carbopol a yield stress fluid, and how does the yield stress behavior come about?

In chapter 3 I presented a simple physical model of a carbopol-like material and showed that a simple simulation of it showed behaved very similarly to experimental measurements I performed on carbopol and hair gel. The physical mechanism that gave rise to the yield stress behavior is that when a small or moderate stress is imposed on the material, the small, soft carbopol particles are resisting reorganization and hence flow since they need to be compressed to move past each other. The energy required to bring a particle over the barrier made by its neighbors is so big that thermal fluctuations of this size will happen so rarely that effectively there is no flow. When the stress on the material is increased the particles are squeezed closer together in the direction of the stress and the energy barrier drops accordingly. Hence thermal fluctuations large enough to surpass the energy barrier happen often, the particles readily reorganizes, and the material flows like a fluid.

What actually happens below the yield stress? Does carbopol flow or not?

In chapter 3 I demonstrated that the many measurements that are used to argue that yield stress materials flow with some constant viscosity below the yield stress are probably artifacts. I tried to reproduce such measurements on identical materials and just as people before me I produced graphs that show a viscosity that becomes constant and finite below a certain stress. But unlike people before me I showed that the value of this viscosity plateau depends on over how long time measurement is done. The longer time the shear rate at some imposed stress is averaged over the higher the apparent viscosity plateau becomes. This is because experiments of an imposed shear stress below the yield stress show that the shear rate is steadily decreasing in time even for measurements lasting hours. This again can be understood from the model of carbopol I have made. When the stress is initially imposed, some particles will be initially in a state where the barrier for reorganization is low and they will have a relatively high rate of relaxing to more

stable states, resulting in a relatively high shear rate. Other particles will initially be in a slightly more stable state, and they will relax more slowly. Hence the shear rate will be decreasing in time. But this will not go on forever. As a particle relaxes, the stress released by the relaxation is redistributed over all the other particles that will then be deformed a bit more and relax a bit more easily than before. A steady state is reached when the distribution of energy barriers is such that particles that relax deform the other particles so that the stress release per unit time is constant. When the imposed stress is above the yield stress this steady state is rapidly reached, but when the stress is below the yield stress the times to reach a steady state become in practice experimentally inaccessible. So carbopol *does* flow with some steady state shear rate - even below the yield stress - (even crystals do) it just takes so long time to measure it that we are unable to do so. So for any practical purpose the viscosity of carbopol diverges without bounds as the imposed stress drops below the yield stress.

Why is the yield stress of so many yield stress fluids so difficult to measure and use to predict flows?

In chapter 5 I demonstrated directly that thixotropic yield stress fluids *can* indeed have a peculiar property that has been theorized for a handful of years: *a steady state flow curve with a negative slope below a critical shear rate*. In the same chapter I showed in detail why such a fluid will result exactly in the reported problems if one tries to apply a standard yield stress fluids model to it. Such a material will not have *one* single yield stress. Rather, for each material “age”, there will exist some critical stress. Below the critical stress the material will age further, develop a higher viscosity, and the flow will slow down, leading eventually to a solid material. Above the critical stress on the other hand, the material will be shear rejuvenated, the viscosity decrease and the shear rate increase by an avalanche behavior that eventually results in the material being sheared at a very high shear rate. I also demonstrated that differences in the initial material age when the experiment is begun can lead to such critical stresses that vary more than one order in magnitude, explaining why “the yield stress” of the material, as defined by a standard yield stress fluids model, is so difficult to measure. The discontinuous transition in the steady state viscosity at the critical stress also explains why the standard yield stress fluid models fail qualitatively since they assume a continuous transition.

Can shear banding of yield stress fluids occur also in homogeneous stress fields?

In chapter 6 I explained how the negative slope of the steady state flow curve demonstrated in chapter 5 will result in shear banding if the imposed average shear rate is below the critical shear rate corresponding to the minimum of the steady state flow curve. *This shear banding will happen even in a completely homogeneous stress field*. This is because the system, preferring to be in the steady state where the least entropy is dissipated, splits into two phases: one that is being sheared at the critical shear rate, and one that is solid. Since the shear rate in the sheared band is equal to the critical shear rate, the fraction of the material that is sheared is equal to the ratio of the imposed average shear rate to

the critical shear rate. This prediction is called the lever rule. Using MRI velocimetry techniques I demonstrate experimentally that indeed shear banding *does* occur even in homogeneous stress fields and that the lever rule holds.

How much liquid should be added to a dry, granular material for the resulting mixture to be strongest, and why? And how does the strength of the mixture depend on the material composition apart from the liquid volume fraction?

In chapter 8 I presented measurements on the elastic shear modulus for different granular materials at different volume fractions of different liquids. The elastic modulus was seen to depend both on the beads and fluid being used and on the liquid volume fraction. Independently of bead and liquid properties however, the measurements showed that the highest elastic modulus was achieved at a liquid volume fraction of 1-3 %. By an investigation of the attractive force that a liquid bridge between two beads result in, and by detecting the distribution of liquid in the material by using index matched fluorescence microscopy, I was able to explain why the optimum is in just this region. Furthermore, by considering in detail the force balance between the attractive bridge force and the elastic response of the beads, I developed a model that successfully explained how the elastic modulus of the material depends on the bead radius, the Young's modulus of the bead material and the surface tension of the added liquid. Combining this model with the index matched fluorescence microscopy, I was able to successfully predict the elastic modulus of different mixtures of granular materials quantitatively.

Appendix A

Numerical code for simulating carbopol

Below I have inserted the code used to simulate the flows of a carbopol-like material consisting of many small, elastically deformable particles squeezed together as described in chapter 3. The code is written in the open source program Octave which is almost identical to the commercial Matlab. The code is *very* short and with the comments given in red it should be fully readable.

```
#Code name: carbopolmodel
#A short numerical code for simulating the response of a
#carbopol-like material to an imposed shear stress.

#Input parameters (in SI units):
#sigma: The imposed stress.
#freq: The molecular trial frequency times exp(-E/x)
      #i.e. the chance per unit time that an unstrained element relaxes.
#l: The spread of the initial gaussian distribution of
   # frozen-in internal strains.
#x: The noise level.
#visc: The limiting viscosity at infinite shear rates.
#dt: The simulation time-step.
#steps: The number of time-steps.
#size: The number of elements simulated.
#k: The elastic shear modulus of an element.

#Output parameters (in SI units):
#rate: The resulting shear rate as function of time.
#L: The final distribution of internal strains.

function [rate,L] = carbopolmodel(sigma,freq,l,x,visc,dt,steps,size,k)
  L=randn(1,size)*l;    #The initial distribution of internal strains is generated.
  rate=0;                #The matrix of times and corresponding
```

```

rate(steps,2)=0;                      #shear rates is created.

#Below, the code is evolved one step to create the initial values of the shear
#rate and strain distribution matrices. See the loop below for details about
#each step.

L=L+dt*(sigma-k*mean(L))/visc;
for i=1:length(L)
    if rand < dt*freq*exp((k*0.5*abs(L(i)).^2)/x)
        L(i)=randn*1;
    endif
end
rate(1,1)=dt;
rate(1,2)=(sigma-k*mean(L))/visc;

#Below, the code is evolved for the number of specified time-steps. Each time
#step all elements are first uniformly strained by the imposed stress, and
#then individually given the chance to relax to the initial distribution of
#internal strains.

for t=2:steps      #The loop runs for the required number of steps.
    L=L+dt*(sigma-k*mean(L))/visc;
                    #All elements are uniformly strained by a strain equal
                    #to the time step times the part of the imposed
                    #stress that is unbalanced by the elastic stress
                    #supported by the elements.

#Below, each element is given a chance to relax to the initial
#distribution of internal strains.

for i=1:length(L)
    if rand < dt*freq*exp((k*0.5*abs(L(i)).^2)/x)
        L(i)=randn*1;
    endif
end
rate(t,1)=rate(t-1,1)+dt;
                    #The time for this step is stored in the time-shear
                    #rate matrix.
rate(t,2)=(sigma-k*mean(L))/visc;
                    #The shear rate for this step is stored in the time-shear
                    # rate matrix.

end
end

```

Appendix B

Publications

On the following pages I have inserted the papers that have been accepted and published based on the work I have done during my PhD at the Laboratoire de Physique Statistique de l'Ecole Normale Supérieure in Paris.

Yield stress and thixotropy: on the difficulty of measuring yield stresses in practice

Peder C. F. Møller,^a Jan Mewis^b and Daniel Bonn^{*ac}

Received 15th December 2005, Accepted 27th January 2006

First published as an Advance Article on the web 17th February 2006

DOI: 10.1039/b517840a

The yield stress of many yield stress fluids has turned out to be difficult to determine experimentally. This has led to various discussions in the literature about those experimental difficulties, and the usefulness and pertinence of the concept of yield stress fluids. We argue here that most of the difficulties disappear when taking the thixotropy of yield stress fluids into account, and will demonstrate an experimental protocol that allows reproducible data to be obtained for the critical stress necessary for flow of these fluids. As a bonus, we will show that the interplay of yield stress and thixotropy allows one to account for the ubiquitous shear localization observed in these materials. However, due to the thixotropy the yield stress is no longer a material property, since it depends on the (shear) history of the sample.

1 Introduction

Fluids that do not flow unless they are subjected to a certain load (stress) are widely used in both cosmetic and industrial applications; well-known examples are mayonnaise (an emulsion), shaving foam, wet and dry sand and toothpaste. Examples well known to the rheologist include many polymer gels like carbopol and colloidal gels like oil drilling fluids. The most important characteristic of these materials is that they can behave as solids under small applied stresses, and as liquids at high stresses. In spite of the macroscopic similarity of these materials, the microscopic mechanism for their behavior is quite different. For granular matter it is the reorganization

of individual particles that resists the motion. For a foam or an emulsion, the individual bubbles resist both deformation and reorganization. In gels, the polymer chains or particles stick



Peder C. F. Møller

^aLaboratoire de Physique Statistique, Ecole Normale Supérieure, 24 Rue Lhomond, F-75231, Paris cedex 05

^bDepartement C.I.T., K.U. Leuven de Crooylaan 46, B-3001, Leuven, Belgium

^cVan der Waals-Zeeman Institute, University of Amsterdam, Valckenierstraat 65, 1018 XE, Amsterdam, The Netherlands



Jan Mewis

Jan Mewis studied chemical engineering at the Katholieke Universiteit Leuven, where he received his masters degree in 1961. While he worked at the IVP Laboratory, the research institute of the Belgian paint and printing ink industry, he obtained his PhD with a thesis on "Tack of Printing Inks". In 1969 he returned to K.U.Leuven as a full time faculty member. Jan Mewis has been quite active in the rheological community. He is a co-founder and former president of the Belgian Group of Rheology, was chairman of the International Committee on Rheology (1992–96) and member of the Executive Committee of the European Society of Rheology.



Daniel Bonn

Daniel Bonn (1967) studied physical chemistry at the University of Amsterdam, where he got his PhD in 1993 on the subject of wetting transitions. He subsequently moved to the Laboratoire de Physique Statistique of the Ecole Normale Supérieure in Paris, where he became a staff member in 1995. He there continued his work on surface phase transitions, but also developed new activities in the field of complex fluids and instabilities. He has been leader of the complex fluids group at the ENS since 1999 and in addition a part-time physics professor at the van der Waals-Zeeman Institute of the University of Amsterdam since 2003.

together and form a mesh, resisting flow. Because of the enormous range of applications of these fluids, they have been studied intensively over the past few decades.

Yield stress fluids can be defined as fluids that can support their own weight to a certain extent *i.e.* can support shear stresses without flowing as opposed to Newtonian fluids. As a consequence, a yield stress fluid on an inclined plane will not flow if the slope is below some critical angle, but will flow as soon as the angle becomes large enough. One of the simplest ways of capturing this phenomenological behavior is given by:¹

$$\sigma = \sigma_y + f(\dot{\gamma}) \quad \text{if } \sigma > \sigma_y \\ \text{and } \dot{\gamma} = 0 \quad \text{if } \sigma \leq \sigma_y$$

with σ being the applied shear stress, σ_y the yield stress and $f(\dot{\gamma})$ some function of the shear rate, $\dot{\gamma}$, satisfying $f(0) = 0$ and $\frac{df}{d\dot{\gamma}} > 0$. A typical example of this is the so-called Herschel–Bulkley (H–B) model: $\sigma = \sigma_y + a\dot{\gamma}^n$, where a and n are positive constants. If $\sigma_y = 0$ and $n = 1$ the H–B fluid degenerates to a Newtonian fluid with viscosity a . In the remainder of this paper the behavior of real yield stress fluids will often be compared with that described by these models for yield stress fluids. As a very prominent representative of this group, the H–B model will be used for those comparisons. The comparisons however remain qualitatively general for the full group of yield stress fluid models.

When subjected to a stress, the response of an H–B fluid is a slow shear flow provided the stress is slightly above the yield point: the viscosity diverges in a continuous fashion when the yield stress is approached from above:

$$\eta = \frac{\sigma}{\dot{\gamma}} = \frac{\sigma_y + f(\dot{\gamma})}{\dot{\gamma}} \rightarrow \frac{\sigma_y}{\dot{\gamma}} \text{ when } \dot{\gamma} \rightarrow 0^{+} \quad ^{2-4}$$

However, there are at least two important, fundamental problems with this conception of yield stress fluids.

The first and most well-known problem is that the yield stress of a given material has turned out to be very difficult to measure. In the concrete industry the yield stress is very important to determine whether air bubbles will remain trapped, and consequently a large number of tests have been developed to determine the yield stress. However the different tests often give different results. Even in controlled rheology experiments the same problem is well documented: depending on the measurement geometry and the detailed experimental protocol, very different values of the yield stress can be found.^{3–7} This underlines the difficulty of measuring “the” yield stress for a given material.

The second and perhaps more fundamental problem is that of shear localization. The H–B model asserts that all shear rates are possible, and presupposes that the flow is always homogeneous at these shear rates. This is provided, of course, that the stress is homogeneous. What happens in reality is that at low shear rates, the shear localizes in a small region with high local shear rate while the remaining part of the fluid behaves like a solid. This is the case even in cone-plate geometries where the stress is essentially constant.^{8–10} Although this effect is general, and well-known to everybody who for instance has tried to make mayonnaise or sugar flow in a homogeneous fashion, this problem has received much less attention than that of the determination of the yield stress.

We show here that by considering another phenomenon also characteristic of yield stress fluids, namely *thixotropy*, most if

not all of the problems disappear. Thixotropy can be defined as a (reversible) decrease of viscosity of the material in time when a material is made to flow. Even though thixotropy and the yield stress are often considered as two entirely different phenomena,^{4,7} they show an intriguing tendency to show up together. In addition, they are indeed believed to be caused by the same fundamental physics. The microstructure present in the fluid that resists large rearrangements is responsible for the yield stress, and the destruction of such a microstructure (we shall become more specific concerning what such a microstructure may be below) by flow is believed to be the origin of thixotropy. This paper summarizes some recent experimental results and a recent addition to a well known group of models describing thixotropy, and shows that indeed the yield stress and thixotropy can be understood and modeled as two effects of the same cause.

2 The problems with the yield stress

2.1 Determination of the yield stress

One fundamental problem with the concept of yield stress fluids as introduced above is the difficulty in determining the yield stress. Theoretically the yield stress is defined to be the stress at which the fluid *just* starts/stops moving, *i.e.* when the viscosity changes between being finite and infinite.^{3,4,7,11} In the H–B model this happens exactly at σ_y . Unfortunately experiments of infinite duration are required in order to distinguish between finite and infinite viscosities, rendering this definition of the yield stress inapplicable for experimentalists. Consequently, they usually define the yield stress to be the highest stress at which no flow is detectable within the duration of the experiment. Hence the measured yield stress may change somewhat depending on the patience of the experimentalist and the experimental protocol. This should not cause huge problems for practical applications.

However, there are huge problems. It turns out that unambiguously determining a yield stress from experiments is very difficult. Depending on the experimental procedure quite different values of the yield stress can be obtained.^{3–7} Indeed it has been demonstrated that a variation of the yield stress of *more than one order of magnitude* can be obtained depending on the way it is measured.⁵ The usual interpretation is that the structure and/or properties of the yield stress fluids are not probed in the same way depending on the measurement method. However, this does not solve the problem of mapping the experimental results onto some yield stress fluid model. The huge variation in yield stress cannot be attributed to the difficulty of distinguishing between a finite and an infinite viscosity, but hinges on more fundamental problems with this ‘ideal’ concept of yield stress fluids. This is of course well known to rheologists, but since no reasonable and easy way of introducing a variable yield stress is generally accepted, researchers and engineers often choose to work with the yield stress nonetheless and often treat it as if it is a material constant which is just tricky to determine. As Nguyen and Boger put it:³ “Despite the controversial concept of the yield stress as a true material property..., there is generally acceptance of its practical usefulness in engineering design and operation of processes where handling and transport of

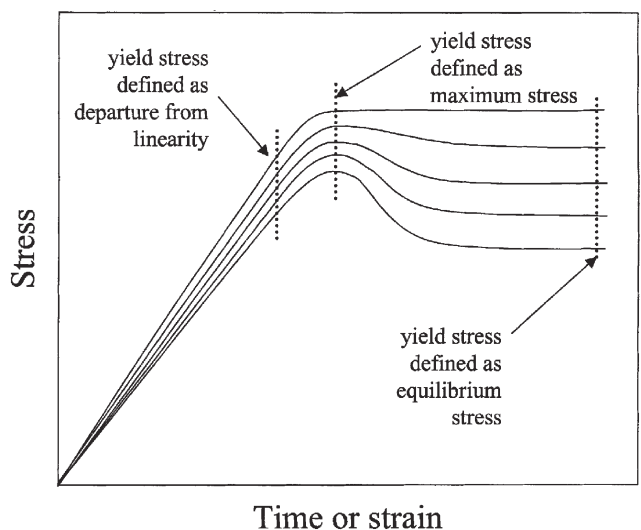


Fig. 1 Schematic time evolution of the stress for imposed shear rate experiments at different imposed rates, and different attempts at defining a yield stress.⁶

industrial suspensions are involved.” One method that has been used for such applications is to work with two yield stresses - one static and one dynamic - or even a whole range of yield stresses (Mujumdar *et al.*¹² and references therein). This of course conflicts with the definition of the yield stress given above.

These difficulties have resulted in lengthy discussions of whether the concept of the yield stress is useful and how it should be defined and subsequently determined experimentally if the model is to be as close to reality as possible. In Fig. 1 schematic time evolutions of the shear forces required to apply different constant shear rates are shown.⁶ As can be seen in the figure, the stress at the end of the linear elastic region, the maximum stress, and the stress at the plateau beyond the peak have all been suggested as possible definitions of the yield stress point. This figure is idealized however, and determining the yield stress from actual data is even more difficult as can be seen from Fig. 2. Perhaps even worse, almost unrelated to the exact definition and method used, yield stresses obtained from experiments quite often turn out to be inadequate to determine the conditions under which a yield stress fluid will flow and how exactly it will flow.^{3,4,6,7,13–15}

2.2 Shear localization

The H–B model and all analogous models suggest that all shear rates are possible in the material. However in practice, as soon as one makes an attempt to create a homogeneous flow, this generally fails: only a small region of the material actually moves, and the rest remains “solid”. There can be two reasons for this: either there is shear banding (localization), or there is wall slip. The latter can usually be controlled by using rough surfaces, and although very interesting, will not be considered here. Hence we focus on the shear localization. In rheological experiments the sample is usually assumed to be homogeneous and the local shear rate is derived from assuming that the globally imposed shear rate distributes accordingly throughout the sample. If shear banding occurs, this will of course *not* be

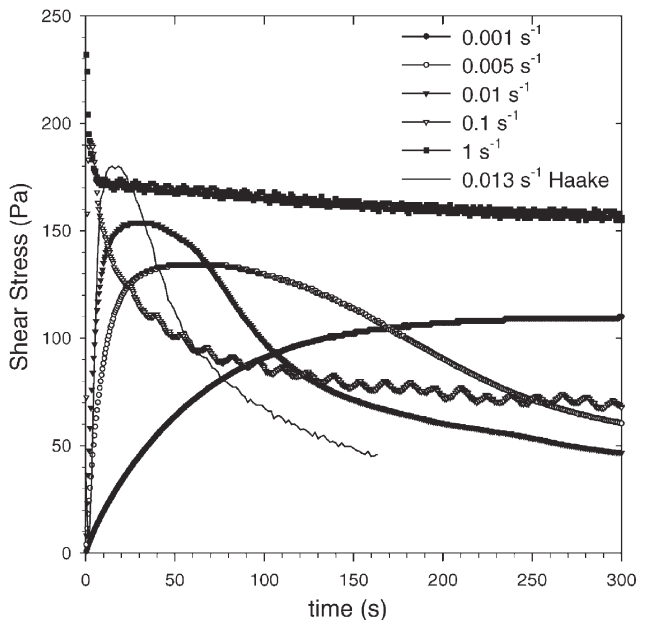


Fig. 2 Time evolution of the stress for actual experiments for the same material at different imposed shear rates and different instruments.¹⁶

the case, and much care must be exercised to avoid misinterpreting rheological data by implicitly assuming the shear rate to be distributed uniformly when a global shear rate is imposed macroscopically.

Using H–B like models, the only possible interpretation of shear localization is that there is a stress variation throughout the sample. Within the sheared region, the stress should then be higher than the yield stress, and outside that region it should be below. In a Couette geometry the stress usually varies as much as 10–20% and the H–B model allows in principle for a transition between a fluid and a solid region. However, in practice the H–B model predicts a much less abrupt transition than what is seen experimentally.^{8,17} In addition shear localization is also observed for instance in cone-plate cells for which the stress is almost completely constant.^{8–10†} Interestingly such shear banding happens only under imposed shear rate and does not appear to be observable under an imposed stress, which also conflicts with H–B behavior. In addition to this, recent very precise experiments strongly suggest that shear localization is the rule below a critical shear rate, $\dot{\gamma}_c$.¹⁷ Below this shear rate, all the flow is localized in a region close to the shearing wall. If the globally imposed shear rate is increased it is not the shear rate in the sheared region that increases, but rather the extent of the sheared region which grows—to fill the entire gap of the shear cell exactly at the critical shear rate.^{8,17,19} See Fig. 3. Huang *et al.*¹⁷ show on a granular paste that the critical shear rate where the sheared region invades the entire gap (determined by MRI measurements)

† The stress in a cone-plate geometry is not entirely constant, but has a typical variation of less than 1%, which in a H–B setting should give shear banding only if the imposed average stress is within 1% of the yield stress. Hence this cannot explain the numerous situations in which shear banding is observed. For a detailed study of stresses in a cone-plate geometry see Cheng¹⁸

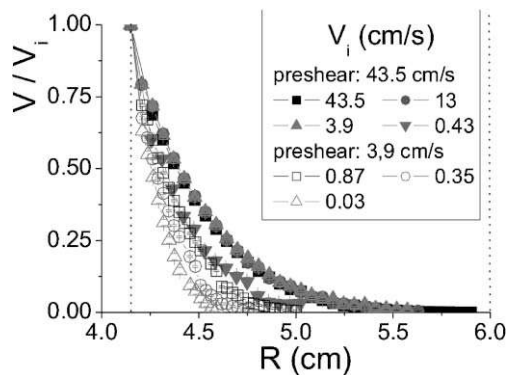


Fig. 3 MRI measurements of the normalized velocity profile of a wet granular paste in a Couette geometry. It is seen that the shear localizes if the macroscopically imposed shear rate is below a certain limit. This limit is found to be $0.4 \pm 0.1 \text{ s}^{-1}$.¹⁷

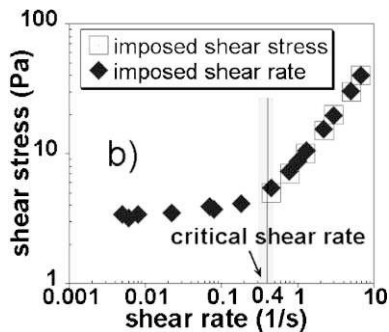


Fig. 4 Imposed shear rate measurements on the same wet granular paste as in Fig. 3. The critical shear rate for transition between the two regions of the flow curve corresponds well with the critical shear rate for localization of shear found from Fig. 3.¹⁷

corresponds exactly to the shear rate for which an abrupt change occurs in the flow curve diagram as seen in Fig. 4. Wall slip is absent in all of these experiments (it would have been observed directly in the MRI experiments). All this therefore suggests that the shear localization is an intrinsic property of yield stress fluids, that always manifests itself at low enough shear rates. The manifestation is in this respect independent of the precise experimental protocol or measurement geometry.

3 Thixotropic fluids, avalanche behavior and discontinuous viscosity—the way out

Thixotropic fluids are fluids with a variable viscosity which reversibly decreases with time under high shear rates. Because of the reversibility, in general the viscosity increases in time at low or zero shear rates.^{7,11,20} For an experimental example of thixotropic behavior, see Fig. 5. The usual explanation of thixotropy is that the viscosity of such fluids is mainly caused by the microstructure of for instance particles in the fluid that interconnect and resist large rearrangements; for a recent detailed study, see Dullaert.²¹ When sheared, this structure is broken down in time and the viscosity consequently decreases in time. When left at rest, the microstructure slowly rebuilds itself and the viscosity increases.

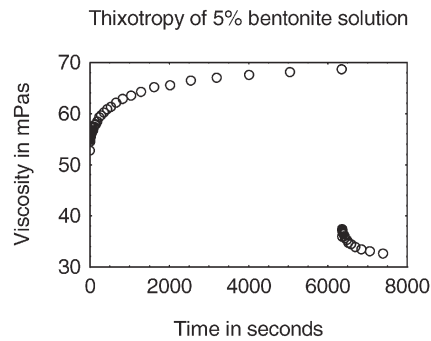


Fig. 5 Time evolution of the viscosity of a 5% bentonite solution under different imposed shear rates. The sample is pre-sheared at $\dot{\gamma} = 100 \text{ s}^{-1}$ for 5000 s. Then a shear rate of 25 s^{-1} is imposed for about 6000 s, after which the shear rate is changed back to 100 s^{-1} .

In the physics literature on soft glassy materials, these concepts have emerged recently; a viscosity increase of a sample left at rest is termed ‘aging’, in analogy to the aging of glasses, and the viscosity decrease in time under shear (thixotropy) is termed ‘shear rejuvenation’. Since there is no large-scale structure in glasses, the microscopic interpretation of these effects is different. However the competition between the two effects will also determine the mechanical behavior of these systems,^{7,11–14,22–25} and rheology experiments on soft colloidal glasses²² show a striking similarity to those on ‘typical’ yield stress fluids. For structured materials such as gels, the ‘aging’ and ‘rejuvenation’ are of course two aspects of the same phenomenon: the build-up and destruction of the microstructure. To retain the generality of our discussion here and include also glassy materials, we will therefore use aging and rejuvenation in the following, rather than build-up and destruction.

How are yield stress and thixotropy interrelated? A very striking demonstration of the interplay between the two is the ‘avalanche behavior’ recently observed for yield stress materials.¹⁴ One of the most simple tests to determine the yield stress of a given fluid is the so-called inclined plane test^{26,27} A large amount of the material is deposited on a plane which is subsequently slowly tilted to some angle. According to the H–B model, the material will just start flowing when an angle is reached for which the yield stress equals the gravitational force per unit area $\sigma_y = \rho g h \sin\theta$, with ρ the density of the material, g the gravitational acceleration and h the height of the deposited material. In reality however, inclined plane tests on a clay suspension (bentonite)¹⁴ reveal that for a given thickness there is a critical slope above which the sample starts flowing. Once it is flowing, the thixotropy leads to a decrease in viscosity. Since fixing the angle implies fixing the stress, this will accelerate the flow. This in turn leads to an even more pronounced viscosity decrease and so on: an avalanche results, transporting the fluid over large distances, where an H–B fluid would move only infinitesimally when the critical angle is slightly exceeded (Fig. 6). In Fig. 7 the experimental data of such inclined plane experiments¹⁴ are compared with the H–B prediction which is clearly an inadequate description. It is interesting to compare the results of the inclined plane tests with experiments showing avalanches in granular materials - a

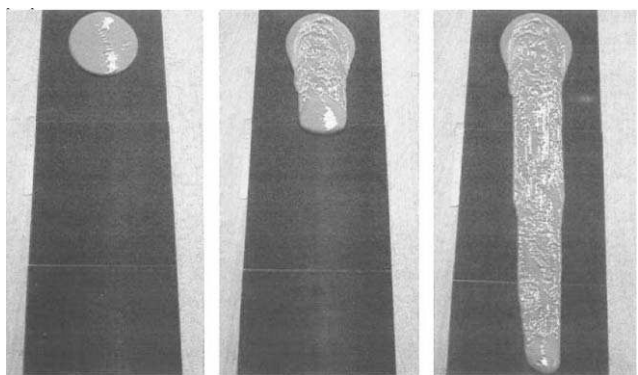


Fig. 6 Avalanche flow of a clay suspension over an inclined plane covered with sandpaper. The experiment was performed just above the critical angle, below which the fluid behaves like a solid.¹⁴

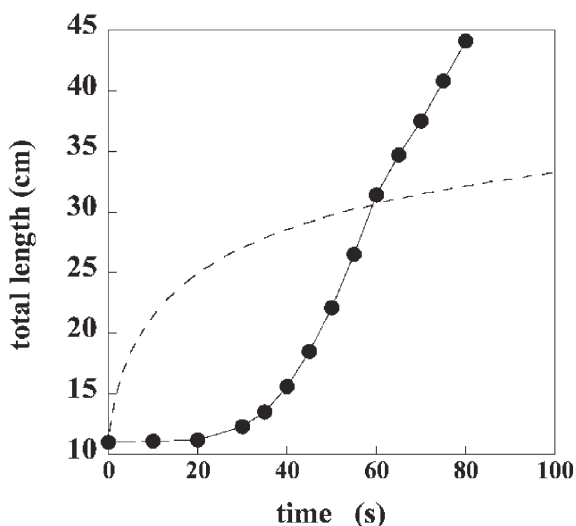


Fig. 7 Distance covered by the fluid front in an inclined plane experiment.¹⁴ The experimental points are compared with the prediction of the H-B model (dashed line).

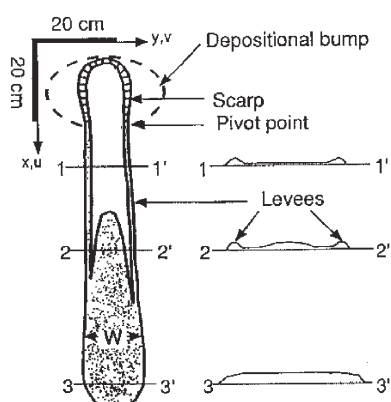


Fig. 8 The inclined plane experiment with a heap of dry sand. The similarity of the resulting avalanche deposit with that of the clay avalanche is striking, especially the very characteristic ‘horseshoe’ form at the top of the plane.²⁹

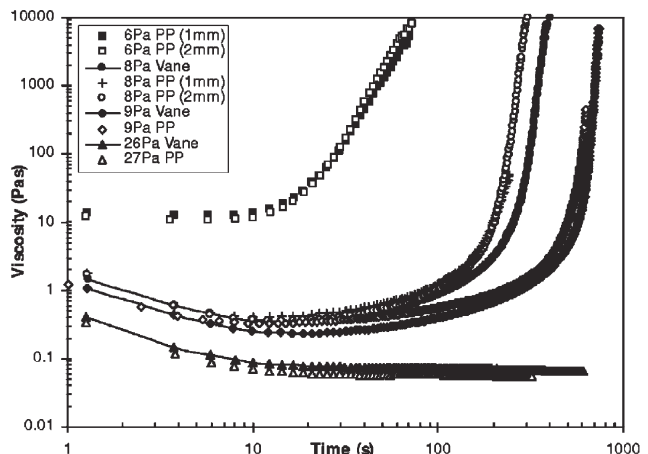


Fig. 9 The time evolution of the viscosity of identical initial states with different applied stresses. A bifurcation in the steady state viscosity is seen to occur at a critical stress, σ_c between 9 and 26 Pa s.¹³

situation for which there is a general agreement that avalanches exist. The exact same experiment had in fact been done earlier for a heap of dry sand, with results that are strikingly similar to those observed for the bentonite, see Fig. 8.

In the more quantitative experiment accompanying the inclined plane test,¹³ a sample of 4.5% bentonite solution, which is a thixotropic fluid as can be seen in Fig. 5 was loaded in different geometries (Couette and plate–plate)‡—and for each experiment brought to the same initial state by a controlled history of shear and rest. Starting from this identical initial condition, different levels of shear stress were imposed on the samples and the viscosity was measured as a function of time. The result is shown in Fig. 9 and deserves some discussion. For stresses smaller than a critical stress, σ_c , the viscosity of the sample increases in time until the flow is halted altogether: the steady-state viscosity is infinite. On the other hand, for a stress only slightly above σ_c , the viscosity decreases with time towards a (low) steady state value η_0 . The important point here is that the transition between these two states is discontinuous as a function of the stress. All this can be understood in terms of the competition between aging and shear rejuvenation.

Aging

At rest or under very slow flow the fluid ages, and consequently its viscosity increases in time. This corresponds physically to the buildup of the colloidal gel of bentonite, and is indeed what is observed in the experiments: the viscosity increases in time without bound, and the end of the experiment corresponds to a viscosity that is too large to be measured accurately by the rheometer. This can be seen pragmatically as the absence of flow: for all stresses smaller than the critical stress the steady-state viscosity is infinite! Note that this is an ‘inverse avalanche’ effect, since the viscosity increases, the shear rate decreases, and the ‘aging’ becomes easier: this is the

‡ Interestingly, in contrast with many experimental tests the results seem independent of the geometry.

reason for which the measured viscosity increases faster near the end of the experiment.

Shear rejuvenation

However, the dominance of the aging process is only assured if the flow rate is small enough. In the experiment, for a stress that can be as little as 1% larger than that for which the aging predominates, the sample starts to flow. Subsequently, the flow destructures the material (breaks down the colloidal gel), which decreases the viscosity. This viscosity decrease causes an acceleration of the flow and so on: due to the avalanche effect discussed above, the steady state viscosity is low.

Consequently, there exists a critical stress that bounds a region of no flow for smaller stresses, and a region of fast flow for higher stresses. The conclusion is that there exists a whole range of steady state shear rates that are not accessible experimentally under an imposed stress: all shear rates between ‘fast’ flow and no flow at all. This also defines the critical shear rate as the lowest shear rate for which the sample still flows, *i.e.*, the shear rate corresponding to the critical stress, σ_c . The steady-state viscosity jumps *discontinuously* from infinity to a finite and low value at σ_c , in sharp contrast with the continuous divergence of an H–B fluid, but agreeing with the conclusions from the inclined plane test. In addition, due to the aging effects the critical stress is no longer a property of the fluid: the longer one waits, the more the sample will age, and consequently the higher the critical stress will be. This again makes perfect sense for instance for the bentonite colloidal gel whose structure is continuously evolving; it explains some of the difficulties one experiences when measuring the yield stress; and it underlines the importance of the experimental protocol: only by controlling the aging history of the sample by a large pre-shear (and optionally a controlled period of rest subsequently), can reproducible results be obtained. An additional difficulty that is worthwhile mentioning in this respect is that the relation between the viscosity and the microstructure is a highly non-trivial one. Two samples of the same thixotropic fluid may have the same viscosity at a given shear rate, but a different structure. This is called ‘structural hysteresis’,^{21,28} and underlines once more the importance of the (shear) history of the sample for its flow properties.

There seem to be very few if any examples of yield stress fluids which are not also thixotropic. Indeed the authors have not been able to find even one such example. The following ‘typical’ yield stress fluids have been investigated: foams, emulsions, colloidal gels, polymer gels (including carbopol), dry and wet granular materials. In addition, colloidal glasses show a behavior that is very similar, stressing the analogy between yield stress fluids and glassy materials proposed earlier.^{30,31} Indeed, the yield stress and the thixotropy of a fluid originate from the same basic physics. For the bentonite example above, the colloidal gel that forms is both responsible for the yield stress - the percolated structure of clay particles confers the elasticity to the material - and the thixotropy: if the flow is strong enough it will partially destroy this structure and hence the viscosity will decrease. Since yield stress and thixotropy thus seem strongly connected and are properties of many (perhaps microscopically different) yield stress fluids,

one might expect the same basic principle giving rise to both phenomena in all these different systems. Such a basic principle must be simple enough to be independent of specific system details in order to be generic for all thixotropic yield stress fluids. Since the competition between aging and shear rejuvenation is known to dominate the structure of the fluid which, in turn, causes both the yield stress and thixotropy, this interplay is a natural starting point for an attempt at a general description of these phenomena. In the following sections one such attempt will be examined and compared with experiments.

4 A simple yield stress model including thixotropy

A large number of models for thixotropy exist (see Dullaert²¹ for a recent overview) and depending on the degree of sophistication one wants to achieve, the models may become rather involved. We will consider here the simplest possible model, in order to establish the minimal ingredients of a model that qualitatively accounts for the behaviors reported above. The model therefore does not account for more complicated effects such as for example the ‘structural hysteresis’,²⁸ but will be very useful in understanding the basic physics of the problem.

A simple model taking into account the interplay between flow, structure and viscosity qualitatively captures the behavior of thixotropic yield stress fluids. The basic assumptions of the model are: (1) there exists a structural parameter, λ , that describes the local degree of interconnection of the microstructure. For the pertinent example of the bentonite colloidal gel, one may think of λ as a measure of the number of connections per unit volume. This can be measured directly, since the elastic modulus of a physical gel is generally taken to be proportional to the number of network connections per unit volume. For a glass, λ should be a measure of the depth of the local minimum in the energy landscape. For a granular material, one might think of it as a measure of how jammed the particles are on average. In a foam (suspension), it could be a combination of the same jamming and the rigidity of the individual bubbles (drops). (2) The viscosity increases with increasing λ . It turns out that if the dependence is sufficiently strong, a yield stress appears naturally. (3) For an aging system at low or zero shear rate, λ increases while if the flow breaks down the structure, λ decreases and reaches a steady state value at sufficiently high shear rates.

The simplest model that has these features consists of an evolution equation for λ :^{13,14}

$$\frac{d\lambda}{dt} = \frac{1}{\tau} - \alpha\lambda\dot{\gamma} \quad (1)$$

coupled to an equation for the viscosity given by either of: $\eta = \eta_0 \exp(\beta\lambda)$ (model I), $\eta = \eta_0 (1 + \beta\lambda^n)$ (model II)

Here τ is the characteristic time of the build-up of the microstructure at rest and η_0 the limiting viscosity at high shear rates; α , β and n are parameters that should be specific for a given material. This simple description of a thixotropic yield stress fluid has a steady state solution

$$\frac{d\lambda}{dt} = 0 \Rightarrow \frac{1}{\tau} = \alpha\lambda_{ss}\dot{\gamma} \Rightarrow \lambda_{ss} = \frac{1}{\alpha\tau\dot{\gamma}}$$

This relation can be used to find the steady state stress if a functional form of $\eta(\lambda)$ is assumed. It is most instructive to look in detail at model II; for the steady-state viscosity, it follows that

$$\sigma_{ss}(\dot{\gamma}) = \dot{\gamma}\eta_0 \cdot (1 + \beta \cdot (\alpha\tau\dot{\gamma})^{-n})$$

which for high shear rates, when all the structure in the fluid is destroyed gives a Newtonian fluid behavior:

$$\sigma_{ss}(\dot{\gamma}) = \dot{\gamma}\eta_0$$

whereas for low shear rates the limiting behavior is

$$\sigma_{ss}(\dot{\gamma}) \propto \dot{\gamma}^{1-n}$$

This last result shows that for a weak dependence of the viscosity on λ , $0 < n < 1$ we find a simple shear-thinning fluid without a yield stress. However, for $n > 1$, a yield stress appears naturally within the model. As can be seen in Fig. 10, there exists a critical stress below which no steady state shear rate can be achieved. This will obviously give rise to yield stress behavior. The flow curve that follows from the model shows that for low shear rates the stress decreases with increasing shear rate, whereas for high shear rates it increases. This defines both a critical stress and a critical shear rate; these are both given by the minimum in the flow curve. For shear rates smaller than the critical shear rate the flow curve has a negative slope. This corresponds to a negative (absolute) viscosity, and signals *unstable flows*.

The requirement for having an unstable flow is:

$$0 > \frac{d\sigma_{ss}}{d\dot{\gamma}} = \eta \left(\frac{1}{\alpha\tau\dot{\gamma}} \right) - \frac{1}{\alpha\tau\dot{\gamma}} \frac{d\eta}{d\lambda}$$

For model I this criterion translates into:

$$\dot{\gamma} < \frac{\beta}{\alpha\tau}$$

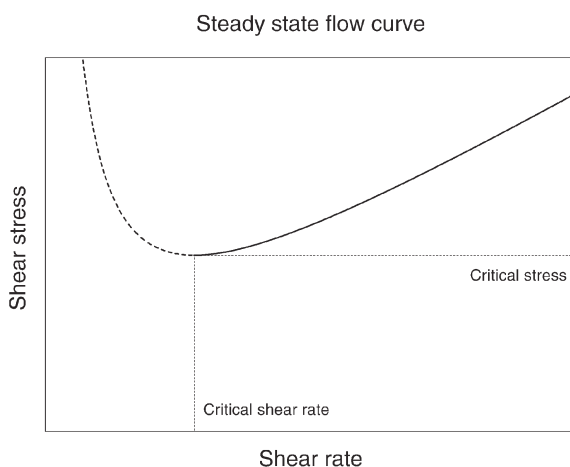


Fig. 10 The steady state flow curve of model II with $n = 2$. The part to the left of the critical shear rate is dashed since the flow is unstable here and the homogeneous flow curve is very difficult to obtain.

And for model II:

$$\dot{\gamma} < \frac{(\beta(n-1))^{-n}}{\alpha\tau}$$

It is seen that for sufficiently small shear rates these criteria will be satisfied for any value of β (for model II again provided that $n > 1$).

Below, we will show that this rather simple addition of thixotropy to the yield stress behavior allows us to account qualitatively for all of the phenomena described above, and consequently solves most of the problems surrounding yield stresses.

5 Comparison with experiments

5.1 The yield stress and the problems with it

In this model, three parameters characterize the material in an experiment at any given time: the stress σ , the shear rate $\dot{\gamma}$, and the structural parameter λ (and through it the viscosity η). If any two of these are given, the third can be found using the dependence $\sigma = \dot{\gamma}\eta(\lambda)$. Now, consider a starting point (*i.e. a pair of $\dot{\gamma}$ and σ coordinates*) for an experiment located at some point above the flow curve of Fig. 10. From eqn 1 it is seen that such a point will move towards lower values of λ —either down or to the right in the flow curve diagram depending on whether the shear rate or stress is imposed. Conversely, a starting point below the steady state curve will move towards higher values of λ either up (imposed shear rate) or to the left (imposed stress). Thus, given an initial value of λ one can predict the critical stress at which the aging exactly balances the rejuvenation. This is the stress corresponding to the intersection between the steady state flow curve and the straight line of the constant viscosity flow curve given by the initial value of λ . See Fig. 11. Above this stress the flow will speed up, below it will slow down. If the intersection is in the unstable region to the left of the critical shear rate, the long term change in shear rate will be very dramatic, so that the association of an ‘actual’ yield stress with this critical stress seems reasonable. However, it should be kept in mind that due to the aging, this yield stress is now a function of the time the sample has been given to rest, and is

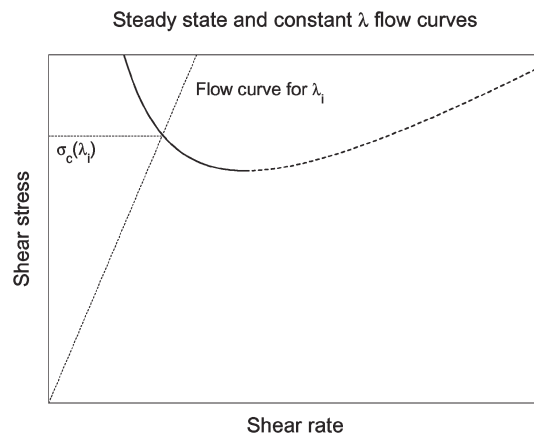


Fig. 11 The intersection between the steady state flow curve and the straight line of the flow curve given by the initial value of λ , gives the value of the shear history dependent yield stress.

therefore not a material property, but rather dependent on both the material and on λ .

As already mentioned one popular way of finding the yield stress is to enforce a constant shear rate on a system and infer the yield stress from the stress over time curve. Based on the discussion above it can be understood why the obtained value depends on both the imposed shear rate and how the sample is treated prior to the experiment. It is also worthwhile noting that if λ is small initially, an applied stress that is below the critical stress could result in flows which might remain measurable for some time. Thus the yield stress is not the stress below which no flow occurs; the times necessary to reach the steady state corresponding to no measurable flows can be as long as an hour in our experiment. Thus a yield stress should be defined as the stress below which no permanent flows occurs. The following procedure allows for finding this newly defined material and history dependent yield stress. Several samples are prepared in an identical fashion (identical histories of pre-shear and rest) and each sample should be subject to a different but constant shear stress. After observing the long time behavior, the yield stress can be identified as the transition stress between the highest stress for which sample comes to a complete halt, and the lowest stress for which permanent flows are observed. This is actually the procedure followed in Fig. 9. The considerations above also demonstrate that the yield stress defined in this way is really not a material property, but depends on the value of λ i.e. the shear history of the system. This we believe is at the heart of the ‘thixotropic obstacles in determining the yield stress’.¹⁶

5.2 The critical stress and avalanche behavior

Solved dynamically, the model reproduces both the bifurcation and the avalanche behavior. When the stress is imposed, in time the viscosity either tends towards infinity or to a small value depending on whether the stress is larger or smaller than the critical value σ_c , as is shown in Fig. 12. In the viscosity bifurcation experiments¹³ the sample is prepared in a certain

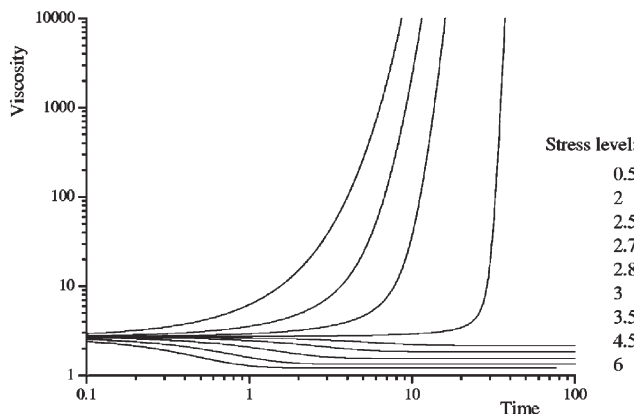


Fig. 12 Dynamical solution of the model equations. The graph shows how the viscosity evolves in time for different imposed shear stresses.¹³ The qualitative resemblance with the experimental data in Fig. 9 is striking.

reproducible initial state (*i.e.* value of λ) and different stresses are applied. If the shear rate history of the sample is such that the stress is smaller than the critical stress, the system will forever move to the left in the flow diagram towards an infinite viscosity. To the contrary, a stress just above the critical stress will make the system move to the right in the flow diagram until the intersection with the flow curve corresponding to a low viscosity and high shear rate. Thus, the viscosity jumps discontinuously to infinity at the critical stress, as was indeed observed in the experiments.^{13,14}

5.3 The critical shear rate and shear banding

If on the other hand, the shear rate is fixed below the critical shear rate corresponding to the minimum of the flow curve, $\dot{\gamma}_c$, the system can accommodate the globally imposed average shear rate by spatially dividing the system into two ‘phases’—one solid part, where the shear rate is zero, and one fluid part, which is sheared roughly at $\dot{\gamma}_c$. The proportion of the fluid phase grows from zero to one when the average shear rate grows from zero to the critical value. Therefore, the shear localization observed in many experiments on yield stress fluids naturally comes out of the proposed model, and all the predictions of the model are in qualitative agreement with imposed shear rate experiments. The latter show that when the shear is sufficiently low localization occurs, and disappears exactly at the critical stress, in line with the conclusions from the model.^{8,15,17}

6 Comparison with models in the literature

Since the thixotropy of a large number of fluids has for a long time been very well established,^{7,11,13,14,32,33} many models for thixotropic behavior through a structural parameter have been proposed.^{12–14,24,25,34–37} Several of them are summarized by Barnes⁷ and in tabular form by Mujumdar *et al.*¹²

A class of models similar to our evolution equation for λ (we will call these λ -models in the following) have been used for a range of very different systems. For instance λ has been used to describe the degree of flocculation for clays,³⁸ as a measure of the free energy landscape for glasses,³⁹ or to give the fraction of particles in effective potential wells for colloidal suspensions.²⁶ This way of introducing an interconnection between the shear history and the viscosity of thixotropic systems was first proposed by F. Moore in 1959⁴⁰ (or in a slightly different wording, identical to the one used here, by Cross in 1965).³⁴ Generally the λ -models all assume:

$$\frac{d\lambda}{dt} = f(\lambda, \dot{\gamma}) - g(\lambda, \dot{\gamma}) \quad (2)$$

$$\sigma = \sigma_y(\lambda) + \dot{\gamma} \cdot \eta(\lambda, \dot{\gamma}) \quad (3)$$

where f is the rate of reconstruction (or aging) of the fluid and g is the rate of destruction (or shear rejuvenation). The complexity chosen for the right hand sides of eqns 2 and 3 may vary quite a bit from model to model.^{7,12–14,35–37,41}

The general assumption is that $\frac{d\sigma}{d\dot{\gamma}} > 0$ causes the slope of the flow curve diagram to be positive everywhere. This holds true for the flow curves of all the models summarized by Mujumdar *et al.*¹² and Barnes.⁷ This implies that the flows are stable: the negative

slope is what leads to instability since a lower stress can sustain a higher shear rate. In a general mathematical treatment of the behavior of any λ -model by Cheng *et al.* in 1965,²⁵ the authors try to argue that the flow curve of all such models *must* have a positive slope everywhere. A very few of the papers summarized by Mujumdar *et al.*¹² and Barnes⁷ may have regions of negative slope of the flow curve for some parameter choices,^{34,42} but the parameters required for this are avoided and the possibility of having unstable flows is not discussed. These models differ therefore significantly from the one explained above, that rationalizes the occurrence of shear localization and in which the yield stress appears naturally.

Very recently, Cheng investigated a model in which he did not presuppose the flow curve to have a positive slope everywhere.²⁴ His mathematical treatment however, does not consider the implications of the spatial extent of the fluid. This removes the possibility of shear banding and Cheng concludes that the region of the flow curve with negative slope, while unstable when constant stress is imposed, will not show any strange behavior if constant shear rate is imposed, which appears to disagree with experiment.

Most of the models summarized in the also recent paper by Mujumdar¹² introduce a yield stress manually, *i.e.* the σ_y term in eqn 3 is nonzero. Probably this is done because a yield stress is known to be present in many fluids, and the positive-only flow curves of the models cannot show yield stress behavior inherently. This ‘artificial’ yield stress seems unnecessary in view of the naturally occurring yield stress from the sections above.

7 Conclusion

Fluids that appear solid for stresses below a critical limit are called yield stress fluids, and are often modeled by yield stress fluid models such as the Herschel–Bulkley model. This review points out some fundamental conflicts between experiments on the one hand and the predictions of such models on the other hand. Indeed problems arise even with the definition and concept of a yield stress as the stress where the fluid just starts/stops flowing. Thixotropy is another prominent feature of many complex fluids and it indeed appears to be present whenever a yield stress is present also. Both phenomena are believed to be caused by the same underlying physics, but have traditionally been modeled as separate phenomena. This short review summarizes a number of recent experimental findings and presents the results of some recent developments within a group of models designed to describe the interplay between yield stress and thixotropy. These new developments allow for a very simple model to explain both thixotropy and yield stress behavior as two effects of the same cause: the interplay between flow and structure of a fluid. This simple model provides a qualitative explanation of many if not all features of real yield stress fluids that are incompatible with the ideal picture of a yield stress. Notably, it suggests that shear localization is an intrinsic property of yield stress fluids, that always manifests itself at low enough shear rates. The experimental data and the understanding brought forth by the new model beg for a redefinition of the concept of the yield stress, which is suggested here.

References

- 1 E. C. Bingham, *Fluidity and Plasticity*. McGraw-Hill, New York, 1922.
- 2 R. B. Bird, G. C. Dai and B. Y. Yarusso, The rheology and flow of viscoplastic materials, *Rev. Chem. Eng.*, 1982, **1**, 1–70.
- 3 Q. D. Nguyen and D. V. Boger, Measuring the flow properties of yield stress fluids, *Annu. Rev. Fluid. Mech.*, 1992, **24**, 47–88.
- 4 H. A. Barnes, The yield stress—a review or ‘ποντα πει—everything flows? *J. Non-Newtonian Fluid Mech.*, 1999, **81**, 133–178.
- 5 A. E. James, D. J. A. Williams and P. R. Williams, Direct measurement of static yield properties of cohesive suspensions, *Rheol. Acta*, 1987, **26**, 437–446.
- 6 H. A. Barnes and Q. D. Nguyen, Rotating vane rheometry – a review, *J. Non-Newtonian Fluid Mech.*, 2001, **98**, 1–14.
- 7 H. A. Barnes, Thixotropy – a review, *J. Non-Newtonian Fluid Mech.*, 1997, **70**, 1–33.
- 8 P. Coussot, J. S. Raynaud, F. Bertrand, P. Moucheront, J. P. Guilbaud, H. T. Huynh, S. Jarny and D. Lesueur, Coexistence of liquid and solid phases in flowing soft-glassy materials, *Phys. Rev. Lett.*, 2002, **88**, 218301.
- 9 F. Pignon, A. Magnin and J.-M. Piau, Thixotropic colloidal suspensions and flow curves with minimum: Identification of flow regimes and rheometric consequences, *J. Rheol.*, 1996, **40**, 573–587.
- 10 M. M. Britton and P. T. Callaghan, Nuclear magnetic resonance visualization of anomalous flow in cone-and-plate rheometry, *J. Rheol.*, 1997, **41**, 1365–1386.
- 11 J. Mewis, Thixotropy – a general review, *J. Non-Newtonian Fluid Mech.*, 1979, **6**, 1–20.
- 12 A. Mujumdar, A. N. Beris and A. B. Metzner, Transient phenomena in thixotropic systems, *J. Non-Newtonian Fluid Mech.*, 2002, **102**, 157–178.
- 13 P. Coussot, Q. D. Nguyen, H. T. Huynh and D. Bonn, Viscosity bifurcation in thixotropic, yielding fluids, *J. Rheol.*, 2002, **46**, 573–589.
- 14 P. Coussot, Q. D. Nguyen, H. T. Huynh and D. Bonn, Avalanche behavior in yield stress fluids, *Phys. Rev. Lett.*, 2002, **88**, 175501.
- 15 J. C. Baudéz and P. Coussot, Abrupt transition from viscoelastic solidlike to liquidlike behavior in jammed materials, *Phys. Rev. Lett.*, 2004, **93**, 128302.
- 16 J. R. Stokes and J. H. Telford, Measuring the yield behavior of structures fluids, *J. Non-Newtonian Fluid Mech.*, 2004, **124**, 137–146.
- 17 N. Huang, G. Ovarlez, F. Bertrand, S. Rodts, P. Coussot and D. Bonn, Flow of wet granular materials, *Phys. Rev. Lett.*, 2005, **94**, 028301.
- 18 D. C.-H. Cheng, Cone-and-plate viscometry: explicit formulae for shear stress and shear rate and the determination of inelastic thixotropic properties, *Br. J. Appl. Phys.*, 1966, **17**, 253–263.
- 19 V. Bertola, F. Bertrand, H. Tabuteau, D. Bonn and P. Coussot, Wall slip and yielding in pasty materials, *J. Rheol.*, 2003, **47**, 1211–1226.
- 20 R. G. Larson, *The Structure and Rheology of Complex Fluids*, Oxford University Press, Oxford and New York, 1999.
- 21 K. Dullaert, *Constitutive equations for thixotropic dispersions*. PhD thesis, Katholieke Universiteit Leuven, 2005.
- 22 B. Abou, D. Bonn and J. Meunier, Aging dynamics in a colloidal glass, *Phys. Rev. E: Stat. Phys., Plasmas, Fluids, Relat. Interdiscip. Top.*, 2001, **64**, 021510.
- 23 L. Berthier, J.-L. Barrat and J. Kurchan, A twotime-scale, two-temperature scenario for nonlinear rheology, *Phys. Rev. E: Stat. Phys., Plasmas, Fluids, Relat. Interdiscip. Top.*, 2000, **61**, 5464–5472.
- 24 D. C.-H. Cheng, Characterisation of thixotropy revisited, *Rheol. Acta*, 2003, **42**, 372–382.
- 25 D. C.-H. Cheng and F. Evans, Phenomenological characterization of the rheological behaviour of inelastic reversible thixotropic and antithixotropic fluids, *Br. J. Appl. Phys.*, 1965, **16**, 1599–1617.
- 26 P. Coussot and C. Ancey, *Rheophysics of Pastes and Suspensions*. EDP Sciences, Paris, 1999.
- 27 P. Coussot and S. Boyer, Determination of yield stress fluid behaviour from inclined plane test, *Rheol. Acta*, 1995, **34**, 534–543.
- 28 J. Mewis, A. J. B. Spauld and J. Helsen, Structural hysteresis, *Nature*, 1975, **253**, 618–619.

- 29 R. R. McDonald and R. S. Anderson, Constraints on eolian flow dynamics through laboratory experiments on sand slopes, *J. Sedimentary Res.*, 1996, **66**, 642.
- 30 D. Bonn, P. Coussot, H. T. Huynh, F. Bertrand and G. Debrégeas, Rheology of soft glassy materials, *Europhys. Lett.*, 2002, **59**, 786–792.
- 31 F. Varnik, L. Bocquet, J.-L. Barrat and L. Berthier, Shear localization in a model glass, *Phys. Rev. Lett.*, 2003, **90**, 095702.
- 32 F. Pignon, A. Magnin and J.-M. Piau, Thixotropic behavior of clay dispersions: combinations of scattering and rheometric techniques, *J. Rheol.*, 1998, **42**, 1349–1373.
- 33 B. Abou, D. Bonn and J. Meunier, Nonlinear rheology under an external drive, *J. Rheol.*, 47, 2003, **47**, 979–988.
- 34 M. M. Cross, Rheology of non-newtonian fluids: A new flow equation for pseudoplastic systems, *J. Colloid Sci.*, 1965, **20**, 417–437.
- 35 C. F. Chan Man Fong and D. De Kee, Yield stress and small amplitude oscillatory flow in transient networks, *Ind. Eng. Chem. Res.*, 1994, **33**, 2374–2376.
- 36 D. Soong and M. Shen, Kinetic network model for nonlinear viscoelastic properties of entangled monodisperse polymers i. steady-state flow, *J. Rheol.*, 1981, **25**, 259–273.
- 37 D. De Kee, R. K. Code and G. Turcotte, Flow properties of time-dependent foodstuffs, *J. Rheol.*, 1983, **27**, 581–604.
- 38 D. Quemada, Rheological modelling of complex fluids: iv thixotropic and thixoelastic behavior. startup and stress relaxation, creep tests and hysteresis cycles, *Eur. Phys. J.: Appl. Phys.*, 1999, **5**, 191–207.
- 39 J. P. Bouchaud, A. Comtet and C. Monthus, On a dynamical model of glasses, *J. Phys. I*, 1995, **5**, 1521–1526.
- 40 F. Moore, The rheology of ceramic slip and bodies, *Trans. Br. Ceramic Soc.*, **58**, 470–494.
- 41 S.-F. Lin and R. S. Brodkey, Rheological properties of slurry fuels, *J. Rheol.*, 1985, **29**, 147–175.
- 42 A. W. Sisko, The flow of lubricating greases, *Ind. Eng. Chem.*, 1958, **50**, 1789–1792.



Fast Publishing? Ahead of the field

To find out more about RSC Journals, visit

www.rsc.org/journals

RSC Publishing

The shear modulus of wet granular matter

P. C. F. MØLLER¹ and D. BONN^{1,2}

¹ Ecole Normale Supérieure, Laboratoire de Physique Statistique - Paris, F-75231 France

² van der Waals-Zeeman Institute - 1018 XE Amsterdam, The Netherlands

received 21 May 2007; accepted in final form 9 September 2007

published online 2 October 2007

PACS 83.80.Fg – Granular solids

Abstract – The strength of different wet granular materials is investigated as a function of the liquid volume fraction by measuring the elastic shear modulus, G' . We show that the optimum strength is achieved at a very low liquid volume fraction of 1–3%. Surprisingly we find that the macroscopic strength of different wet granular materials depends with a power of 2/3 on the microscopic elastic modulus of the individual grains, with a power of $-1/3$ on the radius, and with a power of 1/3 on the surface tension. This can be explained by assuming that the attractive capillary force between two grains deforms the grains elastically, yielding a “spring constant” for further deformation. Averaging over many grain-grain orientations allows us to predict the macroscopic shear modulus in excellent agreement with our experiments.

Copyright © EPLA, 2007

Physicists have for quite some time been fascinated by the far-from-equilibrium properties of granular systems and the phenomena they give rise to. Tremendous activity within the field of granular research gives proof of this [1–3]. Furthermore the properties of granular materials are of huge importance to engineers and it is estimated that about 10% of all energy consumption on Earth is spent on the handling of granular materials [4]. In spite of the huge interest of both scientists and engineers the properties of granular systems are still imperfectly understood [5].

One of the most spectacular and fascinating properties of granular materials is how the addition of a small amount of fluid dramatically changes the macroscopic properties of the material. Just a bit of water turns a boring pile of dry sand into a spectacular sandcastle [6–8] while too much water will destabilize the material, as observed in landslides [9]. A favorite tool for studying the strength of such moist granular systems has been the rotating drum experiment, where the material is put into a slowly rotating drum where the angles of repose and avalanche are recorded as a measure of material strength [8]. This type of experiment by its nature limits one to examining relatively weak, non compacted materials, and does not allow for studying materials of a strength suitable for building sandcastles for instance. In a recent paper Fournier *et al.* imposed oscillatory shear deformation to wet granular materials in a pressure-driven shear cell [10]. They recorded the hysteresis pressure as a measure of the material yield stress as a function of liquid volume

fraction. Because of considerable scatter, the best one can say about the liquid volume fraction at which maximum strength occurs is that it is between 0.1% and 5% and the issue of what volume fraction of water gives the highest elastic strength of the granular assembly remains largely unresolved.

In this letter we measure the elastic modulus as an expression of material strength and give an answer to the question of what the optimum liquid volume fraction is, and provide a quantitative model that is able to account not only for the optimum, but also for the value of the elastic modulus. We use a conventional rheometer (Rheologica, StressTech) to measure the elastic shear modulus, G' , of different partially saturated granular materials as a function of the liquid volume fraction. G' is related to the macroscopic Young's modulus, E_{mac} , by $E_{mac} = 2(1 + \nu)G' \approx 3G'$, ν being Poisson's ratio¹. The grains used in the experiments are; sand (from Fontainebleau, sieved to have a radius between 90 and 110 μm), spherical glass beads of 25 and 100 μm radius, polystyrene beads of 100 μm radius (Dynoseeds, from Microbeads), and PMMA spheres of a 3 μm radius (Calibre, from Microbeads). All beads are thoroughly rinsed and dried before use. The fluids used are ultra pure water and silicone oil (Rhodorsil from CRC Industries, France). The surface tensions of the fluids in the presence

¹In this paper we assume $\nu = 0.5$ which corresponds to that of an incompressible medium. If we choose $\nu = 0.3$ which corresponds to steel, the numerical values of our calculations change by about 4%, so that we are not very sensitive to the exact value of ν .

of beads are determined using the Du Nuoy ring method. For water it is found to be 72 mN/m and 20 mN/m for silicone oil. After preparing a mixture of beads and fluid, a small quantity of this mixture is put in a vane-in-cup geometry in the rheometer. For the almost completely dry and almost completely wet mixtures the yield stress is quite low and the grains reach something resembling a close packing when poured into the rheometer geometry, but for the intermediate liquid volume fractions the yield stress is quite high and the material does not compact under its own weight giving much lower grain filling fractions. In order to compare the elastic moduli at different liquid volume fractions and to get results not depending strongly on how the material is loaded into the cup, the material is after loading compacted by dropping a small thumper (12.5 mm in radius, 40 mm in height and with a 30 g mass) from a small height (about 10 mm) at least 100 times. We found that this ensures a reproducible compaction (a filling fraction of about 0.63 ± 0.01) for all liquid volume fractions and for each loading of the sample. This observation and the fact that the yield stresses of completely dry and wet materials were too low for us to measure their elastic moduli demonstrates that the compaction of the materials does not squeeze the beads together in the cup. Since the capillary rise ($h = 2\gamma\cos\theta/\rho gr$ [11]) in our samples is at least 15 cm and thus much higher than our filling height, we expect that surface tension along with mechanical mixing prior to the experiment prevents drainage and other inhomogeneities of the distribution of liquid among the grains.

The modulus G' is subsequently measured at a frequency of 1 Hz. We use 1 Hz since this allows for rapid measurements; we verified that G' does not depend on frequency for frequencies between 10^{-2} and 10 Hz, the frequencies readily accessible on the rheometer (see fig. 1). To ensure that the measurements probe the linear, elastic response, the shear strain is continuously increased during the course of one experiment and the value of G' is averaged over the linear regime (see fig. 1). At least ten such measurements are performed for each material composition and for each volume fraction. The vane-in-cup geometry used for most of the experiments consists of four vanes of 10 mm in height and 5 mm in width attached to a rod 4 mm in radius, thus giving a total inner radius of 9 mm and a cup outer radius of 13 mm with a 10 mm strip of sandpaper glued on at the same height as the vanes². This gives a 4 mm gap corresponding to at least 20 bead diameters. To ensure that this gap size is sufficient to avoid confinement effects we checked that a vane-in-cup geometry with a much larger outer radius — 22.5 mm (corresponding to a gap of 13.5 mm) — gave results identical to the smaller one

²One needs the above values for the inner and outer radii, r_i and r_o , and height, h , in order to convert the torque, τ , and angular deformation, $\Delta\theta$, measured by the rheometer into a value for G' : $r_i\Delta\theta = \int_{r_i}^{r_o} \gamma dr = \int_{r_i}^{r_o} \sigma/G' dr = \int_{r_i}^{r_o} \tau/2\pi hr^2 G' dr \Rightarrow G' = (\tau/\Delta\theta) \cdot (r_i^{-1} - r_o^{-1})/2\pi h r_i$.

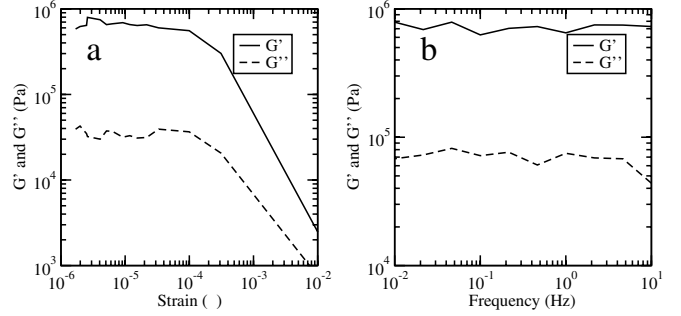


Fig. 1: A typical measurement of the elastic storage and loss moduli G' and G'' as a function of strain at a frequency of 1 Hz (a), and as function of frequency at a fixed strain of $3 \cdot 10^{-6}$ (b). Since G' and G'' are seen to be independent of frequency between 0.01 and 10 Hz, all experiments were done at 1 Hz. Since G' and G'' are seen to be roughly constant for strains between 10^{-6} and 10^{-4} , the average value of G' in this regime is taken for each experiment. The fact that G'' is more than an order of magnitude smaller than G' shows that this regime is one of elastic deformation and without flow. Using a value of Poisson's ratio, G' can be converted into Young's modulus and the bulk modulus so that the exact material deformation to any type of load can be computed. Materials normally have some finite deformation they can sustain before they fail, and knowing both G' and that critical deformation allows one to predict if the material will fail under a given load or not. In (a) the value of G' is reduced by one order of magnitude when the strain is about 10^{-3} , which is a reasonable value to choose for the critical strain. This material can thus sustain a tangential load of about 1 kPa before fracturing, which compares well with the fact that weights on the order of grams are needed to deform a cube centimeter of sand.

(fig. 2). In all cases the distance to the bottom of the cup (which was smooth to allow as much slip as possible) was 10 mm and the total filling height about 30 mm.

Figure 2 depicts the results for a variety of bead materials and fluids. We find that wet sand has a shear modulus similar to that of spherical glass beads, while that of spherical polystyrene beads is much smaller: the latter has a G' that is more than one order of magnitude lower. Apart from this difference in absolute strength the curves show a similar dependence on the liquid volume fraction.

To understand this, we need to look in detail at what happens when one adds a small volume of fluid to a stack of spherical grains. The surface tension of the fluid pulls it into small bridges connecting individual beads (fig. 3). The attractive capillary force between two spheres is $F_{cap} = -\pi r_1^2 \Delta p + 2\pi r_1 \gamma = -\pi r_1^2 C \gamma + 2\pi r_1 \gamma$, where γ is the surface tension and C and r_1 are the curvature and the radius of the bridge, respectively (fig. 3(a)) [12,13]. The curvature is a function of R , r_1 and the separation between beads, d , but for $d = 0$ and $r_1 \ll R$, one can approximate $C \approx -1/r_2 \approx -2R/r_1^2$ so that the force is $F_{cap} \approx 2\pi R \gamma$.

In practice it is well known that surface roughness and finite sphere separations mean that the actual force will

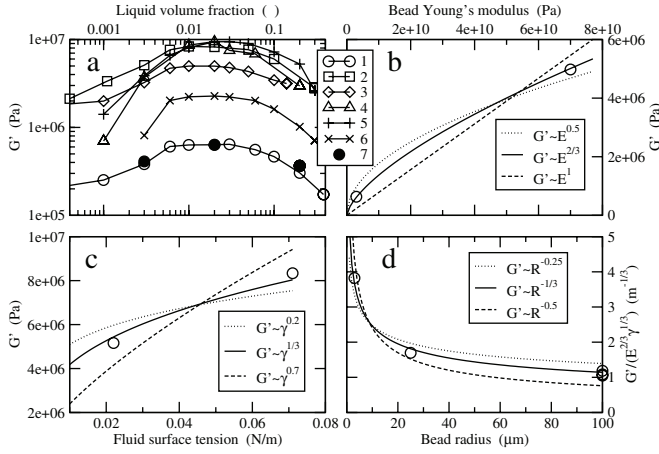


Fig. 2: (a) Measured elastic shear modulus G' as function of liquid volume fraction for different granular materials; 1: 100 \$\mu\text{m}\$ polystyrene beads and silicone oil, 2: 100 \$\mu\text{m}\$ glass beads and water, 3: 100 \$\mu\text{m}\$ glass beads and silicone oil, 4: 100 \$\mu\text{m}\$ sand and water, 5: 25 \$\mu\text{m}\$ glass beads and silicone oil, 6: 3 \$\mu\text{m}\$ PMMA beads and silicone oil, 7: 100 \$\mu\text{m}\$ polystyrene beads and silicone oil in a larger-gap vane-in-cup geometry. Apart from the absolute value of G' , which differs more than an order of magnitude, the curves for different materials are seen to have similar shapes. Most measurements were performed in a geometry with a 4 mm gap, but measurements with a gap of 13.5 mm give identical results as seen in series 7. Note that none of the materials are completely wet or dry. Indeed, for completely wet materials and materials with too low a volume fraction, the elastic strength is too low to be measured by the rheometer. (b), (c): The dependence of G' at a 1% liquid volume fraction on Young's modulus of the bead material and the surface tension of the liquid, respectively. (d) Rescaling G' by the relations found in sub figures (b) and (c), we plot $G'/(E^{2/3}\gamma^{1/3})$ as a function of the bead radius.

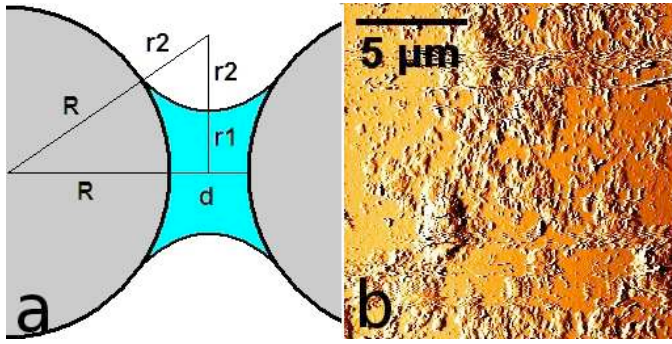


Fig. 3: (a) Schematic of a liquid bridge. The distance between beads has been exaggerated for illustrative purposes. (b) An Atomic Force Microscopy (AFM) picture of the surface of a 100 \$\mu\text{m}\$ glass bead. The height of the surface roughness is on the order of 1 \$\mu\text{m}\$.

not be independent of the bridge volume [14]. While the above formula is a very good approximation at intermediate volume fractions, it overestimates the strength at low ones where the fluid is trapped in the surface roughness and at high ones where single bridges merge into larger

aggregates and loose strength. To allow for this dependence, we multiply the simplified bridge force equation with a factor between 0 and 1, depending on the liquid volume fraction: $F_{cap} = 2\pi R\gamma f(V_f)$. From AFM pictures of the bead surfaces (fig. 3(b)) and fluorescence pictures of the liquid bridges (fig. 5) this factor can be computed as described below.

The bridge force will suck the beads together and deform them elastically until balanced by the elastic response of the beads. The relation between force F , compression δ , of two identical spheres of radius R , and Young's modulus E is given by Hertzian response theory [15]: $F_H = -\frac{4\sqrt{2}}{9}R^{1/2}E\delta^{3/2}$. Linearizing the total force around the new equilibrium position where $F_{cap} + F_H = 0$, gives a spring constant against further displacement of the beads:

$$F_{tot} = -\frac{4\sqrt{2}}{9}R^{1/2}E((\delta_{eq} + \Delta\delta)^{3/2} - \delta_{eq}) \quad (1)$$

$$\approx -\frac{2\sqrt{2}}{3}R^{1/2}E\delta_{eq}^{1/2}\Delta\delta \quad (2)$$

$$\approx -\left(\frac{\pi}{24}\right)^{1/3}R^{2/3}E^{2/3}\gamma^{1/3}f(V_f)^{1/3}\Delta\delta \equiv -k\Delta\delta. \quad (3)$$

To compute how this spring constant results in G' , one needs to average over all sphere-sphere bond orientations with respect to the shearing plane and to the shearing direction. To compute the macroscopic Young's modulus (E_{mac}) however, one needs only average over bond orientations with respect to the stress plane, which is much simpler. G' can subsequently be found from E_{mac} via $E_{mac} = 3G'$. Let Δl be the extension of the material normal to the stress plane and F_e the extensional stress. Then $E_{mac} \equiv \frac{F_e/A}{\Delta l/l}$, where A is the area where the stress is applied and $\Delta l/l$ is the relative elongation. Consider a sphere-sphere bond of length $2R$ oriented with polar angle θ to the stress plane, and azimuthal angle ϕ . Then $\Delta\delta = \Delta l \sin\theta$, $l = 2R\sin\theta$ and $F_e = F\sin\theta$. If one now takes the area where the force is applied to be $(2R)^2$, one gets

$$E_{mac} = \frac{F_e/A}{\Delta l/l} = \frac{F\sin^3\theta}{2R\Delta\delta} = \frac{k}{2R}\sin^3\theta. \quad (4)$$

And averaging over all angles, θ and ϕ ,

$$\langle E_{mac} \rangle = \frac{k}{\pi R} \int_0^{\pi/2} \sin^3\theta \cos\theta d\theta = \frac{k}{4\pi R} \quad (5)$$

leading to

$$\langle G' \rangle = \frac{k}{12\pi R} \approx 0.054 R^{-1/3} E^{2/3} \gamma^{1/3} f(V_f)^{1/3}. \quad (6)$$

This simple formula directly explains why moist polystyrene beads have a much smaller G' than moist sand or glass beads. This is because Young's modulus of sand is like that of glass, namely 68 GPa, while that of polystyrene and PMMA is only 3 GPa [16]. Furthermore the surface tension of water is 72 mN/m, while that of oil

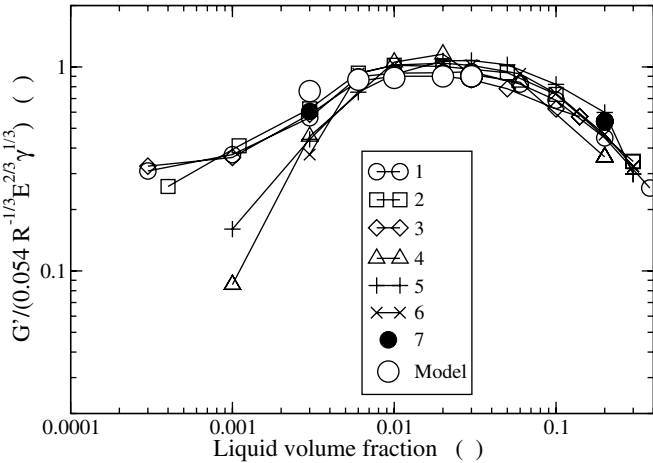


Fig. 4: Master curve of G' for several materials (see the caption of fig. 2 for the legends). The curves for the different materials have been rescaled using: $G' \rightarrow G'/(0.054 R^{-1/3} E^{2/3} \gamma^{1/3})$, where R is the bead radius, E Young's modulus of the beads material and γ the surface tension of the fluid. The theoretical prediction has been computed directly from the known values of these parameters and from the measurements of the liquid bridge diameter for each volume fraction. It contains no fitting parameters.

is 20 mN/m; the difference in the measured value of G' between sand and water on the one side and polystyrene beads and silicone oil on the other is indeed on the order of $(68/3)^{2/3}/(72/20)^{1/3} \approx 12$. This therefore gives a quantitative explanation for the one order of magnitude difference between glass and polystyrene beads observed in fig. 2. Systematically and independently varying the grain size (a factor of 30), fluid surface tension (a factor of 4), and the Young's modulus of the grain material (a factor of 20), we find that the measured elastic moduli collapse onto a single master curve when rescaled in the above way (fig. 4).

The strength of all the grain/liquid systems is thus seen to depend strongly on the liquid volume fraction, with a maximum strength at about 2% of liquid, independently of the system details (fig. 4). Because of the relative low scatter in the data of this figure the liquid volume fraction for maximum strength can be limited to the range of 1–3% which is a significant improvement compared to the previous range of 0.1–5% [10]. Furthermore we demonstrate that the behavior of rough sand is like that of spherical glass beads which was an open question. It is perhaps surprising that our experiments and those of [10] give similar curves for strength as a function of volume fraction. Strength is maximised when the liquid bridge attraction peaks however, which should not depend on the measurement method.

What happens when the bridge volumes grow is well understood [14]. At very low volume fractions, most of the fluid is trapped in the surface roughness, and the bridge force is dominated not by the curvature of the sphere, but by the local roughness. At higher volume fractions,

a significant fraction of the fluid is still caught in the surface roughness but the bridge force is dominated by the curvature of the spheres. At even higher volume fractions, the bridges start merging and loose strength. From fig. 4 it is seen that some materials lose their strength faster as the volume fraction is decreased below about 1%. This is very reasonable since the fraction of fluid caught in the surface roughness increases as the liquid volume fraction is lowered and these materials (4:100 μm sand and water, 5:25 μm glass beads and silicone oil, and 6:3 μm PMMA beads and silicone oil) have higher surface areas per unit volume of material.

Since the elastic moduli of the materials in fig. 4 are rescaled by $G' \rightarrow G'/(0.054 R^{-1/3} E^{2/3} \gamma^{1/3})$, both the experimental data and the prediction are actually showing the shape of $f(V_f)^{1/3} = (F_{cap}/2\pi R\gamma)^{1/3}$. To predict not only how the modulus of a material depends on the bead material, the bead size, and the fluid surface tension, but also on the liquid volume fraction one needs to predict how $f(V_f)$ varies. To get an accurate value of the bridge force one needs to integrate the Laplace equation in cylindrical symmetry: $\Delta p = \gamma(1/r + 1/r')$, where r and r' are the principal radii of curvature [11]. As boundary conditions for this equation, one needs to know the bridge radius, the sphere radius, and the sphere separation³. The sphere radii are known from standard optical microscopy, the sphere separation is taken to be equal to the height of the surface roughness which was found with an AFM (fig. 3), and the bridge radii as a function of volume fraction was found with fluorescence microscopy (fig. 5). Using these values as boundary conditions, the Laplace equation is numerically integrated to give the model prediction in fig. 4. As this calculation assumes that bridges do not merge and needs the bridge radii as input values, predictions can only be made of course in the regime where bridge radii are optically measurable and bridges have not yet merged. Unfortunately single bridges can be observed only between volume fractions of 0.3% and 3% (fig. 5), which limits the theoretical prediction to this range. As seen in fig. 4, the prediction is very good between volume fractions of 0.6% and 3%, while it is too big at 0.3%.

A second effect of the separation between beads is that bridges cannot exist below a critical volume. The number of bridges has been demonstrated to increase abruptly with volume fraction (from about one per sphere to about six) at a volume fraction of about 0.2% [10]. This change in bridge number is not included in our model, and this may be the reason why for the lowest volume fraction the model slightly overestimates the modulus.

In sum, we investigated the impact of the amount of fluid and composite material on the strength of a partially saturated granular material and found that the optimum is

³In principle one also needs to know the contact angle, but since the contact angles in our mixtures are always very low and since the resulting force depends very weakly on the contact angles, they are all assumed to be zero.

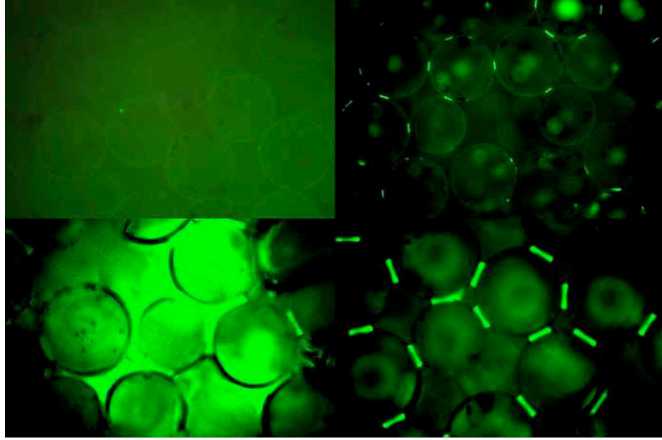


Fig. 5: The liquid bridges between beads as seen in fluorescence microscopy. From the upper left corner and clockwise, volume fractions of 0.1%, 0.3%, 3% and 6%, respectively. At a volume fraction of 0.1% the fluorescence of the fluid caught in the surface roughness is seen to dominate that of the fluid in the bridges. At a volume fraction of 6% a significant number of the bridges are merged into large aggregates. The bridges consist of water with added fluorescein and the interstitial air has been replaced by an oil with an index of refraction matching that of the glass beads.

achieved at a liquid volume fraction as small as 1–3%. We present a very simple model that successfully describes the elastic modulus of wet granular matter. This is of practical interest for civil engineering and soil mechanics, as well as of fundamental interest to come to a better understanding of partially saturated granular materials.

We thank L. HERMANN for making the AFM pictures, C. CHEVALLIER for help with the fluorescence pictures

and J. MEUNIER and X. CHATEAU for helpful discussions, and gratefully acknowledge funding from the EU Framework Programme 6 Marie Curie Research Training Networks scheme (under grant MRTN-CT-2004005728 (PATTERNS)). LPS de l'ENS is UMR 8558 of the CNRS, associated with the Universities Paris VI and VII.

REFERENCES

- [1] DE GENNES P. G., *Rev. Mod. Phys.*, **71** (1999) S374.
- [2] JAEGER H. M., NAGEL S. R. and BEHRINGER R. P., *Rev. Mod. Phys.*, **68** (1996) 1259.
- [3] NAGEL S. R., *Rev. Mod. Phys.*, **64** (1992) 321.
- [4] DURANT J., *Sands, Powders and Grains* (Springer-Verlag) 2000.
- [5] <http://www.sciencemag.org/sciext/125th/> (2005).
- [6] HORNBAKER D. J., ALBERT R., ALBERT I., BARABI A.-L. and SCHIFFER P., *Nature*, **387** (1997) 765.
- [7] SCHIFFER P., *Nat. Phys.*, **1** (2005) 21.
- [8] NOWAK S., SAMADANI A. and KUDROLI A., *Nat. Phys.*, **1** (2005) 50.
- [9] LAMBE T. W. and WHITMAN R. V., *Soil Mechanics* (John Wiley & Sons) 1969.
- [10] FOURNIER Z., GEROMICHALOS D., HERMINGHAUS S., KOHONEN M. M., MUGELE F., SCHEEL M., SCHULTZ M., SCHULTZ B., SCHIER C., SEEMANN R. and SKUDELNY A., *J. Phys.: Condens. Matter*, **17** (2005) S477.
- [11] DE GENNES P.-G., BROCHARD-WYART F. and QUÉRÉ D., *Capillarity and Wetting Phenomena* (Springer-Verlag) 2004.
- [12] MITARAI N. and NORI F., *Adv. Phys.*, **55** (2006) 1.
- [13] HERMINGHAUS S., *Adv. Phys.*, **54** (2005) 221.
- [14] HALSEY T. C. and LEVINE A. J., *Phys. Rev. Lett.*, **80** (1997) 3141.
- [15] TIMOSHENKO S., *Theory of Elastic Stability* (McGraw Hill) 1982.
- [16] <http://www.matweb.com/search/SearchSubcat.asp>.

Spontaneous generation of spiral waves by a hydrodynamic instability

M. HABIBI^{1,2}, P. C. F. MØLLER¹, N. M. RIBE³ and D. BONN^{1,4}

¹ Laboratoire de Physique Statistique, UMR 8550 CNRS, École Normale Supérieure - 24, rue Lhomond, 75231 Paris Cedex 05, France

² Institute for Advanced Studies in Basic Sciences (IASBS) - Zanjan 45195-1159, Iran

³ Institut de Physique du Globe de Paris and Université de Paris-7, CNRS, Tour 14 - 2, place Jussieu, 75005 Paris, France

⁴ Van der Waals-Zeeman Institute, University of Amsterdam - Valckenierstraat 65, 1018 XE Amsterdam, The Netherlands

received 25 April 2007; accepted in final form 4 December 2007

published online 3 January 2008

PACS 83.60.Wc – Flow instabilities

PACS 47.54.-r – Pattern selection; pattern formation

PACS 47.35.-i – Hydrodynamic waves

Abstract – The coiling of a thin filament of viscous fluid falling onto a surface is a common and easily reproducible hydrodynamic instability. Here we report for the first time that this instability can generate regular spiral patterns, in which air bubbles are trapped in the coil and then advected horizontally by the fluid spreading on the surface. We present a simple model that explains how these beautiful patterns are formed, and how the number of spiral branches and their curvature depends on the coiling frequency, the frequency of rotation of the coiling center, the total flow rate, and the thickness of the spreading fluid film.

Copyright © EPLA, 2008

The study of spirals in Nature goes back at least to the seventeenth century, when Swammerdam was among the first to describe the beautiful forms of certain seashells [1]. The standard work on spontaneous pattern formation in Nature, D'Arcy Thompson's *On Growth and Form* [1] describes a multitude of spiral patterns, including those of shells, sunflower seeds, and the helical structure of branches or leaves on growing plant stems. All these spirals are self-organized and obey rather strict mathematical rules. Shells, for example, are generally logarithmic spirals in which the distance between successive loops grows in a precisely determined way with increasing distance from the center [2]. In the case of sunflower seed spirals (phyllotaxis), Douady and Couder [3] used a clever laboratory experiment to show that the spirals form due to a self-organized growth process whereby new seeds are generated in the center at a fixed frequency and then repel each other by steric repulsion. The maximization of the distance between the seeds then leads to a special subtype of the logarithmic spiral pattern: the golden or Fibonacci spiral. The same authors showed how these ideas can be applied to plants, accounting for instance for the sunflower spirals [4].

Not all natural spirals are due to a steric repulsion between constitutive elements, however. Over the past few years, self-organized spiral waves have been studied extensively [5]. These dynamic spirals form spontaneously in excitable media [6,7] and have been observed in contexts as different as catalytic surface oxidation [8], the Belousov-Zhabotinsky chemical reaction [9–13], aggregating colonies of slime mold [14,15] and contracting heart tissue, where such waves are believed to be related to cardiac arrhythmia and fibrillation [16].

Here we demonstrate that spirals can also arise during the coiling of a thin “rope” of viscous fluid falling onto a solid surface (fig. 1) [17–19]. In previous papers we investigated how the frequency and radius of the coiling depends on the orifice diameter, the height of fall, the flow rate, and the fluid viscosity, and we showed that coiling traverses four different dynamical regimes as the fall height increases [20–24]. Here we report that in a limited portion of the parameter space, air bubbles become trapped between successive coils and are then advected radially away to form surprising and very regular spiral patterns. We also present a simple model that explains how these beautiful patterns are formed, and

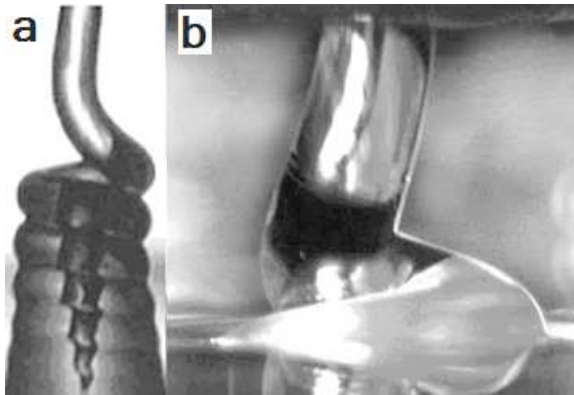


Fig. 1: Liquid rope coiling. Depending on the fluid viscosity, the coils can either build up a tall pile like a corkscrew (a), or vanish into the bulk of the fluid within one coiling period (b). a) silicone oil with $\nu = 1000 \text{ cm}^2/\text{s}$, injected from an orifice of radius $a_0 = 0.034 \text{ cm}$ at a volumetric rate $Q = 0.0044 \text{ cm}^3/\text{s}$. Effective fall height $H = 0.5 \text{ cm}$. The diameter of the portion of the rope shown is 0.06 cm . b) Silicone oil with $\nu = 125 \text{ cm}^2/\text{s}$, falling from an orifice of radius $a_0 = 0.2 \text{ cm}$ at a flow rate $Q = 0.1 \text{ cm}^3/\text{s}$. The fall height is 1.5 cm . The diameter of the portion of the rope shown is 0.4 cm .

how the number of spiral branches and their curvature depends on the total flow rate, the fluid film thickness, and ratio of the coiling frequency to the frequency of precession of the coiling center. We find that the spiral waves occur only when the center of the coil precesses with a frequency that is distinct from that of the coiling itself, and we show that this condition is both necessary and sufficient for the appearance of Fermat spirals in this particular case. This is in contrast to the general case where for instance the standard type ($n = 1$) of Archimedean spiral wave patterns forming in excitable media can exist with a single frequency, which is the primary rotation frequency of the spiral, or alternatively form non-static spirals with two frequencies resulting in a well-studied meandering instability that causes the spiral wave tip to trace out epicycloid trajectories (see for example [5]). The second frequency associated with the meandering instability is generally incommensurate with the primary rotation frequency, which can be formally eliminated by transformation to a co-rotating frame in which the stable rigidly rotating spirals appears stationary. In our experiments the two frequencies are also generally incommensurate, but the second frequency plays a quite different role than in the meandering spirals.

We performed our experiments by ejecting a thin jet of silicone oil from a syringe, driven by a syringe pump with a computer-controlled stepper motor. In a typical experiment, the fluid was ejected continuously at a constant rate Q while the fall height H was varied over a range of discrete values. Silicone oils of viscosities $\nu = 100, 300, 1000$, and $5000 \text{ cm}^2 \text{ s}^{-1}$ were used, but we observed spiral patterns only for $\nu = 300 \text{ cm}^2 \text{ s}^{-1}$. We also used different orifice diameters ($d = 0.68, 1.5, 1.6,$



Fig. 2: Inside a quite narrow region of the control parameter space, the coiling rope traps bubbles of air which form nice spiral patterns. Notice how the subsequent coils are displaced with respect to each other. The diameter of the pile is about 1 cm .

and 2.5 mm). While we saw some irregular patterns for $d = 0.68 \text{ mm}$ with $Q = 0.02 \text{ cm}^3 \text{ s}^{-1}$ and $H = 30 \text{ mm}$, clear spiral patterns were observed only for $d = 1.5$ and 1.6 mm , $Q = 0.047\text{--}0.137 \text{ cm}^3 \text{ s}^{-1}$, and $H = 32\text{--}50 \text{ mm}$.

Figure 1 shows two pictures of steady “liquid rope coiling”. Depending on the fall height and the fluid viscosity, the pile of coils can have different shapes. For low fall heights and high viscosities (“viscous” regime), the pile remains intact for several coiling periods, becomes quite high, and has a shape like a corkscrew (fig. 1a). For somewhat greater heights and/or lower viscosities (called the “gravitational regime”), the pile disappears within one or two coiling periods, and remains low (fig. 1b). No bubbles are generated in either of these cases.

At still larger fall heights (called the “inertial regime”), fluid inertia becomes important. Because the coiling period is much shorter than the time required for an individual coil to coalesce completely with its predecessor, the coiling filament forms a tall liquid tube that builds up, buckles under its own weight at a critical height, and starts rebuilding again with a characteristic period [23]. In this regime we observed bubbles of two different sizes: bubbles smaller than the filament radius that form with a period comparable to that of the coiling; and larger bubbles with sizes comparable to that of the liquid tube that form during the secondary buckling. However, the patterns formed by both types of bubbles are very irregular.

Within a quite narrow portion of the gravitational coiling regime, however, encapsulated air bubbles are observed to form very regular and beautiful spiral patterns (fig. 2). The origin of this behavior is as follows. In all other coiling regimes, each newly formed coil falls exactly on top of the one laid down previously. In this small part of the gravitational regime, by contrast, the center of coiling precesses along a separate circle of its own, with a frequency much smaller ($\approx 25\%$) than that of the coiling itself. As a result, successive coils do not land exactly on top of one another; and it is at the intersections of two such coils that small air bubbles are formed and trapped



Fig. 3: The process of air trapping and bubble formation. Reflection and refraction on the curved surface of the coils makes it difficult to study the details of bubble formation, but one can still follow the dynamics as seen in this series of pictures showing one cycle of bubble formation in two branches —one just above the center of the picture, and one in the upper right corner.

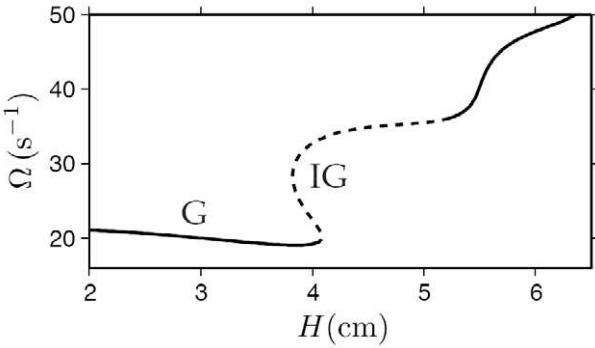


Fig. 4: Angular coiling frequency Ω vs. fall height H for an experiment with $\nu = 300 \text{ cm}^2 \text{ s}^{-1}$, $d = 1.6 \text{ mm}$, and $Q = 0.137 \text{ cm}^3 \text{ s}^{-1}$, predicted numerically using the method of [20]. The symbols G and IG indicate portions of the curve corresponding to gravitational and inertio-gravitational (multivalued) coiling, respectively. The dashed portion of the curve indicates steady coiling states that are unstable to small perturbations, as determined using the method of [24]. Clear spiral patterns were observed in the height range $H = 3\text{--}4 \text{ cm}$, before the turning point in the numerical curve that marks the onset of IG coiling [22]. The experimentally measured angular frequencies of coiling and precision were $17 \pm 1 \text{ s}^{-1}$ and $4 \pm 1 \text{ s}^{-1}$, respectively.

in the liquid due to its high viscosity. The spiral patterns are then generated as the bubbles are advected radially away from the pile of coils by the flow associated with the pile's gravitational collapse (fig. 3).

In our experiments, the behavior of the bubbles showed a clear progression as the fall height was increased. At relatively low heights corresponding to the lower-frequency part of the gravitational regime [20–23], the center of coiling precessed and some irregular bubbles were formed. At somewhat greater heights, the bubble pattern became more regular and some rather unclear spiral patterns were observed. At still greater heights, the patterns become clear spirals. Finally, at heights corresponding to the upper end of the gravitational regime the patterns once more became unclear and finally disappeared. The correspondence between spiral patterns and the gravitational regime is illustrated in fig. 4, which shows a numerical prediction of the steady coiling frequency vs. height for the parameters of one of our laboratory experiments [20]. The

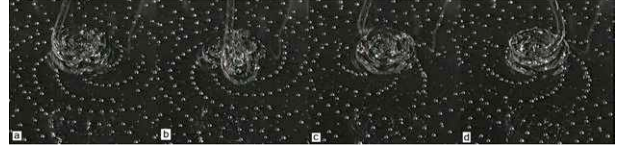


Fig. 5: Time sequence showing how a spontaneous change of coiling direction changes the sign of the curvature of the spiral pattern, for an experiment with $\nu = 300 \text{ cm}^2 \text{ s}^{-1}$, $d = 1.6 \text{ mm}$, $Q = 0.137 \text{ cm}^3 \text{ s}^{-1}$, and $H = 4 \text{ cm}$. (a) $t = 0$: coiling with spirals curving clockwise towards the center; (b) $t = 2 \text{ s}$: in the middle of changing direction, with an “extra” coil outside the pile; (c) $t = 6 \text{ s}$: counterclockwise coiling with a disturbed spiral pattern near the pile; (d) $t = 7 \text{ s}$: completed change of direction: counterclockwise coiling and curvature of the spiral pattern.

portions of the curve corresponding to the gravitational regime and the multivalued “inertio-gravitational” regime are labelled (G) and (IG), respectively [22]. In the experiment in question, we observed clear spiral patterns in the height range $H = 3\text{--}4 \text{ cm}$, which evidently corresponds to the gravitational regime just below the first turning point in the curve in fig. 4. This conclusion is further confirmed by our observation that the coiling frequency in the spiraling regime was nearly constant, as predicted by the numerics for $H = 3\text{--}4 \text{ cm}$ (fig. 4). However, we emphasize that the numerical calculation leading to fig. 4 is for *steady* coiling only, without precession. The precession is due to the interaction of the free portion of the liquid rope with the pile of coils beneath it. At present this interaction is not accounted for in the boundary conditions used in the numerical calculation of the steady coiling frequency. Accordingly, fig. 4 should not be interpreted as a bifurcation diagram for (unsteady) coiling with precession. Rather, its purpose is simply to help “locate” the phenomenon of spiral waves within the now well-understood regime diagram of steady coiling.

In all cases where clear spirals are observed, the spirals have five branches, and five bubbles are generated in approximately four coiling periods. The bubble size increases with increasing flow rate and also depends on the fall height, and is larger for clear spiral patterns than for unclear ones. The curvature of the spiral branches depends on the flow rate, the fall height, and the direction of coiling. If the coiling direction is reversed after an external perturbation of the filament, the curvature of the branches changes sign (fig. 5). Changing the height leads to a change in the coiling frequency and also changes the curvature of the branches (fig. 6). While the branches are strongly curved in most of the relevant parameter region they can be nearly straight (fig. 6(c)). The curvature of the pattern also depends on the radial flow away from the pile along the surface. Thus if we modify the experiment by using a plane with boundaries at some distance from the pile, the radial flow is slower and the branches closer together.

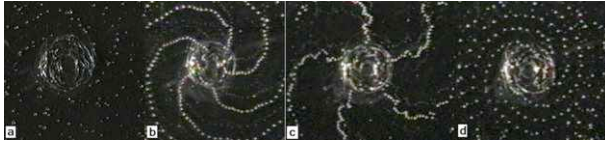


Fig. 6: Effect of fall height on the shape of the spiral branches, for an experiment with $\nu = 300 \text{ cm}^2 \text{ s}^{-1}$, $d = 1.6 \text{ mm}$, and $Q = 0.137 \text{ cm}^3 \text{ s}^{-1}$. (a) $H = 3 \text{ cm}$; (b) $H = 3.5 \text{ cm}$; (c) $H = 3.7 \text{ cm}$; (d) $H = 4 \text{ cm}$. In all photographs, the coiling is in the same direction and the number of spiral branches is 5. Photos were taken from below; reflection of light from the glass substrate is the cause of the extra “ghost” branches.

On the basis of our experimental observations we now propose a simple model for the formation of the spirals. We have seen that the slow precession of the coiling center causes successive coils to be slightly displaced from each other, leading to the trapping of air bubbles which are subsequently transported radially with the stagnation flow. Assumptions of volume conservation and constant height of the fluid film implies that the radial position of a bubble obeys $\frac{dr}{dt} \sim 1/r$ or $r \sim t^{0.5}$. Since the bubble generator moves with constant angular speed, this gives $r = \pm a\theta^{0.5}$, where r is the radius, a some constant, and θ the angle. Spirals obeying this type of equation are called Fermat’s spirals. To model this we assume that the coiling center moves with frequency f_p on a circle with radius r_p . If the radius and frequency of the coiling about this center are r_c and f_c , respectively, then the path laid down by the coiling filament is

$$x(t) = r_p \cos(2\pi f_p t) + r_c \cos(2\pi f_c t), \quad (1a)$$

$$y(t) = r_p \sin(2\pi f_p t) - r_c \sin(2\pi f_c t). \quad (1b)$$

We observe experimentally that the coiling and precession are always in opposite directions and since we want to keep f_c and f_p positive we include the minus sign in (1b). An example of the trajectory given by eq. (1) is shown in fig. 7.

Our experiments show that $f_c/f_p \approx r_c/r_p \approx 4$. Now if $f_c/f_p = 4$ exactly, the path defined by eq. (1) will repeat itself after one precession period and the “spirals” will be straight lines pointing outwards from the origin. If however f_c/f_p differs slightly from 4, the path will shift slightly with each precession period and a curved spiral pattern will emerge (fig. 8). As already mentioned, our numerical code does not include the interaction between the coiling rope and the pile so we do not yet understand what causes this precession. We are currently attempting to correctly include this interaction and understand how the precession frequency varies with the experimental parameters and why $f_c/f_p \approx r_c/r_p \approx 4$ for all experiments we performed. This is however far beyond the scope of the present paper. We did observe, however, that the spiral patterns change smoothly with system parameters, indicating that frequency locking does not occur. Our

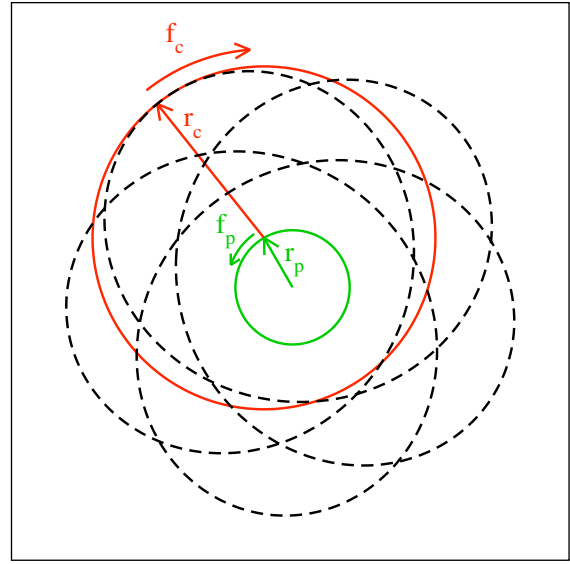


Fig. 7: Rope coiling around a center which moves on a circle of its own. r_c and f_c are the radius and frequency of coiling, while r_p and f_p are the radius and frequency of precession of the coiling center. The direction of precession is opposite to that of the coiling. A figure very similar to this one has been used to explain the meandering of spirals [5,12]. Here $r_c/r_p = 3$ and $f_c/f_p = 4$.

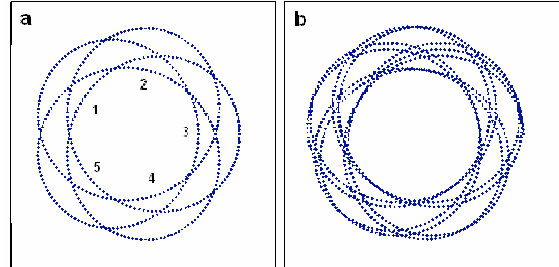


Fig. 8: A model of the path laid down by the coil for the experimentally measured values of $r_c/r_p \approx 4$ and $f_c/f_p \approx 4$. (a) When $f_c/f_p = 4$, the path exactly repeats itself, giving rise to straight radial branches (fig. 9a.) Bubbles are generated at positions 1, 2, 3, 4, and 5. (b) When $f_c/f_p = 3.9$ the path is slightly displaced after each precession period, giving rise to curved spiral branches (fig. 9b.)

experimental observations indicate that during coiling bubbles are trapped at points 1 through 5 in fig. 8, so that five bubbles will be generated for each four coils. Geometrically speaking, a bubble is formed each time the vector $\mathbf{r}_p = r_p(\hat{x} \cos 2\pi f_p t - \hat{y} \sin 2\pi f_p t)$ from the rotation center to the coiling center is antiparallel to the vector $\mathbf{r}_c = r_c(\hat{x} \cos 2\pi f_c t + \hat{y} \sin 2\pi f_c t)$ from the coiling center to the filament laid down (see fig. 7). The frequency of bubble formation is therefore just that of the dot product

$$\mathbf{r}_c \cdot \mathbf{r}_p = r_c r_p \cos 2\pi(f_c + f_p)t, \quad (2)$$

or $f_c + f_p$. The number of bubbles generated per coil is therefore $(f_c + f_p)/f_c$. For the measured value

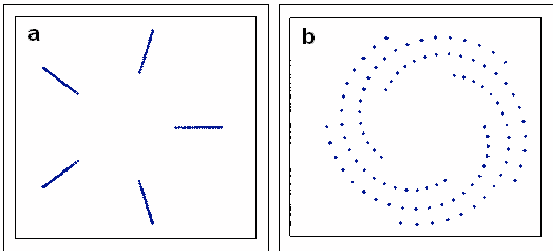


Fig. 9: Patterns of bubbles generated at positions 1, 2, 3, 4, and 5 in fig. 8. a) If $f_c/f_p = 4$ exactly the loop is closed and the bubble branches are radial. b) If f_c/f_p is only approximately 4 (here 3.9) the loop is open and the bubble branches will be curved.

$f_c/f_p \approx 4$, this gives $(f_c + f_p)/f_c \approx 5/4$, as observed in our experiments. From the frequency of bubble generation one can also predict the number of spiral branches to be $n(f_c + f_p)/f_p$, where n is the smallest natural number that makes $n(f_c + f_p)/f_p$ approximately a natural number. The factor n is present because if, e.g., $f_c/f_p = 4.33$, then $(f_c + f_p)/f_p = 5.33$ and it will take three rotations of the coiling center to add a bubble to all branches and start adding to the first one again, yielding a total of 16 branches. The reason that $n(f_c + f_p)/f_p$ need not be exactly a natural number is that if it is sufficiently close, say 4.98, the bubbles will not be seen as defining 50 distinct branches but rather 5 branches that are slightly curved (see fig. 9).

To test our model against the experiments, we did a simple numerical simulation assuming that the precession frequency f_p and the coiling frequency f_c are constants and that the bubbles generated move radially with a speed $v = Q/(2\pi rh)$, where r is the radial position and h the height of the fluid film. Figure 10 shows a “fit” of this simple model to the observations for an experiment with $Q = 0.047 \text{ cm}^3 \text{ s}^{-1}$, $h = 4 \text{ mm}$, $f_c = 2.7 \text{ Hz}$, and $f_p = 0.7 \text{ Hz}$. Because h was measured less accurately than the other parameters, we adjusted its value to obtain the best fit between the experiments and the model. The excellent agreement shown in fig. 10 is obtained for $h = 3.6 \text{ mm}$, very close to the measured value. We attribute the slight difference between the two values to the approximation $v = Q/(2\pi rh)$. Since the bubbles are near the top of the fluid, they will move slightly faster than the average speed assumed here. The average bubble speed assumed in the model must therefore be slightly higher than it is in reality, which requires that the assumed film thickness be slightly lower than the true value, as we found above. This simple model thus yields not only a qualitative picture, but also a quantitatively detailed understanding of the formation of the spiral bubble patterns.

In conclusion, we have shown that surprising and neatly ordered spiral bubble patterns can be formed during liquid rope coiling. In the context of liquid rope coiling, and in contrast to the general case, two frequencies are required

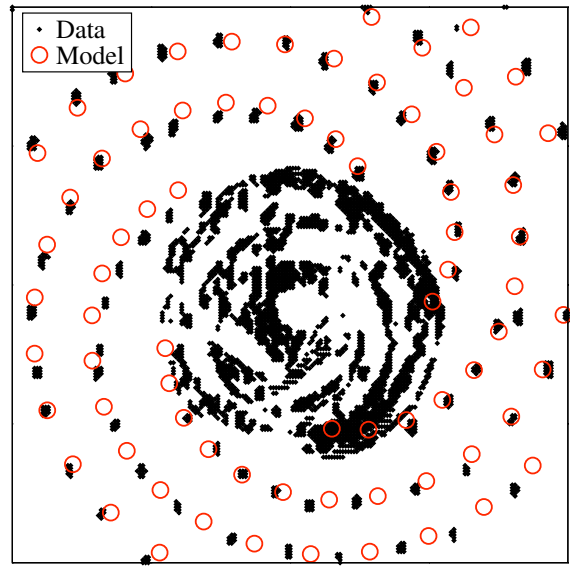


Fig. 10: A fit of the theoretical model for the bubble patterns to the observed pattern, for an experiment with $Q = 0.047 \text{ cm}^3 \text{ s}^{-1}$, $h = 4 \text{ mm}$, $f_c = 2.7 \text{ Hz}$, and $f_p = 0.7 \text{ Hz}$. The model predictions shown are those for the same values of Q , f_c and f_p but $h = 3.6 \text{ mm}$.

for spiral formation, namely the frequencies of the coiling itself and that of the (retrograde) precession of the coiling center. We present a very simple model that explains how the spiral patterns are formed and why two frequencies are needed in this particular case. The specific spiral we observed is a particular type of an Archimedean spiral ($r = a\theta^{1/n}$), namely Fermat’s spiral $r = a\theta^{1/2}$, which arises because the radial and angular positions of the bubbles obey $r \sim t^{1/2}$ and $\theta \sim t$.

REFERENCES

- [1] THOMPSON D’ARCY, *On Growth and Form* (Cambridge University Press) 1917.
- [2] DO CARMO M. P., *Differential Geometry of Curves and Surfaces* (Prentice-Hall) 1976.
- [3] DOUADY S. and COUDER Y., *Phys. Rev. Lett.*, **68** (1992) 2098.
- [4] DOUADY S. and COUDER Y., *J. Theor. Biol.*, **178** (1996) 255.
- [5] HAKIM and KARMA, *Phys. Rev. E*, **60** (1999) 5073.
- [6] WINFREE A. T., *When Time Breaks Down* (Princeton University Press) 1987.
- [7] ZYKOV V. S., *Modelling of Wave Processes in Excitable Media* (Manchester University Press) 1988.
- [8] JAKUBITH S., ROTERMUND H. H., ENGEL W., VON OERTZEN A. and ERTL G., *Phys. Rev. Lett.*, **65** (1990) 3013.
- [9] WINFREE A. T., *Science*, **181** (1973) 937.
- [10] JAHINKE W., SKAGGS W. E. and WINFREE A. T., *J. Phys. Chem.*, **93** (1989) 740.
- [11] PLESSER T. et al., *J. Phys. Chem.*, **94** (1990) 7501.

- [12] SKINNER G. S. and SWINNEY H. L., *Physica D*, **48** (1991) 1.
- [13] BELMONTE A., OUYANG Q. and FLESSELLES J. M., *J. Phys. II*, **7** (1997) 1425.
- [14] LOOMIS W. F., *Dictyostelium Discoideum, A Developmental System* (Academic Press, New York) 1975.
- [15] SIEGERT F. and WEIJER J., *Physica D*, **49** (1991) 224.
- [16] The several review articles in the focus issue of *Chaos*, **8** (1998) 1.
- [17] MAHADEVAN L., RYU W. S. and SAMUEL A. D. T., *Nature*, **392** (1998) 140.
- [18] MAHADEVAN L., RYU W. S. and SAMUEL A. D. T., *Nature*, **403** (2000) 502.
- [19] TAYLOR G. I., *Proceedings of the 12th International Congress of Applied Mechanics* (Springer, Berlin) 1968.
- [20] RIBE N. M., *Proc. R. Soc. London, Ser. A*, **460** (2004) 3223.
- [21] MALEKI M., HABIBI M., GOLESTANIAN R., RIBE N. M. and BONN D., *Phys. Rev. Lett.*, **93** (2004) 214502.
- [22] RIBE N. M., HUPPERT H. E., HALLWORTH M., HABIBI M. and BONN D., *J. Fluid. Mech.*, **555** (2006) 275.
- [23] HABIBI M., MALEKI M., GOLESTANIAN R., RIBE N. and BONN D., *Phys. Rev. E*, **74** (2006) 066306.
- [24] RIBE N. M., HABIBI M. and BONN D., *Phys. Fluids*, **18** (2006) 084102.

Shear banding and yield stress in soft glassy materials

P. C. F. Møller,¹ S. Rodts,² M. A. J. Michels,³ and Daniel Bonn^{1,4}

¹Laboratoire de Physique Statistique, École Normale Supérieure, Paris, F-75231 France

²Navier Institute, University of Eastern Paris, Paris, F-77420 France

³Group Polymer Physics, Eindhoven University of Technology, Eindhoven, The Netherlands

⁴The van der Waals-Zeeman Institute, 1018 XE Amsterdam, The Netherlands

(Received 10 July 2007; published 23 April 2008)

Shear localization is a generic feature of flows in yield stress fluids and soft glassy materials but is incompletely understood. In the classical picture of yield stress fluids, shear banding happens because of a stress heterogeneity. Using recent developments in magnetic resonance imaging velocimetry, we show here for a colloidal gel that even in a homogeneous stress situation shear banding occurs, and that the width of the flowing band is uniquely determined by the macroscopically imposed shear rate rather than the stress. We present a simple physical model for flow of the gel showing that shear banding (localization) is a flow instability that is intrinsic to the material, and confirm the model predictions for our system using rheology and light scattering.

DOI: 10.1103/PhysRevE.77.041507

PACS number(s): 83.50.-v, 83.60.Wc, 83.60.La, 83.60.Pq

If one stirs mayonnaise, sugar, or whipped cream with a spoon, it is easily observed that only a small fraction of the material closest to the spoon will be set in motion, the rest remaining “solid.” This is a generic feature not only of traditional yield stress fluids such as mayonnaise [1] but also of glassy materials; recent simulations have shown for instance that the archetypical Lennard-Jones glass also shows localization of shear or “shear banding” [2].

Recently the analogy between yield stress and glassy materials has received much attention [1–4], and it has been realized not only that glasses have some features of yield stress materials but that the inverse is also true; for instance, *aging* and *shear rejuvenation* [5] are concepts that come from glasses, but their importance for determining the mechanical properties of yield stress fluids is by now well established [3–7]. Because this powerful analogy allowed improvement in our understanding of the mechanical properties of both glassy and yield stress materials, they are now called “soft glassy materials.” The flow behavior of such soft glassy materials has been studied extensively: both colloidal [4,5,8–10] and polymer gels [11], emulsions [12], granular materials [13], colloidal glasses [4,14], pastes [15], and two-dimensional (2D) bubble rafts [16,17].

The most striking and general feature common to all of these systems is the observation of shear banding where the globally imposed shear rate is not distributed homogeneously, but localizes in highly sheared bands, while the remaining part of the fluid is not sheared at all [1,12,15]. In the classical picture of yield stress fluids, the material does not move if it is subjected to a stress smaller than the yield stress, and flows with a finite viscosity for a larger stress. In this case, shear banding is easy to understand as the consequence of a stress heterogeneity: the stress is above the yield stress where the material flows, and below it in the rest of the fluid [18]. However, it has been realized recently that in reality the generic flow curves of soft glassy materials differ from the simple yield stress fluid picture, and that notably very different results are obtained under an imposed shear rate and imposed stress [1,7,15]. This challenges also the “yield stress” view of shear banding.

In this paper we demonstrate that even in a homogeneous stress situation shear banding occurs, and that the width of the flowing band can be directly related to the macroscopically imposed shear rate. We present a simple physical model for a gel under shear flow that suggests that shear banding is a mechanical flow instability that is intrinsic to the material and is caused by an underlying flow curve with a negative slope. We confirm the negative slope by rheometry and the other predictions of the model by magnetic resonance imaging (MRI) velocimetry, rheology and light scattering.

The fluid used for the experiments is a gel formed from an aqueous suspension of charged colloidal particles (Ludox TM-40, Aldrich) in water. If a sufficient amount of salt (NaCl) is added to the solution, the Debye length, which gives the range of the electrostatic repulsions, decreases sufficiently for the van der Waals attraction between spheres to make them stick together. This leads to the formation of fractal, system-spanning networks of particles—a hard physical gel is formed [19]. The fluid is prepared by mixing a stock suspension of Ludox spheres with a 0.1 mass fraction salt water (NaCl) solution in the mass ratio 6:13 (giving a colloid volume fraction of 0.07), after which the fluid is left to age for at least 12 h. After this preparation the fluid gives reproducible results over periods of more than a week. More importantly, at an imposed shear rate the fluid reaches a steady state within minutes that is subsequently stable for hours [20]. Effectively this means that shearing the fluid for a few minutes “erases” the shear history of it prior to that shear, which is very important for practical experiments.

To examine if indeed shear banding can occur even when the stress is homogeneous, the fluid was loaded in a 4° cone-plate geometry with a 6 cm radius in a magnetic resonance imaging facility. Full description of the MRI setup can be found in [21]. For the purpose of our study, special MRI methods, developed to improve measurements of the velocity field inside Couette cells, were modified to suit a cone-plate geometry. As compared to standard MRI methodology [22], it allowed an increase in the usual signal to noise ratio of the experiment by up to two orders of magnitude, and made it possible to get complete 2D maps of the velocity

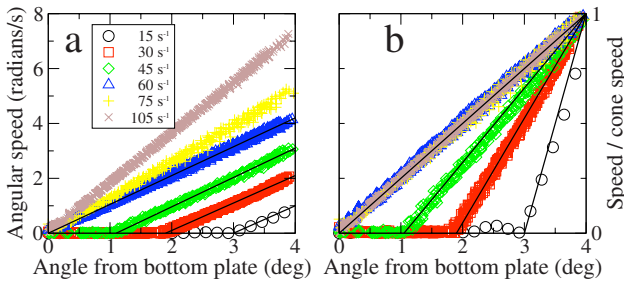


FIG. 1. (Color online) Velocity profiles in a 4° cone-plate geometry for different globally imposed shear rates. Fluid velocity (a) in rad/s and (b) normalized by the cone velocity.

field through an axial plane of the cell with a 0.125 mm axial and 1.2 mm radial space resolution, and with $\pm 40 \mu\text{m}/\text{s}$ typical standard deviation on velocity values. For each MRI measurement, a new sample is loaded into the cell and presheared at 150 s^{-1} for 5 min to have a controlled shear history of the sample. Subsequently, the globally imposed shear rate is lowered to the one chosen for the experiment and the sample is allowed 5 min to reach a steady state before the MRI measurement is begun. Results for several imposed shear rates are shown in Fig. 1. At 60 s^{-1} and above, no shear banding is observed. Below 60 s^{-1} the shear rate is not homogeneous but zero in some parts and high in others, and while the fraction of the fluid that is sheared increases with $\dot{\gamma}_{\text{global}}$, $\dot{\gamma}_{\text{local}}$ in the flowing region is constant. Clearly, quite distinct shear banding occurs even in a homogeneous stress field. That the shear banding is uniquely determined by the macroscopically imposed shear rate is shown in Fig. 2(a), where the fraction of sheared material is given by a simple lever rule: In the sheared region $\dot{\gamma}_{\text{local}} = \dot{\gamma}_{\text{critical}}$, and the fraction sheared is given by $f = \dot{\gamma}_{\text{global}} / \dot{\gamma}_{\text{critical}}$ [7]. The critical shear rate can be extracted from Fig. 2(a) using both methods and they both give $\dot{\gamma}_{\text{critical}} = 60 \pm 1 \text{ s}^{-1}$. Another important observation is that the transition between the sheared and the unsheared regions is very abrupt and the shear rate in the sheared region is constant in space, which is incompatible with a simple yield stress fluid behavior.

For micellar systems somewhat similar shear banding is observed and well understood as a coexistence of two phases in steady state coexistence—with viscosities differing by one to two orders of magnitude [23,24]. Our system is distinctly

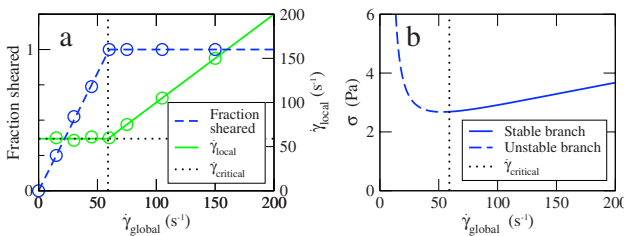


FIG. 2. (Color online) (a) The lever rule giving the fraction of the fluid that is sheared and the shear rate in that fraction depending on the critical shear rate. The data points are extracted from the fits in Fig. 1. (b) Steady state flow curve as given by the model. The branch to the right of the critical shear rate is stable while the branch to the left is unstable.

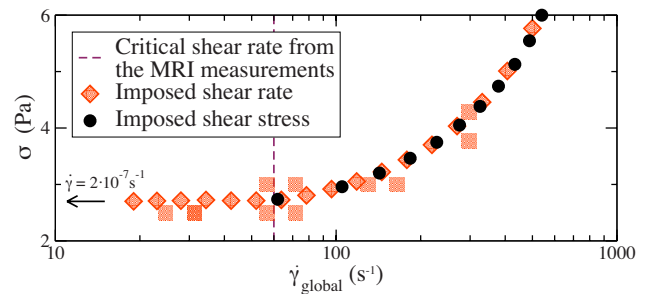


FIG. 3. (Color online) Steady state flow curves at imposed shear rate and shear stress. As predicted by the model the experiments coincide above the critical shear rate while they differ below—showing a stress plateau and no flow, respectively. For imposed shear rates below 20 s^{-1} , the recorded stress value is not stable but fluctuates, showing stick-slip behavior. This may be an indicator that the width of the sheared band becomes as small as the steady state cluster size in the band, leading to jamming. Note that here and elsewhere the microscopic model is applied only to the liquid phase, i.e., in steady state only above $\dot{\gamma}_c$ —also in the shear banding regime. The arrow to the left indicates that for a stress 1% lower than the critical stress the resulting shear rate is $2 \times 10^{-7} \text{ s}^{-1}$, which is solid to the resolution of our rheometer.

different in at least three aspects: (i) it is not in a steady state at low and zero shear rates where it is aging; (ii) it has a stress plateau between a low-viscosity branch and an infinite-viscosity branch, that is, it has a yield stress; and (iii) micellar systems are nonthixotropic in the sense that, given an imposed shear stress (except the plateau stress), they end up in the same final state independent of the initial state, but our system is very strongly thixotropic in the sense that a given imposed stress can result in completely different behavior depending on the initial state of the fluid. Point (i) is demonstrated in Fig. 5, point (ii) in Fig. 3, and point (iii) in Fig. 4. Hence the models for micellar fluids do not apply to our system, which needs a new theoretical understanding, to be provided below.

Although not exactly zero, the relative stress variation in a 4° cone-plate geometry is less than 0.005 and effectively negligible (as shown by the constant shear rate in the sheared band). In addition, results with an 8° cone-plate device (having a stress heterogeneity four times as large) yielded similar results, showing that the shear banding is not due to stress heterogeneities. To understand shear banding in a homogeneous stress field, we develop a simple model to take into account the interplay between viscosity, flow, and the colloidal microstructure in the fluid. To qualitatively capture the observed thixotropic behavior of the gel, we assume the following.

(i) In time the colloidal particles aggregate into fractal clusters that are nondraining [25]; $\phi = \phi(t)$ is then the “hydrodynamic” volume fraction determined by the aggregate radius $R(t)$, rather than the much smaller actual volume fraction ϕ_0 of particles with radius R_0 . The number of fractal aggregates decreases in inverse proportion to the aggregate mass $M \sim R^{d_f}$, while their hydrodynamic volume scales as R^3 , so $\phi(t)/\phi_0 = [R(t)/R_0]^{3-d_f}$. Since $d_f < 3$ it is clear that continued aggregation will lead with time to a percolating gel.

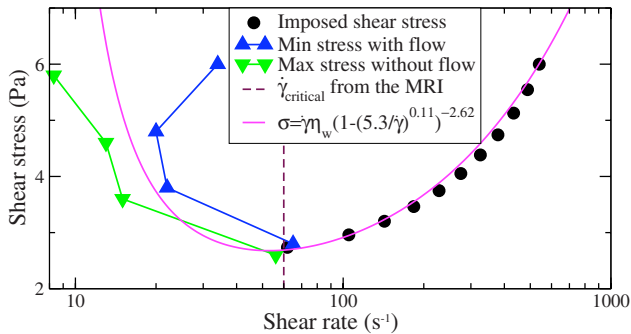


FIG. 4. (Color online) Full steady state flow curve found using two different types of measurements. The stable branch is simply found from imposing the shear stress, while the unstable branch can be pinned from the left and right by (for each of several material ages) finding initial σ - $\dot{\gamma}$ points that respectively slow down and speed up under imposed shear stress. From the lower right corner the aging time after preshear at 150 s^{-1} is 0, 10, 500, and 3000 s. The model is also seen to provide an excellent fit to the data. The fitted parameters $n(3-d_f)=0.11$ and $s=2.62$ are of the right order of magnitude; the value for $n(3-d_f)$ is slightly lower than expected, but not inconsistent with a fractal dimension well above that of, e.g., DLCA, due to compaction under shear.

(ii) The effective viscosity η depends on the hydrodynamic volume fraction ϕ of the dispersed particles via a Krieger-Dougherty [26], mean-field [27,28], or more general scaling-type expression $\eta/\eta_0=(1-\phi/\phi_p)^{-s}$, with η_0 the solvent viscosity and ϕ_p a gel-percolation point well below unity; the exponent s will be 2, $2.5\phi_p$ [26], 1 [27], or left as a fitting parameter, dependent on the chosen expression, but will anyway be of order unity.

(iii) The flow breaks up the aggregates. Via different mechanistic assumptions of aggregation and breakup, different models can be constructed for the rate of change dM/dt of the cluster mass. Depending on the stress or strain rate applied, a steady state $dM/dt=0$ may or may not be reached between spontaneous aggregation and flow-induced breakup, which relates R to $\dot{\gamma}$. Fairly independently of the specific model, e.g., diffusion-limited cluster aggregation (DLCA, $d_f=1.7-1.8$) [29] or shear-induced aggregation [30], size scaling in fracture, etc., one arrives at a relation of the form $R/R_0=(\dot{\gamma}/\dot{\gamma}_0)^{-n}$, with $\dot{\gamma}_0$ some typical high shear rate and n a model-dependent exponent smaller than unity; e.g., DLCA with breakup linearly proportional to the shear rate may be shown to give $n=1/d_f=0.55-0.60$, while for shear-induced aggregation a value $n=1/3$ has been derived, in good agreement with some experimental data [30]. Rheometric studies with a similar modeling approach also show that shear may lead to more compact aggregates, with an increase in d_f toward 2.4–2.5 [31].

Combination of (i), (ii), and (iii) gives an effective steady state shear stress that depends on shear rate:

$$\sigma_{ss}(\dot{\gamma}) = \dot{\gamma}\eta_0 \left[1 - \left(\frac{\dot{\gamma}_p}{\dot{\gamma}} \right)^{(3-d_f)n} \right]^{-s} \quad (1)$$

with $\dot{\gamma}_p$ corresponding to the percolation point ϕ_p also via

(i)–(iii): $\dot{\gamma}_p = \dot{\gamma}_0(\phi_0/\phi_p)^{1/(3-d_f)n}$. The resulting *steady state flow curve* σ_{ss} vs $\dot{\gamma}$ is shown in Fig. 2(b).

The most important feature of the model is that it gives rise to a critical shear rate $\dot{\gamma}_c = \dot{\gamma}_p[1+s(3-d_f)]^{1/(3-d_f)n}$ for which the slope of stress vs strain rate changes sign [3]. The negative slope for $\dot{\gamma} < \dot{\gamma}_c$ implies that such flows are unstable [32] which, as will follow, is the hallmark of shear banding.

Cohen and co-workers recently examined colloidal crystal subjected to oscillatory shear [14]. They observed that the colloids shear band into a hcp crystal and a state where crystal layers slide over each other. These two states can in fact be understood as limiting cases of ours; those of infinite and unit cluster sizes, respectively. This is consistent with the finding of Cohen and co-workers that their system shows a transition between two linearly responding phases—one solid and one liquid.

We will now test the detailed predictions of the model using standard rheology. The rheology was done also with a 4° cone-plate cell but now of 2 cm radius in a Rheologica Stresstech rheometer. The essence of the model is the competition between spontaneous buildup of the colloidal aggregates, increasing the viscosity, and breakdown by the flow, decreasing it. Thus, either the viscosity becomes infinite, or it decreases due to the flow to a steady state and rather low value. If the shear rate is imposed, this can lead to shear banding (the viscosity being infinite in one part and low in the other), but if the stress is imposed the whole material is either solid *or* fluid [7]. This is known as viscosity bifurcation [6]. The model then predicts that measurements at imposed shear stress and imposed shear rate should coincide when $\dot{\gamma}_{global}$ is above $\dot{\gamma}_c$ and differ below it; while the measurements at imposed stress should give an infinite viscosity, the steady state measurements at imposed shear rate should give rise to a stress plateau according to the lever rule. Using imposed shear rate and imposed stress experiments, excellent qualitative agreement with the model predictions and quantitative agreement with the critical shear rate found from the MRI measurements is obtained (Fig. 3).

To obtain the negative slope of the flow curve, we note that all points in Fig. 2(b) can be visited, if only temporarily. In general, a point above the steady state flow curve of Fig. 2(b) is a fluid subject to a stress that is too high for its cluster size to be stable, so it decreases in time and leads to a lower viscosity. Under an imposed shear stress the resulting shear rate increases in time and the flow point moves to the right. Conversely, if one starts out at a point below the steady state flow curve the point moves to the left. The flow curve (in particular the unstable part of it) can then be obtained by looking at the transition between points that move to the right and to the left, as is done in Fig. 4, where it is evident that indeed the flow curve has a negative slope below the critical shear rate. In addition to qualitative agreement between our model and data a quantitative fit of the full flow curve can be made using Eq. (1), which describes the data very well.

Perhaps the strongest prediction of the model is that, if shear banding is observed, the state of the fluid in the flowing part should be significantly different from that in the quiescent part. This contradicts the classical yield stress picture, which claims that shear banding is due to stress inho-

mogeneities and not to “age” inhomogeneities in an otherwise identical material under homogeneous stress. To test this prediction, we measured the structural relaxation time of the fluid in the solid and in the sheared band using diffusing wave spectroscopy (DWS); By measuring the time correlation of laser light diffusing through the fluid, one gains information about the motion of the individual scatterers in the fluid and hence its structural relaxation time and viscosity [33]. To do such a measurement we constructed a Couette cell (inner and outer radii of 75 and 95 mm) with a laser parallel to the rotation axis to perform DWS measurements of the fluid at different positions within the gap. For each gap position the flow was briefly stopped for the duration of the DWS measurement. The DWS measurements give a wealth of information that can be read off from Fig. 5 directly [4]: Longer correlation times correspond to longer structural relaxation times of the fluid and hence higher viscosities. For a material in a liquid, ergodic state the correlation function decays rapidly—as do the measurements in the sheared band. Correlation functions that do not decay to zero, such as those in the nonsheared band, demonstrate that the material is in a nonergodic out-of-equilibrium state that is aging—just like glasses. Very interestingly almost identical findings were reported in a numerical study of the classic Lennard-Jones glass [2]. The fact that aging effects are demonstrated to be crucial for understanding shear banding in both a simple numerical and an actual experimental system hints that the concept of a steady state flow curve with a negative slope may be key to understanding shear banding in many, if not all, aging systems.

In sum, all of our observations agree with the hypothesis that shear banding is not due to a stress heterogeneity, but is intrinsic to the fluid. Using MRI velocimetry we demonstrated that shear banding can occur even in homogeneous

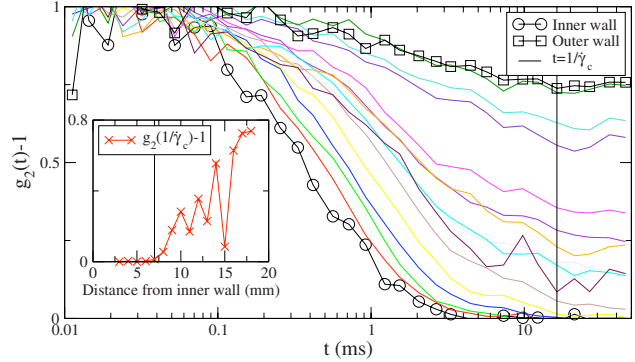


FIG. 5. (Color online) DWS time correlation measurements of the fluid inside and outside the sheared band in a Couette geometry. The inset shows the correlation function at $t=1/\dot{\gamma}_c$ (which is a characteristic relaxation time of the material) as function of the distance from the inner wall. The tendency for much longer correlation times in the solid phase as compared to the sheared phase is very clear, and similar to a simulation of a model glass that exhibits shear banding [2].

stress fields and that the width of the sheared band is simply given by a lever rule: knowing the critical shear rate (for instance from macroscopic rheology experiments), shear banding can be predicted. A simple physical model can account for shear banding as an intrinsic property of the fluid, from which the critical shear rate follows naturally. This is likely to be general for soft glassy materials; it relies on the viscosity bifurcation, which has been observed for a wide variety of systems: colloidal glasses and gels, granular matter, foams and emulsions, and polymer gels, all of which also exhibit shear banding.

-
- [1] P. Coussot, J. S. Raynaud, F. Bertrand, P. Moucheront, J. P. Guilbaud, H. T. Huynh, S. Jarny, and D. Lesueur, Phys. Rev. Lett. **88**, 218301 (2002).
 - [2] F. Varnik, L. Bocquet, J. L. Barrat, and L. Berthier, Phys. Rev. Lett. **90**, 095702 (2003).
 - [3] P. Coussot, Q. D. Nguyen, H. T. Huynh, and D. Bonn, Phys. Rev. Lett. **88**, 175501 (2002).
 - [4] D. Bonn, S. Tanase, B. Abou, H. Tanaka, and J. Meunier, Phys. Rev. Lett. **89**, 015701 (2002).
 - [5] F. Ianni, R. Di Leonardo, S. Gentilini, and G. Ruocco, Phys. Rev. E **75**, 011408 (2007).
 - [6] P. Coussot *et al.*, J. Rheol. **46**, 573 (2002).
 - [7] P. Møller *et al.*, Soft Matter **2**, 274 (2006).
 - [8] S. Manley *et al.*, Phys. Rev. Lett. **93**, 108302 (2004).
 - [9] L. Cipelletti, S. Manley, R. C. Ball, and D. A. Weitz, Phys. Rev. Lett. **84**, 2275 (2000).
 - [10] A. Dinsmore, V. Prasad, I. Y. Wong, and D. A. Weitz, Phys. Rev. Lett. **96**, 185502 (2006).
 - [11] F. K. Oppong, L. Rubatat, B. J. Friskin, A. E. Bailey, and J. P. de Bruyn, Phys. Rev. E **73**, 041405 (2006).
 - [12] L. Becu, S. Manneville, and A. Colin, Phys. Rev. Lett. **96**, 138302 (2006).
 - [13] F. da Cruz, S. Emam, M. Prochnow, J. N. Roux, and F. Cehoir, Phys. Rev. E **72**, 021309 (2005).
 - [14] I. Cohen, B. Davidovitch, A. B. Schofield, M. P. Brenner, and D. A. Weitz, Phys. Rev. Lett. **97**, 215502 (2006).
 - [15] N. Huang, G. Ovarlez, F. Bertrand, S. Rodts, P. Coussot, and D. Bonn, Phys. Rev. Lett. **94**, 028301 (2005).
 - [16] J. Lauridsen, G. Chanan, and M. Dennin, Phys. Rev. Lett. **93**, 018303 (2004).
 - [17] C. Gilbreth, S. Sullivan, and M. Dennin, Phys. Rev. E **74**, 051406 (2006).
 - [18] H. Zhu *et al.*, J. Non-Newtonian Fluid Mech. **129**, 177 (2005).
 - [19] R. G. Larson, *The Structure and Rheology of Complex Fluids* (Oxford University Press, Oxford, 1999).
 - [20] In order to achieve this it was found necessary to gently shear the fluid for 1 min just after mixing.
 - [21] J.-S. Raynaud *et al.*, J. Rheol. **46**, 709 (2002).
 - [22] S. Staph and S. L. Han, *NMR Imaging in Chemical Engineering* (Wiley-VCH, Weinheim, 2006).
 - [23] S. Manneville, A. Colin, G. Waton, and F. Schossele, Phys. Rev. E **75**, 061502 (2007).
 - [24] M. López-González, W. M. Holmes, P. T. Callaghan, and P. J. Photinos, Phys. Rev. Lett. **93**, 268302 (2004).

- [25] P. Wiltzius, Phys. Rev. Lett. **58**, 710 (1987).
- [26] I. M. Krieger, Adv. Colloid Interface Sci. **3**, 111 (1972).
- [27] N. Saito, J. Phys. Soc. Jpn. **5**, 4 (1950); **7**, 447 (1952).
- [28] D. Bedeaux, J. Colloid Interface Sci. **118**, 80 (1987).
- [29] D. A. Weitz, J. S. Huang, M. Y. Lin, and J. Sung, Phys. Rev. Lett. **53**, 1657 (1984).
- [30] R. Wessel and R. C. Ball, Phys. Rev. A **46**, R3008 (1992).
- [31] W. Wolthers *et al.*, J. Rheol. **40**, 799 (1996).
- [32] R. I. Tanner, *Engineering Rheology* (Clarendon, Oxford, 1985).
- [33] D. J. Pine, D. A. Weitz, P. M. Chaikin, and E. Herbolzheimer, Phys. Rev. Lett. **60**, 1134 (1988).

Appendix C

Bibliography

Bibliography

- [1] I Wagstaff and CE Chaffey. Shear thinning and thickening rheology .1. concentrated acrylic dispersions. *Journal of Colloid and Interface Science*, 59(1):53–62, 1977.
- [2] CE Chaffey and I Wagstaff. Shear thinning and thickening rheology .2. volume fraction and size dispersion of particles. *Journal of Colloid and Interface Science*, 59(1):63–75, 1977.
- [3] MM Cross. Relation between viscoelasticity and shear-thinning behaviour in liquids. *Rheol Acta*, 18(5):609–614, 1979.
- [4] ST Milner. Relating the shear-thinning curve to the molecular weight distribution in linear polymer melts. *J Rheol*, 40(2):303–315, 1996.
- [5] SM AlZahrani. A generalized rheological model for shear thinning fluids. *J Petrol Sci Eng*, 17(3-4):211–215, 1997.
- [6] L Bergstrom. Shear thinning and shear thickening of concentrated ceramic suspensions. *Colloid Surface A*, 133(1-2):151–155, 1998.
- [7] MC Newstein, H Wang, NP Balsara, AA Lefebvre, Y Shnidman, H Watanabe, K Osaki, T Shikata, H Niwa, and Y Morishima. Microstructural changes in a colloidal liquid in the shear thinning and shear thickening regimes. *J Chem Phys*, 111(10):4827–4838, 1999.
- [8] GP Roberts, HA Barnes, and P Carew. Modelling the flow behaviour of very shear-thinning liquids. *Chem Eng Sci*, 56(19):5617–5623, 2001.
- [9] MP Escudier, IW Gouldson, AS Pereira, FT Pinho, and RJ Poole. On the reproducibility of the rheology of shear-thinning liquids. *Journal of Non-Newtonian Fluid Mechanics*, 97(2-3):99–124, 2001.
- [10] S Forster, M Konrad, and P Lindner. Shear thinning and orientational ordering of wormlike micelles. *Phys Rev Lett*, 94(1):017803, 2005.
- [11] P. T Reardon, S Feng, A. L Graham, V Chawla, R. S Admuthe, and J Abbott. Shear-thinning of polydisperse suspensions. *J Phys D Appl Phys*, 41(11):115408, 2008.

- [12] WJ Frith, P dHaene, R Buscall, and J Mewis. Shear thickening in model suspensions of sterically stabilized particles. *J Rheol*, 40(4):531–548, 1996.
- [13] J Bender and NJ Wagner. Reversible shear thickening in monodisperse and bidisperse colloidal dispersions. *J Rheol*, 40(5):899–916, 1996.
- [14] SR Raghavan and SA Khan. Shear-thickening response of fumed silica suspensions under steady and oscillatory shear. *Journal of Colloid and Interface Science*, 185(1):57–67, 1997.
- [15] RL Hoffman. Explanations for the cause of shear thickening in concentrated colloidal suspensions. *J Rheol*, 42(1):111–123, 1998.
- [16] YT Hu, P Boltenhagen, E Mattheys, and DJ PINE. Shear thickening in low-concentration solutions of wormlike micelles. ii. slip, fracture, and stability of the shear-induced phase. *J Rheol*, 42(5):1209–1226, 1998.
- [17] YT Hu, P Boltenhagen, and DJ PINE. Shear thickening in low-concentration solutions of wormlike micelles. i. direct visualization of transient behavior and phase transitions. *J Rheol*, 42(5):1185–1208, 1998.
- [18] Abdoulaye Fall, N Huang, F Bertrand, G Ovarlez, and Daniel Bonn. Shear thickening of cornstarch suspensions as a reentrant jamming transition. *Phys Rev Lett*, 100(1):018301, 2008.
- [19] J Zebrowski, V Prasad, W Zhang, LM Walker, and DA Weitz. Shake-gels: shear-induced gelation of laponite-peo mixtures. *Colloid Surface A*, 213(2-3):189–197, 2003.
- [20] V Can and O Okay. Shake gels based on laponite-peo mixtures: effect of polymer molecular weight. *Des Monomers Polym*, 8(5):453–462, 2005.
- [21] J Mewis. Thixotropy - a general review. *Journal of Non-Newtonian Fluid Mechanics*, 6(1):1–20, 1979.
- [22] F Pignon, A Magnin, and JM Piau. Thixotropic colloidal suspensions and flow curves with minimum: Identification of flow regimes and rheometric consequences. *J Rheol*, 40(4):573–587, 1996.
- [23] HA Barnes. Thixotropy - a review. *Journal of Non-Newtonian Fluid Mechanics*, 70(1-2):1–33, 1997.
- [24] N Willenbacher. Unusual thixotropic properties of aqueous dispersions of laponite rd. *Journal of Colloid and Interface Science*, 182(2):501–510, 1996.
- [25] F Pignon, A Magnin, JM Piau, B CABANE, P Lindner, and O Diat. Yield stress thixotropic clay suspension: Investigation of structure by light, neutron, and x-ray scattering. *Phys Rev E*, 56(4):3281–3289, 1997.

- [26] F Pignon, A Magnin, and JM Piau. Butterfly light scattering pattern and rheology of a sheared thixotropic clay gel. *Phys Rev Lett*, 79(23):4689–4692, 1997.
- [27] F Pignon, A Magnin, and JM Piau. Thixotropic behavior of clay dispersions: Combinations of scattering and rheometric techniques. *J Rheol*, 42(6):1349–1373, 1998.
- [28] A Mujumdar, AN Beris, and AB Metzner. Transient phenomena in thixotropic systems. *Journal of Non-Newtonian Fluid Mechanics*, 102(2):157–178, 2002.
- [29] P Coussot, QD Nguyen, HT Huynh, and D Bonn. Viscosity bifurcation in thixotropic, yielding fluids. *J Rheol*, 46(3):573–589, 2002.
- [30] C Martin, F Pignon, JM Piau, A Magnin, P Lindner, and B CABANE. Dissociation of thixotropic clay gels. *Phys Rev E*, 66(2):021401, 2002.
- [31] PCF Moller, J Mewis, and D Bonn. Yield stress and thixotropy: on the difficulty of measuring yield stresses in practice. *Soft Matter*, 2(4):274–283, 2006.
- [32] A Ragouilliaux, G Ovarlez, N Shahidzadeh-Bonn, Benjamin Herzhaft, T Palermo, and P Coussot. Transition from a simple yield-stress fluid to a thixotropic material. *Phys Rev E*, 76(5):051408, 2007.
- [33] EC Bingham. *Fluidity and Plasticity*. McGraw-Hill, New York, 1922.
- [34] CW Macosko. *Rheology. Principles, measurements, and applications*. Wiley-VCH, 1994.
- [35] RG Larson. *The Structure and Rheology of Complex Fluids*. Oxford University Press, 1999.
- [36] WH Herschel and R Bulkley. Measurement of consistency as applied to rubber-benzene solutions. *Proc. Am. Assoc. Test Mater.*, 26, 1926.
- [37] J Piau. Carbopol gels: Elastoviscoplastic and slippery glasses made of individual swollen spongesmeso- and macroscopic properties, constitutive equations and scaling laws. *Journal of Non-Newtonian Fluid Mechanics*, 144(1):1–29, 2007.
- [38] NJ Balmforth, I Frigaard, and et al. Viscoplastic fluids: From theory to application. *Journal of Non-Newtonian Fluid Mechanics, special issue*, 142, 2007.
- [39] HA Barnes. The yield stress - a review or ' $\pi\alpha\nu\tau\alpha\rho\epsilon$ ' - everything flows? *Journal of Non-Newtonian Fluid Mechanics*, 81(1-2):133–178, 1999.
- [40] N Roussel, C Stefani, and R Leroy. From mini-cone test to abrams cone test: measurement of cement-based materials yield stress using slump tests. *Cement Concrete Res*, 35(5):817–822, 2005.

- [41] K Asaga and DM Roy. Rheological properties of cement mixes .4. effects of superplasticizers on viscosity and yield stress. *Cement Concrete Res*, 10(2):287–295, 1980.
- [42] H Tremblay, S Leroueil, and J Locat. Mechanical improvement and vertical yield stress prediction of clayey soils from eastern canada treated with lime or cement. *Can Geotech J*, 38(3):567–579, 2001.
- [43] AW Saak, HM Jennings, and SP Shah. The influence of wall slip on yield stress and viscoelastic measurements of cement paste. *Cement Concrete Res*, 31(2):205–212, 2001.
- [44] AE James, DJA Williams, and PR Williams. Direct measurement of static yield properties of cohesive suspensions. *Rheol Acta*, 26:437–446, 1987.
- [45] HA Barnes and QD Nguyen. Rotating vane rheometry - a review. *Journal of Non-Newtonian Fluid Mechanics*, 98(1):1–14, 2001.
- [46] QD Nguyen and DV Boger. Measuring the flow properties of yield stress fluids. *Annu Rev Fluid Mech*, 24:47–88, 1992.
- [47] P Coussot, QD Nguyen, HT Huynh, and D Bonn. Avalanche behavior in yield stress fluids. *Phys. Rev. Lett.*, 88(17):175501, 2002.
- [48] JC Baudez and P Coussot. Abrupt transition from viscoelastic solidlike to liquidlike behavior in jammed materials. *Phys. Rev. Lett.*, 93(12):128302, 2004.
- [49] J Stokes and J Telford. Measuring the yield behaviour of structured fluids. *Journal of Non-Newtonian Fluid Mechanics*, 124(1-3):137–146, 2004.
- [50] P. Coussot and C. Ancey. *Rheophysics of pastes and suspensions*. EDP Sciences, Paris, 1999.
- [51] P Coussot and S Boyer. Determination of yield stress fluid behaviour from inclined plane test. *Rheol Acta*, 34:534–543, 1995.
- [52] RR McDonald and RS Anderson. Constraints on eolian flow dynamics through laboratory experiments on sand slopes. *J. Sedimentary Res.*, 66:642, 1996.
- [53] F Varnik, L Bocquet, JL Barrat, and L Berthier. Shear localization in a model glass. *Phys. Rev. Lett.*, 90(9):095702, 2003.
- [54] PG de Gennes. *Scaling Concepts in Polymer Physics*. Cornell University Press, Ithaca, New York, 1979.
- [55] E. Leutheusser. Dynamical model of the liquid-glass transition. *Phys. Rev. A*, 29(5):2765–2773, 1984.

- [56] U Bengtzelius, W Gotze, and A Sjolander. Dynamics of supercooled liquids and the glass transition. *J. Phys. C.*, 17(33):5915–5934, 1984.
- [57] P Sollich, F Lequeux, P Hebraud, and ME Cates. Rheology of soft glassy materials. *Phys. Rev. Lett.*, 78(10):2020–2023, 1997.
- [58] P Sollich. Rheological constitutive equation for a model of soft glassy materials. *Phys. Rev. E*, 58(1):738–759, 1998.
- [59] PL Freddolino, AS Arkhipov, SB Larson, A McPherson, and K Schulten. Molecular dynamics simulations of the complete satellite tobacco mosaic virus. *Structure*, 14:437–449, 2006.
- [60] PG de Gennes. Reptation of a polymer chain in presence of fixed obstacles. *J Chem Phys*, 55:572, 1971.
- [61] GC Berry and TG Fox. The viscosity of polymers and their concentrated solutions. *Adv. Polym. Sci.*, 5:261, 1968.
- [62] P. G. de Gennes. Granular matter: a tentative view. *Rev. Mod. Phys.*, 71:S374–S382, 1999.
- [63] H. M. Jaeger, S. R. Nagel, and R. P. Behringer. Granular solids, liquids, and gases. *Rev. Mod. Phys.*, 68:1259–1273, 1996.
- [64] S. R. Nagel. Instabilities in a sandpile. *Rev. Mod. Phys.*, 64:321–325, 1992.
- [65] J. Durant. *Sands, Powders and Grains*. Springer-Verlag, 2000.
- [66] <http://www.sciencemag.org/sciext/125th/>, 2005.
- [67] Xiang Cheng, German Varas, Daniel Citron, Heinrich M Jaeger, and Sidney R Nagel. Collective behavior in a granular jet: Emergence of a liquid with zero surface tension. *Phys Rev Lett*, 99(18):188001, 2007.
- [68] O Pouliquen, C Cassar, P Jop, Y Forterre, and M Nicolas. Flow of dense granular material: towards simple constitutive laws. *J Stat Mech-Theory E*, page P07020, 2006.
- [69] C Cassar, M Nicolas, and O Pouliquen. Submarine granular flows down inclined planes. *Phys. Fluids*, 17(10):103301, 2005.
- [70] Y Amarouchene and H Kellay. Speed of sound from shock fronts in granular flows. *Phys. Fluids*, 18(3):031707, 2006.
- [71] P Jop, Y Forterre, and O Pouliquen. A constitutive law for dense granular flows. *Nature*, 441(7094):727–730, 2006.

- [72] Xiang Cheng, Lei Xu, Aaron Patterson, Heinrich M Jaeger, and Sidney R Nagel. Towards the zero-surface-tension limit in granular fingering instability. *Nat Phys*, 4(3):234–237, 2008.
- [73] J. F Boudet, Y Amarouchene, B Bonnier, and H Kellay. The granular jump. *J. Fluid Mech.*, 572:413–431, 2007.
- [74] X Cheng, JB Lechman, A Fernandez-Barbero, GS Grest, HM Jaeger, GS Karczmar, ME Mobius, and SR Nagel. Three-dimensional shear in granular flow. *Phys Rev Lett*, 96(3):038001, 2006.
- [75] D. J. Hornbaker, R. Albert, I. Albert, A-L. Barabasi, and P. Schiffer. What keeps sandcastles standing? *Nature*, 387:765–765, 1997.
- [76] P. Schiffer. Granular physics: A bridge to sandpile stability. *Nature Phys.*, 1:21–22, 2005.
- [77] S. Nowak, A. Samadani, and A. Kudrolli. Maximum angle of stability of a wet granular pile. *Nature Phys.*, 1:50–52, 2005.
- [78] T. W. Lambe and R. V. Whitman. *Soil Mechanics*. John Wiley & Sons, 1969.
- [79] Peter D Olmsted. Perspectives on shear banding in complex fluids. *Rheol Acta*, 47(3):283–300, 2008.
- [80] Suzanne M Fielding. Complex dynamics of shear banded flows. *Soft Matter*, 3(10):1262–1279, Jan 2007.
- [81] P. C. F Moller, S Rodts, M. A. J Michels, and Daniel Bonn. Shear banding and yield stress in soft glassy materials. *Phys Rev E*, 77(4):041507, 2008.
- [82] F Bautista, JFA Soltero, JH Perez-Lopez, JE Puig, and O Manero. On the shear banding flow of elongated micellar solutions. *Journal of Non-Newtonian Fluid Mechanics*, 94(1):57–66, 2000.
- [83] S. A Rogers, D Vlassopoulos, and P. T Callaghan. Aging, yielding, and shear banding in soft colloidal glasses. *Phys. Rev. Lett.*, 100(12):128304, 2008.
- [84] SM Fielding and PD Olmsted. Spatiotemporal oscillations and rheochaos in a simple model of shear banding. *Phys. Rev. Lett.*, 92(8):084502, 2004.
- [85] SM Fielding and PD Olmsted. Flow phase diagrams for concentration-coupled shear banding. *Eur Phys J E*, 11(1):65–83, 2003.
- [86] SM Fielding and PD Olmsted. Kinetics of the shear banding instability in startup flows. *Phys Rev E*, 68(3):036313, 2003.

- [87] Sébastien Manneville, Gilles Waton, and François Schossele. Wall slip, shear banding, and instability in the flow of a triblock copolymer micellar solution. *Phys. Rev. E*, 75(6):11, 2007.
- [88] DCH Cheng. Characterisation of thixotropy revisited. *Rheol Acta*, 42(4):372–382, 2003.
- [89] Sergio Caserta, Marino Simeone, and Stefano Guido. Shear banding in biphasic liquid-liquid systems. *Phys. Rev. Lett.*, 100(13):4, 2008.
- [90] TA Waigh. Microrheology of complex fluids. *Rep. Prog. Phys.*, 68(3):685–742, 2005.
- [91] S Jabbari-Farouji. *Aging and the Fluctuation-Dissipation Relation in Colloidal Glasses and Gels*. PhD thesis, University of Amsterdam, 2007.
- [92] BJ Berne and R Pecora. *Dynamic Light Scattering*. J Wiley & sons, Inc., 1975.
- [93] DJ Pine, DA Weitz, PM Chaikin, and E Herbolzheimer. Diffusing-wave spectroscopy. *Phys Rev Lett*, 60(12):1134–1137, 1988.
- [94] DJ Shlien. Inexpensive method of generation of a good quality laser-sheet for flow visualization. *Exp Fluids*, 5(5):356–358, 1987.
- [95] JJ Miau, EG Chiu, and JH Chou. Laser-sheet flow visualization of the confined wake behind a ring. *Fluid Dyn Res*, 9(5-6):255–265, 1992.
- [96] U Lackermeier, C Rudnick, J Werther, A Bredebusch, and H Burkhardt. Visualization of flow structures inside a circulating fluidized bed by means of laser sheet and image processing. *Powder Technol*, 114(1-3):71–83, 2001.
- [97] JP Prenel, R Porcar, and A Elrhassouli. Tomographic analysis of 3-dimensional flow using a static laser sheet in translation. *Opt Commun*, 65(2):101–106, 1988.
- [98] MH Chestnut. Confocal microscopy of colloids. *Curr Opin Colloid In*, 2(2):158–161, 1997.
- [99] NAM Verhaegh, D Asnaghi, and HNW Lekkerkerker. Transient gels in colloid-polymer mixtures studied with fluorescence confocal scanning laser microscopy. *Physica A*, 264(1-2):64–74, 1999.
- [100] AD Dinsmore, ER Weeks, V Prasad, AC Levitt, and DA Weitz. Three-dimensional confocal microscopy of colloids. *Appl Optics*, 40(24):4152–4159, 2001.
- [101] AI Campbell and P Bartlett. Fluorescent hard-sphere polymer colloids for confocal microscopy. *Journal of Colloid and Interface Science*, 256(2):325–330, 2002.
- [102] DGAL Aarts and HNW Lekkerkerker. Confocal scanning laser microscopy on fluid-fluid demixing colloid-polymer mixtures. *J Phys-Condens Mat*, 16(38):S4231–S4242, 2004.

- [103] J Cleaver and WCK Poon. Network formation in colloid-liquid crystal mixtures studied by confocal microscopy. *J Phys-Condens Mat*, 16(19):S1901–S1909, 2004.
- [104] V Prasad, D Semwogerere, and Eric R Weeks. Confocal microscopy of colloids. *J Phys-Condens Mat*, 19(11):113102, 2007.
- [105] AE Chiou, W Wang, GJ Sonek, J Hong, and MW Berns. Interferometric optical tweezers. *Opt Commun*, 133(1-6):7–10, 1997.
- [106] EJG Peterman, MA van Dijk, LC Kapitein, and CF Schmidt. Extending the bandwidth of optical-tweezers interferometry. *Rev Sci Instrum*, 74(7):3246–3249, 2003.
- [107] E Schonbrun, R Piestun, P Jordan, J Cooper, KD Wulff, J Courtial, and M Padgett. 3d interferometric optical tweezers using a single spatial light modulator. *Opt Express*, 13(10):3777–3786, 2005.
- [108] A Casaburi, G Pesce, P Zemanek, and A Sasso. Two- and three-beam interferometric optical tweezers. *Opt Commun*, 251(4-6):393–404, 2005.
- [109] C Nouar and IA Frigaard. Nonlinear stability of poiseuille flow of a bingham fluid: theoretical results and comparison with phenomenological criteria. *Journal of Non-Newtonian Fluid Mechanics*, 100(1-3):127–149, 2001.
- [110] TF Wang, JF Wang, F Ren, and Y Jin. Application of doppler ultrasound velocimetry in multiphase flow. *Chem Eng J*, 92(1-3):111–122, 2003.
- [111] C Nouar. Thermal convection for a thermo-dependent yield stress fluid in an axisymmetric horizontal duct. *Int J Heat Mass Tran*, 48(25-26):5520–5535, 2005.
- [112] G Delaplace, R. K Thakur, L Bouvier, C Lepretre, C Llnyzckyj, C Andre, and C Nouar. Influence of rheological behavior of purely viscous fluids on analytical residence time distribution in straight tubes. *Chem Eng Technol*, 31(2):231–236, 2008.
- [113] V Herle, S Manneville, and P Fischer. Ultrasound velocimetry in a shear-thickening wormlike micellar solution: Evidence for the coexistence of radial and vorticity shear bands. *Eur Phys J E*, 26(1-2):3–12, 2008.
- [114] Daniel Bonn, Stephane Rodts, Maarten Groenink, Salima Rafai, Noushine Shahidzadeh-Bonn, and Philippe Coussot. Some applications of magnetic resonance imaging in fluid mechanics: Complex flows and complex fluids. *Annu Rev Fluid Mech*, 40:209–233, 2008.
- [115] JC Baudez, S Rodts, X Chateau, and P Coussot. New technique for reconstructing instantaneous velocity profiles from viscometric tests: Application to pasty materials. *J Rheol*, 48(1):69–82, 2004.

- [116] S Jarny, N Roussel, S Rodts, F Bertrand, R Le Roy, and P Coussot. Rheological behavior of cement pastes from mri velocimetry. *Cement Concrete Res*, 35(10):1873–1881, 2005.
- [117] S Rodts, JC Baudez, and P Coussot. From "discrete" to "continuum" flow in foams. *Europhys Lett*, 69(4):636–642, 2005.
- [118] N Huang, G Ovarlez, F Bertrand, S Rodts, P Coussot, and D Bonn. Flow of wet granular materials. *Phys Rev Lett*, 94(2):028301, 2005.
- [119] S Rodts, F Bertrand, S Jarny, P Poullain, and P Moucheront. Recent developments in mri applications to rheology and fluid mechanics. *Cr Chim*, 7(3-4):275–282, 2004.
- [120] JS Raynaud, P Moucheront, JC Baudez, F Bertrand, JP Guilbaud, and P Coussot. Direct determination by nuclear magnetic resonance of the thixotropic and yielding behavior of suspensions. *J Rheol*, 46(3):709–732, 2002.
- [121] S Rodts, F Bertrand, S Jarny, P Poullain, and P Moucheront. Developpements recents dans l'application de l'irm a la rheologie et a la mecanique des fluides. *C.R. Chimie*, 7:275, 2004.
- [122] S Stapf and S Han. *NMR Imaging in Chemical Engineering*. Wiley-VCH, 2006.
- [123] P Coussot. *Rheometry of pastes, suspensions, and granular materials*. Wiley-Interscience, 2005.
- [124] HA Barnes and K Walters. The yield stress myth. *Rheol Acta*, 24(4):323–326, 1985.
- [125] AY Malkin. *Rheology Fundamentals*. ChemTec Publishing, 1994.
- [126] R Buscall, JI McGowan, and AJ Mortonjones. The rheology of concentrated dispersions of weakly attracting colloidal particles with and without wall slip. *J Rheol*, 37(4):621–641, 1993.
- [127] HA Barnes. A review of the slip (wall depletion) of polymer solutions, emulsions and particle suspensions in viscometers: its cause, character, and cure. *Journal of Non-Newtonian Fluid Mechanics*, 56(3):221–251, 1995.
- [128] ID Evans. On the nature of the yields stress. *J Rheol*, 36(7):1313–1316, 1992.
- [129] RD Spaans and MC Williams. At last, a true liquid-phase yield stress. *J Rheol*, 39(1):241–246, 1995.
- [130] JP Hartnett and RYZ Hu. The yield stress - an engineering reality. *J Rheol*, 33(4):671–679, 1989.
- [131] J Schurz. The yield stress - an empirical reality. *Rheol Acta*, 29(2):170–171, 1990.

- [132] HA Barnes. The 'yield stress myth?' paper - 21 years on. *Appl Rheol*, 17(4):43110, 2007.
- [133] P Uhlherr, J Guo, C Tiu, X Zhang, J Zhou, and T Fang. The shear-induced solid-liquid transition in yield stress materials with chemically different structures. *Journal of Non-Newtonian Fluid Mechanics*, 125(2-3):101–119, 2005.
- [134] DD Atapattu, RP Chhabra, and PHT Uhlherr. Creeping sphere motion in herschel-bulkley fluids - flow-field and drag. *Journal of Non-Newtonian Fluid Mechanics*, 59(2-3):245–265, 1995.
- [135] DD Atapattu, RP Chhabra, and PHT Uhlherr. Wall effect for spheres falling at small reynolds-number in a viscoplastic medium. *Journal of Non-Newtonian Fluid Mechanics*, 38(1):31–42, 1990.
- [136] François Lequeux and Armand Ajdari. Averaging rheological quantities in descriptions of soft glassy materials. *Phys. Rev. E*, 63(3):3, 2001.
- [137] D Bonn, P Coussot, HT Huynh, F Bertrand, and G Debregas. Rheology of soft glassy materials. *Europhys Lett*, 59(5):786–792, 2002.
- [138] B Abou, D Bonn, and J Meunier. Nonlinear rheology of laponite suspensions under an external drive. *J Rheol*, 47(4):979–988, 2003.
- [139] L Berthier, JL Barrat, and J Kurchan. A two-time-scale, two-temperature scenario for nonlinear rheology. *Phys. Rev. E*, 61(5):5464–5472, 2000.
- [140] C Derec, A Ajdari, and F Lequeux. Mechanics near a jamming transition: a minimalist model. *Faraday Disc.*, 112:195–207, 1999.
- [141] F Varnik, L Bocquet, and JL Barrat. A study of the static yield stress in a binary lennard-jones glass. *J Chem Phys*, 120(6):2788–2801, 2004.
- [142] P Hebraud and F Lequeux. Mode-coupling theory for the pasty rheology of soft glassy materials. *Phys Rev Lett*, 81(14):2934–2937, 1998.
- [143] V Viasnoff, S Jurine, and F Lequeux. How are colloidal suspensions that age rejuvenated by strain application? *Faraday Disc.*, 123:253–266, 2003.
- [144] F Lequeux and A Ajdari. Averaging rheological quantities in descriptions of soft glassy materials. *Phys Rev E*, 63(3):030502, 2001.
- [145] RML Evans, ME Cates, and P Sollich. Diffusion and rheology in a model of glassy materials. *Eur Phys J B*, 10(4):705–718, 1999.
- [146] EW Flick. *Cosmetic Additives: An Industrial Guide*. William Andrew Inc., 1990.

- [147] NJ Alderman, GH Meeten, and JD Sherwood. Vane rheometry of bentonite gels. *Journal of Non-Newtonian Fluid Mechanics*, 39(3):291–310, 1991.
- [148] P Coussot, JS Raynaud, F Bertrand, P Moucheront, JP Guilbaud, HT Huynh, S Jarny, and D Lesueur. Coexistence of liquid and solid phases in flowing soft-glassy materials. *Phys. Rev. Lett.*, 88(21):218301, 2002.
- [149] R Mas and A Magnin. Rheology of colloidal suspensions - case of lubricating greases. *J Rheol.*, 38(4):889–908, 1994.
- [150] HJ Butt, K Graf, and M Kappl. *Physics and Chemistry of Interfaces*. Wiley-VCH, 2006.
- [151] R Buscall, PDA MILLS, and GE YATES. Viscoelastic properties of strongly flocculated polystyrene latex dispersions. *Colloid Surface*, 18(2-4):341–358, 1986.
- [152] CJ Rueb and CF Zukoski. Viscoelastic properties of colloidal gels. *J Rheol.*, 41(2):197–218, 1997.
- [153] DCH Cheng and F Evans. Phenomenological characterization of the rheological behaviour of inelastic reversible thixotropic and antithixotropic fluids. *Brit J Appl Phys*, 16(11):1599–&, 1965.
- [154] O Radulescu, PD Olmsted, JP Decruppe, S Lerouge, JF Berret, and G Porte. Time scales in shear banding of wormlike micelles. *Europhys Lett*, 62(2):230–236, 2003.
- [155] Erik Miller and Jonathan P Rothstein. Transient evolution of shear-banding wormlike micellar solutions. *Journal of Non-Newtonian Fluid Mechanics*, 143(1):22–37, 2007.
- [156] D Bonn, J Meunier, O Greffier, A Al-Kahwaji, and H Kellay. Bistability in non-newtonian flow: Rheology of lyotropic liquid crystals. *Phys Rev E*, 58(2):2115–2118, 1998.
- [157] Pierre Ballesta, M. Paul Lettinga, and Sebastien Manneville. Superposition rheology of shear-banding wormlike micelles. *J Rheol.*, 51(5):1047–1072, 2007.
- [158] Michael Dennin. Discontinuous jamming transitions in soft materials: coexistence of flowing and jammed states. *J Phys-Condens Mat*, 20(28):283103, 2008.
- [159] Christopher Gilbreth, Scott Sullivan, and Michael Dennin. Flow transitions in two-dimensional foams. *Phys Rev E*, 74(5):051406, 2006.
- [160] N Huang, G Ovarlez, F Bertrand, S Rodts, P Coussot, and D Bonn. Flow of wet granular materials. *Phys. Rev. Lett.*, 94:028301, 2005.
- [161] RC Brown. The use of the variational principle in the solution of stokes flow problems in fibrous filters. *J Phys D Appl Phys*, 16(5):743–754, 1983.

- [162] ME Cates and SJ Candau. Statistics and dynamics of worm-like surfactant micelles. *J Phys-Condens Mat*, 2(33):6869–6892, 1990.
- [163] F Lequeux. Structure and rheology of wormlike micelles. *Curr Opin Colloid In*, 1(3):341–344, 1996.
- [164] F Lequeux. Reptation of connected wormlike micelles. *Europhys Lett*, 19(8):675–681, 1992.
- [165] A Khatory, F Lequeux, F Kern, and SJ Candau. Linear and nonlinear viscoelasticity of semidilute solutions of wormlike micelles at high salt content. *Langmuir*, 9(6):1456–1464, 1993.
- [166] V Schmitt, F Schosseler, and F Lequeux. Structure of salt-free wormlike micelles - signature by sans at rest and under shear. *Europhys Lett*, 30(1):31–36, 1995.
- [167] A Khatory, F Kern, F Lequeux, J Appell, G Porte, N Morie, A Ott, and W Urbach. Entangled versus multiconnected network of wormlike micelles. *Langmuir*, 9(4):933–939, 1993.
- [168] MM Britton and PT Callaghan. Shear banding instability in wormlike micellar solutions. *Eur Phys J B*, 7(2):237–249, 1999.
- [169] JB Salmon, A Colin, S Manneville, and F Molino. Velocity profiles in shear-banding wormlike micelles. *Phys Rev Lett*, 90(22):228303, 2003.
- [170] MR Lopez-Gonzalez, WM Holmes, PT Callaghan, and PJ Photinos. Shear banding fluctuations and nematic order in wormlike micelles. *Phys Rev Lett*, 93(26):268302, 2004.
- [171] L Becu, S Manneville, and A Colin. Spatiotemporal dynamics of wormlike micelles under shear. *Phys Rev Lett*, 93(1):018301, 2004.
- [172] Lydiane Becu, Domitille Anache, Sébastien Manneville, and Annie Colin. Evidence for three-dimensional unstable flows in shear-banding wormlike micelles. *Phys Rev E*, 76(1):011503, 2007.
- [173] D Bonn, S Tanase, B Abou, H Tanaka, and J Meunier. Laponite: Aging and shear rejuvenation of a colloidal glass. *Phys. Rev. Lett.*, 89(1):015701, 2002.
- [174] P Wiltzius. Hydrodynamic behavior of fractal aggregates. *Phys. Rev. Lett.*, 58:710, 1987.
- [175] IM Krieger. Rheology of monodisperse lattices. *Adv. Colloid Interface Sci.*, 3:111–136, 1972.

- [176] N Saito. Concentration dependence of the viscosity of high polymer solutions 1, a remark on the hydrodynamical theory of the viscosity of solutions of macromolecules. *J. Phys. Soc. Japan*, 5, 7:4, 447, 1950, 1952.
- [177] D Bedeaux. The effective viscosity for a suspension of spheres. *J. Colloid Interface Sci.*, 118:80, 1987.
- [178] DA Weitz, JS Huang, MY LIN, and J Sung. Dynamics of diffusion-limited kinetic aggregation. *Phys Rev Lett*, 53(17):1657–1660, 1984.
- [179] R Wessel and RC Ball. Fractal aggregates and gels in shear flow. *Phys. Rev. A*, 46:R3008, 1992.
- [180] W Wolthers, MHG Duits, D vandenEnde, and J Mellema. Shear history dependence of the viscosity of aggregated colloidal dispersions. *J Rheol*, 40(5):799–811, 1996.
- [181] Z. Fournier, D. Geromichalos, S. Herminghaus, M. M. Kohonen, F. Mugele, M. Scheel, M. Schultz, B. Schultz, Ch. Schier, R. Seemann, and A. Skudelny. Mechanical properties of wet granular materials. *J. Phys.: Condens. Matter*, 17:S477–S502, 2005.
- [182] P.-G. de Gennes, F. Brochard-Wyart, and D. Quéré. *Capillarity and Wetting Phenomena*. Springer, 2004.
- [183] N. Mitarai and F. Nori. Wet granular materials. *Adv. Phys.*, 55:1–45, 2006.
- [184] S. Herminghaus. Dynamics of wet granular matter. *Adv. Phys.*, 54:221–261, 2005.
- [185] T. C. Halsey and A. J. Levine. How sandcastles fall. *Phys. Rev. Lett.*, 80:3141–3144, 1997.
- [186] S. Timoshenko. *Theory of Elastic Stability*. McGraw Hill, 1982.
- [187] <http://www.matweb.com/search/SearchSubcat.asp>.

Bandes de cisaillement et la transition solide/liquide dans les fluides à seuil

Ce travail présente une étude expérimentale de la transition solide/liquide dans les fluides à seuil non thixotrope qui est complétée par une analyse théorique simple ainsi que par des simulations numériques. Nous remettons en cause dans ce travail l'existence d'un état stationnaire qui mènerait à une limite newtonienne en dessous de la contrainte seuil. Nous introduisons alors un modèle physique simple pour décrire le comportement de ces fluides à seuil. Ce modèle est testé grâce à des simulations numériques qui reproduisent quantitativement les expériences. Nous avons également étudié comment l'existence supposée d'un minimum à $\dot{\gamma}_c$ dans la courbe d'écoulement modifie la transition solide/liquide, ce qui nous a amener à effectuer des tests sur un fluide fortement thixotrope spécialement préparé. Ces tests démontrent ainsi qu'un tel matériau possède effectivement un tel minimum. Nous montrons ensuite que pour de tels matériaux des bandes de cisaillement apparaissent même dans des champs de contraintes homogènes si le taux de cisaillement est inférieur à $\dot{\gamma}_c$ et que le rapport entre la largeur de la bande cisaillée et la largeur total de l'entrefer suit la loi des règles. En plus de ce travail nous avons examiné la contrainte dans les matériaux granulaires humides et introduit un modèle détaillé vérifié expérimentalement qui décrit comment le module élastique de ces matériaux dépend de la taille des grains, de la tension de surface du fluide, du matériau granulaire et de la fraction volumique en liquide.

Shear banding and the solid/liquid transition in yield stress fluids

We study experimentally the solid/liquid transition in non-thixotropic yield stress fluids, and supplement those experiments with simple modeling and simulation. We demonstrate that the usual picture of a Newtonian limit below the yield stress, is in fact due to erroneous measurements, arising from falsely concluding that a steady state has been reached. We introduce a simple physical model for the yielding behavior of such materials and perform simulations that reproduce the experiments. We also study how the existence of a theoretically suggested minimum at $\dot{\gamma}_c$ in the flow curve for thixotropic yield stress fluids would affect the solid/liquid transition, and based on this understanding we perform experimental tests on a highly thixotropic fluid we have made, and demonstrate that indeed this material *has* the theoretically suggested minimum. We go on to demonstrate experimentally that for such materials shear banding occurs even in completely homogeneous stress fields if the imposed shear rate is below $\dot{\gamma}_c$, and that the ratio of the width of the sheared band to the total width of the gap, w_s/w_{tot} follows the 'lever rule': $w_s/w_{\text{tot}} = \dot{\gamma}_{\text{imposed}}/\dot{\gamma}_c$. In addition to this work we examine the strength of moist granular materials and present a detailed model for how the elastic modulus of such materials depends on grain size, fluid surface tension, grain material, and liquid volume fraction that we verify experimentally.